UNIVERSIDADE FEDERAL DO RIO GRANDE DO SUL
INSTITUTO DE GEOCIÊNCIAS
PROGRAMA DE PÓS-GRADUAÇÃO EM GEOCIÊNCIAS

ESTUDO INTEGRADO DOS PEGMATITOS, DA MINERALIZAÇÃO DE URÂNIO E DA GENTHELVITA NO DEPÓSITO Sn-Nb-Ta (ETR, U, Th, F) MADEIRA (MINA PITINGA, AM): A TRANSIÇÃO MAGMÁTICO-HIDROTERMAL E SUAS IMPLICAÇÕES METALOGENÉTICAS

INGRID WEBER HADLICH

ORIENTADOR – Prof. Dr. Artur Cezar Bastos Neto
COORIENTADOR – Prof. Dr. Vitor Paulo Pereira

Porto Alegre, 2023

UNIVERSIDADE FEDERAL DO RIO GRANDE DO SUL
INSTITUTO DE GEOCIÊNCIAS
PROGRAMA DE PÓS-GRADUAÇÃO EM GEOCIÊNCIAS

ESTUDO INTEGRADO DOS PEGMATITOS, DA MINERALIZAÇÃO DE URÂNIO E DA GENTHELVITA NO DEPÓSITO Sn-Nb-Ta (ETR, U, Th, F) MADEIRA (MINA PITINGA, AM): A TRANSIÇÃO MAGMÁTICO-HIDROTERMAL E SUAS IMPLICAÇÕES METALOGENÉTICAS

INGRID WEBER HADLICH

ORIENTADOR – Prof. Dr. Artur Cezar Bastos Neto
COORIENTADOR – Prof. Dr. Vitor Paulo Pereira

BANCA EXAMINADORA
Prof. Dra. Lydia Maria Lobato – Instituto de Geociências, Universidade Federal de Minas Gerais
Dra. Lucy Takehara Chemale – Serviço Geológico do Brasil
Prof. Dr. José Carlos Frantz – Instituto de Geociências, Universidade Federal do Rio Grande do Sul

Tese de Doutorado apresentada como requisito parcial para a obtenção do Título de Doutor em Ciências.

Porto Alegre, 2023

CIP - Catalogação na Publicação

Hadlich, Ingrid Weber
ESTUDO INTEGRADO DOS PEGMATITOS, DA MINERALIZAÇÃO DE URÂNIO E DA GENTHELVITA NO DEPÓSITO Sn-Nb-Ta (ETR, U, Th, F) MADEIRA (MINA PITINGA, AM): A TRANSIÇÃO MAGMÁTICO-HIDROTERMAL E SUAS IMPLICAÇÕES METALOGENÉTICAS / Ingrid Weber Hadlich. -- 2023.
215 f.
Orientador: Artur Cezar Bastos Neto.

Coorientador: Vitor Paulo Pereira.

Tese (Doutorado) -- Universidade Federal do Rio Grande do Sul, Instituto de Geociências, Programa de Pós-Graduação em Geociências, Porto Alegre, BR-RS, 2023.

1. evolução magmático-hidrotermal. 2. pegmatitos. 3. mineralização de urânio. 4. genthelvita. I. Bastos Neto, Artur Cezar, orient. II. Pereira, Vitor Paulo, coorient. III. Título.

Elaborada pelo Sistema de Geração Automática de Ficha Catalográfica da UFRGS com os dados fornecidos pelo(a) autor(a).

Dedico este trabalho ao Esdras C. Villela, grande companheiro dos estudos geólogicos e da vida, com o qual muito aprendo todos os dias.

AGRADECIMENTOS

A elaboração desta tese foi financiada pelo Conselho Nacional de Desenvolvimento Científico e Tecnológico (CNPq) através dos projetos “Geologia, mineralogia e caracterização tecnológica do minério no depósito do Granito Madeira e em planta piloto, com vistas à exploração de ETRP na mina Pitinga (AM): avaliação do potencial para ETRP de granitos análogos na Província Estanífera de Goiás” (CNPq - 405839/2013-8), e “Depósitos Polimetálicos de Metais Raros: modelagem metalogenética dos depósitos Madeira (Mina Pitinga) e Morro dos Seis Lagos e estudos de casos análogos” (CNPq - 304990/2017-5). Ambos os projetos são vinculados ao Grupo de Pesquisa Mineralogia e Geoquímica de Depósitos Minerais da Universidade Federal do Rio Grande do Sul (UFRGS).

Este trabalho foi apoiado pelo CNPq através de concessão de bolsa de doutorado, pelo Programa de Pós-Graduação de Geociência (PPGGEO) da UFRGS, e por colaboradores do Instituto de Geociências da Universidade de Brasília, do Centro de Engenharias da Universidade Federal de Pelotas, e do Instituto de Geociências da Leibniz University (Hannover, Alemanha). O orientador Artur C. Bastos Neto e o coorientador Vitor P. Pereira desempenharam um papel fundamental no desenvolvimento desta tese. Suas valiosas contribuições foram de inestimável importância para a qualidade e o sucesso deste trabalho acadêmico.

RESUMO

Este trabalho apresenta o estudo integrado dos pegmatitos, da mineralização de urânio e da genthelvita no albita granito Madeira (1,8 Ga). Este é um granito peralcalino do tipo-A e corresponde ao singular depósito de Sn-Nb-Ta (ETR, Th, U) Madeira (164 Mt) (Pitinga, AM), tendo sido fortemente afetado por fluidos hidrotermais ricos em F. A mineralização de U apresenta teores (328 ppm UO_2) comparáveis aos principais depósitos intrusivos no mundo, além de possuir reservas significativas (52 kt U). No entanto, contrasta com estes depósitos em quatro aspectos chave: mineralização homogeneamente dispersa; U-Pb-ETRL-pirocloro como único mineral de minério primário; mineralizações de U e Th formados em diferentes estágios magmáticos; e alteração hidrotermal intensa, formando como produtos de alteração pirocloro secundário, columbita, fluoretos de ETRL, galena e silicatos ricos em U (Th, Zr, ETR, Y, Pb). Estas características são atribuídas às condições especiais impostas pela riqueza em flúor do magma peralcalino. Os complexos de flúor transportaram por todo o plúton e enriqueceram a fusão residual com Li, Na, K, Rb e metais raros (U, Th, ETR, Be, Zr, Nb, Ta), contribuindo para o enriquecimento progressivo de ETRP e F em direção à paragênese dos pegmatitos associados. O albita granito hospeda quatro tipos de pegmatitos: pegmatitos de borda, albita granito pegmatítico, pegmatito miarolítico e veios de pegmatito. A própria rocha hospedeira serviu como fonte para os fluidos que originaram todos estes pegmatitos. Assim como a rocha parental, os pegmatitos apresentam uma paragênese exótica rica em metais raros, incluindo pirocloro (herdado do albita granito), cassiterita, zircão, torita, xenotima, gagarinita-(Y), criolita e genthelvita. A origem destes pegmatitos está associada a vários processos físico-químicos que ocorreram durante diferentes estágios da evolução magmática, cada tipo associado com mecanismos de colocação distintos. Nos veios de pegmatito, a redução efetiva na fugacidade de H_2S e a alta atividade de oxigênio em um ambiente alcalino e subaluminoso, sob temperaturas relativamente altas (>375ºC), permitiu a estabilidade da genthelvita entre os estágios magmático tardio e hidrotermal precoce na evolução do sistema albita granito. A transição magmático-hidrotermal ocorreu para cada corpo rochoso individualmente – albita granito, pegmatitos –, quando a fase aquosa residual foi exsolvida da rocha cristalizada, com uma composição refletindo o grau de fracionamento do magma no ponto de saturação de H_2O. O fluido hidrotermal exsolvido rico em F causou alteração (autometassomatismo) nos minerais magmáticos e precipitou minerais secundários.

Palavras chave: mineralização de urânio, pegmatitos, transição magmático-hidrotermal, flúor.

ABSTRACT

This work presents an integrated study of pegmatites, uranium and genthelvite mineralization in the albite-enriched granite Madeira (1.8 Ga). This is an A-type peralkaline granite and corresponds to the Sn-Nb-Ta (REE, Th, U) Madeira (164 Mt) (Pitinga, AM) deposit, having been heavily affected by F-rich hydrothermal fluids. The U mineralization presents grades (328 ppm UO_2) comparable to the main intrusive deposits in the world, and holds significant reserves (52 kt U). However, it contrasts with these deposits in four key respects: homogeneously dispersed mineralization; U-Pb-LREE-rich pyrochlore as the only primary ore mineral; mineralizations of U and Th formed in different magmatic stages; and intense hydrothermal alteration, forming secondary pyrochlore, columbite, LREE-rich fluorides, galena, and U-rich silicates (Th, Zr, REE, Y, Pb) as alteration products. These characteristics are attributed to the special conditions imposed by the fluorine richness of the peralkaline magma. Fluorine complexes transported throughout the pluton and enriched the residual fusion with Li, Na, K, Rb and rare metals (U, Th, REE, Be, Zr, Nb, Ta), contributing to the progressive enrichment of HREE and F towards the paragenesis of the associated pegmatites. The albite-enriched granite hosts four types of pegmatites: border pegmatites, pegmatitic albite-enriched granite, miarolitic pegmatite, and vein pegmatite. The host rock itself served as a source for the fluids that gave rise to all these pegmatites. Like the parent rock, the pegmatites exhibit an exotic paragenesis rich in rare metals, including pyrochlore (inherited from the albite-enriched granite), cassiterite, zircon, thorite, xenotime, gagarinite-(Y), cryolite and genthelvite. The origin of these pegmatites is associated with several physical-chemical processes that occurred during different stages of magmatic evolution, each type associated with different emplacement mechanisms. In the pegmatite veins, the effective reduction in the fugacity of H_2S and the high oxygen activity in an alkaline and subaluminous environment, under relatively high temperatures (>375ºC), allowed the stability of genthelvite between the late magmatic and early hydrothermal stages in the evolution of the albite-enriched granite system. The magmatic-hydrothermal transition occurred for each rock body individually – albite-enriched granite, pegmatites –, when the residual aqueous phase was exsolved from the crystallized rock, with a composition reflecting the degree of fractionation of the magma at the point of H_2O saturation. The F-rich exsolved hydrothermal fluid caused alteration (autometasomatism) in the magmatic minerals and precipitated secondary minerals.

Keywords: uranium mineralization, pegmatites, magmatic-hydrothermal transition, fluorine.

SUMÁRIO

1 INTRODUÇÃO 5
1.1 Objetivos 6
1.2 Estrutura da Tese 7
2 GEOLOGIA LOCAL 9
2.1 A Suíte Estanífera Madeira 9
2.2 A facies mineralizada albita granito Madeira 10
2.3 O Depósito Madeira 12
2.4 Modelo genético do albita granito 13
3 URÂNIO 15
3.1 Depósitos de U 15
3.2 Minérios de U 16
3.3 Pirocloro 16
3.3.1 Alteração do pirocloro 16
3.4 Geoquímica do U 17
4 PEGMATITOS GRANÍTICOS 19
4.1 O que é um pegmatito? 19
4.2 Composição dos pegmatitos graníticos 19
4.3 Colocação dos pegmatitos 20
4.4 Stockscheider: os pegmatitos de borda 20
4.5 Classificação para pegmatitos 20
4.6 Gênese dos pegmatitos graníticos 22
4.7 Comparando os modelos de gênese dos pegmatitos 23
5 GENTHELVITA 26
5.1 Cristaloquímica comparativa de Be, Zn, Fe e Mn 26
5.2 Estabilidade da genthelvita 27
5.3 Ocorrências de genthelvita 28
6 RESULTADOS 29
6.1 Uranium mineralization in the Madeira Sn-Nb-Ta (U, Th, REE, F) world-class deposit (Pitinga, Amazonas State, Brazil): pyrochlore and its alteration products under hypogene conditions 29
6.2 Pegmatites hosted by the albite-enriched granite at the Madeira Sn-Nb-Ta-F world-class deposit, Pitinga Province, Amazonas, Brazil 87

6.3 Mn-Fe-rich genthelvite from pegmatites associated with the Madeira Sn-Nb-Ta world-class deposit (Pitinga, Brazil): new constraints on the magmatic-hydrothermal transition in the albite-enriched granite system 165

7 CONCLUSÃO 200

8 BIBLIOGRAFIA 204

9 ANEXOS 211

9.1 Anexo A – Mapa Geológico Regional 211

9.2 Anexo B – Minerais da Mina de Pitinga e suas fórmulas químicas 212

1 INTRODUÇÃO

O albita granito é uma intrusão peralcalina do tipo-A (1,8 Ga, Bastos Neto et al., 2014), com cerca de 1 km^2, localizado na Província Estanífera de Pitinga (Bettencourt *et al*., 2016), Amazonas. Esta rocha é a fácies mais tardia e evoluída do Granito Madeira (Costi *et al*., 2009; Ferron *et al*., 2010), e corresponde ao Depósito Madeira (164 Mt), um depósito mineral de classe mundial de Sn, tendo como subproduto uma liga de Nb-Ta, e apresentando como potenciais subprodutos uma vasta gama de elementos, principalmente F, Zr, Y, ETR, Th, U e Li (Bastos Neto *et al*., 2005, 2009).

Toda a paragênese mineral do albita granito foi alterada por fluidos hidrotermais tardi-magmáticos (Bastos Neto et al., 2005, 2009; Minuzzi et al., 2008; Ronchi *et al*., 2011; Nardi *et al*., 2012; Hadlich et al., 2019). Criolita magmática e hidrotermal ocorre disseminada pelo núcleo do albita granito, e um depósito hidrotermal de criolita maciça (10 Mt, 37 wt.% Na_3AlF_6) ocorre no eixo central deste corpo rochoso (Bastos Neto *et al*., 2005; 2009), evidenciando a riqueza em F deste sistema magmático-hidrotermal.

A ocorrência de criolita juntamente com estanho, nióbio e vários outros metais raros dentro do mesmo granito peralcalino que abriga um depósito de criolita maciça é incomparável em todo o mundo. Além disso, foram observados hospedados pelo albita granito pegmatitos de elementos raros na forma de veios e cavidades miarolíticas (Paludo *et al*., 2018; Ronchi *et al*., 2019), diques de granito pegmatítico (Bastos Neto *et al*., 2009; Stolnik, 2015), além de pegmatitos de borda (Costi, 2000; Lengler, 2016), localizados no limite com as fácies mais antigas do Granito Madeira. Estes pegmatitos têm sido lavrados indistintamente junto com o minério disseminado na Mina Pitinga.

Grande parte dos pegmatitos graníticos representam o estágio terminal no fracionamento dos magmas graníticos, mas se eles são rochas ígneas, tardias e diferenciadas, ou se são precipitados por fluidos subsolidus e hidrotermais, ainda é um tema em discussão (Valley, 2012). O estudo dos processos de formação de pegmatitos é um desafio à nossa capacidade de discernir, além de qualquer dúvida razoável, o que é ígneo e o que é hidrotermal (London & Kontak, 2012). Nesta tese, investigamos os possíveis mecanismos de formação dos pegmatitos associados ao albita granito. Utilizou-se uma abordagem integrada que combina dados estruturais, geoquímica de rocha total e estudos cristaloquímicos de minerais específicos, como riebeckita, polilithionita, gagarinita e genthelvita, obtidos pelo grupo de pesquisa da Universidade Federal do Rio Grande do Sul. Além disso, foi realizada uma comparação abrangente com a rocha hospedeira para maior compreensão da evolução metalogenética e da transição magmático-hidrotermal deste sistema granito-pegmatitos extremamente rico em flúor.

A Mina Pitinga é reconhecida como uma das mais radioativas do Brasil. Com as projeções de aumento da demanda por urânio na indústria de energia nuclear, especialmente devido à construção de novos reatores nucleares (IAEA, 2016, 2020), torna-se imperativo investigar depósitos potenciais desse elemento. Esta tese contribui para aprofundar o entendimento sobre os aspectos metalogenéticos da mineralização de urânio do albita granito, através do estudo detalhado do mineral de minério primário pirocloro e seus produtos de alteração hipogênica. Este trabalho completa o estudo dos elementos radioativos da Mina Pitinga, iniciado pela pesquisa anterior que se concentrou na mineralização de torita, realizada por Hadlich *et al*. (2019), e destaca a influência do flúor na formação deste depósito de U, que contrasta com outros depósitos intrusivos em vários aspectos cruciais. Além disto, esta pesquisa apresenta as variações nos produtos da alteração do pirocloro primário entre as subfacies do albita granito e os tipos de pegmatitos associados, trazendo novas descobertas sobre a origem e a composição dos fluidos hidrotermais envolvidos, bem como uma compreensão mais profunda da transição magmático-hidrotermal que ocorreu associada à esta intrusão peralcalina verdadeiramente excepcional.

Por fim, esta tese demonstra que a ocorrência de genthelvita ($Zn_4Be_3Si_3O_{12}S$) mais importante do Brasil é a observada no Depósito Madeira, situada nos pegmatitos hospedados pelo albita granito. A presença de genthelvita é de notável importância devido à sua extrema raridade no mundo, tornando-o um mineral de destaque nos pegmatitos do albita granito. A raridade da genthelvita resulta, em grande parte, do seu estreito intervalo de estabilidade (Burt, 1980, 1988; Deer *et al*., 2004). Este mineral é altamente sensível às condições de oxirredução, à presença de sulfetos e à alcalinidade do sistema, o que limita consideravelmente as condições propícias para a sua formação. Neste contexto, o estudo cristaloquímico da genthelvita e de suas associações minerais desempenhou um papel importante na compreensão das implicações de sua formação para as condições físico-químicas envolvidas na gênese dos pegmatitos hospedeiros.

1.1 *Objetivos*

Os objetivos gerais desta tese são (1) definir o potencial da mineralização de urânio do Depósito Madeira em comparação a outros depósitos de urânio do tipo intrusivo, (2) propor um modelo para a formação e a origem dos pegmatitos hospedados pelo albita granito, (3) distinguir as diferenças nos eventos hidrotermais entre os tipos de pegmatitos e o albita granito, e (4) contribuir para o entendimento da evolução metalogenética e da transição magmático-hidrotermal do sistema albita-granito e dos pegmatitos associados.

As seguintes metas compõem os objetivos específicos:

(i) Analisar espacialmente e estatisticamente os teores de urânio no albita granito; investigar a formação do mineral de minério de urânio primário, o pirocloro; caracterizar os fluidos hidrotermais que alteraram o pirocloro através das variações nos seus produtos de alteração no albita granito e nos pegmatitos associados; discutir o enquadramento da mineralização de urânio na evolução do depósito Madeira.

(ii) Caracterizar os pegmatitos hospedados pelo albita granito em termos petrológicos, mineralógicos e composicionais; comparar a composição química de minerais chave entre pegmatitos e a rocha hospedeira (pirocloro, polilithionita, riebeckita, gagarinita).

(iii) Caracterizar a genthelvita nos pegmatitos associados ao albita granito; discutir as implicações da ocorrência da genthelvite nas condições de formação dos pegmatitos hospedeiros.

1.2 *Estrutura da Tese*

As considerações iniciais sobre o albita granito Madeira, a formulação do problema de investigação, e os objetivos da pesquisa são apresentadas no capítulo 1 (Introdução).

Na sequência, são apresentadas revisões bibliográficas refletindo a geologia local (capítulo 2) e o estado da arte para os temas da pesquisa, incluindo a geoquímica e geologia econômica do urânio (capítulo 3), o entendimento atual sobre pegmatitos graníticos (capítulo 4) e as condições especiais necessárias para a ocorrência da rara genthelvita (capítulo 5).

Os resultados (capítulo 6) estão divididos em 3 artigos submetidos em periódicos internacionais:

(i) Artigo submetido na revista Economic Geology (A1): *Uranium mineralization in the Madeira Sn-Nb-Ta (U, Th, REE, F) world-class deposit (Pitinga, Amazonas State, Brazil): pyrochlore and its alteration products under hypogene conditions* (capítulo 5.1) – este artigo apresenta o albita granito Madeira como um depósito de urânio comparável com os principais depósitos do tipo intrusivo, com uma caracterização detalhada do piroclоro primário e de sua alteração hidrotermal no albita granito; apresenta-se ainda uma discussão sobre os processos atuantes na formação deste depósito, cujas características contrastam em vários aspectos com os de outras localidades.

(ii) Artigo submetido na revista International Geology Review (A2): *Pegmatites hosted by the albite-enriched granite at the Madeira Sn-Nb-Ta-F world-class deposit, Pitinga Province, Amazonas, Brazil* (capítulo 5.2) – neste artigo, apresenta-se de forma integrada dados estruturais, texturais, mineralógicos e composicionais dos diferentes tipos de pegmatitos hospedados pelo albita granito; são discutidas suas diferentes origens e modelos de formação; a comparação da química de minerais específicos dos pegmatitos e do albita granito aprofundou o entendimento da evolução metalogenética do sistema magmático, e as variações nos produtos de alteração do pirocloro trouxeram insights importantes sobre a origem do fluido hidrotermal e a transição magmático-hidrotermal do sistema granito-pegmatito.

(iii) Artigo submetido na revista Mineralogical Magazine (A4): *Mn-Fe-rich genthelvite from pegmatites associated with the Madeira Sn-Nb-Ta world-class deposit (Pitinga, Brazil): new constraints on the magmatic-hydrothermal transition in the albite-enriched granite system* (capítulo 5.3) – por fim, este artigo apresenta a ocorrência da rara genthelvita nos pegmatitos estudados, com uma variação composicional inédita, refletindo as condições físico-químicas de seu ambiente de formação.

O fechamento da tese com a integração dos três artigos é apresentado na Conclusão (capítulo 7). As referências bibliográficas são aprsentadas no capítulo 8.

2 GEOLOGIA LOCAL

2.1 *A Suíte Estanífera Madeira*

O Cráton Amazônico comporta uma ampla gama de províncias metalogenéticas de classe mundial (Bettencourt *et al*., 2016). Os depósitos de elementos raros mais importantes estão nas Províncias Estaníferas de Pitinga e Rondônia. A Província Estanífera de Pitinga está localizada na porção sul do Escudo das Guianas (Almeida *et al*., 1981), próximo a divisa das Províncias Tectônicas Amazonia Central e Ventuari-Tapajós (Bettencourt *et* al., 2016) (Anexo A). A Província Estanífera de Pitinga é a maior produtora de Sn do Brasil. Os depósitos de minério aluvial foram descobertos em 1979 (Veiga *et al*., 1979) e estão quase exauridos. Os minérios primários estão associados com dois granitos principais portadores de Sn, os granitos tipo-A Madeira e Água Boa (Fig. 1). Ambos os granitos fazem parte da Suíte Madeira, com cerca de 1,83 Ga (Costi, 2000). A Suíte Madiera é hospedada pelas rochas do Grupo Iricoumé (Veiga *et al*., 1979), que predominam na Província de Pitinga (Fig. 1). Elas possuem idades $^{207}Pb/^{206}Pb$ (zircão) entre 1.881±2 e 1.890±2 Ma (Ferron *et al*., 2006). Elas são em sua maioria riolitos efusivos e hipabissais, ignimbritos, tufos ignimbríticos, e depósitos de surge formados em um ambiente subaéreo com atividades efusivas e explosivas cíclicas (Pierosan *et al*., 2011).

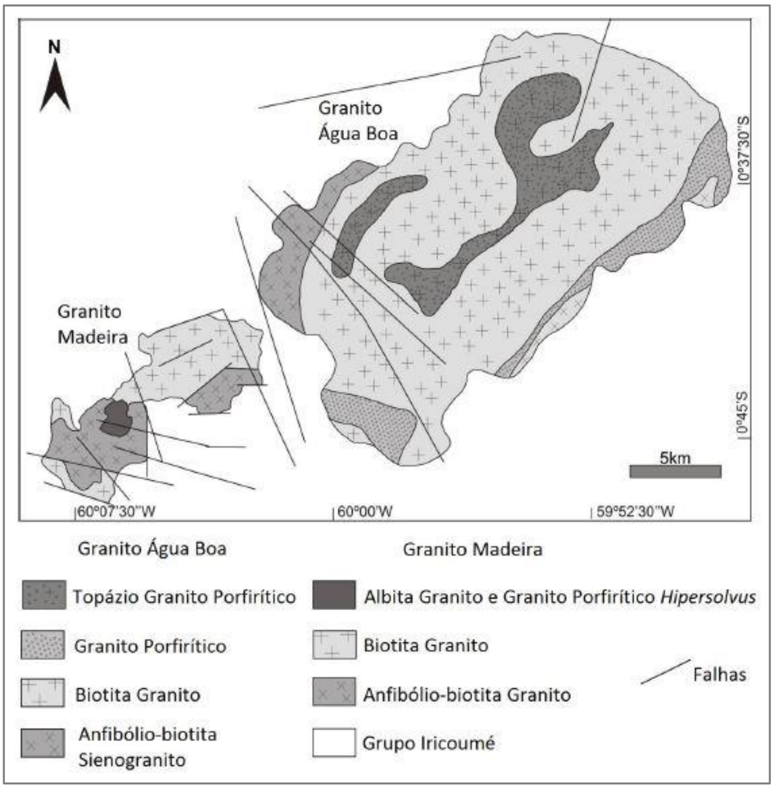

Figura 1. Mapa geológico dos Granitos Madeira e Água Boa (Costi, 2000).

O Depósito Madeira, que vem sendo explotado desde 1989, está associado ao Granito Madeira. Adicionalmente, um número de pequenos greisens associados ao Granito Água Boa tem sido explotados de forma intermitente. O Granito Madeira possui quatro fácies (Fig. 1). A fácies mais antiga consiste em um anfibólio-biotita sienogranito (granito *rapakivi*). Na sequência, instaurou-se a fácies biotita-K-feldspato granito, que é peraluminosa, equigranular, e localmente porfirítica. Por fim, as facies feldspato alcalino granito (*hipersolvus*) e albita granito se colocaram simultaneamente (Costi, 2000), interagindo e intrudindo em meio às fácies mais antigas. A facies *hipersolvus* é porfirítica, possuindo fenocristais de K-feldspato em uma matriz de granulação fina a média, dominantemente composta por quartzo e K-feldspato.

2.2 ***A facies mineralizada albita granito Madeira***

A fácies albita granito do Granito Madeira é um corpo de forma ovalada na direção N-S, com uma superfície aflorante de aproximadamente 2 km de comprimento e 1,5 km de largura (Fig. 2). O albita granito cristalizou entre 1.822 ± 22 Ma e 1.794 ± 19 Ma (Lenharo, 1998). Esta fácies é subdividida nas subfacies albita granito de núcleo e albita granito de borda, devido às características geoquímicas, petrograficas e metalogenéticas das mesmas (Horbe *et al*., 1985). As relações de contato entre ambas as subfácies são marcadas por alterações tardias, caracterizando uma zona transicional, denominada albita granito transicional (Costi, 2000).

O albita granito de núcleo é um granito peralcalino *subsolvus*, com textura porfirítica e localmente seriada, granulação fina a média, e composto por quartzo, albita e K-feldspato em proporções similares (25-30%). Os minerais acessórios são criolita (5%), polilithionita (4%), mica tetraférrica (anita, 3%), zircão (2%) e riebeckita (2%). Em menores proporções ocorrem cassiterita, pirocloro, columbita, torita, xenotima, esfalerita, hematita, e galena, compondo em conjunto 4% do total da rocha. Os minerais gagarinita e fluocerita, entre outros, são mais raros. O albita granito de borda é peraluminoso e possui as mesmas texturas e mineralogia essencial que o albita granito de núcleo, exceto por ser mais rico em zircão (5%), pela presença de fluorita ao invés de criolita, e pela ausência de minerais silicáticos ricos em Fe, os quais desapareceram quase completamente devido a um processo autometassomático (Costi, 2000; Costi *et al*., 2010). Os principais minerais da Mina Pitinga e suas respectivas fórmulas químicas são listados no Anexo B.

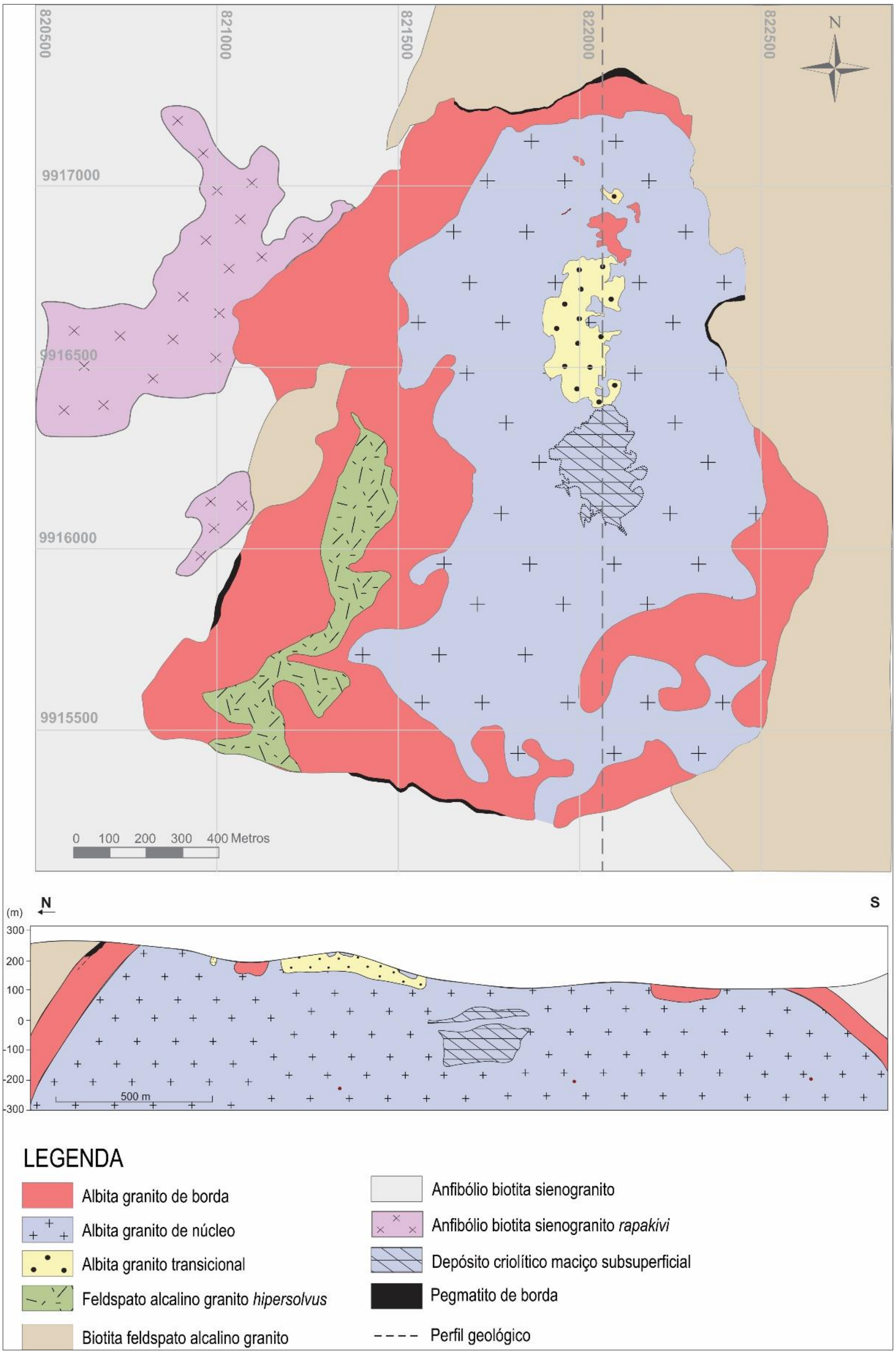

Figura 2. Mapa geológico do albita granito Madeira (adaptado de Minuzzi, 2005).

Toda a paragênese magmática foi afetada por uma alteração hidrotermal (1.784±4 Ma, Lenharo, 1998) relacionada a fluidos aquosos residuais enriquecidos em Na e F, os quais causaram a oxidação, silicificação, fluoritização e argilização das subfacies do albita granito (Ronchi *et al*., 2011). A evolução hidrotermal da paragênese magmática inclui a alteração de K-feldspato e albita em sericita e argilas (ilita, caolinita); alteração da riebeckita e da mica tetraférrica em clorita e óxidos de ferro; a alteração do U-Pb-pirocloro em columbita e galena; a formação de halos de óxido de ferro nos grãos de torita; e a solubilização parcial de zircão (Bastos Neto *et al*., 2005; Costi *et al*., 2005; Minuzzi *et al*., 2006; Weber *et al*., 2007; Ronchi *et al*., 2011; Nardi *et al*., 2012; Hadlich *et al*., 2019). Adicionalmente, este fluido hidrotermal promoveu o enriquecimento da criolita disseminada, e foi responsável pela formação de um depósito de criolita maciça no eixo central do pluton (Bastos Neto *et al*., 2005).

2.3 ***O Depósito Madeira***

O Depósito Madeira corresponde ao albita granito (núcleo+borda). Os teores do minério disseminado são 0,17 wt.% Sn (cassiterita), 0,20 wt.% Nb_2O_5 e 0,024 wt.% Ta_2O_5 (ambos em pirocloro e columbita), em um total de 164 Mt de rocha (Bastos Neto *et al*., 2005). Os subprodutos em potencial do minério disseminado são F (4,2% em peso F, criolita), U (0,03% em peso U, pirocloro e zircão), Th (0,07% em peso Th, torita), Y e ETRP (xenotima, gagarinita-(Y)), Zr e Hf (zircão) (Bastos Neto *et al*., 2005; Minuzzi *et al*., 2006; Pires, 2010; Nardi *et al*., 2012; Hadlich *et al*., 2019). Além disso, na porção central do Depósito Madeira, em subsuperfície, ocorre um Depósito de Criolita Maciça hidrotermal de 10 Mt (31,9% em peso de Na_3AlF_6), constituído por corpos sub-horizontais, de até 300 m de comprimento e 30 m de espessura, compostos por cristais de criolita (87% em volume), quartzo, zircão e feldspato (Bastos *et al*., 2005, 2009; Minuzzi *et al*., 2006).

Uma feição importante do albita granito é a homogeneidade na distribuição dos minerais de Sn, Nb, Ta, ETR, Th, U, que se deve à abundância em F. De acordo com Bastos Neto *et al*. (2009), complexos de F transportaram e distribuíram estes metais de forma homogênea por todo o corpo granítico. Apesar do caráter disseminado das mineralizações do albita granito, existem pequenas zonas de enriquecimento nas quais minerais específicos podem ser consideravelmente abundantes. A existência destas zonas foi citada por diversos autores, e caracterizações parciais foram realizadas pelo grupo de pesquisa da Universidade Federal do Rio Grande do Sul, não tendo sido realizado até a presente data um estudo integrador para esses dados. Estas zonas enriquecidas são o albita granito de núcleo pegmatítico (Bastos Neto *et al*., 2009; Stolnik, 2015), os pegmatitos em cavidades miarolíticas (Bastos *et al*., 2014; Paludo *et al*., 2018; Ronhi *et al*., 2019), os veios de pegmatitos (Costi, 2000; Minuzzi *et al*., 2006; Pires, 2010; Bastos Neto *et al*., 2014; Paludo *et al*., 2018; Ronchi *et al*., 2019) e os pegmatitos de borda (Costi, 2000; Lengler, 2016).

2.4 ***Modelo genético do albita granito***

A temperatura máxima estimada para o início da cristalização do anfibólio-biotita sienogranito (fácies mais antiga do Granito Madeira) é de 930ºC, a uma profundidade aproximada de 15 km (5 kbar) e, para a formação do albita granito, a temperatura máxima é <650ºC, a uma profundidade de cerca de 1 km (1 kbar) (Lenharo *et al*., 2003). A temperatura do *solidus* do albita granito de núcleo é estimada em cerca de 500ºC (Costi *et al*., 2009).

A colocação geotectônica do albita granito foi interpretada de forma diferente por diversos autores: no contexto de uma zona de cisalhamento de direção NE-SW lateral-esquerda (Bastos Neto *et al*., 2014) ou lateral-direita (Siachoque *et al*., 2017), ou ainda pela influência de estruturas N-S (Costi *et al*., 2000; Minuzzi *et al*., 2006). Mais recentemente, Ronchi *et al*. (2019) propuseram que as estruturas contracionais do albita granito não estão relacionadas a regimes transpressivos, mas sim aos esforços finais gerados durante a amalgamação dos terrenos juvenis (2,0 – 1,8 Ga) que resultaram na formação da Província Ventuari-Tapajós.

Dois modelos genéticos principais foram propostos para explicar a origem do albita granito. Costi *et al.* (2009) consideram o albita granito de núcleo como resultado de um processo de separação de fases, ou imiscibilidade, na qual a fase peralcalina é separada do magma parental, provavelmente levemente peralcalino a metaluminoso. Por outro lado, Bastos Neto *et al*. (2009, 2014) consideram que o magmatismo do tipo-A de Pitinga evoluiu de um ambiente distensivo pós-colisional, provavelmente em um cenário intra-placa. Neste contexto, três estágios de ascenção isotermal podem ser identificados (Bastos Neto *et al*., 2009): o primeiro estágio estaria associado ao magmatismo Iricoumé; o segundo estágio levaria a formação das fácies mais antigas do Granito Madeira; e o magma do albita granito estaria relacionado ao terceiro estágio, que teria ocorrido quando o fluido do manto ascendeu ainda mais na crosta, promovendo reações do tipo fenitização em rochas previamente enriquecidas em Sn, e introduzindo elementos como F, Nb, Y, ETR e Th em concentrações anômalas. Durante este último estágio, teria ocorrido a injeção do fluido rico em F, gerando metassomatismo e tornando a rocha fusível.

Lenharo (1998) e Costi (2000) consideram que o magma evoluiu em direção a uma fração residual extremamente enriquecida em Na e F. Lenharo (1998) propôs que o depósito de criolita maciça teria se formado a partir de um magma residual rico em F que se tornou imiscível com o magma silicático. Costi (2000) interpretou que, no ponto de saturação do H_2O, o fluido residual extremamente rico em F se dividiu em uma fase aquosa relativamente pobre em F e em uma fase depletada em H_2O e rica em Na-Al-F. A fase rica em Na-Al-F teria resultado na formação do depósito criolítico maciço, enquanto a fase aquosa pobre em F teria formado as rochas pegmatíticas associadas.

De acordo com Bastos Neto *et al*. (2009), o extremo enriquecimento em F no magma residual dificilmente teria ocorrido, pois o conteúdo de F foi sendo incorporado durante a cristalização da criolita magmática disseminada. Além disso, os dados de inclusões fluidas (Bastos Neto et al., 2009; Ronchi et al., 2011) demonstraram que o depósito de criolita maciça se formou a partir de um fluido aquoso e salino hidrotermal. A maior temperatura de homogeneização de 400ºC obtidas para a criolita determina a temperatura mínima de início do processo hidrotermal; a formação da criolita continuou até cerca de 100ºC. Mesmo com o albita granito de núcleo já totalmente consolidado, o fluido hidrotermal rico em Na-F continuou dissolvendo os minerais magmáticos, criando espaço para o desenvolvimento da criolita maciça (Bastos Neto *et al*., 2005). A criolita maciça hidrotermal mais tardia apresenta salinidades sistematicamente menores, comumente <5 wt.% NaCl, o que pode indicar o aumento de influxo de água meteórica misturando com os fluidos hidrotermais tardios, acarretando também nas alterações de oxidação, silicificação e argilização (Bastos Neto *et al*., 2005; Ronchi *et al*., 2011).

3 URÂNIO

O mercado de geração de energia elétrica é o principal consumidor de urânio. Cerca de 11% da eletricidade global é gerada por 438 reatores nucleares, que requerem até 66.883 t de urânio anualmente (WNA, 2015). À medida que a utilização da energia nuclear aumentou, a procura de combustível nuclear também continuou a crescer. Isto levou a novos desafios, uma vez que os recursos de urânio de alto teor se tornaram mais escassos nos últimos anos. Por esta razão, o foco no processamento de minerais de urânio mais difíceis de extrair (refratários), como a betafita (McMaster, 2016), tornou-se de importância crescente. Além disso, há uma ênfase no processamento mais direcionado de depósitos de menor teor, uma vez que o rejeito radiotivo é significativamente problemático nestes depósitos (Pownceby & Johnson, 2014).

3.1 *Depósitos de U*

O U é um elemento extensamente difundido na crosta, porém com concentrações baixas, com média de 1,7 ppm U (Clark et al., 1966). Nos granitos/riolitos as concentrações médias de urânio são de 4,5 ppm (Kyser & Cuney, 2015). Em depósitos minerais, as concentrações de U variam de 300 ppm U (baixo teor), até 2% (20.000 ppm U) para um depósito de alto teor, embora concentrações de até 20% U já tenham sido registrados (AIEA, 2014).

O urânio é normalmente encontrado em 15 tipos de depósitos classificados pela Agência Internacional de Energia Atômica (AIEA, 2020). Nos depósitos relacionados à cristalização fracionada, geralmente os recursos são de alta tonelagem, mas com teores baixos. Entre os principais depósitos de U deste tipo estão o depósito de Kvanefjeld na Groenlândia (U+ETR, Zn, Be, F, Nb, Th) (Sørensen *et al*., 2011), com 0,22 Mt em teores de ~240 ppm UO_2 (Kyser & Cuney, 2015), o depósito de Bokan Mountain, no Alaska, com 89.000 t em teores de 0,85% UO_2 (Staatz, 1978) e o depósito de Ghurayytah, na Arábia Saudita (U+Ta, Th, Nb, ETR, Y, Zr), com 45.700 t e teor de 120 ppm UO_2 (Drysdall *et al*., 1984).

Nestes depósitos, quando a fusão tipicamente peralcalina cristaliza, são formados complexos de óxido, fosfato e silicato de U-Th-Zr-ETR-Nb, os quais são muito refratários para a recuperação econômica do U. Somente a extração simultânea dos metais associados ao U pode tornar economicamente viável a mineração de tais depósitos (Cuney, 2014).

3.2 *Minérios de U*

Nos depósitos de urânio, este elemento geralmente está distribuído em vários minerais, dependendo da gênese do minério. Os mais de 200 minerais contendo urânio foram subdivididos em minerais primários, secundários e refratários. Os minerais mais comuns são os primários, com U^{4+} reduzido (ex. uraninita, coffinita) que se formam durante a cristalização do magma e geralmente são encontrados em associação com feldspato e quartzo. A maioria dos demais minerais de urânio exploráveis são os secundários, comumente encontrados no estado de oxidação U^{6+} (ex. carnotita, autunita, uranofano). Outros minerais de urânio menos comumente explorados são os refratários (ex. brannerita, davidita e minerais do supergrupo pirocloro) (Pownceby & Johnson, 2014).

3.3 *Pirocloro*

O pirocloro pertence ao grupo espacial Fd3m, e sua composição química é descrita pela fórmula geral de $A_{2-m}B_2X_{6-w}Y_{1-n} \cdot pH_2O$, onde m = 0–1,7, w = 0–0,7, n = 0–1 e p = 0–2 (Hogarth, 1977; Lumpkin & Ewing, 1992, 1995, 1996; Atencio *et al*., 2010). O sítio A é geralmente ocupado por Na, Ca, Sr, Pb, Sn^{2+}, Sb^{3+}, Y, U, Mn, Sc, Ba, Fe^{2+}, REE, Bi^{3+}, Th, H_2O e □ (vacância). O sítio B é comumente ocupado por Ta, Nb, Ti, Sb^{5+}, W, V^{5+}, Sn^{4+}, Zr, Hf, Fe^{3+}, Mg, Al e Si. Os sítios X e Y são ocupados por O, OH, F, H_2O, K, Cs, Rb e □ (Lumpkin & Ewing, 1995; Atencio *et al*., 2010). Este mineral é geralmente encontrado em rochas graníticas e sieníticas e suas fácies pegmatíticas (Bea, 1996).

3.3.1 Alteração do pirocloro

Estudos experimentais em minerias do supergrupo pirocloro ricos em U, sob condições hidrotermais (T = 100–300°C), revelaram comportamento de dissolução incongruente, com diferentes taxas de liberação para vários elementos (Roberts *et al*., 2000; Xu *et al*., 2004; Pöml *et al*., 2011). Na maioria dos casos, a alteração do pirocloro resulta na formação de porosidade, como microfissuras nos limites dos grãos entre a fase original e as fases secundárias, o que promove a migração de fluidos. Por sua vez, a lixiviação leva à formação de uma camada amorfa e/ou várias fases cristalinas na superfície do pirocloro.

O pirocloro pode se transformar em minerais não-pirocloro, dos quais a columbita e a fersmita foram definitivamente identificadas (Van der Veen, 1963). James & McKie (1958) descreveram bordas e veios de columbita em grão de pirocloro, bem como pseudomorfos de columbita nos carbonatitos Mbeya e Ngualla em Tanganica. Sorum (1955) e Saerther (1957) mencionaram um composto intermediário entre pirocloro e columbita.

3.4 *Geoquímica do U*

O urânio, de número atômico 92 e massa atômica 238,0289 amu, é um metal branco a cinza-prateado de densidade muito elevada (19.050 kg/m^3). Na coordenação VIII, o U^{4+} possui raio iônico de 0,97 Å, e o U^{6+} possui raio iônico de 0,86 Å (KRAUSKOPF, 1967). Em magmas com baixa fugacidade do oxigênio domina a ocorrência do U^{4+}, o qual é altamente imóvel em solução e em ambiente de baixa temperatura, precipitando na forma de minerais insolúveis (Cuney & Kyser, 2008). As condições de Eh e pH que tornam o U^{4+} estável praticamente coincidem com as condições que estabilizam as espécies reduzidas de S (H_2S, HS^- e S^{-2}), sendo comum por exemplo, a ocorrência simultânea de uraninita (UO_2) e da pirita (FeS_2) (Chaves, 2005). Por outro lado, o U^{6+} é típico de condições oxidantes e é mais solúvel em líquidos silicáticos. Em solução, o U^{6+} forma o íon uranila (UO_2^{2+}), que possui alta mobilidade e constitui complexos com ânions como CO_3^{2-}, SO_4^{2-} e PO_4^{2-} para mover-se em solução (Cuney & Kyser, 2008; Langmuir, 1978).

Os principais mecanismos de transferência do U^{4+} do manto para a crosta terrestre são a fusão parcial e a cristalização fracionada (Cuney, 2010). Em fusões silicáticas o U dissolve de acordo com o grau de despolimerização do magma, que, por sua vez, depende da composição da fusão. Concentrações altas de K, Ca e principalmente Na, são responsáveis pela quebra das cadeias tetraédricas de Si-Al na fusão, permitindo a despolimeralização e solubilididade de íons de alto potencial iônico, como o Th, U, Zr e ETR (Cuney & Kyser, 2008; Pointer, 1987). Por este motivo, nas rochas ígneas, o urânio é intimamente associado com Th, Zr, Ti, Nb, Ta e ETR, sendo particularmente abundante em rochas peralcalinas, ocorrendo em menor proporção em rochas metaluminosas e muito pouco em rochas peraluminosas (Cuney & Kyser, 2008).

Entretanto, em fusões portadoras de F, a quantidade de álcalis e a fugacidade de oxigênio se tornam negligentes no controle da solubilidade do urânio. Isso ocorre, pois o flúor reage com o Al para formar o AlF_6^{-3}, despolimerizando a trama tetraédrica alumino-silicática (Cuney & Kyser, 2008). Além disso, o F pode complexar com o U, formando o

UF_6, que podem ser retidos na fusão ou removidos deste ao ser fracionado em fases fluidas durante processo de autometassomatismo (Pointer, 1987).

As principais características que tornam granitoides potenciais depósitos magmáticos de U são as seguintes: possuir composição peralcalina, cálcio-alcalina metaluminosa de alto-K ou peraluminosa; ser um pegmatóide anatético; haver enriquecimento em voláteis como H_2O e F, com minerais como fluorita e micas; ter sua colocação ao longo de zonas de falha; possuir idade paleoproterozoica; e possuir afinidade do tipo-A com ocorrência de minerais refratários (Abdalla *et al*., 1996; Cuney, 2014).

4 PEGMATITOS GRANÍTICOS

4.1 *O que é um pegmatito?*

As rochas pegmatíticas são rochas cristalinas de granulometria muito grossa, as quais, em parte, contêm cristais gigantes de feldspato, quartzo ou mica que contrastam fortemente com granitos composicionalmente similares, geralmente presentes nas proximidades. Estas características chamam a atenção de empresários, engenheiros de minas e entusiastas de minerais para estas acumulações de minerais industriais e raros (Dill, 2015). Texturas pegmatíticas podem ser encontradas em rochas ígneas principalmente de composições graníticas (cálcio-alcalinas) e sieníticas (alcalinas), que também diferem entre si quanto ao conteúdo de elementos raros. O primeiro tipo, presente em regimes geodinâmicos orogênicos, contém, por exemplo, Li, U, Ta, B, enquanto o outro tipo, confinado a regimes anorogênicos, é enriquecido em Nb, Zr, Th e Mo (Dill, 2015).

4.2 *Composição dos pegmatitos graníticos*

A grande maioria dos pegmatitos graníticos possuem composições haplograníticas, muito próximas à composição térmica mínima dos granitos naturais no sistema $NaAlSi_3O_8$–$KAlSi_3O_8$–Al_2O_3–SiO_2, que inclui rochas com proporções quase iguais de quartzo, plagioclásio sódico e feldspato potássico (London & Kontak, 2012).

O quartzo e os feldspatos são os minerais dominantes que se cristalizam a partir das fusões graníticas, e os elementos raros são altamente incompatíveis nesses minerais. Assim, o fracionamento extremo resultante da cristalização prolongada de quartzo e feldspatos pode gerar concentrações muito altas de elementos raros em fusões residuais. Da mesma forma, pegmatitos individuais também consistem em grande parte de quartzo e feldspato, e os elementos raros são concentrados em pequenos volumes (Stilling *et al*., 2006).

O processo de enriquecimento de elementos raros dentro dos pegmatitos parece ocorrer em um sistema essencialmente fechado, proveniente de uma fração menor de líquido silicatado residual derivado de um corpo magmático muito maior. Apesar disso, apenas uma pequena fração de pegmatitos (<1%) exibe associações com fases minerais incomuns contendo elementos raros, como lítio, berílio, césio, boro, fósforo e tântalo (London & Kontak 2012).

4.3 *Colocação dos pegmatitos*

Os pegmatitos possuem uma representação tridimensional na natureza, tendo sido colocado em relação ao espaço de acomodação fornecido pelos processos geológicos. São, por isso, relacionados no tempo e no espaço às perturbações estruturais, como parte de uma orogênia ou ainda à evolução geodinâmica de uma porção da rocha crustal e sua porção subcrustal subjacente (Dill, 2015).

Segundo Dill (2015), ignorar os parâmetros geológicos se torna um obstáculo para um progresso real na compreensão da origem e colocação dos pegmatitos e oculta ainda mais o escopo da geologia econômica dos pegmatitos. Os efeitos dos processos geológicos crustais e subcrustais na colocação e alteração de pegmatitos e o posicionamento dos pegmatitos em relação à evolução geodinâmica da crosta são demonstrados nas províncias pegmatíticas Paleozoica Européia-Americana e na Pré-Cambriana Afro-Americana no minucioso trabalho de Dill (2015).

4.4 *Stockscheider: os pegmatitos de borda*

Os pegmatitos de borda, ou pegmatitos de contato, foram inicialmente estudados na região minerária de Erzgebirge, Alemanha, onde eles foram chamados de *stockscheiders*, termo alemão que significa literalmente 'separador de *stock*'. O termo *stockscheider* se difundiu no mundo para definir pegmatitos dispostos nos limites de contato entre intrusões magmáticas e suas rochas encaixantes mais antigas, embora este termo não conste oficialmente no Glossário de Geologia do Instituto Americano de Geologia (Bates & Jackson, 1987).

Estas auréolas pegmatíticas registradas no mundo não estão restritas a um tipo específico de mineralização, textura, profundidade de colocação ou composição da intrusão, embora comumente sejam encontrados nas margens de intrusões graníticas associadas com mineralizações de Sn-W, e sua mineralogia seja comumente dominada por K-feldspato, com orientação dos cristais perpendiculares ao contato com a rocha a qual bordeia.

4.5 *Classificação para pegmatitos*

O sistema mais difundido de classificação de pegmatitos graníticos os distingue em classes com base no ambiente de suas rochas hospedeiras (classe abissal), mineralogia (classe muscovita), composição elementar (classe elemento raro) e textura (classe miarolítica), com uma conotação implícita de seu ambiente de colocação, mais ou menos equivalente à profundidade de formação (Černý & Ercit, 2005). As subclasses, tipos e subtipos de pegmatitos de Černý e Ercit (2005) podem ser atribuídos com pouca ambiguidade às famílias LCT (Li, Cs e Ta) ou NYF (Nb, Y e F). Os pegmatitos LCT, muito mais comuns que os NYF, geralmente são gerados por granitos tipo-S, podendo ser extremamente peraluminosos, sendo formados principalmente em regimes sinorogênicos a regimes orogênicos tardios. Os protólitos iniciais podem ser atribuídos a fontes sedimentares quimicamente maduras (Černý et al., 2012). Os pegmatitos que pertencem à família NYF são distinguidos pela presença de óxidos e silicatos quimicamente complexos que hospedam elementos terras raras pesados, Ti, U, Th e Nb>Ta. A maioria dos pegmatitos pertencentes à família NYF são provenientes de granitos do tipo-A, que se formam em fendas intracontinentais (Černý e Ercit, 2005). A origem dos granitos do tipo-A é mais complexa do que a origem dos granitos do tipo S, podendo envolver episódios sucessivos de injeção crustal ou do manto (Černý et al., 2012).

A maioria dos pegmatitos são corpos intrusivos e, portanto, posteriores às suas rochas hospedeiras imediatamente adjacentes. A pressão e a temperatura na qual o pegmatito cristaliza, portanto, pode ter pouca ou nenhuma relação direta com as condições de formação e com as assembleias minerais de seus hospedeiros. Por estas razões, a aplicação das classes pegmatíticas é repleta de contradição e ambiguidade (Černý *et al*., 2012). A divisão dos pegmatitos com base nos seus elementos traços nas famílias NYF e LCT também recebe muitas críticas. Dill (2015) argumenta que este sistema pode ser usado em alguns casos, mas na maioria das vezes ele não se aplica, como por exemplo, na Província Pegmatítica Hagendorf-Pleystein, onde o Li está presente em três stocks de pegmatitos, enquanto outros aplitos e pegmatitos tabulares são estéreis. Nos corpos com Li, o Cs não desempenha um papel significativo, e o Nb sempre prevalece sobre o Ta, contradizendo, portanto, qualquer classificação destes pegmatitos como pertencendo à família LCT. Embora na literatura pertinente estes pegmatitos sejam categorizados como de elementos raros, da família LCT e do tipo berilo, o berílio ocorre de forma subordinada, estando muito atrás de outros elementos como P e Zn. Além disso, a menos de 1 km de distância do pegmatito LCT, intrude um aplito que pertenceria à família NYF, com altos valores de Ti, Nb, U, Zr, Y, ETR e Th. A consequência desta classificação LCT-NYF é que os sistemas granito-pegmatito LCT são considerados relacionados com granitos tipo-S em ambientes orogênicos, enquanto os sistemas granito-pegmatito NYF são considerados derivados de granitos tardi- a pós-tectônicos anorogênicos do tipo-A. E não é razoável pensar que um sistema de pegmatitos consanguíneos tenha se formado em dois ambientes geodinâmicos tão diferentes em uma escala de 1 km (Dill, 2015).

Um novo esquema de classificação para pegmatitos e aplitos é proposto por Dill (2015), inspirado no seu "Esquema de Classificação de Depósitos Minerais" (Dill, 2010). O esquema de classificação de Dill (2015) é chamado pelo acrônimo CMS, relativo aos parâmetros observados: composição química, assembleia mineral, e geologia estrutural. Esa classificação é essencialmente descritiva, e considera que cada grupo de elementos e cada assembleia mineral dos pegmatitos são divididos em grupos de commodities, que por sua vez serão analisados quanto ao papel geológico e geodinâmico que desempenham no tempo e no espaço. Segundo este modelo, os principais ambientes geradores de pegmatitos são os seguintes: ambientes análogos à orogênia Variscana, caracterizada por espessamento crustal; ambientes do tipo orogênia Alpina, caracterizada por cinturões dobrados; e ambientes do tipo rifte, com afinamento da crosta, e comumente magmatismo alcalino, como por exemplo, no Graben de Oslo, Noruega (Dill, 2015).

4.6 *Gênese dos pegmatitos graníticos*

Os pegmatitos têm sido vistos como rochas essencialmente ígneas devido às suas composições totais. Porém, atualmente não existe um modelo unificado para explicar a origem dos pegmatitos graníticos. Dois conceitos de formação de pegmatitos dominaram o pensamento científico por um século:

(1) Gênese dos pegmatitos pela cristalização fracionada de uma fusão granítica de baixa viscosidade: através deste processo ocorreria a evolução química dos pegmatitos (entre corpos pegmatíticos e dentro de corpos individuais), nos quais elementos raros (Li, Be, Ta, etc.), complexantes (B, P, F, etc.) e outros componentes voláteis (H_2O, Cl, etc.), que são excluídos da cristalização inicial de quartzo e feldspatos, tornariam-se concentrados em direção ao centro dos corpos em uma fração decrescente de fusão residual; eventualmente, esta fusão ficaria saturada em minerais contendo estes componentes exóticos (Cameron *et al*., 1949); e

(2) Gênese dos pegmatitos pela separação por densidade de um fluido aquoso a partir da fusão silicática, e os consequentes efeitos sobre a redistribuição dos componentes: neste processo o magma silicático é a fonte dos elementos constituintes, e as texturas e o zoneamento mineralógico dos pegmatitos são atribuídos à cristalização a partir de um fluido aquoso que "varreu" determinados elementos da fusão silicática e os

redistribuiu para cristais em crescimento em todas as partes do corpo de pegmatito (Jahns & Burnham, 1969).

Um modelo mais recente sobre a formação dos pegmatitos combina aspectos dos conceitos de Cameron *et al*. (1949) e Jahns e Burnham (1969):

(3) Gênese dos pegmatitos pela formação de uma camada de um fluido silicático (enriquecido em elementos complexantes) no limite da frente de cristalização: este fluido granítico hidratado possuiria condições especiais de subresfriamento (~200ºC abaixo do *liquidus*) e, juntamente com a viscosidade do meio de cristalização e o atraso na nucleação dos cristais, seria de vital importância para a ocorrência das texturas dos pegmatitos, incluindo uma borda aplítica e, no centro, o crescimento dos mega cristais e intercrescimentos gráficos (London, 2008).

Embora a maior parte das características químicas e texturais internas dos pegmatitos sejam reconciliadas pela teoria de London (2008), outro grupo de pesquisadores que trabalha com os regimes físico-químicos dos pegmatitos tem apresentado resultados discordantes:

(4) Thomas *et al*. (2000; 2008; 2009a,b) defendem que a formação dos pegmatitos é caracterizada por uma combinação de reações metassomáticas e cristalização magmática a partir de uma fusão silicática extremamente hidratada: neste processo, a fusão geradora do pegmatito não estaria em equilíbrio com a intrusão parental, e o granito e o pegmatito seriam dissociados em um nível físico-químico, não sendo possível, portanto, segundo estes autores, que o subresfriamento do *liquidus* seja a causa preponderante para a formação dos pegmatitos.

De acordo com Dill (2018, 2019), a elaboração de um modelo realista de mineralização pegmatítica, de acordo com a natureza, tem sido impedida pela recusa de ideias alternativas para a formação de granitos de elementos raros, como, por exemplo, pela superposição de pegmatitos estéreis induzida por fluidos. Outra hipótese para a formação de pegmatitos félsicos é por anatexia, a partir de rochas crustais e mantélicas previamente retrabalhadas por reações metassomáticas (Martin & Vito, 2005).

4.7 *Comparando os modelos de gênese dos pegmatitos*

Todos os modelos apresentados para a formação de pegmatitos graníticos concordam que sua gênese está associada a processos tardi-magmáticos, a partir de magmas residuais altamente fracionados. Também concordam que a formação do pegmatito implica na cristalização e fracionamento químico rápidos e sequenciais de uma fusão granítica das margens do corpo em direção ao centro sob condições envolvendo um equilíbrio térmico e químico bastante delicado.

O modelo de London (2008) difere do conceito clássico de cristalização fracionada de Cameron *et al*. (1949) principalmente no que diz respeito à distribuição dos componentes incompatíveis, os quais se tornam mais concentrados em um volume menor de rocha através do Refinamento da Zona Constitucional, explicando a transição abrupta entre o pegmatito quimicamente simples e o quimicamente complexo.

Tanto o modelo de London (2008) quanto o de Jahns e Burnham (1969) implicam na presença de um fluido de baixa viscosidade entre as superfícies dos cristais pegmatíticos e a fusão de alta viscosidade. Também o modelo de Thomas *et al*. (2009a; 2009b) sugere que os pegmatitos se formam a partir de magmas com viscosidades muito baixas. A baixa viscosidade do fluido nestes modelos aumenta muito a difusividade de cátions de alto potencial iônico, como Al e Si.

Enquanto o modelo de Jahns e Burnham (1969) apresenta este fluido de baixa viscosidade como uma saturação do vapor aquoso do qual o pegmatito se forma, o modelo de London (2008) propõe a ocorrência de apenas uma camada limítrofe de líquido silicático de baixa viscosidade rico em elementos complexantes. O Refinamento da Zona Constitucional de London (2008) concilia a necessidade de altas concentrações de elementos complexantes com sua abundância manifestamente baixa na maioria dos pegmatitos: a camada limítrofe de líquido silicático na frente de cristalização concentra os elementos complexantes da fusão, e transportaria cerca de 100 vezes mais massa de soluto por unidade de volume de fluido do que o vapor aquoso simples de Jahns e Burnham (1969).

O modelo proposto por Thomas *et al*. (2009a; 2009b), por sua vez, difere do modelo de London (2008) por sugerir que os pegmatitos cristalizam não através de uma camada limítrofe de fluido aquoso de baixa viscosidade, mas sim a partir de todo um sistema evolutivo magmático-hidrotermal de baixa viscosidade, muito dinâmico, em ebulição e com convexões violentas.

Enquanto London (2008) interpreta que as texturas gráficas dos pegmatitos se formam sob condições de subresfriamento (até ~200ºC abaixo do *liquidus*) em um meio de crescimento de alta viscosidade, Thomas *et al*. (2009b) interpretam que o subresfriamento do *liquidus* não pode ser mantido, pois a fusão geradora do pegmatito irá reagir com as paredes da rocha hospedeira até atingir o equilíbrio, formando a textura gráfica em um processo magmático-metassomático de alta temperatura.

Mesmo com esse estado de entendimento, várias peças importantes do quebra-cabeça ainda estão faltando. Em essência, não há nenhum entendimento conclusivo de quando e como os pegmatitos são derivados de seus granitos de origem. No atual paradigma de resfriamento rápido, não há explicação adequada para como os cristais gigantes crescem em um estado de energia térmica que está diminuindo rapidamente. Uma questão importante transcende o problema dos pegmatitos: quando na sua história os granitos se tornam saturados em uma fase de baixa densidade predominantemente aquosa, e quais são as marcas dessa transição, se não pegmatitos? (London & Morgan, 2012).

5 GENTHELVITA

O grupo da helvina é composto por silicatos anidros, os quais formam um sistema de solução sólida entre helvina ($Mn_4Be_3Si_3O_{12}S$), danalita ($Fe_4Be_3Si_3O_{12}S$) e genthelvita ($Zn_4Be_3Si_3O_{12}S$). Foi constatada miscibilidade completa entre os membros Fe^{2+} e Zn^{2+}, porém, existe uma lacuna aparente entre os membros finais Mn^{2+} e Zn^{2+}, embora a existência de soluções sólidas intermediárias entre helvina e genthelvita tenha sido reportada (Dunn, 1976; Larsen, 1988; Perez *et al*., 1990; Langhof *et al*., 2000). Resultados cristalográficos e estruturais, o raio iônico dos cátions M, e o modelo geométrico estrutural, indicaram que uma miscibilidade completa deveria existir entre os três termos finais (Hassan & Grundy, 1985).

Algumas das questões interessantes relativas à genthelvita são por que este mineral é tão raro quando comparado com minerais de Be ou mesmo com outros membros do grupo da helvina, por que sua ocorrência é essencialmente restrita a um tipo de rocha (granito alcalino), e o que a sua estabilidade tem a dizer com relação a cristaloquímica comparativa de Be e Zn, de um lado, e de Zn, Fe e Mn, do outro.

5.1 *Cristaloquímica comparativa de Be, Zn, Fe e Mn*

O Zn é menos abundante na crosta que o Fe e o Mn, entretanto, ele é relativamente comum na esfalerita. O Fe é mais abundante que o Mn, e ainda assim, a danalita é mais rara que a helvina. Além disso, Zn, Fe e Mn são todos mais concentrados por cristalização fracionada do que o Mg. Ou seja, a raridade geoquímica do Zn por si só não é suficiente para explicar a raridade da genthelvita (Burt, 1988).

O único silicato em que o Zn e o Be ocorrem juntos é a genthelvita, além de em pequenas soluções sólidas de, por exemplo, Be na willemita. O Be e o Zn possuem diferentes raios iônicos e afinidades químicas, porém, possuem também algumas semelhanças, como sua tendência a serem concentrados por cristalização fracionada e a tendência anômala do Zn em buscar a coordenação IV, assim como ocorre para o Be (Burt, 1988).

A tendência anômala do Zn em buscar a coordenação IV em silicatos deveria tornar a genthelvita mais comum que a helvina ou que a danalita, nos quais o Mn e o Fe, que são os bivalentes maiores, são forçados na coordenação IV. A explicação para a raridade relativa da genthelvita deve, portanto, ser buscada no estudo dos parâmetros físico-químicos (Burt, 1988).

5.2 *Estabilidade da genthelvita*

A rara ocorrência dos minerais do grupo da helvina, e principalmente da genthelvita, resulta do seu pequeno campo de estabilidade. Estes minerais são sensíveis aos estados de redução e sulfetação, bem como à alcalinidade do sistema, e sua ocorrência é restrita às condições de estabilidade para a coexistência de sulfetos e silicatos (Burt, 1980, 1988).

Os elementos que compõe os minerais do grupo da helvina – Zn, Mn, Fe, Be, S – são comumente encontrados como elementos traços em sistemas graníticos altamente fracionados. Portanto, os minerais do grupo da helvina são fases tardias, típicas de sistemas em estágio tardio de diferenciação, cuja estabilidade se deve a condições locais e transitórias, geralmente atípicas na consolidação de pegmatitos graníticos, incluindo baixa atividade de alumina, e condições relativamente redutoras que acomodam S^{2-} (Burt, 1980, 1988; Bilal & Fonteilles, 1988).

A estabilidade da genthelvita em uma paragênese depende diretamente da atividade de S. Devido ao comportamento calcófilo de Zn>>Fe>Mn, em sistemas altamente ricos em SO^{-1} (sob fugacidades de H_2S suficientemente altas) em que os componenetes FeS ou MnS da helvina estariam estáveis, o componente Zn_2SiO_4 teria sido sulfetizado para ZnS, formando esfalerita ao invés de genthelvita. Isto restringe a formação de genthelvita a sistemas nas quais a atividade de S é muito baixa (Burt, 1988). Ao contrário, sob condições de baixo conteúdo de SO^{-1} necessárias para estabilizar a genthelivta, a danalita e a helvina não são estáveis, pois a instabilidade dos componentes FeS e, particularmente, o MnS, se presentes, levariam a formação de silicatos ou óxidos coexistentes. Desta forma, a cristalização de danalita e helvina requerem atividades de S mais altas, condições nas quais a formação da genthelvita seria impedida em prol da cristalização de uma assembleia contendo esfalerita, fenaquita e quartzo (Burt, 1988).

Os experimentos de Fursenko (1982) demostraram que a genthelvita é favorecida sob condições alcalinas, enquanto a danalita é formada quando os fluidos são mais ácidos. A estabilidade da danalita também é sensível à fugacidade de oxigênio, sendo estável apenas em um campo estreito de fO^{2-}, abaixo do qual ocorre o campo de estabilidade da faialita, e acima do qual ocorre a formação de assembleias portadoras de hematita ou magnetita (Burt, 1980; Nimis *et al.*, 1996). A helvina é normalmente observada em sistemas mais sulfetados e ricos em Mn, cristalizando a fugacidades de oxigênio moderadas e um campo de fugacidade de enxofre mais amplo quando comparada a genthelvita (Burt, 1988).

Além disso, as altas atividades de Na e K em um magma de natureza alcalina leva a formação de fenaquita e feldspatos ao invés de berilo. E o Al disponível tende a formar minerais feldspatoides, favorecendo a formação de minerais do grupo da helvina ao invés de berilo (Burt, 1980; Finch, 1990; Perez *et al*., 1990). Minerais comumente associados com a genthelvita são quartzo, feldspatos, micas, e outras fases portadoras de Zn, como esfalerita, willemita e gahnita, bem como outras fases portadoras de Be, como fenaquita e bertrandita (Burt, 1988). Também há a ocorrência comum de willemita nestas associações, particularmente aquelas em rochas peralcalinas.

5.3 *Ocorrências de genthelvita*

A genthelvita é um raro mineral acessório que ocorre tipicamente em granitos alcalinos a peralcalinos e sienitos, e em seus respectivos pegmatitos, greisens e depósitos metassomáticos associados, além de em skarns de rochas cálcio-silicáticas (Burt, 1988; Grew, 2002). A formação de genthelvita, quando comparada com os outros membros do grupo da helvina, é favorecida por condições alcalinas (Bilal & Fonteilles, 1991).

A genthelvita, assim como a danalita e a helvina, está entre os últimos minerais a se formarem na maioria dos espécimes observados na matriz. A cristalização tardia é indicada pela associação muito comum com fluorita, e pela frequência com que os membros do grupo ocorrem preenchendo veios em quartzo (Dunn, 1976). Geralmente este mineral é encontrado como cristais euédrico em cavidades em veios de quartzo ou em cavidades miarolíticas em pegmatitos de granitos (Deer et al., 2004).

6 RESULTADOS

6.1 *Uranium mineralization in the Madeira Sn-Nb-Ta (U, Th, REE, F) world-class deposit (Pitinga, Amazonas State, Brazil): pyrochlore and its alteration products under hypogene conditions*

Artigo submetido à revista Economic Geology (A1) dia 07/06/2023.

Submission Confirmation for Uranium mineralization in the Madeira Sn-Nb-Ta (U, Th, REE, F) world-class deposit (Pitinga, Amazonas State, Brazil): pyrochlore and its alteration products under hypogene conditions

De	Economic Geology <em@editorialmanager.com>
Remetente	<em.seg.0.83ddbd.fc6a2a86@editorialmanager.com>
Para	Ingrid Weber Hadlich <ingrid.hadlich@ufrgs.br>
Responder p...	Economic Geology <econgeoljournal@gmail.com>
Data	2023-06-07 19:31

Dear Dr. Hadlich,

Your manuscript entitled "Uranium mineralization in the Madeira Sn-Nb-Ta (U, Th, REE, F) world-class deposit (Pitinga, Amazonas State, Brazil): pyrochlore and its alteration products under hypogene conditions" has been received by my office at Economic Geology. I will examine it for suitability for publication and then arrange for an associate editor to begin the review process. We aim to complete the review process within three months.

You will be able to check on the progress of your paper by logging on to Editorial Manager as an author. The URL is https://www.editorialmanager.com/seg/.

Your manuscript will be given a reference number once an Editor has been assigned.

Thank you for submitting your work to Economic Geology.

Kind regards,

Larry Meinert
Editor
Economic Geology

____

Uranium mineralization in the Madeira Sn-Nb-Ta (U, Th, REE, F) world-class deposit (Pitinga, Amazonas State, Brazil): pyrochlore and its alteration products under hypogene conditions

Ingrid W. Hadlich[a,*]; Artur C. Bastos Neto[a]; Vitor P. Pereira[a]; Harald G. Dill[b]; Nilson F. Botelho[c]

[a]Instituto de Geociências, Universidade Federal do Rio Grande do Sul, Avenida Bento Gonçalves 9500, Porto Alegre 91501-970, RS, Brazil; [b]Gottfried Wilhelm Leibniz University, Welfengarten 1, D-30167 Hannover, Germany; [c]Instituto de Geociências, Universidade de Brasília, Campus Universitário Darcy Ribeiro, Asa Norte, 70910-900 Brasília, DF, Brazil.

*Corresponding author e-mail: ingrid.hadlich@ufrgs.br

Abstract

The U mineralization in the Madeira deposit is associated with the albite-enriched granite facies of the A-type Madeira granite (Pitinga, Brazil). It stands out as a remarkable example of an intrusive-type deposit. The primary ore mineral of U is exclusively early magmatic U-Pb-LREE-enriched pyrochlore, which is homogeneously dispersed in the pluton. All pyrochlore crystals were strongly affected by hydrothermal alteration caused by F-rich, low-T aqueous fluids. During the alteration process under hypogene conditions, different cations (such as LREE, Nb, and F) were selectively released, while others (like Fe and Si) were incorporated. This resulted in the successive formation of various secondary pyrochlore varieties and the relative enrichment of U (up to 13.73 wt% UO_2). The alteration of pyrochlore ultimately leads to the breakdown of its structure, resulting in the formation of pseudomorph U-bearing columbite and the precipitation of U-rich silicates (up to 34.35 wt% UO_2) within pyrochlore cavities. The U mineralization in the Madeira deposit exhibits grades (328 ppm UO_2) comparable to the main U intrusive type deposits and holds significant reserves (52 kt U). However, it is in stark contrast to those deposits in four key aspects: homogeneous dispersion of mineralization, pyrochlore as the exclusive primary ore mineral, U and Th mineralizations formed at different stages, and being affected by intense hydrothermal alteration. These characteristics are attributed to the special conditions imposed by the fluorine-rich nature of the peralkaline magma.

Keywords: uranium mineralization, uraniferous pyrochlore, columbite, hydrothermal alteration, peralkaline magma, Madeira deposit

Introduction

The Madeira Sn-Nb-Ta (U, Th, REE, F) deposit stands out as a remarkable example of U-Th mineralization of intrusive type (IAEA, 2020). Unlike most U-Th deposits, where U and Th mineralizations occur together, in this deposit, they formed at different stages of magmatic evolution and concentrated in distinct minerals: early pyrochlore and late thorite, respectively. Subsequently, both minerals underwent intense hydrothermal alteration, leading to the development of two distinct mineral associations. Recognizing the unique nature of this deposit, we previously published a dedicated article focusing on Th mineralization (Hadlich et al. 2019). In this current study, we shift our attention to the U mineralization, providing a comprehensive analysis and understanding of its characteristics and implications.

Intrusive type U deposits are commonly associated with carbonatites and granites, and consist of primary, usually non refractory, uranium minerals, with uraninite, uranothorianite and uranothorite being the dominant species. These deposits are generally low-grade (20-500 ppm) but may contain substantial resources (more than 100 kt U). Pyrochlore supergroup minerals are found in several uranium-bearing ores that are currently being processed, including Rössing Deposit in Namibia (Berning et al., 1976), which is currently the world's 5th largest producer of uranium, with 246,500 tU at a grade of 300 ppm (Kyser and Cuney, 2015). There is a focus on targeted processing of lower-grade deposits due to the significant challenges posed by gangue mineralogy in these deposits (Pownceby and Johnson, 2014). Only through the simultaneous extraction of metals associated with U can the mining of such deposits be economically viable (Cuney, 2014). Moreover, in recent years, there has been increased interest in gaining a better understanding of the structure and chemical factors that influence U leaching from minerals. As a result, uranium-enriched pyrochlore in the Madeira deposit has received increased attention due to its abundance and refractory nature.

Uranium dissolution in silicate melts is influenced by the degree of depolymerization of the magma, which is controlled by the melt composition (Cuney, 2010). In alkaline melts, high contents of K, Ca, and Na promote depolymerization, allowing for the solubility of U, Th, Zr, and REE (Cuney and Kyser, 2008). However, the presence of abundant F suppresses alkalinity by reacting with Al to form AlF_6^{-3}, which also depolymerizes the aluminum-silicate tetrahedral chain (Cuney and Kyser, 2008). The high solubility of U and other high field strength (HFS) elements leads to their continuous and simultaneous enrichment during magma fractionation. U^{4+} and Th^{4+} exhibit similar geochemical behavior due to their comparable charge and ionic radii of 1.02 A and 0.97 A (coordination VIII), respectively, resulting in their incorporation into the same minerals (Krauskopf, 1967). The high charge and large ionic radii of U and Th prevent them from fitting into most common silicates, leading to their inclusion in complex accessory minerals of U, Th, Zr, Y, REE, Nb and Ta during late-stage magmatic differentiation (Pointer, 1987; Dill, 2015). Consequently, U and Th are expected to be present in the same minerals in intrusive-type U deposits (IAEA, 2020), formed during later paragenesis.

Pyrochlore is a group of Nb–Ta–Ti oxides with the ideal structural formula $A_2B_2O_6Z$ (Hogarth et al., 2000; Atencio et al., 2010; Mitchell et al., 2020). The crystal structure of pyrochlore-group minerals is versatile and allows for the incorporation of various elements in the A- [Na, Ca, Mn, Ba, Fe, Sr, Sn, Pb, Sb, Y, REE, Th, U, (□), H_2O] and B- (Nb, Ta, Sb, W, Ti, Si, Zr, Hf, Sn, Fe, Al, V) sites. The Z-site is primarily occupied by F, OH, O, □, H_2O, or large monovalent cations (K, Rb, or Cs) (Dey et al., 2021). Primary pyrochlore crystals are enriched in Ca, Na, Nb, Ta, and F. Late-stage pyrochlore, formed through hypogene and supergene alteration of primary pyrochlore, undergo a series of complex substitutions involving A- and B-site cations. The most common composition of late-stage pyrochlore is $[(Ba, Sr, REE, Pb, Ca, U, Th)_{\Sigma<<2}(Nb, Ti, Ta,Zr, Fe^{3+}, Si)_2(O, OH)_6(OH, F)_{\Sigma<<1}zH_2O]$ (Lumpkin and Ewing, 1995; Dey et al., 2021).

Uranium-bearing columbite also occurs in the Madeira deposit and is considered a primary mineral by Lenharo (1998) and Costi (2000), while Minuzzi et al. (2006) consider it a secondary mineral formed through pyrochlore alteration. This aspect holds significant importance for the current study. In addition to fluorine, experimental research by Tang et al. (2022) suggests that other factors as T, increase in the A/CNK ratio, and concentrations of essential compositional components (ESCs) of pyrochlore also influence the preferential formation of pyrochlore over columbite in peralkaline granitic magmas.

This paper focuses on the U mineralization associated with the world-class Madeira Sn-Nb-Ta (U, Th, REE, Li, cryolite) deposit (Bastos Neto et al. 2009; Costi et al. 2009). It is noteworthy that the association of these metals in the same peralkaline rock, specifically an albite-enriched granite (AEG) (~1.830 Ma), which also hosts a massive cryolite deposit, is unparalleled worldwide. The main objectives of this work are as follows: (1) assess the U mineralization potential of the Madeira deposit in comparison to other intrusive type U deposits; (2) investigate the formation of the primary U ore mineral, pyrochlore, and its relationship with columbite; (3) investigate the primary pyrochlore alteration under hypogene conditions; and (4) evaluate the implications of the study results for the overall evolution of the albite-enriched granite system.

Geological Setting

The Pitinga Province is located (Fig. 1) in the southern portion of the Guyana Shield (Almeida et al., 1981), in the Tapajos-Parima Tectonic Province (Santos et al., 2000). The Pitinga Province is the largest Sn producer in Brazil. The alluvial ore deposits were discovered in 1979 (Veiga et al., 1979) and are almost exhausted. The primary ores are associated with two main tin-bearing granites, the Madeira and Agua Boa A-type granites (Fig. 1). Both are part of the ∼1.830 Ma Madeira Suite (Costi, 2000). The Madeira deposit, which has been exploited since 1989, is associated with the Madeira granite (Fig. 2). Moreover, a number of small greisens associated with the Agua Boa granite have been intermittently exploited. The volcanic rocks of the Iricoume Group (Veiga et al., 1979) predominate in the Pitinga Province and host the Madeira Granite (Fig. 1). They have 207Pb/206Pb zircon ages between 1881 ± 2 and 1890 ± 2 Ma (Ferron et al., 2006). They comprise mostly effusive and hypabyssal rhyolites, highly welded ignimbrites, ignimbritic tuffs, and surge deposits formed in a subaerial environment with cyclic effusive and explosive activities (Pierosan et al., 2011a, 2011b; Simoes et al., 2014).

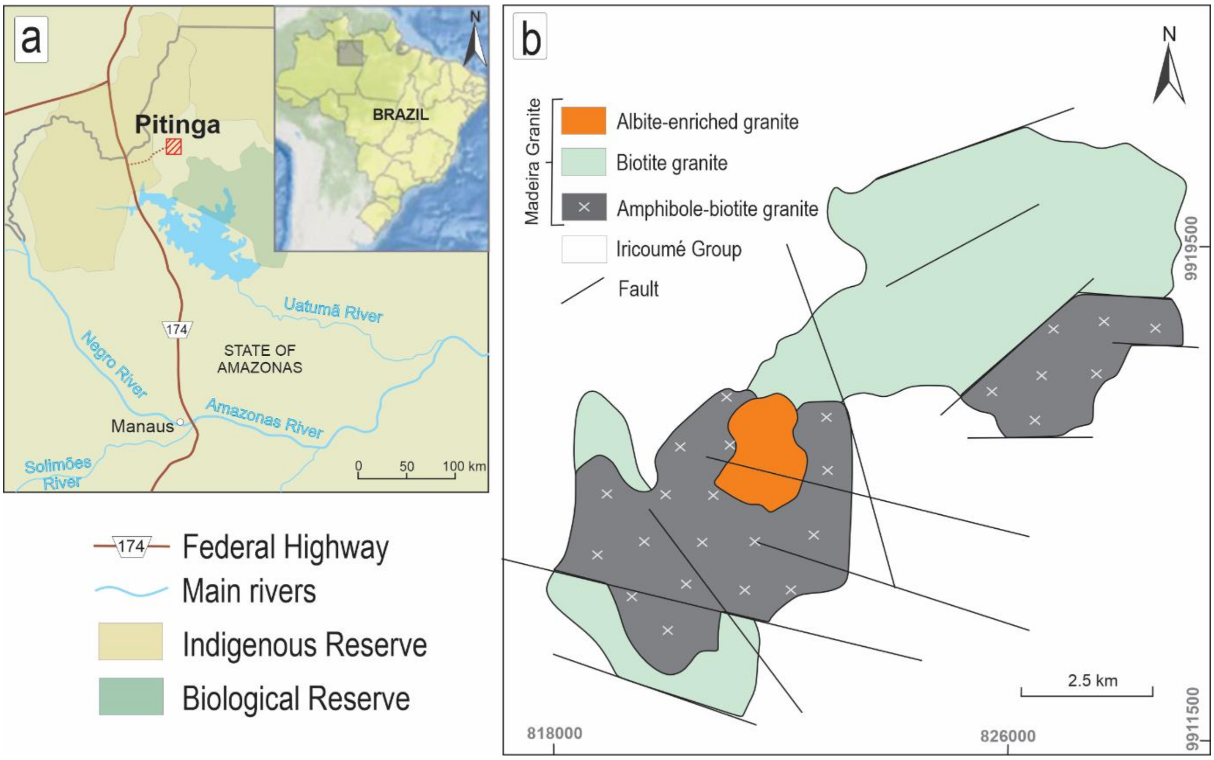

Fig. 1. A) Location map; B) Geological map of the Madeira Granite (modified from Costi, 2000).

The Madeira granite (Figs. 1 and 2) contains four facies (Horbe et al., 1991; Lenharo et al., 2003; Costi et al., 2005, 2009; Bastos Neto et al., 2009). The early mostly metaluminous porphyritic amphibole-biotite granite (1824 ± 2 Ma, Costi et al., 2000a) contains plagioclase-mantled K-feldspar megacrysts, sometimes also reverse-zoned Kfs-mantled plagioclase ovoids and is usually referred to as the "rapakivi granite". The amphibole-biotite granite was followed by somewhat younger metaluminous biotite granite (1822 ± 2 Ma, Costi et al., 2000a) which contains its xenoliths. The alkali feldspar hypersolvus porphyritic granite facies (1818 ± 2 Ma, Costi et al., 2000a) has K-feldspar phenocrysts in a fine- to medium-grained matrix dominantly composed of K-feldspar and quartz. According to Costi (2000), the hypersolvus granite (Fig. 2) and the AEG were emplaced simultaneously, and then interacted and intruded into the older facies. The age of the AEG is only very roughly constrained at 1822 ± 22 Ma (Bastos Neto et al., 2014) due to the metasomatic alteration of zircons. The Madeira deposit (Fig. 2) corresponds to the AEG. It is an oval-shaped body with an aerial extension of approximately 2×1.3 km at outcrop. It is divided into subfacies albite-enriched granite core (AGC) and albite-enriched granite border (AGB). The AGC is a peralkaline subsolvus granite, porphyritic to seriate in texture, fine- to medium-grained, and composed of quartz, albite and K-feldspar in approximately equal proportions (25–30%). The accessory minerals are cryolite (4%), polylithionite (4%), green–brown mica (3%), zircon (2%), and riebeckite (2%). Pyrochlore, cassiterite, xenotime, columbite, thorite, magnetite and galena occur in minor proportions. The AGB is peraluminous and presents types of texture and essential mineralogy like the AGC, except for being richer in zircon, for the presence of fluorite instead of cryolite, and absence of iron-rich silicate minerals, which have almost completely disappeared due to an autometasomatic process (Costi et al., 2000, 2010).

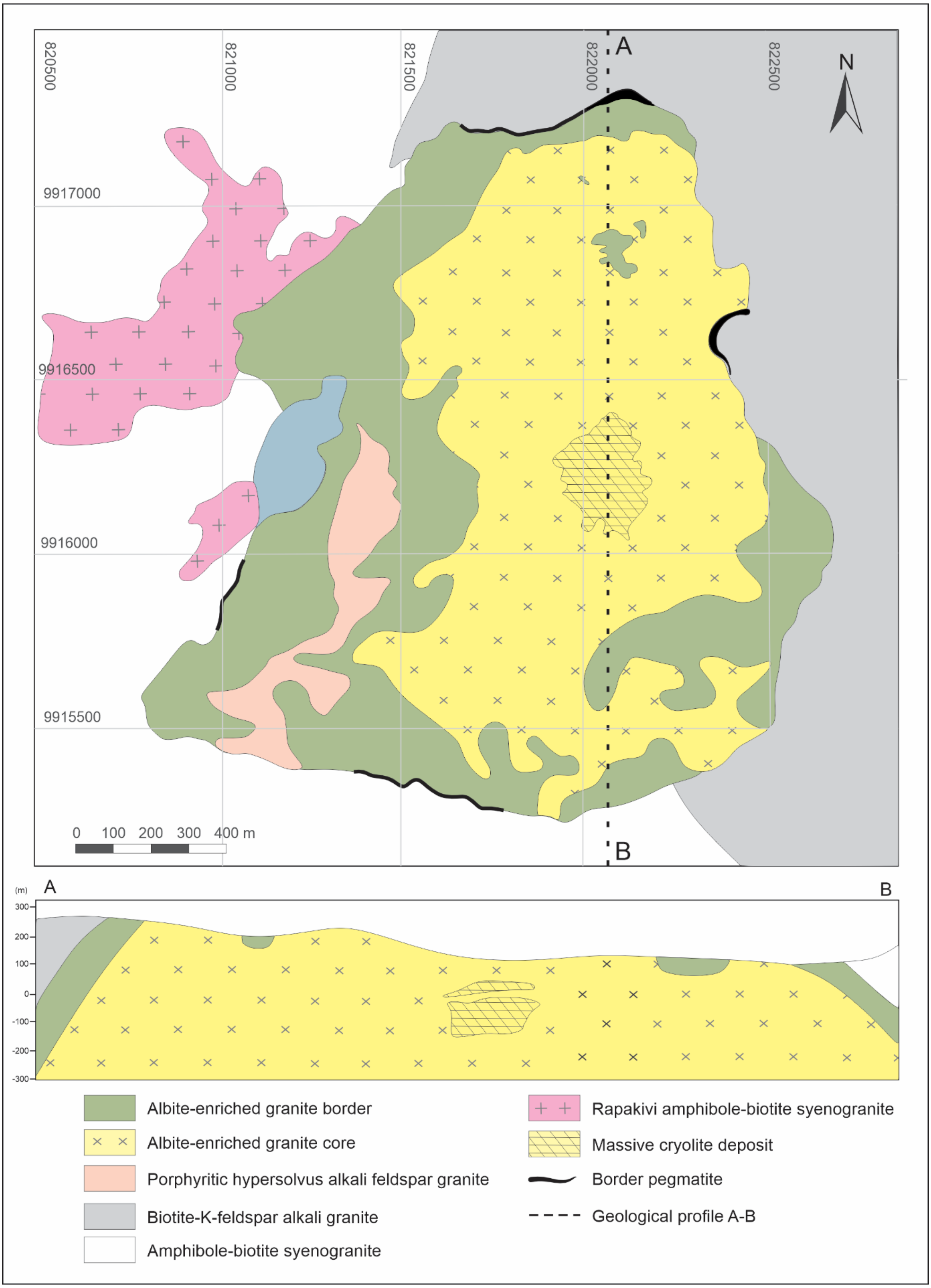

Fig. 2. Geological map of the albite-enriched granite (modified from Minuzzi, 2005).

The ore grade of the disseminated ore (AGC + AGB) stands at 0.17 wt.% Sn (cassiterite), 0.20 wt.% Nb_2O_5) and 0.024 wt.% Ta_2O_5 (both in pyrochlore and columbite). The potential by-products of the disseminated ore are F (4.2 wt.% cryolite), Y and HREE [xenotime and gagarinite-(Y)], Zr and Hf (zircon), Th (0.07 wt.% ThO_2, thorite), and U (pyrochlore). Despite the disseminated character of the AEG mineralizations, there are zones of enrichment associated with the granite in which specific minerals may be considerably abundant, and these are:

(1) ~50-cm thick pods and bands of the pegmatitic AEG (rarely, up to 10m thick; Stolnik, 2015). They have almost the same minerals as the AGC, but with grain sizes much larger. Polylithionite, riebeckite, xenotime and thorite are much more abundant than in the AGC.

(2) Border pegmatites (BPEG) that are at the contact between the AGB and the older facies (Fig. 2). They are characterized by the increased sizes and amounts of K feldspar, quartz and zircon, advanced alterations of K-feldspar and biotite, and by local enrichments in fluorite, polylithionite, thorite and secondary hematite (Lengler, 2016).

(3) Pegmatite veins which are not mappable, occur more commonly in the central, northern and northwest parts of the AGC, and have thicknesses ranging from a few centimeters to 2 m. They are heterogeneous and more commonly porphyritic. The phenocrystals may be of quartz, K-feldspar, xenotime, thorite, cryolite, polylithionite and riebeckite. The matrix is composed of albite, quartz, K-feldspar, polylithionite, cryolite and riebeckite; the accessory minerals are zircon, cassiterite, pyrochlore, columbite, galena, sphalerite, hematite, gagarinite and genthelvite (Paludo et al., 2018).

(4) The massive cryolite deposit (Fig. 2) formed by several bodies of hydrothermal massive cryolite intercalated with AGC and hypersolvus granite; these are sub-horizontal, up to 300 m long and 30 m thick, and composed of cryolite crystals (~87 vol%), quartz, zircon and feldspar (Minuzzi et al., 2006a).

Zircon and pyrochlore are the only U bearing minerals identified in the AEG prior to this study, and the pyrochlore was investigated with focus in the Nb and Ta mineralization (Minuzzi et al. 2006a, Bastos Neto et al, 2009). The high grades of U in the AEG have been attributed to the primary U-Pb-pyrochlore (12.2 wt% UO_2, 29.8 wt% PbO). The zircons from the AEG have incorporated preferentially Hf instead of Th (Zr/Hf < 20; Lenharo, 1998; Nardi et al., 2012). The AGC zircons present average concentrations of 1.55 ppm UO_2, 8.24 ppm ThO_2, and a Th/U ratio of 5.31, whereas the AGB zircons present average concentrations of 2.97 ppm UO_2, 6.65 ppm ThO_2 and a Th/U ratio of 2.23 (Nardi et al., 2012). Xenotime grains from the AEG do not have significant concentrations of Th and U (Bastos Neto et al., 2012).

Costi et al. (2009) consider the AEG to be the result of a phase-separation process, or immiscibility, similar to that registered by Thomas et al. (2006) in the Variscan Erzgebirge granites, Germany. Bastos Neto et al. (2009, 2014) consider that the AEG magma would have been related to the isotherm rise, which occurred when the mantle fluid ascended further into the crust promoting fenitization-type reactions (Martin, 2006) in rocks previously enriched in Sn, and introduced elements such as F, Nb, Y, REE, and Th in anomalous concentrations. The input of a F-rich fluid took place, and generated metassomatism causing the rock to become fusible. Lenharo (1998) and Costi (2000) considered that the magma of the AEG evolved towards an extremely Na-, F-enriched residual melt. In accordance with Bastos Neto et al. (2009), the extreme fluorine enrichment in the residual melt is unlikely to have been attained, since the F content was buffered by crystallization of magmatic cryolite (Dolejs and Baker, 2007).

Materials and methods

For this study, we had a collection of more than 500 rock samples and their respective thin sections from the Universidade Federal do Rio Grande do Sul (UFRGS) research group. A total of 70 samples were selected for more detailed studies. To obtain detailed textural data, thin sections were examined by scanning electron microscopy (SEM) with qualitative analysis using an energy-dispersive X-ray detector (Zeiss, model EVO MA10) at the Center for Microscopy and Microanalysis in UFRGS.

Electron probe microanalysis (EPMA) were carried out at the EPMA Laboratory of the Universidade de Brasília (UnB), with a JEOL JXA-8230 equipped with five WDS spectrometers for quantitative analyses and one EDS for qualitative analyses. The concentrations of F, Mg, Zn, Al, Si, Hf, Nb, P, Cl, S, Bi, Ti, Mn, Y, Ta, Sn, Ca, Zr, Fe, V and Rb were determined with an accelerating voltage of 15 kV and 10 nA of sample current, whereas the concentrations of Na, Er, Tm, Yb, Ho, Lu, K, Pb, Dy, Tb, Sm, Gd, Eu, Sr, Th, Pr, Nd, Ce, La, Ba and U were determined with an accelerating voltage of 20 kV and 50 nA. Each element was analyzed with a beam diameter of 1 μm. The counting times on the peaks were 10s for all elements, and half that time for background counts on both sides of the peaks. The following crystals were used: TAP, PETJ, PETH, LIFH, and LDE1 (for F). Interference corrections were applied in all cases of peak overlap. Galena calibration: Pb (Mα) and S (Kα) were determined with na accelerating voltage of 20 kV and current of 50 nA and 20 nA, respectively, using the PETJ crystal for both elements, and as standards PbS (Pb) and pyrite (S).

Chemical data of the AEG and associated pegmatites were revised in order to define the potential of each subfacies for U. Most of the whole-rock geochemical data (268 analyses) were obtained by the UFRGS research group, and are available in Bastos Neto et al. (2005, 2009), Minuzzi et al. (2005, 2006a, 2006b, 2008), Pires (2005, 2010), Paludo (2015), Stolnik (2015), and Lengler (2016). The samples were collected from drill cores and fresh outcrops, and the analyses were performed at Actlabs (Canada). Major elements were determined by ICP-AES, the minor and trace elements by ICP-MS, and the F by ISE. The data base was completed with data published by other research groups, which may be accessed in Lenharo (1998), Costi (2000), and Costi et al. (2005, 2009).

Results

Mineralogy and petrography

Pyrochlore: Pyrochlore from the AGC and AGB occurs as individual crystals dispersed within a matrix of quartz, albite, and orthoclase (Fig. 3A-B). It can also be included in quartz (Fig. 3C), polylithionite, and zircon (Fig. 3G), or surrounded by recrystallized quartz (Fig. 3E). In the AGC, it can be surrounded by hydrothermal cryolite (Fig. 3D, F), while in the AGB, it can be surrounded by hydrothermal (Fig. 3G-I). The crystal sizes range from 0.1 to 0.9 mm, similar to other minerals in the matrix. The grains are typically partially rounded, but pseudo-cubic crystals can also be observed. Under natural light, they appear as dark yellow in color (Fig. 3C-D). These rounded grains result from the in situ alteration of pyrochlore by hydrothermal fluids, leading to the formation of columbite. The associated columbite grains in both granite facies are opaque (Fig. 3G, H). Even the well-preserved pyrochlore grains show incipient alteration along their edges and internal microfractures, mainly occurring in the AGC (Fig. 3C-D). Advanced alteration is more prevalent in the AGB and central part of the AGC, where only remnants of the original pyrochlore can be observed (Fig. 3G-I).

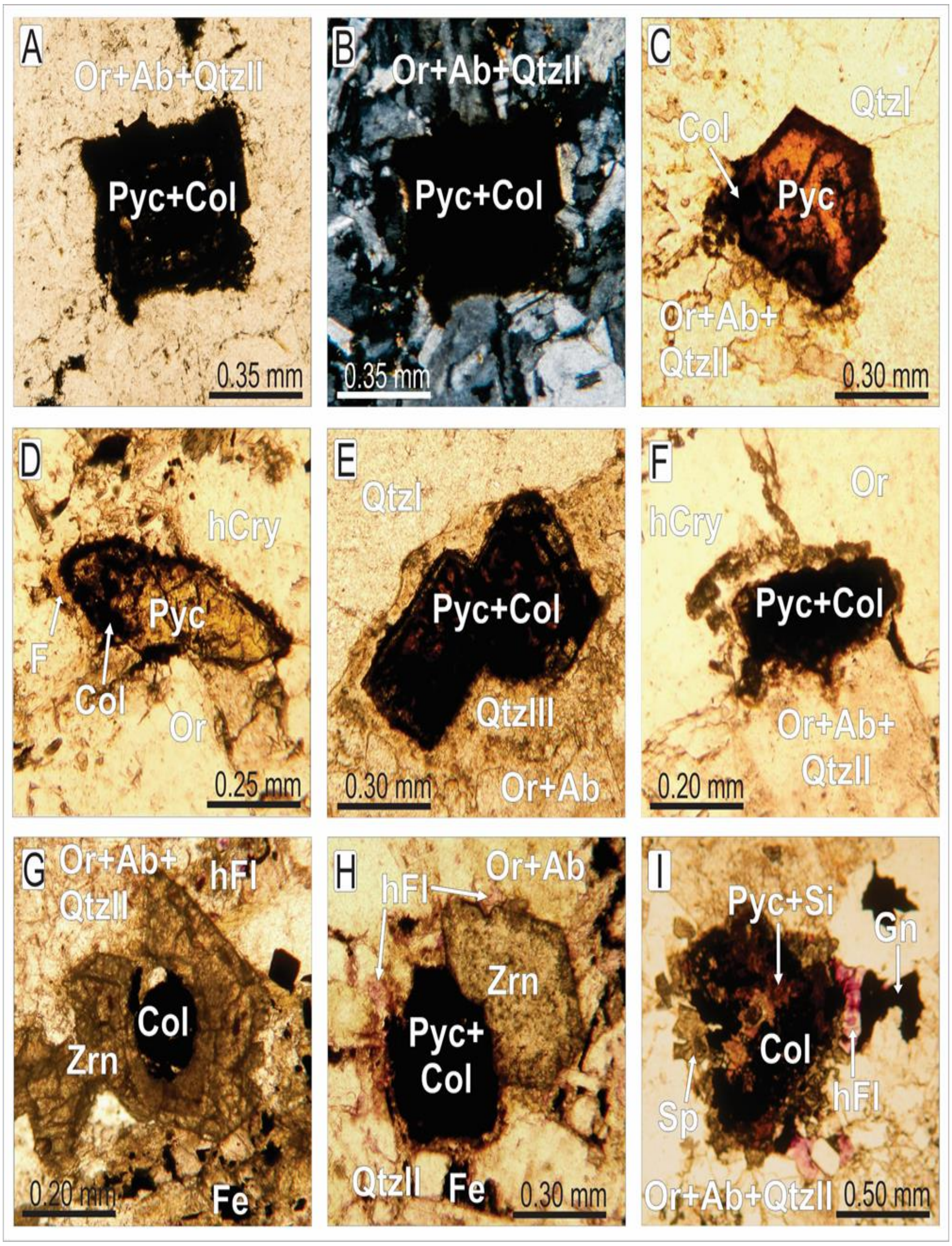

Fig. 03. Photomicrographs illustrating various features of pyrochlore from the albite-enriched granite. (A) Typical pyrochlore from the albite-enriched granite, showing advanced alteration to columbite, P.l. (B) Same as (A), pyrochlore in the matrix with albite, quartz, and K-feldspar, X.l. (C) Euhedral pyrochlore grain partially included in quartz, P.l. (D) Incipiently altered pyrochlore in contact with LREE-rich fluoride, P.l. (E) Geminated pyrochlore crystals surrounded by recrystallized quartz, P.l. (F) Rounded pyrochlore section partially surrounded by hydrothermal cryolite, P.l. (G) Columbite grain included in zircon, P.l. (H) Pyrochlore and zircon intergrowth, the set is surrounded by hydrothermal fluorite, P.l. (I) Pyrochlore and columbite associated with a U-Si-rich phase, hydrothermal fluorite, galena and sphalerite, P.l. Abbreviations: Ab= albite, Col= columbite, Fe= iron oxide, Gn= galena, Cry= cryolite, Fl= fluorite, Or= orthoclase, Pyc= pyrochlore, Qtz I= quartz phenocryst, Qtz II= quartz matrix, Qtz III= recrystallized quartz, F= LREE-rich fluoride, Si= Th-U-rich silicate, Sp= sphalerite, Zrn= zircon.

Twinning of pyrochlore crystals (Fig. 3E) and intergrowth with zircon (Fig. 3G) are observed in several cases. When included within quartz, the pyrochlore retains its well-formed euhedral crystal shape (Fig. 3C). However, the contact between pyrochlore and the matrix minerals exhibits slight reactivity and undulation (Fig. 3A). The contact between pyrochlore and hydrothermal cryolite in the AGC (Fig. 3F) and hydrothermal fluorite in the AGB (Fig. 3H) shows even more corrosive features. In such cases, pyrochlore and columbite grains become highly rounded. A similar feature is observed at the interfaces between hydrothermal cryolite and fluorite with zircon crystals. Hydrothermal alteration of pyrochlore leads to the formation of columbite and iron oxide, which exsolve along the grain edges (Fig. 3E, H). In a few instances from the AGB and central AGC, sphalerite is also associated (Fig. 3I).

Due to the observed petrographic features, pyrochlore in both the AGC and AGB is considered a primary mineral that crystallized during the early magmatic stage. Subsequent hydrothermal events rich in fluorine affected and altered the pyrochlore throughout the AEG, with greater intensity in the AGB and central portion of the AGV. Columbite formation occurred during the early hydrothermal stage but was later corroded by fluids, leading to the formation of cryolite in the AGC and fluorite in the AGB. Analysis using X-ray dispersive energy spectroscopy (EDS) on numerous pyrochlore grains allowed for the identification of alteration products from the early and late hydrothermal stages. The following representative cases illustrate these differences.

Well-preserved pyrochlore crystals appear homogeneous with light gray tones in backscattered electron images (Fig. 4A) and primarily consist of U-Pb-LREE-rich pyrochlore. Along the grain borders, microfractures and cavities are surrounded by white U-LREE-Pb-rich pyrochlore (Fig. 4B). This white coloration is attributed to gradual enrichment in Pb, because the concentrations of other elements do not vary significantly (Fig. 4C). The grain showing incipient alteration (Fig. 4D) consists of U-LREE-Pb-rich pyrochlore, displaying lower Pb concentration in its central portions (min. 7.5 wt.% PbO, light gray) and higher Pb concentrations along the grain border and microfractures (max. 14.5 wt.% PbO, white). Within the same grain, Fe-U-Pb-rich pyrochlore is surrounded by columbite (Fig. 4E), exhibiting an irregular shape and a composition depleted in LREE-Nb-Ta-F but enriched in U-Pb-Fe-Si compared to U-LREE-Pb-rich pyrochlore (Fig. 4F). Thus, even in the best-preserved pyrochlore grains, there is evidence of alteration, likely resulting from hydration and significant leaching in magmatic pyrochlore. As the degree of alteration increases, compositional heterogeneity becomes more pronounced, primarily attributed to the early hydrothermal process. This process gave rise to secondary phases enriched in Pb found at the grain borders and along microfractures, and to formation of columbite. Consequently, the most extensively altered pyrochlore remnants are included within columbite. Grains exhibiting advanced alteration no longer contain primary pyrochlore but instead show remnants of hydrothermal pyrochlore, along with abundant columbite and/or iron oxide, as well as other secondary minerals.

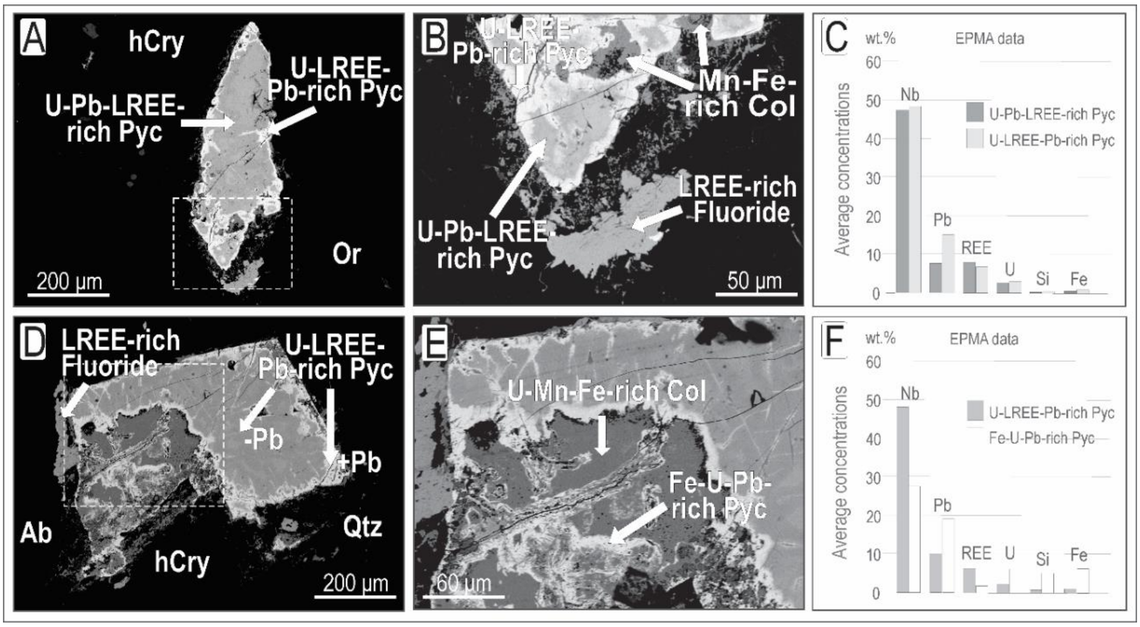

Fig. 04. BSE images of magmatic pyrochlore from the albite-enriched granite. (A) Grain of magmatic U-Pb-LREE-rich pyrochlore (gray); early hydrothermal U-LREE-Pb-rich pyrochlore (white) occur along the borders and microfractures. (B) Detail of A, the grain border is altered, and voids are filled with Mn-Fe-rich columbite and LREE-rich fluoride. (C) Comparison on EPMA data for pyrochlore in A-B shows Pb enrichment during its alteration. (D) U-LREE-Pb-rich pyrochlore grain partially altered, with higher Pb concentration along the borders and microfractures. (E) Detail of D, Fe-U-Pb-rich pyrochlore occurs surrounded by U-Mn-Fe-rich columbite. (F) EPMA data for pyrochlore in D-E shows Pb-U-Si-Fe enrichment and REE-Nb loss during alteration. Abbreviations: Ab = albite, Col = columbite, Cry = cryolite, Or = orthoclase, Pyc = pyrochlore, Qtz = quartz.

Columbite: Different varieties of columbite formed in conjunction with hydrothermal pyrochlore. The predominant phase is Mn-Fe-rich columbite, present in both the AGC and the AGB. This phase initially formed at the borders of the pyrochlore grains, and the fluid responsible for its crystallization advanced through cleavages and other areas of weakness, corroding and filling microfractures and cavities within the crystal (Fig. 4). Advanced stages of alteration are more prevalent in the AGB and central portion of the AGC.

In the AGB, columbite within the same grain may exhibit heterogeneous composition. Mn-Fe-rich columbite is the predominant variety, with some portions enriched in elements inherited from pyrochlore, primarily U (Fig. 5). The completely columbitized grain in Fig. 5A consists predominantly of Mn-Fe-rich columbite, with subordinately Mn-U-Fe-rich columbite. The latter appears as irregular-shaped masses disseminated throughout the grain and has lower concentrations of Fe, Mn, and Nb, but higher concentrations of U and Si compared to the former (Fig. 5B). Similarly, the grain in Fig. 5C is composed of Mn-Fe-rich columbite, which surrounds irregular-shaped masses gradually richer in U. These masses consist of U-Mn-Fe-rich columbite and a Fe-U-Nb-rich phase, with the latter exhibiting significantly higher concentrations of U and Si (Fig. 5D). The grain in Fig. 5E is comprised of Mn-U-Fe-rich columbite with anomalously high Si (Fig. 7F), which surrounds irregular masses of Fe-U-Si-Nb-rich phase. Columbite is commonly surrounded by iron oxide and quartz, and in the AGC, by hydrothermal cryolite, or in the AGB, by hydrothermal fluorite. This results in a rounded or irregular shape of the previously prismatic pyrochlore crystals (Fig. 5). These secondary minerals also fill microfractures and voids in columbite and surround fragments of columbite.

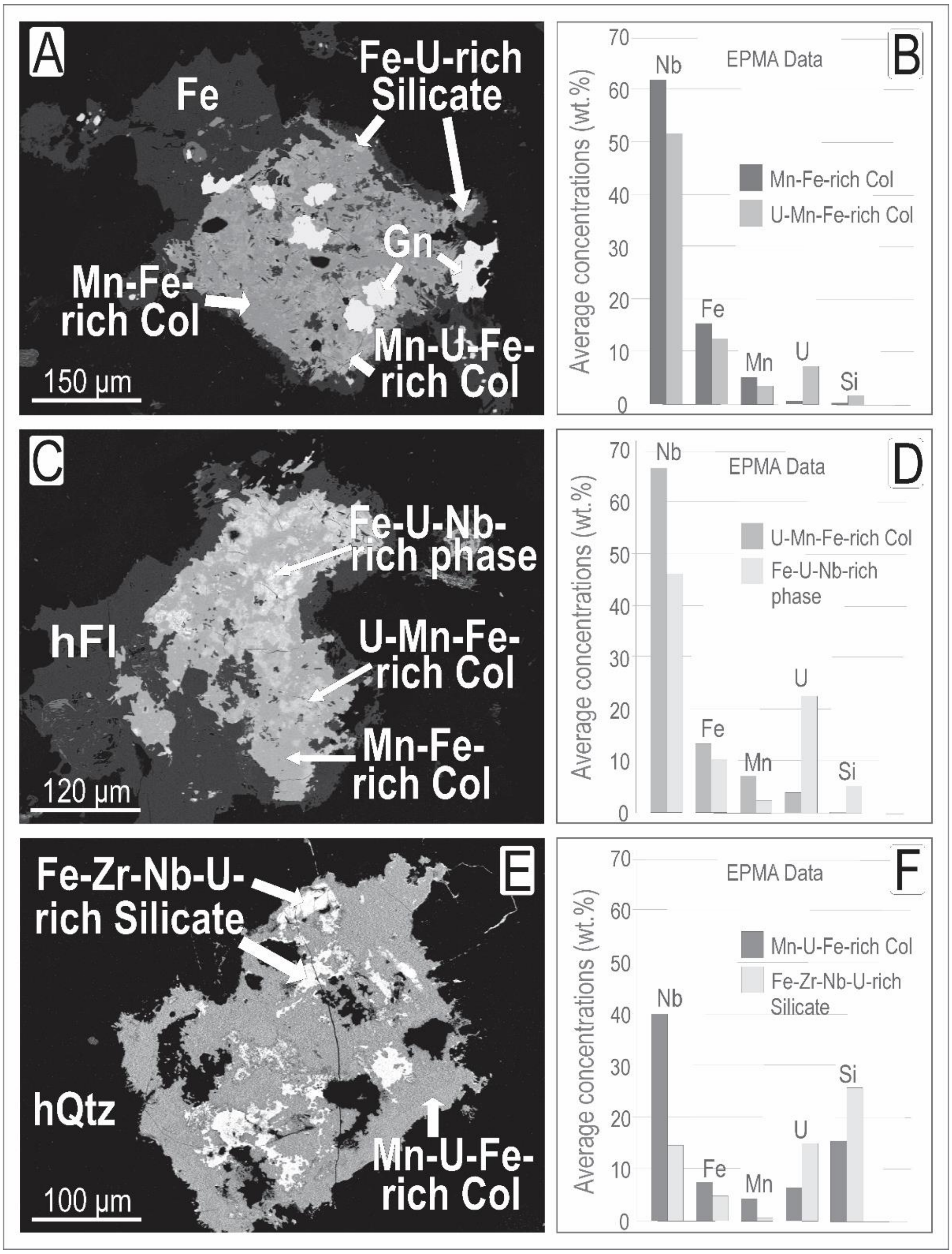

Fig. 05. BSE images of fully columbitized grains from the albite-enriched granite. (A) Grain constituted by Mn-Fe-rich Col (dark gray) with disseminated Mn-U-Fe-rich Col (light gray), galena (white) and U-rich silicate; the set is surrounded by iron oxide. (B) EPMA data for columbite in A shows that high U content comes along with high Si and lower Nb, Mn and Fe grades. (C) Grain predominantly composed by Mn-Fe-rich Col (dark gray) encompassing masses gradually richer in U composing U-Mn-Fe-rich Col (light gray) and Fe-U-Nb-rich phase (white); the set is surrounded by hydrothermal fluorite. (D) EPMA data for columbite in C presents the same pattern as in B. (E) Mn-U-Fe-rich Col grain (dark gray) with irregular masses of Fe-U-Si-Nb-rich phase (white). (F) EPMA data for the phases in E. Abbreviations: Col = columbite, Fe = iron oxide, Gn = galena, hFl = hydrothermal fluorite, hQtz = hydrothermal quartz.

Other products of pyrochlore alteration: Both in the AGC and AGB, silicatic phases composed of U-Th-Zr-Y-REE and F are associated with columbite and pyrochlore grains showing advanced alteration. These silicates likely represent intermediate phases within the coffinite-thorite-zircon-xenotime solid solution system, potentially comprising Zr-Y-HREE-rich coffinite and thorite grains with variable enrichments in Nb, F, and P. They are observed (i) as irregular-shaped masses surrounded by columbite, exhibiting reactive contact with it, such as the Th-U-rich silicate in Fig. 6A; (ii) filling cavities within pyrochlore and columbite (Fig. 6B); and (iii) included in the matrix adjacent to columbite. The textural relationships suggest that these silicates formed simultaneously with columbite and were significantly affected and corroded by late-stage hydrothermal fluids that precipitated cryolite (AGC), fluorite (AGB), iron oxide, and quartz.

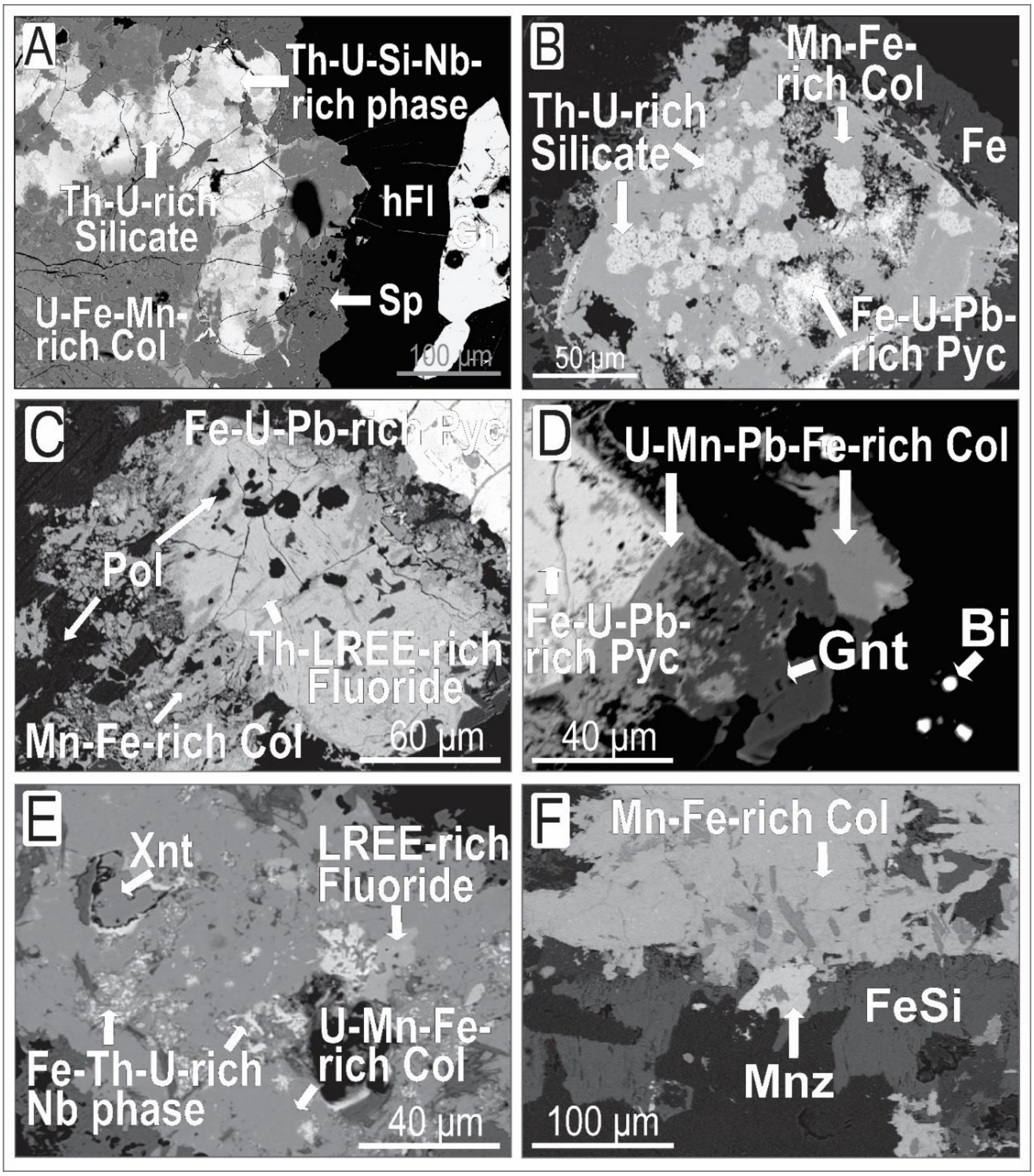

Fig. 6. BSE images of other products of pyrochlore alteration from the albite-enriched granite. (A) Detail of a U-Fe-Mn-rich Col surrounded by sphalerite, hydrothermal fluorite and galena; inside the grain occur a relict of a Th-U-Si-Nb-rich phase and Th-U-rich silicate. (B) Inside the Mn-Fe-rich Col grain (gray) occur rounded pockets of Th-U-rich silicate (light gray) and relicts of Fe-U-Pb-rich Pyc (white); the set is surrounded by iron oxide (dark gray). (C) Th-LREE-rich fluoride grain (light gray), located at the edge of a Fe-U-Pb-rich Pyc grain (white), in contact with Mn-Fe-rich Col (gray) and polylithionite (black); detail of Fig. 3D. (D) Likely genthelvite (dark gray) associated with U-Mn-Pb-Fe-rich Col (gray) at the border of Fe-U-Pb-rich Pyc; micrograins of native Bi occurs included in the matrix. (E) Inside the U-Mn-Fe-rich Col occurs grains of xenotime, LREE-rich fluoride and of a Fe-Th-U-Nb-rich phase. (F) Monazite in between Mn-Fe-rich Col and Fe-rich silicate. Abbreviations: Bi = native bismuth, Col = columbite, Fe = iron oxide, FeSi = iron-rich silicate, Gnt = genthelvite, hFl = hydrothermal fluorite, Mnz = monazite, Pyc = pyrochlore, Sp = sphalerite, Xnt = xenotime.

LREE-rich fluorides are frequently associated with pyrochlore grains exhibiting incipient alteration (AGC) as well as with intensely altered grains (AGB). They can be enriched in Th, Y, and Ca and occur (i) arranged along the edges of the pyrochlore grains, in contact with or surrounded by columbite, displaying reactive contact with columbite, iron oxide, and quartz (Figs. 4B, 6C); and (ii) disseminated within pyrochlore and columbite grains as rounded and irregular-shaped masses in reactive contact with the associated minerals (Fig. 6E). In contexts (i) and (ii), the LREE-rich fluoride encompasses columbite fragments, and vice versa, suggesting simultaneous formation of these minerals. The LREE-rich fluoride underwent alteration by a hydrothermal fluid that created cavities subsequently filled by quartz and iron oxide.

Galena, associated with pyrochlore alteration, is found in the AGC only in the central part, near to the massive cryolite deposit. It appears as rounded crystals included in columbite, exhibiting an abrupt contact with columbite. In the AGB, galena is more common and occurs within or near completely columbitized grains, where it is included in iron oxide, fluorite, or other minerals. The contacts with all minerals are abrupt and irregular (Fig. 5A). Less frequently, the following secondary phases have been observed associated with columbite: (i) Mn-Fe-Zn-rich sulfo-silicate (likely genthelvite) in the AGC and AGB, surrounding columbite with a corrosive contact (Fig. 6D); (ii) sphalerite in the AGB and central part of the AGC, surrounding columbite grains and showing reactive contact with it (Fig. 6A); (iii) Y-HREE-rich phosphate (probably xenotime) in the AGC and AGB, occurring as inclusions in columbite (Fig. 6E) and in the matrix minerals with a dissolution-like appearance; (iv) LREE-rich phosphate (Fig. 6F, probably monazite) in the AGB, situated between columbite grains and the surrounding iron silicate, with reactive contact with these minerals and included in the matrix; and (v) native Bi and Bi sulfide, in the AGC and AGB, measuring up to 5 μm, and occurring as inclusions in the matrix minerals surrounding pyrochlore, columbite, zircon, and thorite grains (Fig. 6D).

Late hydrothermal alterations: The hydrothermal fluid, which gradually became enriched in F and Si, partially corroded the minerals formed during the early hydrothermal stage, such as columbite and U-rich silicates. Among these minerals, columbite was particularly affected by the late hydrothermal fluid, while secondary pyrochlore showed greater resistance. The columbitized borders of the pyrochlore grains underwent significant dissolution, and the leached Fe from columbite may have been the primary source for the formation of surrounding iron oxide. This iron oxide fills microfractures and cavities within the columbite and pyrochlore grains (Fig. 5A).

Following the crystallization of cryolite and fluorite, the remaining hydrothermal fluid, which was predominantly siliceous, caused intense hydraulic fracturing in both the pyrochlore grains of the AGC and the AGB (Fig. 4). These fractures affected magmatic and hydrothermal pyrochlore, columbite, and other early secondary minerals, and were subsequently filled with hydrothermal quartz. Associated with these fractures are cavities that are also filled with quartz (Fig. 5E). Hydrothermal quartz is also observed in reactive contact with iron oxide (Fig. 5A) and fluorite (Fig. 5B), causing disaggregation of these minerals and filling the resulting cavities.

Pegmatites: We conducted analyses (including petrography, EDS, EPMA, and whole-rock geochemistry) on a few dozen pegmatite samples, specifically examining pegmatite veins within the AGC, pegmatitic AGC, and border pegmatites. The pyrochlores found in these pegmatites are clearly inherited from the AGC and AGB, with no other primary U-rich minerals observed. However, due to the limited size and scope of the pegmatites, we will not provide detailed information about these pyrochlores and their alterations in this study. Instead, a separate article dedicated to the alteration of pyrochlore will cover these aspects extensively.

Mineral composition

Pyrochlore: The representative compositions of pyrochlore are provided in Table 1. The structural formula of pyrochlore ($A_{2-m}B_2X_{6-w}Y_{1-n}\ pH_2O$; m = 0-1.7, w = 0-0.7, n = 0-1, p = 0-2) was calculated based on the assumptions of Ercit et al. (1994) and Atencio et al. (2010). These assumptions include: (i) charge balance in the crystal structure; (ii) full occupancy of octahedral B-sites by Nb^{5+}, Ta^{5+}, Ti^{4+}, Si^{4+}, and Sn^{4+} (*i.e.* site VI = 2); (iii) presence of a vacancy in the cubically coordinated A-site, which can be occupied by M^{4+} (U, Th), M^{3+} (Y, REE), M^{2+} (Pb, Fe, Ca, Mn), and Na^+ (*i.e.* site VIII = 2-□); (iv) substitution of oxygen in the X-site by F^- and OH^-; and (v) occupancy of the Y-site by F^-, OH^-, H_2O, and O^{2-}. The OH content was calculated by considering the total cationic charges at sites A and B. In addition to these elements, concentrations of P, V, Zr, Hf, Al, Bi, Mg, Zn, Sr, Ba, K, Rb, Cl, and S were also analyzed and found to be present in the pyrochlore samples in concentrations ranging from hundreds to thousands of ppm. These elements were not included in the totals of the analyses and structural calculations.

Tab. 1. EPMA data (in wt.%) for (1) U-Pb-LREE-rich pyrochlore, (2,3) U-LREE-Pb-rich pyrochlore, (4) LREE-U-Pb-rich pyrochlore, (5) LREE-Pb-U-rich pyrochlore, (6,7,8) Fe-U-Pb-rich pyrochlore, (9) Pb-Fe-U-rich pyrochlore, (10,11) Fe-U-rich pyrochlore, (12) Fe-Mn-U-rich pyrochlore.

Facies	Core albite-enriched granite								Boder albite-enriched granite			
Crystal	**(1)**	(2)	(3)	**(4)**[1]	(5)[1]	(6)	(7)[1]	(8)	(9)	**(10)**	(11)	(12)
Nb_2O_5	46.20	50.83	48.01	40.10	45.81	27.55	32.10	21.69	53.78	31.93	52.23	39.26
Ta_2O_5	06.13	06.15	06.25	02.47	03.72	05.99	02.43	04.56	04.99	01.69	04.75	02.66
SiO_2	00.21	00.21	00.19	00.42	00.18	03.19	00.89	08.31	01.62	13.82	01.35	00.16
SnO_2	01.16	02.72	02.31	00.72	02.60	01.11	00.90	00.00	00.00	d.l.	00.00	00.08
TiO_2	01.05	00.47	00.50	00.92	d.l.	d.l.	01.17	00.81	01.43	01.45	00.90	02.61
UO_2	02.81	02.24	03.08	06.97	06.54	04.06	07.39	13.51	08.38	12.64	08.56	13.73
ThO_2	01.77	02.24	01.64	00.49	00.29	01.21	00.10	00.00	00.75	00.84	00.45	00.92
Y_2O_3	01.00	00.71	00.78	00.13	00.25	d.l.	00.00	00.00	00.11	00.25	00.30	00.16
La_2O_3	01.04	00.63	01.12	00.57	00.75	00.04	00.08	00.00	00.06	00.06	00.12	00.00
Ce_2O_3	03.43	02.19	03.77	02.38	03.15	00.58	00.93	00.33	00.85	00.62	01.19	00.47
Pr_2O_3	00.39	00.27	00.43	00.26	00.38	d.l.	00.00	00.00	00.06	00.18	00.15	00.06
Nd_2O_3	01.60	01.12	01.75	00.74	00.92	00.27	00.35	00.15	00.52	00.49	00.65	00.24
Sm_2O_3	00.56	00.43	00.35	00.13	00.21	d.l.	00.11	00.00	00.27	00.24	00.37	00.00
Eu_2O_3	d.l.	d.l.	00.00	00.00	00.04	00.00	00.00	00.00	d.l.	00.05	00.00	00.09
Gd_2O_3	d.l.	00.20	00.00	00.00	00.00	d.l.	00.00	00.00	00.06	00.24	00.00	00.00
Dy_2O_3	00.46	00.13	00.35	d.l.	00.00	d.l.	00.00	00.00	00.08	00.59	00.10	00.00
Ho_2O_3	d.l.	00.00	00.00	d.l.	d.l.	00.21	00.00	00.14	d.l.	00.20	00.00	00.00
Er_2O_3	00.18	00.13	00.11	00.05	00.21	00.00	00.00	00.00	00.10	00.39	00.00	00.00
Tm_2O_3	00.07	00.16	00.17	00.07	00.18	00.12	00.00	00.00	00.14	00.04	00.14	00.00
Yb_2O_3	00.20	00.08	00.00	00.08	00.05	00.08	00.00	00.00	00.23	00.25	00.06	00.00
Lu_2O_3	d.l.	d.l.	00.00	00.00	00.10	d.l.	00.00	00.00	00.12	00.16	00.17	00.00
FeO[(2)]	00.69	00.28	00.16	01.70	00.10	02.71	02.93	03.10	05.92	03.24	04.30	04.62
CaO	01.42	01.73	01.30	01.04	03.01	d.l.	00.20	00.00	00.30	00.34	01.83	00.00
MnO	00.11	00.19	00.22	00.23	d.l.	00.00	00.12	00.09	01.20	00.49	00.66	05.98
PbO	07.23	14.51	07.52	13.98	05.56	30.69	17.23	25.94	02.85	00.02	02.19	00.64
Na_2O	00.76	00.20	00.30	00.18	00.70	00.06	00.61	00.20	00.49	00.31	00.42	00.00
F	02.73	02.96	02.73	00.85	02.79	00.40	00.23	00.20	00.45	00.21	02.50	00.00
$F{=}O_2$	-01.15	-01.24	-01.15	-00.36	-01.17	-00.17	-00.10	-00.08	-00.19	-00.09	-01.05	-00.00
Total[(3)]	**80.08**	**89.57**	**83.03**	**74.18**	**76.41**	**78.12**	**67.67**	**78.93**	**83.94**	**69.34**	**82.33**	**71.69**
Structural formula based on a sum of 2 a.p.f.u. in the $^{[6]}B$ site												
U^{4+}	0.052	0.038	0.055	0.154	0.127	0.105	0.190	0.301	0.131	0.189	0.141	0.296
Th^{4+}	0.034	0.039	0.030	0.011	0.006	0.032	0.003		0.012	0.013	0.008	0.020
Y^{3+}	0.044	0.029	0.033	0.007	0.012				0.004	0.009	0.012	0.008
La^{3+}	0.032	0.018	0.033	0.021	0.024	0.002	0.003		0.002	0.002	0.003	
Ce^{3+}	0.105	0.061	0.111	0.087	0.101	0.025	0.039	0.012	0.022	0.015	0.032	0.017
Pr^{3+}	0.012	0.007	0.012	0.010	0.012				0.001	0.005	0.004	0.002
Nd^{3+}	0.048	0.030	0.050	0.026	0.029	0.011	0.014	0.005	0.013	0.012	0.017	0.008
Sm^{3+}	0.016	0.011	0.010	0.005	0.006		0.004		0.007	0.006	0.010	0.003
Eu^{3+}					0.001					0.001		
Gd^{3+}		0.005							0.002	0.005	0.002	
Dy^{3+}	0.012	0.003	0.009						0.002	0.013		
Ho^{3+}						0.008		0.004		0.004		
Er^{3+}	0.005	0.003	0.003	0.002	0.006				0.002	0.008	0.003	
Tm^{3+}	0.002	0.004	0.004	0.002	0.005				0.003	0.001	0.001	
Yb^{3+}	0.005	0.002		0.002	0.001	0.003			0.005	0.005	0.004	
Lu^{3+}					0.003				0.003	0.003		
Pb^{2+}	0.162	0.297	0.163	0.373	0.131	0.958	0.537	0.700	0.054		0.044	0.017
Fe^{2+}	0.048	0.018	0.011	0.141	0.008	0.263	0.283	0.260	0.349	0.182	0.267	0.375
Mn^{2+}	0.008	0.013	0.015	0.020			0.011	0.007	0.072	0.028	0.042	0.491
Ca^{2+}	0.127	0.141	0.112	0.111	0.282		0.025		0.023	0.024	0.146	
Na^{+}	0.123	0.030	0.046	0.035	0.119	0.013	0.138	0.038	0.067	0.041	0.060	
$\Sigma_{[8]A}$	**0.835**	**0.750**	**0.698**	**1.006**	**0.872**	**1.423**	**1.248**	**1.329**	**0.774**	**0.565**	**0.797**	**1.238**
Nb^{5+}	1.739	1.747	1.744	1.795	1.805	1.441	1.677	0.982	1.714	0.968	1.753	1.721
Ta^{5+}	0.139	0.127	0.137	0.067	0.088	0.189	0.076	0.124	0.096	0.031	0.096	0.070
Si^{4+}	0.017	0.016	0.016	0.042	0.016	0.370	0.104	0.833	0.115	0.929	0.100	0.016
Sn^{4+}	0.039	0.083	0.074	0.028	0.091		0.041					0.003
Ti^{4+}	0.066	0.027	0.030	0.069			0.102	0.061	0.076	0.073	0.050	0.190
$\Sigma_{[6]B}$	**2.000**	**2.000**	**2.000**	**2.000**	**2.000**	**2.000**	**2.000**	**2.000**	**2.000**	**2.000**	**2.000**	**2.000**
O^{2-}	4.878	4.672	4.667	5.328	4.983	5.789	5.559	5.349	4.643	3.580	4.771	5.938
OH^{-}	1.122	1.328	1.333	0.672	1.017	0.211	0.441	0.651	1.357	2.420	1.229	0.062
Σ_X	**6.000**	**6.000**	**6.000**	**6.000**	**6.000**	**6.000**	**6.000**	**6.000**	**6.000**	**6.000**	**6.000**	**6.000**
F^{-}	0.721	0.713	0.695	0.268	0.771	0.148	0.085	0.062	0.101	0.046	0.588	
OH^{-}	0.279	0.287	0.305	0.732	0.229	0.852	0.915	0.938	0.899	0.954	0.412	1.000

Σ_Y	**1.000**	**1.000**	**1.000**	**1.000**	**1.000**	**1.000**	**1.000**	**1.000**	**1.000**	**1.000**	**1.000**	**1.000**

[1]Center of the core albite-enriched granite; [2]Total Fe as FeO; [3]Calculated. Abbreviations: d.l. = below detection limit.

The systematically low totals observed in the pyrochlore analyses can be attributed to several factors, including strong hydration of the mineral, metamictization (amorphization due to radiation damage), and the presence of voids. Niobium is the dominant substituent at the B-site in all pyrochlore crystals, with Nb_2O_5 concentrations ranging from 21.69 to 53.78 wt%. Based on the relative proportions of Nb, Ta, and Ti in the B-site, all the samples belong to the pyrochlore group (Fig. 7), as defined by Hogarth (1977). Silica (SiO_2) is clearly substituting for Nb in the B-site, with concentrations ranging from 0.16 to 13.82 wt%. There is a strong negative correlation (-0.97) between the amount of silica and niobium content (Fig. 8A). While Hogarth (1977) considered silicon to be present as an impurity in pyrochlore, it has been reported by Lumpkin and Mariano (1996) and by Johan and Johan (2004) that high SiO_2 contents can be incorporated into the B-site of the pyrochlore lattice, reaching up to 7.9 wt% and 10.12 wt%, respectively.

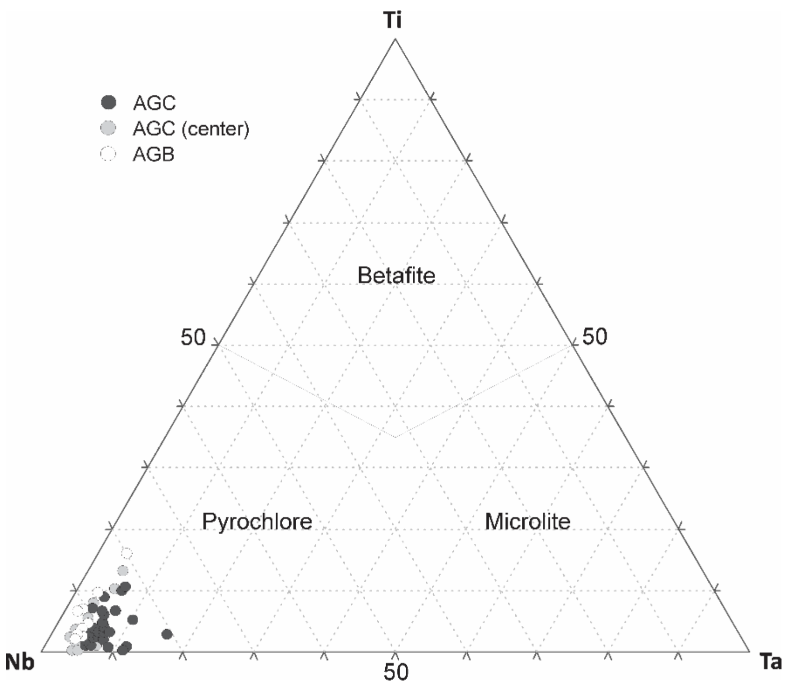

Fig. 7. Pyrochlore-microlite-betafite classification expressed as percentages of Nb + Ta + Ti atoms (Hogarth, 1977). Abbreviations: AGC = albite-enriched granite core, AGB = albite-enriched granite border.

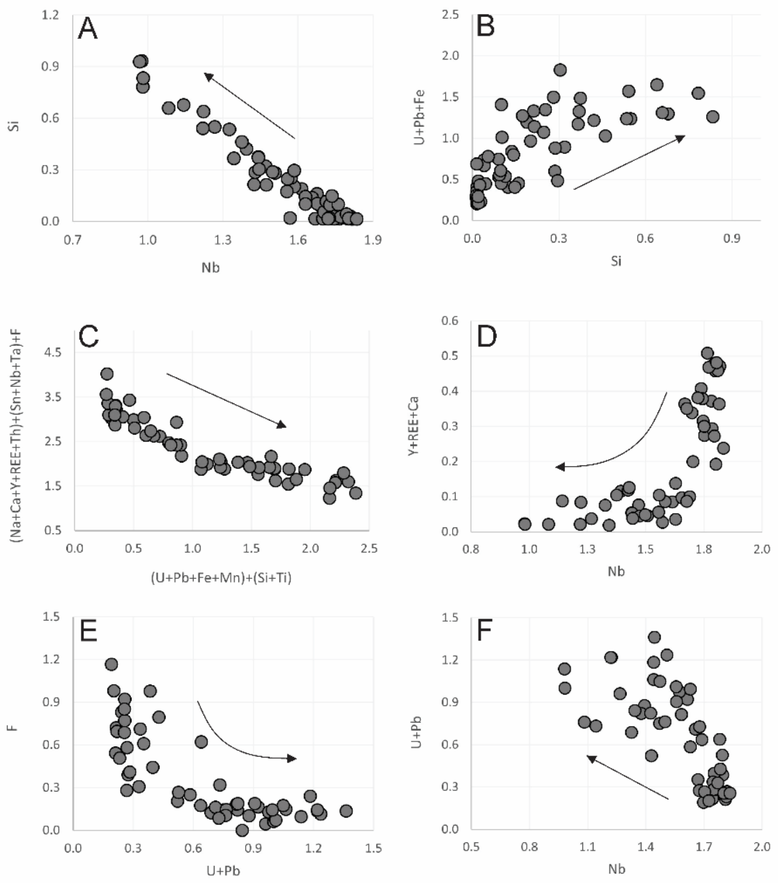

Fig. 8. Binary diagrams for pyrochlore from the albite-enriched granite. (A) Si *versus* Nb. (B) U+Pb+Fe *versus* Si. (C) (Na+Ca+Y+REE+Th)+(Sn+Nb+Ta)+F *versus* (U+Pb+Fe+Mn)+(Si+Ti). (D) Y+REE+Ca *versus* Nb. (E) F *versus* U+Pb. (F) U+Pb *versus* Nb. Concentrations are expressed in percentages of atoms.

In Hogarth's (1977) pyrochlore classification scheme, the individual varieties within the subgroup are defined by the A-site cations. In the AEG, various pyrochlore varieties can be found, including U-Pb-LREE-rich, U-LREE-Pb-rich, LREE-Pb-U-rich pyrochlore, Fe-U-Pb-rich, and Fe-U-rich pyrochlores (Tab. 1), as well as others with less common proportions of A-site cations such as U, Pb, Fe, LREE, Ca, Th, Na, and Mn. The diverse compositions of pyrochlore reflect the intense hydrothermal alteration that affected the original magmatic pyrochlore. In this work, the classification scheme proposed by Atencio et al. (2010) was not utilized. Instead, the terminology and descriptive terms introduced by Hogarth (1977) were employed, as they were more suitable for the SEM analysis conducted in this investigation. The highly altered and hydrated nature of the pyrochlore crystals necessitated the use of more descriptive terms to maintain coherence and continuity with the SEM-based observations.

The pyrochlore samples analyzed in this study exhibit a range of U contents, with concentrations varying from 2.24 to 13.73 wt% UO_2. Pyrochlore crystals in the AGB and central portion of the AGC generally show higher U enrichment (average ~7.75 wt% UO_2) compared to the rest of the AGC (average ~5.05 wt% UO_2). Among the pyrochlore species analyzed, the Fe-U-Pb-rich pyrochlore demonstrates the highest U content (4.06 to 13.51 wt% UO_2) and is also associated with significant concentrations of Pb (17.23 to 30.69 wt% PbO_2). The maximum observed Th content in pyrochlore is 2.24 wt% ThO_2, and it occurs in the U-LREE-Pb-rich species. In the U-rich species, Th content is generally lower than 1 wt% ThO_2 or absent. Fluorine is the dominant anion in the Y-site of the LREE-enriched pyrochlore species, with concentrations of up to 2.96 wt% F, while OH is dominant in the Fe-U-Pb-enriched species. According to Johan and Johan (1994), the high U concentrations in the A-site of defect pyrochlore ($A^{2+} \square B_2^{5+} O_6 \square$) can lead to the appearance of significant M^{4+} in the B-site, which supports the presence of Si, Ti, and Sn in the B-structural site of the AEG pyrochlore. The high vacancies in the A-site can be explained by a hypothetical end-member $U^{4+} \square B_2^{4+} O_6 \square$. Another compatible substitution scheme is $2Ca^{2+} + 2(Nb, Ta)^{5+}$ or $Na^{+}REE^{3+} + 2(Nb, Ta)^{5+} \leftrightarrow (Pb, Fe)^{2+}U^{4+} + 2(Si, Ti)^{4+}$. This is supported by the positive correlation (0.76) observed between U + Pb + Fe and Si concentrations (Fig. 8B).

The central portions of the less altered grains in the AGC can be considered as relict varieties of primary pyrochlore, which are relatively rich in LREE, as observed in Tab. 1. These crystals are (1) U-Pb-LREE-rich pyrochlore, (2, 3) U-LREE-Pb-rich pyrochlore, (4) LREE-U-Pb-rich pyrochlore, and (5) LREE-Pb-U-rich pyrochlore. Some grains of U-LREE-Pb-rich pyrochlore (Tab. 1, analyzes 2, 3) also exhibit a pattern where the central portions have lower Pb concentration (min. 7.5 wt.% PbO), while higher Pb concentration are observed along the border and microfractures (max. 14.5 wt.% PbO). In this case, there is an inverse correlation between Pb and LREE (-0.93), and the U content does not show significant variation.

The alteration of U-Pb-LREE-rich pyrochlore in both AGC and AGB involves the loss of LREE and Nb, resulting in a progressive enrichment of Pb, U, Fe, and Si. This overall trend is shown in Fig. 8C, although it should be noted that the alteration process is not a continuous evolution. Through the detailed SEM study, corroborated by EPMA analyses, it was possible to compare samples with different degrees of pyrochlore alteration. This comparison reveals that the alteration process involved preferential leaching of specific cations in successive stages. It is important to note that the enrichments observed were not solely relative; there was also incorporation of elements by the pyrochlore. Figure 9 summarizes the main exchanges that occurred during the alteration process. The first stage of alteration involved the leaching of LREE (Fig. 8D). In the second stage, the loss of LREE was accompanied by losses of Nb and F, while Fe and Si were incorporated, leading to a significant relative enrichment in U and Pb (Fig 8E, F). This stage resulted in the formation of the most common variety of pyrochlore in the AGC, the Fe-U-Pb-rich pyrochlore (Tab. 1, analysis 6, 7, 8). In the third stage, losses of Pb and Fe began, along with continued losses of Nb and F. This gave rise to the varieties Pb-Fe-U-rich pyrochlore, Fe-U-rich-pyrochlore, and Fe-Mn-U-rich pyrochlore (Tab. 1, analysis 9, 10, 11, 12), which are the richest in U and are commonly found in the AGB and central zone of the AGC. Previous studies by Minuzzi et al. (2005) described continuous losses of Pb and Fe since the initial stage of alteration, which they attribute to the relative enrichment in U. However, these authors did not recognize and analyze the pyrochlores corresponding to the first two stages described in this study.

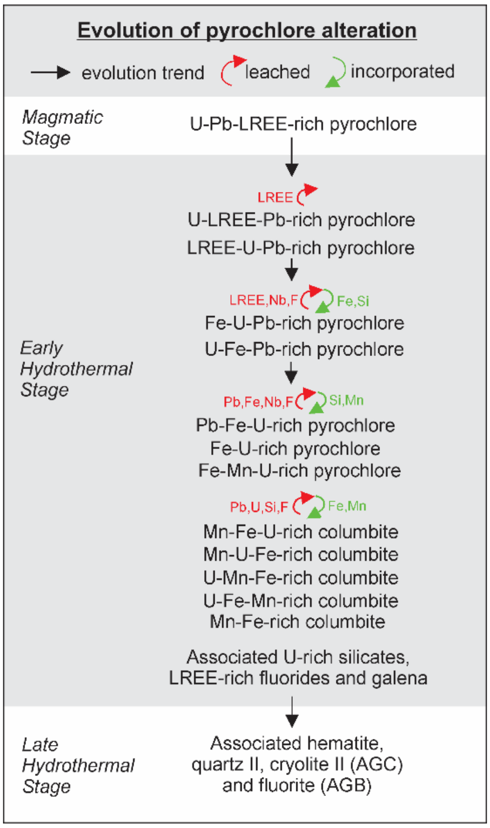

Fig. 9. Evolutionary progression of pyrochlore alteration in the albite-enriched granite.

Columbite: As the pyrochlore alteration progresses, a significant leaching of Pb occurs from its structure, leading to the collapse of the pyrochlore phase and the formation of columbite and other hydrothermal phases. Table 2 presents examples of columbite compositions, showcasing variations in Fe, Mn, and U contents. The observed compositions include: (a) Mn-Fe-rich columbite, which is the most common composition found in both AGC and AGB (crystals 1, 2); (b) U-Mn-Fe-rich columbite, characterized by ~3 wt% UO_2 (crystals 3, 4); (c) U-Fe-Mn-rich columbite (up to 10.05 wt% MnO_2, crystal 5), observed only in the AGB and the central zone of AGC; and (d) Mn-U-Fe-rich columbite, typically exhibiting high U content (~6 wt% UO_2, crystals 6, 7, 8). The U-enriched columbite species are commonly associated with highly or completely altered pyrochlore grains. The presence of U in columbite is often, but not always, associated with Si, which ranges from 0.15 to 15.8 wt% SiO_2. In the general formula AB_2O_6, both U and Si occupy the B-site, substituting Nb and Ta, along with Pb and Ti (Fig. 10A). The systematic excess in the B-site and the vacancy in the A-site are associated with high Si contents (correlation of 0.84, Fig. 10B), suggesting a coupled substitution mechanism involving both the A- and B-sites in the columbite crystal structure. *i.e.*, $(Fe, Mn)^{2+} + 2(Nb, Ta)^{5+} \rightarrow \square_A + 3(Si, U, Th, Ti, Sn)^{4+}$. The contents of REE_2O_3 (0.26-2.68 wt.%) in the columbite compositions are also unusually high compared to general studies of columbite composition (Ercit et al., 1995; Wise et al., 1998). The A-site in the columbite structure is occupied by Fe and Mn, which can substitute for each other (Fig. 10C). All columbite crystals exhibit enrichment in Fe (from 7.69 to 16.13 wt% FeO), and the majority of them are classified as columbite-(Fe) (Burk, 2008), with Mn/(Mn + Fe) atomic ratios ranging from 0.184 to 0.549 (Fig. 10D).

Tab. 2. EPMA data (in wt.%) for (1,2) Mn-Fe-rich columbite, (3,4) U-Mn-Fe-rich columbite, (5) U-Fe-Mn-rich columbite and (6,7,8) Mn-U-Fe-rich columbite.

Facies	AGC	AGB	AGB	AGB	AGB	AGB	AGC	AGB
Crystal	(1)	(2)	(3)	(4)	(5)	(6)	(7)	(8)
Nb_2O_5	66.74	68.93	65.61	66.67	63.63	51.29	40.31	57.12
Ta_2O_5	03.32	05.87	05.72	05.17	04.21	05.10	03.17	04.64
SiO_2	00.51	00.15	00.57	00.18	01.70	04.60	15.80	00.68
SnO_2	d.l.	d.l.	d.l.	01.72	00.20	d.l.	00.84	d.l.
TiO_2	02.57	01.26	02.36	01.63	03.20	01.14	02.74	02.74
UO_2	01.15	00.61	03.64	03.48	05.19	06.34	06.72	08.82
ThO_2	d.l.	00.05	00.18	00.32	00.44	01.48	00.56	00.78
Y_2O_3	00.12	d.l.	00.07	d.l.	d.l.	d.l.	d.l.	00.22
La_2O_3	d.l.	00.06	d.l.	d.l.	d.l.	00.13	d.l.	d.l.
Ce_2O_3	00.05	00.07	00.18	00.13	00.33	00.42	00.11	00.42
Pr_2O_3	d.l.	d.l.	d.l.	d.l.	d.l.	d.l.	d.l.	d.l.
Nd_2O_3	d.l.	d.l.	00.05	00.05	00.10	00.14	00.03	00.29
Sm_2O_3	00.17	00.10	00.18	00.14	d.l.	00.25	d.l.	00.28
Eu_2O_3	d.l.	d.l.	d.l.	d.l.	d.l.	00.04	d.l.	00.12
Gd_2O_3	00.08	d.l.	d.l.	d.l.	d.l.	d.l.	d.l.	00.15

Dy_2O_3	d.l.	d.l.	d.l.	d.l.	d.l.	d.l.	d.l.	00.40
Ho_2O_3	d.l.	d.l.	00.15	d.l.	00.13	00.10	d.l.	00.15
Er_2O_3	d.l.	00.07	00.16	00.18	00.09	00.10	d.l.	00.38
Tm_2O_3	d.l.	d.l.	00.16	d.l.	00.09	00.13	00.06	00.11
Yb_2O_3	d.l.	00.05	00.15	00.07	00.07	00.10	00.06	00.31
Lu_2O_3	d.l.	d.l.	d.l.	d.l.	d.l.	d.l.	d.l.	00.07
FeO[2]	15.33	11.79	16.13	12.27	08.37	10.08	07.69	13.85
CaO	00.40	00.37	d.l.	00.25	00.28	00.99	d.l.	d.l.
MnO	06.70	08.72	04.92	07.28	10.05	02.25	04.39	04.99
PbO	00.81	d.l.	00.06	00.13	00.38	02.83	03.78	00.36
Na_2O	d.l.	00.03	00.04	00.07	d.l.	00.76	d.l.	00.11
F	d.l.	d.l.	d.l.	d.l.	d.l.	00.44	d.l.	d.l.
$F{=}O_2$	-00.00	-00.00	-00.00	-00.00	-00.00	-00.18	-00.00	-00.00
Total[3]	**97.89**	**98.03**	**99.74**	**99.73**	**98.45**	**88.50**	**86.15**	**95.71**
Structural formula based on 3 cations and 6 oxygens								
Fe^{2+}	0.725	0.571	0.771	0.598	0.408	0.551	0.385	0.708
Mn^{2+}	0.321	0.428	0.238	0.359	0.496	0.125	0.223	0.258
$\Sigma_{[8]A}$	**1.046**	**0.999**	**1.009**	**0.957**	**0.903**	**0.676**	**0.607**	**0.966**
Nb^{5+}	1.704	1.803	1.693	1.754	1.674	1.515	1.089	1.578
Ta^{5+}	0.051	0.093	0.089	0.082	0.067	0.091	0.052	0.077
Si^{4+}	0.029	0.008	0.032	0.010	0.099	0.301	0.946	0.042
Sn^{4+}				0.040	0.005		0.020	
Ti^{4+}	0.109	0.055	0.101	0.071	0.140	0.056	0.123	0.126
U^{4+}	0.014	0.008	0.046	0.045	0.067	0.092	0.089	0.120
Th^{4+}		0.001	0.002	0.004	0.006	0.022	0.008	0.011
Y^{3+}	0.004		0.002					0.007
La^{3+}		0.001				0.003		
Ce^{3+}	0.001	0.002	0.004	0.003	0.007	0.010	0.002	0.009
Pr^{3+}								
Nd^{3+}			0.001	0.001	0.002	0.003	0.001	0.006
Sm^{3+}	0.003	0.002	0.004	0.003		0.006		0.006
Eu^{3+}						0.001		0.002
Gd^{3+}	0.002							0.003
Dy^{3+}								0.008
Ho^{3+}			0.003		0.002	0.002		0.003
Er^{3+}		0.001	0.003	0.003	0.002	0.002		0.007
Tm^{3+}			0.003		0.002	0.003	0.001	0.002
Yb^{3+}		0.001	0.003	0.001	0.001	0.002	0.001	0.006
Lu^{3+}								0.001
Pb^{2+}	0.012		0.001	0.002	0.006	0.050	0.061	0.006
Ca^{2+}	0.025	0.023		0.016	0.017	0.069		
Na^{+}		0.004	0.004	0.007		0.096		0.013
$\Sigma_{[8]B}$	**1.954**	**2.001**	**1.991**	**2.043**	**2.097**	**2.324**	**2.393**	**2.034**
Mn/(Mn+Fe)	0.307	0.428	0.236	0.375	0.549	0.184	0.367	0.267
Ta/Ta+Nb)	0.029	0.049	0.050	0.045	0.038	0.056	0.045	0.047

[1]Center of the core albite-enriched granite; [2]Total Fe as FeO; [3]Calculated. Abbreviations: AGC = albite-enriched granite core, AGB = albite-enriched granite border, d.l. = below detection limit.

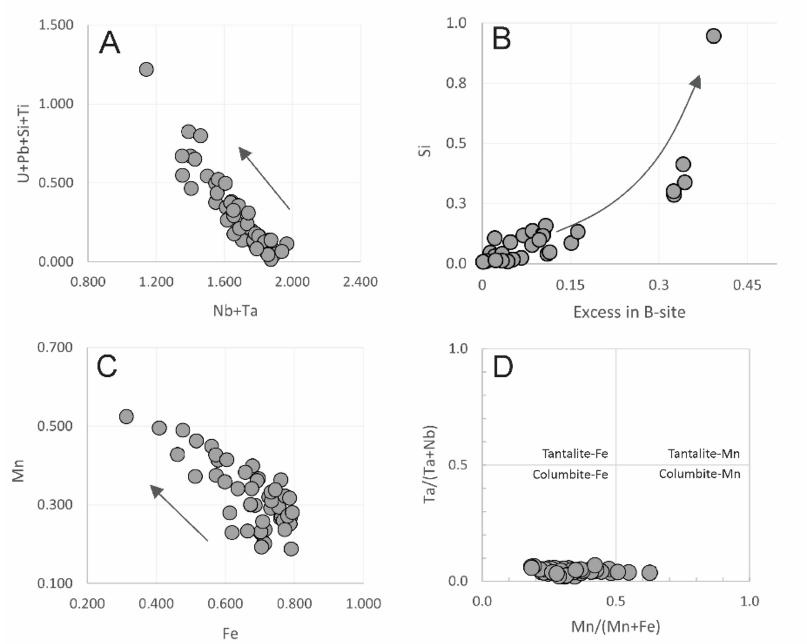

Fig. 10. Compositional variations in columbite crystals from the albite-enriched granite. (A) U+Pb+Si+Ti *versus* Nb+Ta. (B) Si *versus* excess in B-site. (C) Mn *versus* Fe. (D) Columbite-group classification diagram. Concentrations are expressed in percentages of atoms.

Other products of pyrochlore alteration: Secondary minerals associated with columbite formation exhibit enrichment in U and often have a non-stoichiometric multivariate composition (Tab. 3). In the AGB, a Pb-Fe-U-Nb-rich hydrothermal phase commonly observed displays Nb content up to 53 wt.% Nb_2O_5 (Tab. 3, crystal 1). However, the mineral species nature remains unclear, as its composition is intermediate between pyrochlore and columbite, and the stoichiometry resembles that of either a U-rich columbite or a highly vacant U-rich pyrochlore (Tab. 3, crystals 1, 2). Another hydrothermal phase, Si-Fe-U-Nb-rich with higher U (22.94 wt% UO_2, Tab. 3, crystal 3) could potentially be an oxi-petcheskite [$U^{4+}(Fe^{3+}{}_{2/3}\,\square_{1/3})(Nb, Ta)_2O_7(O, OH)$] (Mücke and Strunz, 1978) if Si occupies the U structural site. The calculated structural formula, assuming (Nb + Ta) = 2 a.p.f.u. is $(U^{4+}{}_{0.41}\,Si_{0.43}\,Th_{0.02}\,Y_{0.01}\,REE_{0.03}\,Ca_{0.02}\,Na_{0.07})_{0.99}$ $(Fe^{3+}{}_{0.62}\,Mn_{0.16}\,\square_{0.22})_{0.78}\,(Nb_{1.67}\,Ta_{0.11}\,Ti_{0.22})_2\,O_7\,(O_{0.6}\,OH_{0.4})$. Petcheskite occurrences are typically associated with pyrochlore supergroup minerals, but none have Si contents. Petscheckite found in the Hagendorf-Süd pegmatite in Germany (Mücke and Keck, 2008) was discovered included in columbite, while in the Antsakoa I pegmatite in Madagascar (Mücke and Strunz, 1978), columbite and petscheckite form a primary diataxial intergrowth. Heating experiments on the liandratite-petschekite series (Mücke and Strunz, 1978) at 1000°C reveal that hydroxy-petscheckite reacts towards a uraniferous pyrochlore composition. Hence, it is reasonable to suggest that the inverse reaction may have occurred during pyrochlore alteration in the AEG, involving continuous hydration of U-enriched pyrochlore with a Fe-enriched fluid. Furthermore, the Fe-U-Si-Nb-rich hydrothermal phase (Fig. 5E) is enriched in Si (10.19 wt% SiO_2, Tab. 3, crystal 4) and likely represents an intermediate phase in a solid solution system between U-enriched pyrochlore and U-enriched silicate. Similarly, the Th-U-Si-Nb-rich hydrothermal phase (Fig. 6A) contains up to 42.38 wt% UO_2 and 8.23 wt% ThO_2 (Tab. 3, crystal 5).

Tab. 3. EPMA data (in wt.%) for the following secondary minerals: (1) Pb-Fe-U-Nb-rich phase; (2) REE-Mn-Fe-U-Nb-rich phase; (3) Fe-U-Nb-rich phase; (4) Fe-U-Si-Nb-rich phase; (5) Th-U-Si-Nb-rich phase; (6) Th-U-rich silicate; (7) REE-Y-U-rich silicate; (8) U-Th-rich silicate; (9) U-Pb-Th-Zr-rich silicate; (10) U-LREE-rich fluoride; (11) Th-LREE-rich fluoride.

Facies	AGB	AGC	AGB				AGC				
Crystal	(1)	(2)[1]	(3)	(4)	(5)	(6)	(7)	(8)[1]	(9)	(10)[1]	(11)
Nb_2O_5	53.78	49.58	46.52	16.23	13.48	03.54	00.40	01.13	06.52	00.09	02.49
Ta_2O_5	04.99	03.03	04.97	01.98	00.33	d.l.	d.l.	d.l.	01.41	d.l.	d.l.
P_2O_5	d.l.	d.l.	d.l.	d.l.	d.l.	00.43	03.52	01.04	01.05	00.07	00.10
SiO_2	01.62	02.62	05.42	10.19	07.75	14.02	14.13	11.53	14.39	00.04	00.07
SnO_2	d.l.	0.79	d.l.	d.l.	d.l.	d.l.	d.l.	00.23	d.l.	d.l.	d.l.
TiO_2	01.43	02.37	03.71	01.97	01.80	00.41	d.l.	00.15	01.18	d.l.	00.22
UO_2	08.38	13.35	22.94	19.91	42.38	34.35	21.21	17.34	04.48	03.81	00.65
ThO_2	00.75	05.19	01.08	01.48	08.23	10.00	04.70	30.39	11.82	03.13	11.61
ZrO_2	d.l.	d.l.	d.l.	00.61	0.848	00.68	00.18	02.52	13.32	d.l.	d.l.
Y_2O_3	00.11	00.21	00.18	00.33	d.l.	01.07	10.27	03.51	01.89	d.l.	01.72
La_2O_3	00.06	00.02	00.06	00.04	00.08	00.05	d.l.	d.l.	d.l.	09.08	05.82
Ce_2O_3	00.85	00.44	00.47	00.22	00.85	00.68	00.02	00.18	00.23	26.33	17.03
Pr_2O_3	00.06	00.08	00.05	d.l.	00.15	00.19	d.l.	00.09	d.l.	03.55	02.22
Nd_2O_3	00.52	00.40	00.20	00.05	00.51	00.63	00.10	00.25	00.27	08.89	08.34
Sm_2O_3	00.27	00.18	00.15	00.06	00.19	00.21	d.l.	00.63	00.24	00.87	02.94
Eu_2O_3	d.l.	00.11	00.05	d.l.	d.l.	00.08	00.08	d.l.	d.l.	00.37	00.40
Gd_2O_3	00.06	00.35	00.10	d.l.	00.07	00.08	00.50	00.77	00.29	d.l.	00.38
Dy_2O_3	00.08	00.72	00.12	d.l.	d.l.	d.l.	02.43	00.23	00.71	d.l.	00.69
Ho_2O_3	d.l.	d.l.	d.l.	00.10	d.l.	00.24	00.49	01.00	00.14	00.13	00.28
Er_2O_3	00.10	00.54	00.19	00.11	00.12	00.21	02.06	01.64	00.44	00.30	00.26
Tm_2O_3	00.14	00.09	d.l.	00.04	d.l.	d.l.	00.26	00.30	00.11	d.l.	d.l.
Yb_2O_3	00.23	00.39	00.14	00.22	00.25	00.48	02.09	00.85	00.28	00.08	00.12
Lu_2O_3	00.12	00.11	d.l.	d.l.	d.l.	00.13	00.57	d.l.	00.14	d.l.	00.11
FeO[(1)]	05.92	12.09	10.28	05.63	00.49	00.17	00.80	00.25	01.47	00.12	01.50
CaO	00.30	d.l.	00.28	d.l.	00.23	d.l.	00.62	00.34	00.65	d.l.	02.11
MnO	01.20	05.47	02.32	00.25	00.23	d.l.	00.13	d.l.	00.38	00.12	00.48
PbO	02.85	01.30	d.l.	00.58	00.08	d.l.	00.09	01.23	10.70	00.55	00.29
Na_2O	00.49	00.14	00.44	00.26	d.l.	d.l.	00.02	00.04	00.17	00.12	00.24
F	00.45	00.49	d.l.	d.l.	01.24	02.97	03.92	04.54	02.61	17.31	10.75
$F{=}O_2$	-00.19	-00.21	-00.00	-00.00	-00.52	-01.25	-01.65	-01.91	-01.10		
Total[(2)]	**83.94**	**101.88**	**99.22**	**61.66**	**80.13**	**69.43**	**66.94**	**81.10**	**73.99**	**74.96**	**70.82**

[1]Center of the core albite-enriched granite; [2]Total Fe as FeO; [3]Calculated. Abbreviations: AGC = albite-enriched granite core, AGB = albite-enriched granite border, d.l. = below detection limit.

Pyrochlore alteration typically yields U-rich silicates and LREE-rich fluorides, along with columbite. Uranium-rich silicates occur in highly or completely altered pyrochlore grains, making them more common in the AGB and the central zone of the AGC. Uranium content ranges from 4.48 to 34.35 wt% UO_2, along with variable concentrations of Th, Y, REE, and Zr (Tab. 3, crystals 6-9), consistent with intermediate compositions in the coffinite-thorite-xenotime-zircon solid solution system. However, the general formula ABX_4 (A = U, Th, Y, REE, Pb, Fe, Mn, Ca, Na; B = Si, Ti, Sn, P, Nb, Ta; X = O, F, OH) calculated to yield X = 4 reveals a systematic deficit in both A and B-sites $[A_{1-\square}B_{1-\square}X)_4]$, with $\square_A$=0.01-0.39 and $\square_B$=0.01-0.42, likely due to high Nb^{5+} contents in the B-site (up to 6.52 wt% Nb_2O_5, Tab. 3, crystal 9). Incorporation of Nb associated with high F amounts (2.97 to 4.54 wt% F, Tab. 3) limits the occurrence of OH in the structure, although considerable amounts of molecular H_2O should be considered given the low totals of all secondary minerals in this solid solution system. LREE-rich fluorides are often found alongside pyrochlore grains with incipient alteration (AGC) as well as with intensely altered grains (AGB) and can be enriched in U (up to 3.81 wt% UO_2) Th, Y and Ca (Tab. 3, crystals 10, 11).

Geochemical distribution of Uranium in the albite-enriched granite and pegmatites

The average concentrations of U and Th, as well as the Th/U ratios, in the albite-enriched granite (AEG) subfacies and the associated pegmatites are presented in Table 4. The average U concentration in the AGC is 321.72 ppm UO_2, with values reaching as high as 1600 ppm UO_2. The AGB exhibits a slightly higher average U content of 344.95 ppm UO_2, with a maximum of 796 ppm UO_2. The pegmatite veins associated with the AGC display the highest U concentrations, averaging at 553.13 ppm UO_2. Regarding Th, the average content in the AGC is 800.16 ppm ThO_2, while in the AGB, it is 695.55 ppm ThO_2, with a maximum content of 1,8 wt% ThO_2 observed in pegmatites. The combined AEG (AGC+AGB) has average U and Th concentrations of 328.65 ppm and 759.79 ppm, respectively. Consequently, the U content in the Pitinga mine exceeds the average U concentration in granites/rhyolites (4.5 ppm) by a factor of over 73 (Cuney and Kyser, 2008). The average Th/U ratio ranges from 1.85 (AGB) to 3.82 (AGC), both of which are lower than the world average Th/U ratio for acid igneous rocks (5.6). However, rocks that have undergone significant alterations with post-magmatic mobilization typically exhibit Th/U ratios below 3 (Killeen, 1979).

Table 4. U and Th contents and Th/U ratios in the albite-enriched granite core (AGC), albite-enriched border (AGB) and pegmatites (PEG). Number of analyses in parentheses (Hadlich et al., 2019).

	UO_2 ppm			ThO_2 ppm			Th/U		
	Min.	Max.	Avg.	Min.	Max.	Avg.	Min.	Max.	Avg.
AGC	40.00	1,610.00	321.72 (111)	70.00	2,388.00	800.16 (113)	0.29	30.40	3.82 (110)
AGB	34.00	796.00	344.95 (54)	36.10	2,419.00	695.55 (71)	0.13	8.94	1.85 (53)
PEG	20.00	1,180.00	553.13 (64)	1,080.00	18,400.00	5,127.13 (98)	3.30	389.50	19.85 (64)

The maps depicting U, Th, Nb, and Zr concentrations in the AEG (Fig. 11) reveal distinct patterns. The highest U values are observed in the northern, northeastern, and central regions of the granite body. The areas with the highest U grades coincide with the regions exhibiting elevated Nb concentrations. However, the distribution of U does not correspond to that of Zr, as Zr contents remain relatively consistent throughout the AEG. These findings suggest that the U mineralization within the AEG is predominantly associated with pyrochlore and its alteration products. While zircon is abundant, it exhibits low U grades, averaging 1.55 ppm UO_2 in the AGC and 2.97 ppm UO_2 in the AGB (Nardi et al., 2012). Notably, xenotime grains from the AEG do not display significant U concentrations (Bastos Neto et al., 2012), and thorite exhibits an average U content of 0.35 wt% UO_2 (Hadlich et al., 2019).

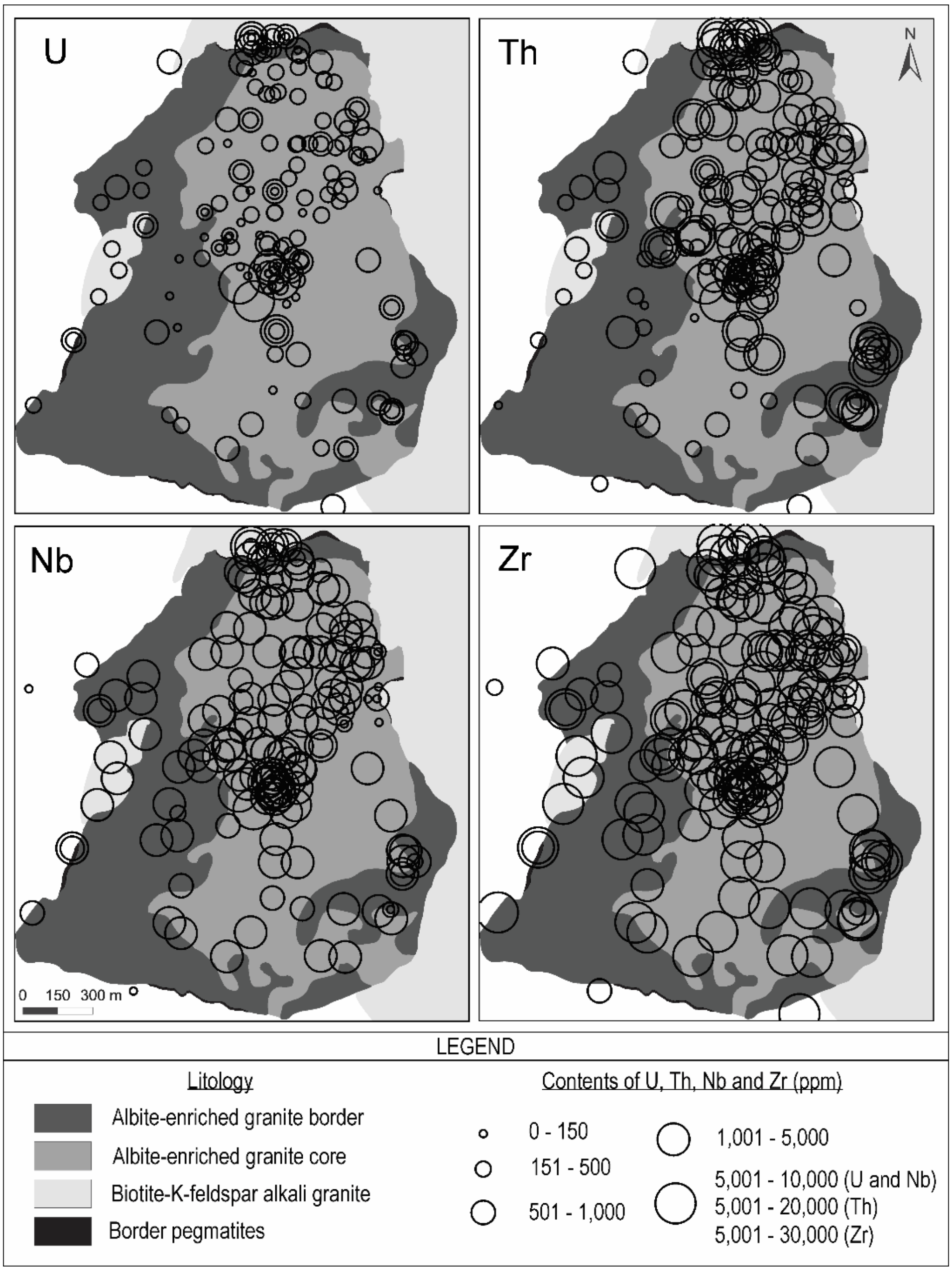

Fig. 11. Distribution maps of U, Th, Nb, and Zr in the albite-enriched granite.

Discussion

Primary pyrochlore: formation, U-enrichment, and distribution in the AEG

Uranium-bearing deposits typically encompass various uranium minerals, which vary depending on the ore genesis. The primary minerals uraninite (UO_2) and coffinite ($USiO_4$), both reduced U^{4+} minerals, are the most common. These minerals form during magma crystallization and are often found in association with feldspar and quartz. On the other hand, the majority of exploitable uranium minerals are considered secondary uranium minerals. They include pitchblende (U_3O_8), carnotite $[K_2(UO_2)_2(VO_4)_2\ xH_2O]$, autunite $[Ca(UO_2)_2(PO_4)_2\ xH_2O]$, and uranophane $[Ca(UO_2)_2(HSiO_4)_2xH_2O]$. Additionally, there are less common refractory uranium minerals such as brannerite (UTi_2O_6), davidite $[(La,Ce,Ca)(Y,U)(Ti,Fe^{3+})_{20}O_{38}]$ and betafite $[(Ca,U)_2(Nb,Ti,Ta)_2O_7]$ (Pownceby and Johnson, 2014).

According to Bea (1996), the nature, composition, and associations of the primary assemblage of accessory minerals rich in U, Th, REE and Y vary according on the aluminosity of the rock. In peraluminous granites, the primary assemblage includes monazite, xenotime, apatite, zircon, Th-orthosilicates, uraninite, and betafite-pyrochlore. Metaluminous granites are associated with allanite, sphene, apatite, zircon, monazite, and Th-orthosilicates. Peralkaline granites exhibit an assemblage of arscinite, fergusonite, samarskite, bastnaesite, fluocerite, allanite, sphene, zircon, monazite, xenotime, and Th-orthosilicates. The size and density of these accessory minerals, rich in U, Th, REE and Y, are too small to settle by gravity in the magmatic chamber. As a result, these minerals form at the beginning of magmatic crystallization and remain suspended in the magmatic melt until they are included into the crystallization of some major mineral (Bea, 1996).

The characteristics and concepts described above do not apply to the Pitinga deposit, as both the primary U ore mineral and the secondary paragenesis differ significantly from the aforementioned descriptions. Th/U ratio averages of 1.85 in the AGB and 3.82 in the AGC (Hadlich et al., 2019) attest the high availability of U in the earlier stages of magma evolution. The zircon abundance in the AGB (5 vol.%, Th/U_{avg}= 2.23) relative to AGC (2 vol.%, Th/U_{avg}= 5.33) (Bastos Neto et al., 2005; Nardi et al., 2012) suggests that the enrichment in U of the AGB is more likely due to primary magmatic crystallization rather than to post-magmatic processes, as suggested by Killeen (1979) for rocks with Th/U ratio below 3 (Hadlich et al., 2019). Fluorine-bearing complexes transported Sn and HFS elements throughout the melt, leading to the dispersed nature of cassiterite and U-Pb-pyrochlore mineralization during the early magmatic stage (Bastos Neto et al., 2009). However, the extreme enrichment of F in the residual melt (Lenharo, 1998) was prevented due to the buffering effect of magmatic cryolite crystallization (Dolejs and Baker, 2007). This crystallization process hindered the formation of zones with higher concentrations of ore.

The early occurrence of pyrochlore in F-rich magmas, which led to the formation of granites containing disseminated cryolite, has been documented in the albite arfvedsonite granite of the Ririwai Complex (Ogunleye et al., 2006). The preferential crystallization of pyrochlore over columbite in this context was attributed to the high fluorine content in the system (Linnen and Keppler, 1997). It is important to note that the early formation of pyrochlore does not solely rely on an extremely high concentration of fluorine in the melt. The solubility product (Ksp) of pyrochlore in only weakly influenced by the fluorine content when concentrations exceed 1 wt% (Tang et al. 2022).

In peralkaline granitic melts with A/CNK < 1, the Ksp values of pyrochlore are lower than those of columbite. Conversely, in peraluminous melts with A/CNK > 1, the Ksp values of pyrochlore are higher than those of columbite. In subaluminous melts, the Ksp values of pyrochlore and columbite are nearly the same (Tang et al., 2022). Tang et al. (2022) proposed three specific controls on pyrochlore crystallization during the evolution of peralkaline magma. (1) The Ksp of pyrochlore decreases significantly with decreasing temperature; in order for magmas to exist at low temperature, they must be highly fluxed, which may explain the common occurrence of Nb mineralization in F-rich granites. (2) Increase in the A/CNK ratio of the melt, related to processes such as fractionation, assimilation, and alkali diffusion active during magma evolution. (3) Pyrochlore crystallize when the concentrations of the essential components (ESCs) that compose pyrochlore reach the solubility product. At the AEG, the F richness, as well as the lower temperature of the magma, were the key factors determining the crystallization of primary pyrochlore instead of columbite.

The primary pyrochlore has ~2% F, which corresponds to an OH site occupation of ~30%. This F content may seem relatively low considering the richness of F in the magma and the high concentration of U in the mineral, given the affinity between these two elements. The interaction of columbite and uraninite with a fluid–magma system, consisting of a melt of Li–F-granite and fluoride fluid at 750°C and P = 2300 bar (Redkin and Borodulin, 2009), leads to the formation of zonal pyrochlores with considerably distinct uranium and fluorine contents. The fluorine-rich pyrochlores (7-12 wt% F) preserve the Nb/U ratio of the initial columbite (15-30). Conversely, uranium-bearing pyrochlores contain 2-4 times less amounts of fluorine, above 2 at% U, and the Nb/U molar ratio decreases to 5-15. The trends in Ca, U, and F concentrations suggest the influence of temperature on the reactions involving the exchange of Ca^{2+} and U^{4+} cations. The concentrations of U and F in the U-Pb-LREE-rich pyrochlore in the present study are similar to those found in the uranium-bearing pyrochlore from the experiment. Therefore, the enrichment of uranium in the U-Pb-LREE-rich pyrochlore within the magma likely accompanied the loss of F and Ca.

The greater stability of HREE in F-bearing complexes (Nardi et al., 2012) contributed to the preferential incorporation of LREE into pyrochlore. Zircon crystallization in the early magmatic stage was greatly inhibited due to high F content and alkalinity (Whalen et al., 1987). As the crystallization of hydrous Na-bearing silicates commenced, the reduction in alkalinity enabled intensified zircon crystallization, accompanied by the formation of xenotime and thorite. Consequently, zircon originated from a magma that was previously depleted in U, Nb, Ta and LREE (Hadlich et al., 2019).

Primary pyrochlore hydrothermal alteration and its products

All pyrochlore crystals in the AGC and AGB were affected by hydrothermal alteration caused by F-rich aqueous fluids that formed the massive cryolite deposit. In the most altered grains, only remnants of hydrothermal pyrochlore included in columbite are observed, along with other products resulting from pyrochlore alteration. Extensive research has been conducted on the transformation of pyrochlore through hydrothermal and weathering processes, with a predominant focus on carbonatite occurrences. While the original composition of pyrochlore influences the specific variety formed, the weathering-induced transformation of secondary pyrochlores tends to follow well-defined sequences at each locality (Giovannini et al., 2017). At Mount Weld, pyrochlore alteration is characterized by a gradual leaching of Ca and Na, with partial replacement by varying proportions of Sr and Ce (Lottermoser and England, 1988). In the Nb-deposit of Catalão I, the pyrochlore is considered secondary and, with increasing weathering, it undergoes enrichment in Ba and an increase in vacancies due to the loss of Ca and Na (Cordeiro et al., 2011). Lumpink and Ewing (1995) observed hydrothermal alteration of ‘uranpyrochlore’ during the later stages of granitic pegmatite evolution. This alteration process was characterized by a decrease in Na and F, accompanied by an increase in Ca and vacancies in the A- and Y-site, represented by the coupled substitutions $^{A}\square^{Y}\square \rightarrow {}^{A}Ca^{Y}O$, $^{A}Na^{Y}F \rightarrow {}^{A}Ca^{Y}O$, and $^{A}Na^{Y}OH \rightarrow {}^{A}Ca^{Y}O$. Exchange reactions between pyrochlore and fluid indicate that this alteration occurred at ~450-650 °C and 2-4 kbar. The fluid-phase composition was characterized by relatively low a_{Na+}, high a_{Ca2+}, and high pH. In the present study, the first cations to be leached from pyrochlore were the LREE. In the second stage, the loss of LREE were accompanied by the losses of Nb and F, and by the incorporation of Fe and Si, with a great relative enrichment in U and Pb. In the third stage, losses of Pb and Fe began, while Nb and F losses continued. This resulted in the formation of various pyrochlore varieties including Pb-Fe-U-rich pyrochlore, Fe-U-rich-pyrochlore and Fe-Mn-U-rich pyrochlore, which exhibit the highest U content (up to 13.82 wt.% UO_2). Thus, a selective release of different cations occurred throughout the alteration process. The occurrence of this mechanism is also supported by experimental studies investigating the alteration of uranium-containing pyrochlore supergroup minerals under hydrothermal conditions (T = 100-300°C), which demonstrated incongruent dissolution behavior, with varying release rates for different elements (Roberts et al., 2000; Xu et al., 2004; Pöml et al., 2011).

To maintain charge balance, the increase in U concentration at Pitinga also led to an increased number of vacancies at the A-site in the pyrochlore structure. The presence of vacancies at the A-site has been attributed to selective leaching of cations during hydrothermal processes (e.g., Johan and Johan, 1994; Seifert et al., 2000; Bambi et al., 2012) and to the presence of uranium and other radioactive elements, as they can produce amorphization of the structure (e.g., Viladkar and Bismayer, 2010). In the case of the analyses presented here, it is believed that both mechanisms contribute to the observed variations in the number of A-site vacancies. The preferential loss of Na and F and the corresponding increase in A-site vacancy can also be observed in the pyrochlore group minerals found in the A-type granitic rocks of the Katugin complex-ore deposit, which contains Nb, Ta, Y, REE, U, Th, Zr, and cryolite (Starikova et al., 2019). Whitin this deposit, three main types of pyrochlore have been identified: (i) primary magmatic pyrochlore, characterized by high concentrations of Na, REE, and F (with minor amounts of Ca, U, Th, and Pb); this type crystallized during the late magmatic stage, when the presence of Fe in the melt hindered the crystallization of columbite; (ii) secondary post-magmatic pyrochlore, which follows cracks or replaces primary pyrochlore in grain rims; it exhibits similar composition to the early phase, but with lower concentration of Na and F and less complete occupancy of the A- and Y-sites; (iii) secondary hydrothermal pyrochlore, formed through late-stage hydrothermal alteration; this type shows a wide range of element variations and contains minor amounts of K, Ba, Pb, Fe, and U (up to 5.6 wt%), as well as significant Si concentrations (up to 9.2 wt%); notably, it exhibits low Na and F concentrations.

In the AEG, the incorporation of Si and Fe during a specific stage of pyrochlore alteration was found to be significant. According to Johan and Johan (1994) the high concentration of U in the A-site of defective pyrochlore ($A^{2+} \square B_2^{5+} O_6 \square$) could explain the presence of notable amounts of M^{4+} in the B-site, suggesting a hypothetical end-member composition of $U^{4+} \square B_2^{4+} O_6 \square$. This model provides an explanation for the occurrence of Si, as well as Ti and Sn, in the B-structural site of the pyrochlore from the AEG, along with the high vacancy content in the A-site. Another compatible substitution scheme involves the exchange of $2Ca^{2+} + 2(Nb, Ta)^{5+}$ or $Na^{+}REE^{3+} + 2(Nb, Ta)^{5+} \leftrightarrow (Pb, Fe)^{2+}U^{4+} + 2(Si, Ti)^{4+}$. This substitution scheme is supported by the positive correlation (0.76) observed between U + Pb + Fe and Si concentrations (Fig. 8B). The incorporation of Fe and Si, along with Sr and Ba, from the fluids was also documented in the Miaoya complex (Wu et al., 2021), where the ultimate in situ replacement was represented by secondary ferrocolumbite, along with uraninite and Nb-bearing rutile.

A notable experiment conducted by Geisler et al. (2005a, b) on pyrochlore alteration yielded results inconsistent with a solid-state diffusion mechanism. Natural pyrochlore was treated in a solution containing 1M HCl and 1M $CaCl_2$ at 175 °C, selectively removing Ca and Na from the pyrochlore. This process resulted in a rim of depleted composition while retaining the crystal structure (Geisler et al. 2005a). The rapid reaction rate at moderate temperatures, the observation of a sharp nanometer-scale reaction interface through transmission electron microscopy (Geisler et al. 2005b), and the incorporation of ^{18}O from an enriched fluid into the pyrochlore structure support the notion of a pseudomorphic reaction. This reaction involves the dissolution of the pyrochlore parent and simultaneous reprecipitation of a defect pyrochlore at a moving reaction interface. In fact, in several cases, the alteration of pyrochlore under hydrothermal conditions led to its recrystallization (Xu et al., 2004; Leturcq et al., 2005; Pöml et al., 2007, 2011).

The alteration of pyrochlore in the AEG culminates in the breakdown of the pyrochlore structure and formation of columbite, as suggested by Minuzzi et al. (2006). The AEG Mn-Fe-rich columbite is considered a secondary pseudomorph phase. The reaction of pyrochlore with the hydrothermal fluid caused the complete or partial removal of Na, Ca, REE, Pb, U and Si and incorporation of Fe and Mn. The M^{3+} cations (Y, REE) are supposedly incorporated in the B-site along with anomalous high concentrations of M^{4+} cations (mostly U, Si and Ti) and minor M^{2+} cations (Pb, Ca), resulting in vacancies in the A-site, as in the scheme $(Fe, Mn)^{2+} + 2(Nb, Ta)^{5+} \rightarrow \square_A + 3(Si, U, Th, Ti, Sn)^{4+}$. Hydrothermal fluid reactions may result in the replacement of pyrochlore by columbite-(Fe) (Van Wambeke ,1965; Nasraoui and Bilal, 2000) following the reaction: $H^+ + Fe^{2+} + (CaNaNb_2O_6F)_{(S)} = FeNb_2O_6 + Ca^+ + Na^+ + HF$. In order to facilitate the removal of Na, Ca and F, and the influx of Fe, these exchange reactions should take place at low pH, low Ca and Na activities and relatively elevated activity of Fe. The replacement of 'uranpyrochlore' by 'ferrocolumbite', rather than by lueshite ($NaNbO_3$) or fersmite ($CaNb_2O_6$) in the Miaoya carbonatite (Wu et al., 2021) also indicates a moderate to high Fe^{2+}, but low Na^+ and Ca^{2+} environment, which is corroborated by phase diagrams of pyrochlore in the system of Na-Ca-Fe-Nb-O-H (Lumpkin and Ewing, 1992, 1995).

Columbite is a typical product of the hydrothermal alteration of pyrochlore in many carbonatites, syenites and alkali granites during the later stages of alteration. As examples, Uher et al. (2009) found columbite-(Fe) forming rare irregular intergrowths with Nb-Ta-rich rutile in the Prasivá granitic pegmatites, Slovakia. Doroshkevich et al. (2009) described columbite + quartz replacing pyrochlore in the Amba Dongar carbonatite complex, Gujarat, India. Columbite-(Fe) in syenogranites and related greisen from the reduced A-type Desemborque Pluton (Siachoque et al., 2020) are mainly associated with hydrothermal origin during the post-magmatic stage of crystallization. The columbite-1 is characterized by zoned crystals, which record two hydrothermal stages of crystallization: early Nb-rich core, and later Ta-rich rims. In contrast, columbite-2 is defined by irregular crystals with patchy textures, and its formation is related to disequilibrium processes driven by fluid-induced hydrothermal alterations involving the partial replacement of fluorite and/or cassiterite at the final post-magmatic stage. The chemical contrasts among the columbite types are related to disequilibrium crystallization processes (columbite-1) and to hydrothermal alterations during the post-magmatic evolution (columbite-2).

During fluid assisted alteration of the AEG pyrochlore, the released compounds, either leached or remained of coupled dissolution-reprecipitation processes, also resulted in the formation of phases with non-stoichiometric intermediate compositions between pyrochlore and columbite, suggesting the involvement of an additional process in the redistribution of uranium. The alteration of pyrochlore commonly leads to the formation of an amorphous layer and/or various crystalline phases on pyrochlore surfaces. These phases often form micro- and nanoparticles deposited on the pyrochlore surface, along grain boundaries, pores, and fractures, forming secondary veins. In most cases, pyrochlore alteration leads to the development of porosity, such as micro-cracks at grain boundaries between the original material and secondary phases, which further facilitates the migration of fluids (e.g., Forbes et al., 2011; Deditius et al., 2015). In our study, we identified secondary minerals associated with columbite that likely precipitated within the opened cavities in the pyrochlore structure. These minerals exhibit intermediate compositions between U-enriched pyrochlore and U-enriched silicate, as well as intermediate compositions within the coffinite-thorite-xenotime-zircon solid solution system. Additionally, galena and LREE-rich fluorides were observed. These findings support the notion that these secondary minerals incorporated leached U, Pb, and LREE from pyrochlore, as well as compounds derived from a hydrothermal fluid that was previously enriched in HFSE (Zr, Th, Y, HREE) and S. If the formation of petscheckite or its hydrated forms did occur, it was not a significant process in the AEG. The uranium incorporated in primary pyrochlore was relatively enriched in secondary pyrochlore, until the breakage of pyrochlore occurred, leading to the distribution of U throughout the secondary minerals, with preferential incorporation into Si-rich phases. The subsequent precipitation of iron oxide (hematite) shows the high Fe activity in the hydrothermal fluids during columbite formation.

Significant concentrations of U, Nb, and Ti are observed in Fe-rich veins on the surface of pyrochlore grains, indicating their mobilization and migration from the pyrochlore, and that the Fe-rich environment provides favorable conditions for the immobilization of these elements (Deditius et al., 2015). While liberation of U and other A-site cations from pyrochlore is driven by gradients in chemical potential (Lumpkin and Ewing, 1992, 1995), the presence of Nb and Ti in secondary phases implies the decomposition of the relatively stable B_2X_6 framework of metamict pyrochlore during alteration (Lumpkin and Ewing, 1996). It is concluded that reduced forms of actinide species can be immobilized as AcO_{2+x} immediately at the surface of various waste forms during alteration under reducing, or mildly oxidizing conditions in geological repositories (Lumpkin and Ewing, 1996).

Typology and importance of U mineralization

The main U transfer mechanisms from the mantle to the crust are fractional crystallization and partial melting (Cuney, 2010). Due to its incompatible nature, U become highly enriched in magmatic fluids in late stages of differentiation (Pointer, 1987). Deposits related to magmatic fractionation may occur through extreme fractional crystallization, mostly of peralkaline magmas, as well as by partial melting of U-enriched supracrustal rocks (Cuney and Kyser, 2008). The extreme fractional crystallization of peralkaline and syenite magmas may lead to the formation of very large and lowgrade U and Th resources, such as the Kvanefjeld deposit at Ilimaussaq, Greenland (Sørensen, 2001). Other occurrences of this type are: Poços de Caldas, Brazil (Fraenkel et al., 1985); Bokan Mountain, Alaska (MacKevett, 1936); Lovozero Massif, Russia (Balashov, 1968), and the Kaffo Valley, Nigeria (Bowden and Turner, 1974).

The U mineralization of the Pitinga mine can be classified among the Intrusive Plutonic Deposit of Peralkaline Complexes, associated with magmatic differentiation processes (Kyser and Cuney, 2015). This categorization is equivalent to the type of deposit Fractional Crystallization of Magmas (Cuney, 2009), in which mineralization is more efficient in peralkaline fusions. When the peralkaline fusion crystallizes, U-Th-Zr-REE-Nb oxide, phosphate and silicate complexes are formed, which are very refractory. The mineralization of U-Th-REE-Y-Zr-Nb in granitoids with associated hydrothermal processes, with greater or lesser enrichment of U, occur in several geological contexts (Tab. 5) as in the Rössing Deposit (Berning et al., 1976), the Kvanefjeld deposit (Sørensen et al., 1974), the Bokan Mountain deposit (Staatz, 1978), and the Ghurayyah deposit (Drysdall et al., 1984). Other examples with less U mineralization are the Beauvoir albite granite in France (Aubert, 1969; Cuney et al., 1992); the Ririwai Complex in Nigeria (Kinnaird et al., 1985; Pointer et al, 1988a, 1988b) and the Erzgebirge Li-mica granites in Germany (Förster et al., 1995; Förster, 2006).

The granite-hosted Rössing Deposit (Tab. 5) is between the ten largest world producers of uranium (McMaster, 2016). The main primary uranium mineral is magmatic uraninite, and approximately 5% of the uranium reserves occur in high-Nb + Ti betafite. Secondary uranium mineralization, due to hydrothermal or surficial weathering, takes the form of uranophane, beta-uranophane, gummite, torbernite/metatorbenite, carnotite, metahawaiweeite and thorogummite (Berning et al., 1976; Berning, 1986; Cuney, 1980). The crystallization of uraninite was related to the boiling of the magma and unmixing of a H_2O-CO_2-NaCl brine. The low oxygen fugacity allowed the uranium to be present in the quadrivalent state, preventing it to be lost with the solution during the boiling of the magma (Cuney, 1980).

Tab. 5. Uranium mineralization in the Madeira deposit and comparison with major uranium rock-hosted deposits in the world. The table was compiled using the following sources: Armstrong (1985); Berning (1986); Berning et al., (1976); Costi et al. (2000); Cuney (1980); Cuney and Kyser (2008); Drysdall et al. (1984); Lalande (1977); Lenharo (1998); MacKevett (1936); Sørensen et al. (1974); Staatz (1978); Stoezer (1986); Thompson (1988); Ulbrich et al. (2002).

Deposit and location	Tectonic setting	Ore age (Ma)	Deposit type	Host rock/structure (other associated rocks)	Ore minerals (minerals of potential interest)	Economic Parameters
Madeira, Pitinga, North Brazil	Guianas Shield, Amazonas craton	1.822 - 1.794	Alkaline rock-hosted	Albite granite (alkali-feldspar granite and amphibole-biotite-granite)	Pyrochlore, columbite cassiterite (thorite, xenotime, cryolite)	164 Mt at 328 ppm UO_2 (52 kt U)[a]
Rössing, Namibia	Fengcheng Mamatic Massif, Damara Orogen	510±3 – 429±17	Alkaline rock-hosted	Pegmatitic leucogranite - alaskite (biotite-amphibole gneiss, amphibole-biotite schist)	Uraninite, pitchblende, betafite, beta-uranophane, gummite (monazite, zircon, apatite)	246.500 tU at 300 ppm UO_2[b]
Kvanefjeld, Ilimassauq, South Greenland	Eastern Gardar intracratonic rifting Province	1.280 - 1.140	Alkaline rock-hosted	Nepheline syenite and lujavrite (alkali granite, pulaskite, and nauajite)	Steenstrupine, monazite, eudialyte (pyrochlore, thorite, rinkite)	673 Mt at 248 ppm U_2O_3 (184 kt U)[c]
Bokan Mountain, Southeast Alaska	Alexander terrane, western Canadian Cordillera	151 ± 5	Alkaline rock-hosted	Aegirine granite, veins and shear zones (riebeckite granite and aegirine syenite)	U-rich thorite, uraninite, U-rich thorianite, coffinite, allanite	562 kt at 0.15-0.33 wt% UO_2 (635 t U)[d]
Ghurayyah, Hijaz region, Saudi Arabia	Northwestern Arabian Shield	620 – 530	Alkaline rock-hosted	Leucocratic microgranite	Uraninite (monazite, thorite, pyrochlore, columbite, cassiterite, xenotime)	440 Mt at 117 ppm UO_2 (635 t U)[e]
Morro do Ferro, Brazil	Poços de Caldas plateau	83 – 64	Carbonatite hosted	Lateritic profile (magnetite dyke and syenitic rocks)	Uranothorite (fluorcarbonates)	100 t U; 110-120 ppm UO_2[f]

[a]Hadlich et al. (2019); [b]Kyser and Cuney (2015); [c]U total resources and grade from Energy Transition Minerals Ltd. (2015), cut-off at 150 ppm U_3O_8; [d]Potential resources and grades from the United States Geological Survey-USGS (Staatz et al. 1980); [e]Preliminary estimates of tonnage and grade from Drysdall et al. (1984); [f]Grades and tonnage after Gentile and Figueiredo Filho (1996).

The Kvanefjeld deposit (Tab. 5) is associated with the nepheline syenite and with the highly differentiated lujavrite enriched in U and as well as in Nb, Th, Zr, Be, Li, F and REE. The highest U concentrations occur in the upper part and at the contact of the lujavrite with enclosing altered volcanic rocks. The main U-Th minerals are eudialyte, rinkite, monazite, lovozerite, steenstrupine, thorite and pyrochlore (Sørensen et al., 1974). In the Bokan Mountain (Kyser and Cuney, 2015), the U-T mineralization is associated with a desilicified and albitized part of the pluton, forming plunging pipe-like bodies along the contact with the aegirine granite or occurring as pods in an echelon NW-striking shear zone. The main ore minerals are U-rich thorite, uraninite and U-rich thorianite with sulfides disseminated in nearly pure albite.

In the Ririwai Kaffo Valey ring complex, Nigeria (Bowden and Kinnaird, 1984; Pointer et al., 1988a, b), the albite-enriched granite is identical to that from Pitinga (except for the absence of a massive cryolite deposit). However, the U-Th mineralization is metasomatic, hosted in a biotite granite that has undergone extensive post-magmatic metassomatism to produce an albitized, microclinized and greisenized rock that carries late coffinite, thorite and xenotime. In the Ghurayyah deposit (Drysdall et al., 1984), Saudi Arabia, the rare metal mineralization is disseminated in peralkaline microgranites, and the main ore minerals are uraninite, thorite, monazite, pyrochlore, samarskite, aescinite, cassiterite, columbite-tantalite, and xenotime (Lalande, 1977).

The Madeira deposit with 164 Mt at 328 ppm UO_2 (52 kt U) is comparable in grades and reserves to the deposits above (Tab. 5). However, this deposit is in stark contrast to those deposits in five aspects: (1) the uranium mineralization is homogeneously dispersed in the AEG (with grade of 328 ppm UO2); (2) the whole U-Th paragenesis is simple; (3) there is only one primary U ore mineral (U-Pb-LREE-enriched pyrochlore); (4) the U and Th mineralizations are divided into different minerals formed in distinct stages of magma evolution (early U-Pb-LREE-enriched pyrochlore and late thorite); and (5) both mineralizations were affected by intense hydrothermal alterations related to F-rich hydrothermal fluids. As discussed above, these characteristics are related to special conditions imposed by the fluorine-rich fluids on the evolution of the magma and, consequently, on the evolution of the Th/U ratio and on the paragenesis.

Despite the homogeneous distribution of the primary ore mineral, the U mineralization exhibits zonation on the deposit scale related to the degree of hydrothermal alteration of the pyrochlore. The alteration is more intense in the AGB and in the central zone of the AGC (closer to the massive cryolite deposit). In these regions, the more common pyrochlore varieties are Pb-Fe-U-rich pyrochlore, Fe-U-rich-pyrochlore and Fe-Mn-U-rich pyrochlore (the richest in U, up to 13.82 wt.% UO_2). Uranium-enriched varieties of columbite are also more abundant in these areas, along with intermediate compositions of the coffinite-thorite-xenotime-zircon solid solution system and galena. In the other parts of the AGC, Fe-U-Pb-rich pyrochlore predominates. Both in the AGC and AGB, the Mn-Fe-columbite is the more common species, and secondary LREE-rich fluorides are also present.

Conclusions

The U mineralization in the Madeira Sn-Nb-Ta (U, Th, REE, cryolite) world-class deposit is disseminated in the AEG facies (AGC + AGB), as well as in pegmatite veins within the AGC, where pyrochlore is inherited. The primary ore mineral of U is exclusively early magmatic U-Pb-LREE-enriched pyrochlore. The U mineralization is homogeneously dispersed due to transportation of fluorine-bearing complexes that carried HFS elements throughout the melt, and the buffering of F content in the magma prevented the formation of zones with higher enrichment. The peralkaline magma, F richness, and the low magma temperature conditioned the crystallization of pyrochlore instead of columbite. The enrichment of U in pyrochlore in the magma resulted in the loss of Ca and F. In the late stage of magmatic evolution, as zircon crystallization became more intense and accompanied by xenotime and thorite, the magma was previously depleted in U, Nb, Ta and LREE. Therefore, the U and Th mineralization in the Madeira deposit were formed at different stages, associated with different primary minerals, and have distinct secondary minerals.

All pyrochlore crystals in AGC and AGB underwent hydrothermal alteration caused by F-rich aqueous fluids. The alteration process selectively released different cations, leading to the successive formation of various secondary pyrochlore varieties and the relative enrichment of U. The Fe-Mn-U-rich pyrochlore, which contains the highest U content, can reach up to 13.82 wt.% UO_2. The alteration of pyrochlore culminates in the breakdown of the pyrochlore structure and formation of U-bearing columbite. The most intense alteration occurs in the central part of the AGC, close to the massive cryolite deposit, and in the AGB, where the secondary pyrochlores richer in U and U-bearing columbite are more abundant.

The U mineralization in the Madeira deposit is classified as an intrusive deposit type according to IAEA (2020). It exhibits grades (328 ppm UO_2) comparable to the main deposits of this type and significant reserves (52 kt U). However, it is in stark contrast to those deposits in four key aspects: homogeneous dispersion of mineralization; pyrochlore as the exclusive primary ore mineral; U and Th mineralizations formed at different stages; and, being affected by intense hydrothermal alterations. These characteristics are attributed to the special conditions imposed by the fluorine-rich nature of the peralkaline magma.

Acknowledgements

This work was supported by Conselho Nacional de Desenvolvimento Científico e Tecnológico (CNPq) through the Project 405839/2013-2018 and for granting scholarship. The authors thank the reviewers and editors for contributing to improve the manuscript.

Competing interests: The authors declare that they have no known competing financial interests or personal relationships that could have appeared to influence the work reported in this paper.

References

Almeida, F.F.M., Hasui, Y., Brito Neves, B.B., and Fuck, R.A., 1981, Brazilian structural Provinces: an introduction: Earth Sciences Review, v. 17, p. 1-29.

Armstrong, R.L., 1985, Rb-Sr dating of the Bokan Mountain Granite Complex and its country rocks: Canadian. Journal of Earth Sciences, v. 22(8), p. 1233-1236.

Atencio, D., Andrade, M.B., Christy, A.G., Gieré, R., and Kartashov, P.M., 2010, The pyrochlore supergroup of minerals: nomenclature: The Canadian Mineralogist, v. 48, p. 673-698.

Aubert, G., 1969, Les coupoles granitiques de Montebras et d'Echassières (Massif Central français) et la genèse de leurs minéralisations en étain, lithium, tungstène et beryllium: Mémoires du Bureau de Recherches Géologiques et Minières, v. 46, 345 p.

Balashov, Y.A., 1968, The geochemistry of the Lovozero alkaline massif: Canberra, Australian National University Press, 395 p.

Bambi, A.C.J.M., Costanzo, A., Gonçalves, A.O., and Melgarejo, J.C., 2012, Tracing the chemical evolution of primary pyrochlore from plutonic to volcanic carbonatites: the role of fluorine: Mineralogical Magazine, v. 76(2), p. 377-392.

Bastos Neto, A.C., Ferron, T.M.M., Chauvet, A., Chemale, F., Lima, E.F., Barbanson, L., and Costa, C.F.M., 2014, U-Pb dating of the Madeira Suite and structural control of the albite-enriched granite at Pitinga (Amazônia, Brazil): evolution of the A-type magmatism and implications for the genesis of the Madeira Sn-Ta-Nb (REE, cryolite) world-class deposit: Precambrian Research, v. 243, p. 181-196.

Bastos Neto, A.C., Pereira, V.P., Pires, A.C., Barbanson, L., and Chauvet, A., 2012, Fluorine-rich xenotime from the Nb-Ta-Sn Madeira world-class deposit associated with the albite-enriched granite at Pitinga, Amazonia, Brazil: The Canadian Mineralogist, v. 50, p. 1019-1032.

Bastos Neto, A.C., Pereira, V.P., Ronchi, L.H., Lima, E.F., and Frantz, J.C., 2009, The world-class Sn, Nb, Ta, F (T, REE, Li) deposit and the massive cryolite associated with the albite-enriched facies of the Madeira A-type granite, Pitinga

Mining District, Amazonas State, Brazil: The Canadian Mineralogist, v. 47, p. 1329-1357.

Bastos Neto, A.C., Pereira, V.P., Lima, E.F., Ferron, J.M., Minuzzi, O., Prado, M., Ronchi, L.H., Flores, J.A., Frantz, J.C., Pires, A., Pierosan, R., Hoff, R., Botelho, N.F., Rolim, S.B., Rocha, F., and Ulmann, L., 2005, A jazida de criolita da Mina Pititnga (Amazonas), *in* Marini, O.J., Queiroz, E.T., and Ramos, B.W., eds., Caracterização de Depósitos Minerais em Distritos Mineiros da Amazônia: Brasília, DNPM-CT/MINERAL-ADIMB, p. 481-547.

Bea, F., 1996, Residence of REE, Y, Th and U in granites and crustal protoliths: implications for the chemistry of crustal melts: Journal of Petrology, v. 37(3), p. 521-552.

Benaouda, R., Kraemer, D., Sitnikova, M., Goldmann, S., Freitag, R., Bouali, A., Mouttaqi, A., El Haloui, R., Essaadaoui, M., and Bau, M., 2020, Thorium-poor monazite and columbite-(Fe) mineralization in the Gleibat Lafhouda carbonatite and its associated iron-oxide-apatite deposit of the Ouled Dlim Massif, South Morocco: Gondwana Research, v. 77, p. 19-39.

Berning, J., Cooke, R., Hiemstra, S.A., and Hoffman, U., 1976, The Rössing uranium deposit, South West Africa: Economic Geology, v. 71, p. 351-368.

Berning, J., 1986, The Rössing uranium deposit, southwest Africa/Namibia, *in* Anhaeusser, C.R., and Maske, S., eds., Mineral Deposits of Southern Africa: Johannesburg, Geological Society of South Africa, p. 1819-1832.

Bowden, P., and Turner, D.C., 1974, Peralkaline and associated ring-complexes in the Nigeria-Niger Province, West Africa, *in* Sørensen, H., ed., The alkaline rocks: London, John Wiley, p. 330-351.

Bowden, P., and Kinnaird, J.A., 1984, Geology and mineralization of the Nigerian Anorogenic Ring Complexes: Geologisches Jahrbuch, v. 56, p. 3-56.

Burke, E.A.J., 2008, Tidying up mineral names: An IMA-CNMNC scheme for suffixes, hyphens and diacritical marks: Mineralogical Record, v. 39, p. 131-135.

Chakhmouradian, A.R., Reguir, E.P., Kressall, R.D., Crozier, J., Pisiak, L.K., Sidhu, R., and Yang, P., 2015, Carbonatite-hosted niobium deposit at Aley, northern British Columbia (Canada): mineralogy, geochemistry and petrogenesis: Ore Geology Reviews, v. 64, p. 642-666.

Chaves, A.M.D.V., 2005, Mineralogia e geoquímica supergênicas do urânio – Província Uranífera de Lagoa Real, Caetité – Bahia: M.Sc. thesis, Belo Horizonte, Brasil, Comissão Nacional de Energia Nuclear, 101 p.

Clark, S.P. Jr., Peterman, Z.E., and Heier, K.S., 1966, Abundances of uranium, thorium and potassium, *in* Clark, S.P., ed., Handbook of physical constants: Geological Society of America, v. 97, p. 521-541.

Cordeiro, P.F.O., Brod, J.A., Palmieri, M., Oliveira, C.G., Barbosa, E.S.R., Santos, R.V., Gaspar, J.C., and Assis, L.C., 2011, The Catalão I niobium deposit, central Brazil: resources, geology and pyrochlore chemistry: Ore Geology Reviews, v. 41(1), p. 112-121.

Costi, H.T., Dall'agnol, R., Pichavant, M., and Ramo, O.T., 2009, The peralkaline tin-mineralized Madeira cryolite albite-rich granite of Pitinga, Amazonian Craton, Brazil: petrography, mineralogy and crystallization processes: The Canadian Mineralogist, v. 47, p. 1177-1203.

Costi, H.T., Dall’Agnol, R., Pichavant, M., and Ramo, O.T., 2010, The peralkaline tin-mineralized Madeira cryolite albite-rich granite of Pitinga, Amazonian craton, Brazil: petrography, mineralogy and crystallization processes: The Canadian Mineralogist, v. 47, p. 1301-1327.

Costi, H.T., Borges, R.M., and Dall'agnol, R., 2005, Depósitos de estanho da mina Pitinga, estado do Amazonas, *in* Marini, O.J., Queiroz, E.T., and Ramos, B.W., eds., Caracterização de Depósitos Minerais em Distritos Mineiros da Amazônia: Brasília, DNPM-CT/MINERAL-ADIMB, p. 391-475.

Costi, H.T., 2000, Petrologia de granitos alcalinos com alto flúor mineralizados em metais raros: o exemplo do Albita-granito da Mina Pitinga, Amazonas, Brasil: Ph.D. thesis, Belém, Brasil, Universidade Federal do Pará, 345 p.

Costi, H.T., Dall’agnoll, R., and Moura, C.A.V., 2000, Geology and Pb-Pb Geochronology of Paleoproterozoic volcanic and granitic rocks of Pitinga province, Amazonian craton, northern Brazil: International Geology Reviews, v. 42, p. 832-849.

Cuney, M. 1980, Preliminary results on the petrology and fluid inclusions studies of the Rössing uraniferous alaskites: Geological Society of South Africa, v. 83, p. 39-45.

Cuney, M., Marignac, C., and Weisbrod, A., 1992, The Beauvoir topaz-lepidolite albite granite (Massif Central, France); the disseminated magmatic Sn-Li-Ta-Nb-Be mineralization: Economic Geology, v. 87(7), p. 1766-1794.

Cuney, M., and Kyser, K., 2008, Recent and not-so-recent developments in uranium deposits and implications for exploration. Québec: Mineralogical Association of Canada, Short Course Series, v. 39, 257 p.

Cuney, M., 2010, Evolution of uranium fractionation processes through time: driving the secular variation of uranium deposit types: Economic Geology, v. 105, p. 449-465.

Cuney, M., Emetz, A., Mercadier, J., Mykchaylov, V., Shunko, V., and Yuslenko, A., 2012, Uranium deposits associated with Na-metasomatism from central Ukraine: a review of some of the major deposits and genetic constraints: Ore Geology Reviews, v. 44, p. 82-106.

Cuney, M., 2014, Felsic magmatism and uranium deposits: Bulletin de la Société Géologique de France, v. 185(2), p. 75-92.

Deditius, A.P., Reich, M., Kesler, S.E., Utsunomiya, S., Chryssoulis, S.L., Walshe, J., and Ewing, R.C., 2014, The coupled geochemistry of Au and As in pyrite from hydrothermal ore deposits: Geochimica et Cosmochimica Acta, v. 140, p. 644-670.

Dey, M., Bhattacharjee, S., Chakrabarty, A., Mitchell, R.H., Pal, S., and Sen, A.K., 2021, Compositional variation and genesis of pyrochlore, belkovite and biotite from the Sevattur carbonatite complex, India: Mineralogical Magazine, v. 85(4), p. 588-606.

Dill, H.G., 2015, Pegmatites and aplites: Their genetic and applied ore geology: Ore Geology Reviews, v. 69, p. 417-561.

Dolejs, D., and Baker, D.R., 2007, Liquidus equilibria in the system K_2O-Na_2O-Al_2O_3-SiO_2-F_2O to 100 MPa 2: differentiation paths of fluorosilicic magmas in hydrous systems: Journal of Petrology, v. 48, p. 807-828.

Doroshkevich, A.G., Veksler, I.V., Klemd, R., Khromova, E.A., and Izbrodin, I.A., 2017, Trace element composition of minerals and rocks in the Belaya Zima carbonatite complex (Russia): implications for the mechanisms of magma evolution and carbonatite formation: Lithos, v. 284, p. 91-108.

Doroshkevich, A.G., Viladkar, S.G., Ripp, G.S., and Burtseva, M.V., 2009, Hydrothermal REE mineralization in the Amba Dongar carbonatite complex, Gujarat, India: The Canadian Mineralogist, v. 47, p. 1105-1116.

Drysdall, A.R., Jackson, J., Ramsay, C.R., Douch, C.J., and Hackett, D., 1984, Rare element mineralization related to Precambrian alkali granites in the Arabian Shield: Economic Geology, v. 79(6), p. 1366-1377.

Energy Transition Minerals Ltd., 2015, Kvanefjeld Mineral Resources (https://etransmin.com/kvanefjeld-project/).

Ercit, T.S., 1994, The geochemistry and crystal chemistry of columbite-group minerals from granitic pegmatites southwestern Grenville Province, Canadian Shield: The Canadian Mineralogist, v. 32, p. 421-438.

Ercit, T.S., Wise, M.A., and Černý, P., 1995, Compositional and structural systematics of the columbite group: American Mineralogist, v. 80, p. 613-619.

Ferron, J.M.T.M., Bastos Neto, A.C., Lima, E.F., Costi, H.T., Moura, C.A.V., Prado, M., and Galarza, M.A., 2006, Geologia e cronologia Pb-Pb de rochas graníticas e vulcânicas ácidas a intermediárias paleoproterozóicas da Província de Pitinga, Cráton Amazônico: Revista Brasileira de Geociências, v. 36(3), p. 499-512.

Forbes, T.Z., Radha, A.V., and Navrotsky, A., 2011, The energetics of nanophase calcite: Geochimica et Cosmochimica Acta, v. 75, p. 7893-7905.

Förster, H.J., Seltimann, R., and Tischendorf, G., 1995, High-fluorine, low-phosphorus A-type (post-collision) silicic magmatism in the Erzgebirge: Terra Nostra, v. 7, p. 32-35.

Förster, H.J., 2006, Compostition and origin of intermediate solid solutions in the system thorite-xenotime-zircon-coffinite: Lithos, v. 88, p. 35-55.

Fraenkel, M.O., Santos, R.C., Loureiro, F.E.V.L., and Muniz, W.S., 1985, Jazida de uranio do planalto Poços de Caldas, Minas Gerais, *in* Schobbenhaus, C., and Coelho, C.E.S., eds., Principais depósitos minerais do Brasil: Brasília, DNPM/CVRD, p. 89-103.

Gentile, E., and Figueiredo Filho, P.M., 1996, Minerais radioativos: São Paulo, Associação Brasileira de Metalurgia e Materiais.

Giovannini, A.L., Bastos Neto, A.C., Porto, C.G., Pereira, V.P., Takehara, L., Barbanson, L., and Bastos, P.H.S., 2017, Mineralogy and geochemistry of laterites from the Morro dos Seis Lagos Nb (Ti, REE) deposit (Amazonas, Brazil): Ore Geology Reviews, v. 88, p. 461-480.

Hadlich, I.W., Bastos Neto, A.C., Botelho, N.F., and Pereira, V.P., 2019, The thorite mineralizations in the Madeira Sn-Nb-Ta world-class deposit (Pitinga, Brazil): Ore Geology Reviews, v. 105, p. 445-466.

Hogarth, D.D., 1977, Classification and nomenclature of the pyrochlore group: American Mineralogist, v. 62(5-6), p. 403-410.

Hogarth, D.D., Williams, C.T., and Jones, P., 2000, Primary zoning in pyrochlore group minerals from carbonatites: Mineralogical Magazine, v. 64, p. 683-697.

Horbe, M.A., Horbe, A.C., Costi, H.T., and Teixeira, J.T., 1991, Geochemical characteristics of cryolite-tin-bearing granites from the Pitinga mine, northwestern Brazil – a review: Journal of Geochemical Exploration, v. 40, p. 227-249.

Horbe, M.A., Horbe, A.C., Teixeira, J.T., and Costi, H.T., 1985, Granito Madeira: petrologia, petroquímica e mineralizações [ext. abs.]: Simpósio de Geologia da Amazônia, 2th, Manaus, Brasil, 1985, Extended Abstracts, p. 284-320.

IAEA, 2020, International Atomic Energy Agency: Annual Report, 191 p. (https://www.iaea.org/sites/default/files/publications/reports/2020/gc65-5.pdf).

IAEA, 2009, World distribution of uranium deposits (UDEPO) with uranium deposit classification: Vienna, International Atomic Energy Agency, 126 p.

Johan, Z., and Johan, V., 2004, Accessory minerals of the Cínovec (Zinnwald) granite cupola, Czech Republic: indicators of petrogenetic evolution: Mineralogy and Petrology, v. 83, p. 113-150.

Johan, V., and Johan, Z., 1994, Accessory minerals of the Cinovec (Zinnwald) granite cupola, Czech Republic, part 1: Nb-, Ta and Ti-bearing oxides: Mineralogy and Petrology, v. 51, p. 323-343.

Killeen, P.G., 1979, Gamma ray spectrometric methods in uranium explorations: application and interpretation, *in* Hood, P.J., ed., Geochemistry in the search for metallic ores: Economic Geology, v. 31, p. 163-229.

Kinnaird, J.A., Bowden, P., Ixer, R.A., and Odling, N.W.A., 1985, Mineralogy, geochemistry and mineralization of the Ririwai complex, northern Nigeria: Journal of African Earth Sciences, v. 3(1), p. 185-220.

Kinnaird, J.A., and Nex, P.A.M., 2007, A review of geological controls on uranium mineralization in sheeted leucogranites within the Damara Orogen, Namibia: Applied Earth Sciences: Transactions of the Institute of Mining and Metallurgy, v. 116(2), p. 68-85.

Krauskopf, K.B., 1967, Introduction to geochemistry: New York, McGraw-Hill, 721 p.

Kyser, K., and Cuney, M., 2015, Geology and geochemistry of uranium and thorium deposits, Québec: Mineralogical Association of Canada, Short Course Series, v. 46, 345 p.

Lalande, P.G., 1977, Final report on preliminary geological and geophysical investigations on the Ghurayyah radioactive granite, Kingdom of Saudi Arabia, Saudi Arabia: Directorate General Mineral Resources Open-File Report, v. 605(3).

Langmuir, D., 1978, Uranium solution-minerals equilibria at low temperatures with applications to sedimentar ore deposits: Geochimica et Cosmochimica Acta, v. 42, p. 547-569.

Lengler, H.F., 2016, Pegmatitos do albita granito Madeira: avaliação do minério para fins de beneficiamento. Monography, Porto Alegre, Brasil, Universidade Federal do Rio Grande do Sul, 118 p.

Lenharo, S.L.R., 1998, Evolução magmática e modelo metalogenético dos granitos mineralizados da região de Pitinga, Amazonas, Brasil: Ph.D. thesis, São Paulo, Brasil, Universidade de São Paulo, 290 p.

Lenharo, S.L.R., Pollard, P.J., and Born, H., 2003, Petrology and textural evolution of granites associated with tin and rare-metals mineralization at the Pitinga mine, Amazonas, Brazil: Lithos, v. 66, p. 37-61.

Linnen, R.L., and Keppler, H., 1997, Columbite solubility in granitic melts: consequences for the enrichment and fractionation of Nb and Ta in the Earth’s crust: Contributions to Mineralogy Petrology, v. 128, p. 213-227.

Lottermoser, B.G., and England, B.M., 1988, Compositional variation in pyrochlores from the Mt. Weld carbonatite laterite, Western Australia: Mineralogy and Petrology, v. 38, p. 37-51.

Lumpkin, G.R., and Mariano, A.N., 1996, Natural occurrence and stability of pyrochlore in carbonatites, related hydrothermal systems, and weathering environments, *in* Murphy, W.M., and Knecht, D.A., eds., The Scientific Basis for Nuclear Waste Management: Pittsburgh, Materials Research Society, v. 412, p. 831-838.

Lumpkin, G.R., and Ewing, R.C., 1995, Geochemical alteration of pyrochlore group minerals: pyrochlore subgroup: American Mineralogy, v. 80, p. 732-743.

Lumpkin, G.R, and Ewing, R.C., 1992, Geochemical alteration of pyrochlore group minerals: microlite subgroup: American Mineralogist, v. 77(1-2), p. 179-188.

Macdonald, R., Baginski, B., Kartashov, P.M., Zozulya, D., and Dzierzanowski, P., 2015, Hydrothermal alteration of a chevkinite-group mineral to a bastnasite-(Ce)-ilmenite-columbite-(Fe) assemblage: interaction with a F-, CO2-rich fluid: Mineralogy and Petrology, v. 109, p. 659-678.

MacKevett, E.M., 1936, Geology and ore deposits of the Bokan Mountain area, Southeastern Alaska: United States Geological Survey Bulletin, v. 1154, 125 p.

Martin, R.F., 2006, A-type granites of crustal origin ultimately result from open-system fenitization-type reactions in an extensional environmental: Lithos, v. 91, p. 125-136.

McMaster, S.A., 2016, Investigation into the synthesis, characterization and uranium extraction of the pyrochlore mineral betafite: Ph.D. these, Melbourne, Australia, RMIT University, 244 p.

Minuzzi, O.R.R., Bastos Neto, A.C., Formoso, M.L.L., Andrade, S., Janasi, V.A., and Flores, J.A., 2008, Rare Earth elements and yttrium geochemistry applied to the genetic study of cryolite ore at the Pitinga Mine (Amazon, Brazil): Anais da Academia Brasileira de Ciências, v. 80(4), p. 719-733.

Minuzzi, O.R.R., Bastos Neto, A.C., Pereira, V.P., and Flores, J.A.A., 2006a, The massive cryolite deposit and the disseminated ore of cryolite from the Pitinga mine (Amazon, Brazil): Revista Brasileira de Geociências, v. 36, p. 104-123.

Minuzzi, O.R.R., Bastos Neto, A.C., Pereira, V.P., and Nunes, L., 2006b, A columbitização do pirocloro do albita granito na mina de Pitinga (AM): relações com a mineralização de criolita: Revista Brasileira de Geociências, v. 35(1), p. 123-137.

Minuzzi, O.R.R., 2005, Gênese e evolução da mineralização de criolita, pirocloro e columbita da subfacies albita granito de núcleo, Mina Pitinga, Amazonas, Brasil: Ph.D. thesis, Porto Alegre, Brasil, Universidade Federal do Rio Grande do Sul, 249 p.

Mitchell, R.H., Wahl, R., and Cohen, A., 2020, Mineralogy and genesis of pyrochlore apatite from The Good Hope Carbonatite, Ontario: a potential Nb deposit: Mineralogical Magazine, v. 84(1), p. 81-91.

Mücke, A., and Struntz, H., 1978, Petscheckite and liandratite, two new pegmatite minerals from Madagascar: American Mineralogist, v. 63, p. 941-946.

Mücke, A., and Keck, E., 2008, Untersuchungen an columbiten $(Fe,Mn)(Nb,Ta)_2O_6$ und dem mit columbit verwachsenen neufund petscheckit $U(Fe,Mn)(Nb,Ta)_2O_8$ aus dem pegmatite von Hagendorf-Süd/Oberpfalz: Aufschluss, v. 59(6), p. 373-392.

Nardi, L.V.S., Formoso, M.L.L., Jarvis, K., Oliveira, L., Bastos Neto, A.C., and Fontana, E., 2012, REE, Y, Nb, U and Th contents and tetrad effect in zircon from a magmatic-hydrothermal F-rich system of Sn-rare metal-cryolite mineralized granites from the Pitinga Mine, Amazonia, Brazil: Journal of South America Earth Sciences, v. 33, p. 34-42.

Nasraoui, M., and Bilal, E., 2000, Pyrochlores from the Lueshe carbonatite complex (Democratic Republic of Congo): a geochemical record of different alteration stages: Journal of Asian Earth Sciences, v. 18, p. 237-251.

Ogunleye, P.O., Garba, I., and Ike, E.C., 2006, Factors contributing to enrichment and crystallization of niobium in pyrochlore in the Kaffo albite arfvedsonite granite, Ririwai Complex, Younger Granites province of Nigeria: Journal of African Earth Sciences, v. 44(3), p. 372-382.

Paludo, C.M., Bastos Neto, A.C., Pereira, V.P., Botelho, N.F., 2018, Mineralogia e geoquímica de pegmatites ricos em ETR, F e metais alcalinos associados à facies albita granito no depósito de Sn-Nb-Ta-(F, ETR, U, Th) Madeira (mina Pitinga, AM, Brasil): Pesquisas em Geociências, v. 45, p. 1-28.

Paludo, C.M., 2015, Caracterização dos minerais de ETR e Y nos pegmatites do Albita Granito Madeira, Pitinga, AM. Monography, Porto Alegre, Brasil, Universidade Federal do Rio Grande do Sul, 76 p.

Pierosan, R., Lima, E.F., Nardi, L.V.S., Campos, C.P., Bastos Neto, A.C., Ferron, J.M.T.M., and Prado, M., 2011a, Paleoproterozoic (~ 1.88 Ga) felsic volcanism of the Iricoumé Group in the Pitinga Mining District area, Amazonian Craton, Brazil: insights in ancient volcanic processes from field and petrological data: Anais da Academia Brasileira de Ciências, v. 83, p. 921-937.

Pierosan, R., Lima, E.F., Nardi, L.V.S., Bastos Neto, A.C., Campos, C.P., Ferron, J.M.T.M., and Prado, M., 2011b, Geochemistry of Paleoproterozoic volcanic rocks of the Iricoumé Group, Pitinga Mining District, Amazonian craton, Brazil: International Geology Reviews, v. 53, p. 946-976.

Pires, A.C., 2010, Xenotima, gagarinita, fluocerita e waimirita da Mina Pitinga (AM): mineralogia e avaliação preliminar do potencial do albita granito para exploração de elementos terras raras e ítrio: Ph.D. thesis, Porto Alegre, Brasil, Universidade Federal do Rio Grande do Sul, 201 p.

Pires A.C., Bastos Neto A.C., Pereira V.P., Botelho N.F., and Minuzzi O.R.R., 2006, Gagarinita-(Y) com polimorfo de fluocerita: provável caso de formação de um novo mineral por exsolução de ETRL a partir de fluoreto de ETRLP (Mina Pitinga – AM): Revista Brasileira de Geociências, v. 36(1), p. 155-164.

Pires, A.C., 2005, A gagarinita e fases associadas no Granito Madeira (Pitinga, Amazonas): M.Sc. thesis, Porto Alegre, Brasil, Universidade Federal do Rio Grande do Sul, 122 p.

Pointer, C.M., Ashworth, J.R., Ixer, R.A., 1988a, The zircon-thorite mineral group in metasomatized granite, Ririwai, Nigeria 1: geochemistry and metastable solid solution of thorite and coffinite: Mineralogy and Petrology, v. 38, p. 245-262.

Pointer, C.M., Ashworth, J.R., and Ixer, R.A., 1988b, The zircon-thorite mineral group in metasomatized granite, Ririwai, Nigeria 2: zoning, alteration and exsolutions in zircon: Mineralogy and Petrology, v. 39, p. 21-37.

Pointer, C.M., 1987, Remobilisation of uranium and thorium by ore-forming fluids: a mineralogical study: Ph.D. thesis, Birmingham, England, University of Aston, 311 p.

Pöml, P., Geisler, T., Cobos-Sabaté, J., Wiss, T., Raison, P.E., Schmid-Beurmann, P., Deschanels, X., Jégou, C., Heimink, J., and Putnis, A., 2011, The mechanism of the hydrothermal alteration of cerium- and plutonium-doped zirconolite: Journal of Nuclear Materials, v. 410, p. 10–23.

Pownceby, M.I., and Johnson, C., 2014, Geometallurgy of Australian uranium deposits: Ore Geology Reviews, v. 56, p. 25-44.

Redkin, A.F., and Borodulin, G.P., 2009, Pyrochlores as indicators of the uranium-bearing potential of magmatic melts: Geochemistry, v. 432, p. 787-790.

Roberts, S. K., Bourcier, W.L., and Shaw, H.F., 2000, Aqueous dissolution kinetics of pyrochlore, zirconolite and brannerite at 25, 50, and 75 °C: Radiochimica Acta, v. 88(9-11), p. 539-546.

Ronchi, L.H., Bastos Neto, A.C., Gedoz, S.C., Weber, M.L., Pereira, V.P., and Andrek, M., 2011, A transição magmático-hidrotermal registrada por inclusões fluidas no albita-granito de núcleo, Mina Pitinga, Amazonas, *in* Frantz, J.C., Charão, J.M., and Jost, H., eds., Contribuições à metalogenia do Brasil: Porto Alegre, CPRM-UFRGS, cap. 10.

Sakoma, E.M., and Martin, R.F., 2002, Oxidation-induced postmagmatic modifications of primary ilmenite, NYG-related aplite dyke, Tibchi granite complex, Kalato, Nigeria: Mineralogical Magazine, v. 66, p. 591-604.

Santos, J.O.S., Hartmann, L.A., Gaudete, H.E., Groves, D.I., McNaughton, N.J., and Fletcher, L.R.A., 2000, New understanding of the Provinces of Amazon Craton based on Integration of Field Mapping and U-Pb and Sm-Nd geochronology: Gondwana Research, v. 3(4), p. 453-488.

Seifert, W., Kämpf, H., and Wasternack, J., 2000, Compositional variation in apatite, phlogopite and other accessory minerals of the ultramafic Delitzsch complex, Germany: implication for cooling history of carbonatites: Lithos, v. 53, p. 81-100.

Siachoque, A., Garcia, R., and Vlach, S.R.F., 2020, Occurrence and composition of columbite-(Fe) in the reduced A-type Desemborque Pluton, Graciosa Province (S-SE Brazil): Minerals, v. 10, p. 411-428.

Simões, M.S.S., Almeida, M.E., Souza, A.G.H., Silva, B.D.P.B., and Rocha, P.G., 2014, Characterization of the volcanic and hypabyssal rocks of the Paleoproterozoic Iricoumé Group in the Pitinga region and Balbina Lake area, Amazonian craton, Brazil: petrographic distinguishing features and emplacement conditions: Journal of Volcanology and Geothermal Research, v. 286, p. 138-147.

Seifert, W., Kämpf, H., and Wasternack, J., 2000, Compositional variation in apatite, phlogopite and other accessory minerals of the ultramafic Delitzsch complex, Germany: implication for cooling history of carbonatites: Lithos, v. 53, p. 81-100.

Siachoque, A., Garcia, R., and Vlach, S.R.F., 2020, Occurrence and composition of columbite-(Fe) in the reduced A-type Desemborque Pluton, Graciosa Province (S-SE Brazil): Minerals, v. 10, p. 411-428.

Skirrow, R.G., Jaireth, S., Huston, D.L., Bastrakov, E.N., Schofield, A., Wielen, A.E., and Barnicoat, A.C., 2009, Uranium mineral systems: processes, exploration criteria and a new deposit framework: Geoscience Australia, v. 20, 44 p.

Sørensen, H., 2001, The Ilímassauq complex, South Greenland: status of mineralogical research with new results: Geological Survey of Greenland Bulletin, v. 190, 167 p.

Sørensen, H., Rose-Hansen, J., Nielsen, B.L., Lovborg, L., Sørensen, E., and Lundgaard, T., 1974, The uranium deposit at Kvanefjeld, the Ilímaussaq intrusion, South

Greenland: geology, reserves, benefication: Geological Survey of Greenland Bulletin, v. 60, 54 p.

Staatz, M.H., 1978, I and L uranium and thorium vein system, Bokan Mountain, southern Alaska: Economic Geology, v. 73(4), p. 512–523.

Staatz, M.H., Hall, R.B., Macke, D.L., Armbrustmacher, T.J., and Brownfields, I.K., 1980, Thorium resources of selected regions in the United States: United States Geological Survey Circular, v. 824, 32 p.

Starikova, A.E., Bazarova, E.P., Savel'eva, V.B., Sklyarov, E.V., Khromova, E.A., and Kanakin, S.V., 2019, Pyrochlore-group minerals in the granite-hosted Katugin rare-metal deposit, Transbaikalia, Russia: Minerals, v. 9, p. 490-507.

Stoezer, D.B., 1986, Distribution and tectonic setting of plutonic rocks of the Arabian Shield: Journal of African Earth Sciences, v. 4, p. 31-46.

Stolnik, D., 2015, Caracterização da xenotima na fácies pegmatítica do albita granito de núcleo, Pitinga (AM): Monography, Porto Alegre, Brasil, Universidade Federal do Rio Grande do Sul, 67 p.

Tang, N., Gritsenko, Y., Kimura, K., Bhattacharjee, S., Sakai, A., Fu, M., Takeda, H., Man, H., Sugawara, K., Matsumoto, Y., Shimura, Y., Wen, J., Broholm, C., Sawa, H., Takigawa, M., Sakakibara, T., Zherlitsyn, S., Wosnitza, J., Moessner, R., and Nakatsuji, S., 2022, Spin-orbital liquid state and liquid-gas metamagnetic transition on a pyrochlore lattice: Nature Physics, v. 19, p. 92-98.

Teixeira, J.T., Costi, H.T., Minuzzi, O.R.R., Soares, E.A.A., 1992, Depósitos primários de criolita, cassiterita, xenotímio e columbita em apogranito – Mina de Pitinga (AM) [ext. abs.]: Congresso Brasileiro de Geologia, 37th, São Paulo, Brasil, Extended Abstracts, p. 212-213.

Thomas, R., Webster, J.D., Rhede, D., Seifert, W., Rickers, K., Förster, H.J., Heinrich, W., and Davidson, P., 2006, The transition from peraluminous to peralkaline granitic melts: evidence from melt inclusions and accessory minerals: Lithos, v. 91, p. 137-149.

Thompson, T.B., 1988, Geology and uranium-thorium mineral deposits of the Bokan Mountain Granite Complex, Southeastern Alaska: Ore Geology Reviews, v. 3, p. 193-210.

Uher, P., Ondrejka, M., and Konečny, P., 2009, Magmatic and post-magmatic YREE-Th phosphate, silicate and Nb-Ta-Y-REE oxide minerals in A type metagranite: an example from the Turčok massif, the Western Carpathians, Slovakia: Mineralogical Magazine, v. 73, p. 1009-1025.

Ulbrich, H.H., Vlach, S.R.F., Ulbrich, M.N.C., and Kawashita, K., 2002, Penecontemporaneous syenitic-phonolitic and basic-ultrabasic-carbonatitic rocks at the Poços de Caldas alkaline massif, SE Brazil: geologic and geochronologic evidence: Revista Brasileira de Geociências, v. 32, p. 15-26.

Van Wambeke, L., 1965, A Study of some Niobium-bearing minerals of the Lueshe Carbonatite Deposit (Kivu, Republic of Congo), Report of European Atomic Energy Community-Euratom. EUR 2110.

Veiga Jr., J.P., Nunes, A.C.B., Fernandes, A.S., Amaral, J.E., Pessoa, M.R., and Cruz, S.A.S., 1979, Projeto Sulfetos de Uatumã. Relatório Final: Manaus, DNPM/CPRM.

Viladkar, S.G., and Ghose, I., 2002, U-rich pyrochlore in carbonatite of Newania, Rajasthan (India): Neues Jahrbuch für Mineralogie, v. 3, p. 97-106.

Viladkar, S.G., and Bismayer, U., 2010, Compositional variation in pyrochlores of Amba Dongar carbonatite complex, Gujarat: Journal of Geological Society of India, v. 75, p. 495-502.

Whalen, J.B., Currie, K.L., and Chappell, B.W., 1987, A-type granites: geochemical characteristics, discrimination and petrogenesis: Contributions to Mineralogy and Petrology, v. 95, p. 407-419.

Wise, M.A., Černý, P., and Falster, A.U., 1998, Scandium substitution in Columbite-group minerals and ixiolite: The Canadian Mineralogist, v. 36, p. 673-680.

Wu, B., Hu, Y.Q., Bonnetti, C., Xu, C., Wang, R.C., Zhang, Z.S., Li, Z.Y., and Yin, R., 2021, Hydrothermal alteration of pyrochlore group minerals from the Miaoya carbonatite complex, central China and its implications for Nb mineralization: Ore Geology Reviews, v. 132, p. 1040-1059.

Xu, H.F., Wang, Y.F., Zhao, P.H., Bourcier, W.L., Konynenburg, R.V., and Shaw, H.F., 2004, Investigation of pyrochlore-based U-bearing ceramic nuclear waste: uranium leaching test and TEM observation: Environment Science & Technology, v. 38, p. 1480-1486.

Yin, R., Wang, R.C., Zhang, A.C., Hu, H., Zhu, J.C., Rao, C., and Zhang, H., 2015, Chemical evolution and late-stage re-equilibration of Zr-Hf-U-bearing columbite-group minerals in the Koktokay no. 1 granitic pegmatite, Altai, northwestern China: The Canadian Mineralogist, v. 53, p. 461-478.

Zurevinski, S.E., and Mitchell, R.H., 2004, Extreme compositional variation of pyrochlore group minerals at the Oka Carbonatite Complex, Quebec: evidence of magma mixing?: The Canadian Mineralogist, v. 42, p. 1159-1168.

6.2 *Pegmatites hosted by the albite-enriched granite at the Madeira Sn-Nb-Ta-F world-class deposit, Pitinga Province, Amazonas, Brazil*

Artigo submetido à revista International Geology Review (A2) dia 04/09/2023.

Gmail Ingrid Weber Hadlich <ingrid.hadlich@gmail.com>

Submission received for International Geology Review (Submission ID: 233723414)

journalshelpdesk@taylorandfrancis.com <journalshelpdesk@taylorandfrancis.com> 4 de setembro de 2023 às 17:15
Para: ingrid.hadlich@gmail.com

Taylor & Francis
Taylor & Francis Group

Dear Ingrid Hadlich,

Thank you for your submission.

Submission ID	**233723414**
Manuscript Title	**Pegmatites hosted by the albite-enriched granite at the Madeira Sn-Nb-Ta-F world-class deposit, Pitinga Province, Amazonas, Brazil**
Journal	**International Geology Review**

If you made the submission, you can check its progress and make any requested revisions on the Author Portal

Thank you for submitting your work to our journal.
If you have any queries, please get in touch with journalshelpdesk@taylorandfrancis.com.

Kind Regards,
International Geology Review Editorial Office

Pegmatites hosted by the albite-enriched granite at the Madeira Sn-Nb-Ta-F world-class deposit, Pitinga Province, Amazonas, Brazil

Ingrid W. Hadlich[a*]; Artur C. Bastos Neto[a]; Vitor P. Pereira[a]; Harald G. Dill[b]; Nilson F. Botelho[c]

[a]Instituto de Geociências, Universidade Federal do Rio Grande do Sul, Avenida Bento Gonçalves 9500, Porto Alegre 91501-970, RS, Brazil; [b]Gottfried Wilhelm Leibniz University, Welfengarten 1, D-30167 Hannover, Germany; [c]Instituto de Geociências, Universidade de Brasília, Campus Universitário Darcy Ribeiro, Asa Norte, 70910-900 Brasília, DF, Brazil

*Corresponding author e-mail: ingrid.hadlich@ufrgs.br

Abstract

This study is centered on pegmatites exhibiting exceptionally rare mineralogical and chemical compositions, hosted by the equally exceptional albite-enriched granite Madeira (1,8 Ga). This is a peralkaline A-type granite and corresponds to the renowned Madeira Sn-Nb-Ta-F (REE, Th, U) world-class deposit (164 Mt) (Pitinga, Brazil). The entire pluton underwent alteration by F-rich hydrothermal fluids and, in its central portion, occurs a massive cryolite deposit (10 Mt, 37 wt.% Na_3AlF_6). The albite-enriched granite hosts four distinct types of pegmatites: border pegmatite, pegmatitic albite-enriched granite, miarolitic pegmatite, and pegmatite veins. The host rock itself has served as the source for the fluids that gave rise to all these pegmatites. Just as observed in the parent rock, the pegmatites exhibit an exotic primary paragenesis rich in rare metals, including pyrochlore, cassiterite, riebeckite, polylithionite, zircon, thorite, xenotime, gagarinite-(Y), genthelvite, and cryolite. The origin of these pegmatites is linked to various physicochemical processes that took place during different stages of magmatic evolution, each associated with distinct emplacement mechanisms. The magmatic-hydrothermal transition occurred for each pegmatite body when the residual aqueous phase exsolved from the crystallized rock, with a composition reflecting the degree of melt fractionation at the point of H_2O saturation. The exsolved hydrothermal fluid caused alteration (autometasomatism) in the magmatic minerals and precipitated secondary minerals. The unparalleled abundance of F in the parental rock and in the pegmatites (up to 35 wt.% F in pegmatite veins), played an important role in both the magmatic and hydrothermal stages of the albite-enriched granite system.

Keywords: pegmatite, rare-metal ore, fluorine, magmatic-hydrothermal transition, albite-enriched granite.

Introduction

Pegmatitic rocks are very coarse-grained crystalline rocks which, in places, contain giant crystals of feldspar, quartz or mica that render this felsic lithology to strongly contrast with compositionally similar granites often lying in their close vicinity. These features draw the attention of entrepreneurs, mining engineers and mineral enthusiasts to these accumulations of industrial and rare minerals (Dill 2015). Pegmatitic textures can be found in igneous rocks mainly of granitic (calc-alkaline) and syenitic (alkaline) compositions which also differ from each other regarding their rare element contents. The first type present in orogenic geodynamic regimes contains, e.g., Li, U, Ta, B, whereas the other type, confined to anorogenic regimes, is enriched in Nb, Zr, Th and Mo (Dill 2015). The enrichment process of rare elements within pegmatites appears to occur in an essentially closed system, stemming from a minor fraction of residual silicate liquid derived from a much larger magmatic body. Despite this, only a small fraction of pegmatites (<1%) exhibits associations with uncommon mineral phases bearing rare elements such as lithium, beryllium, cesium, boron, phosphor, and tantalum (London and Kontak 2012).

There is no unified model to explain the origin of granitic pegmatites. According to Dill (2018, 2019) the pegmatite genesis pendulum swings towards anatectic mode of formation, as evidenced through extensive mineralogical, chemical, and field geology data for the “Variscan-type” pegmatites in the German basement. Another model, historically accepted, is that most granitic pegmatites represent the terminal stage in the fractionation of low-viscosity granitic magmas. However, the debate continues as to whether they are igneous, late-stage differentiated rocks (Cameron *et al.* 1949), or if they precipitate from subsolidus and hydrothermal fluids (Jahns and Burnham 1969; Jahns 1982; London 2008). The model put forth by Thomas *et al.* (2000, 2006, 2008) proposes that pegmatites are a product of melt-melt immiscibility, coupled with metasomatic reactions. In this regard, pegmatites register important chemical and physical variations that take place during the transition from the magmatic to the hydrothermal phases in volatile-rich magmatic systems.

The albite-enriched granite is a peralkaline A-type granite (1,8 Ga) (Bastos Neto *et al.* 2014) and corresponds to the Madeira Sn-Nb-Ta-F (REE, Th, U) word-class deposit (164 Mt). The albite-enriched granite represents the most evolved facies of the Madeira Granite (Costi *et al.* 2009; Ferron *et al.* 2010) and is situated in the Tin Province of Pitinga (Bettencourt *et al.* 2016) in Amazonas, Brazil. The entire albite-enriched granite pluton underwent intense alteration by aqueous, F-rich hydrothermal fluids and, within the central region of the albite-enriched granite, a hydrothermal massive cryolite deposit with 10 Mt (37 wt.% Na_3AlF_6) is present (Bastos Neto *et al.* 2009). The occurrence of cryolite alongside tin, niobium and various other rare metals within the same peralkaline granite that hosts a massive cryolite deposit, is unparalleled worldwide. The scope of this study centers on pegmatites exhibiting very uncommon mineralogical and chemical compositions hosted by this remarkable rock.

The research team from the Universidade Federal do Rio Grande do Sul conducted an extensive study on the pegmatites associated to the albite-enriched granite. This investigation comprised a series of specific studies, some of which have not yet been published. These findings, combined with new mineral data, are being integrated for the first time within this study. Structural, mineralogical (including detailed compositions of key minerals), and geochemical data were combined to accomplish three main objectives: (i) to provide an overall characterization of the different types of pegmatites associated with the albite-enriched granite; (ii) to propose a comprehensive model for the genesis and source of these pegmatites; and (iii) to examine the implications of these findings for a deeper understanding of the albite-enriched granite's system evolution. Moreover, this research introduces novel insights into primary pyrochlore hydrothermal alteration, with the aim of distinguishing differences in hydrothermal events between the pegmatite types and the albite-enriched granite by analyzing variations in their alteration products. Furthermore, the study emphasizes two significant themes: the magmatic-hydrothermal transition and the role of fluorine within both magmatic and hydrothermal environments.

Geological setting and the history of geoscientific studies

Geological setting from the oldest to the youngest lithologies

The Pitinga Province is located (Fig. 1) in the southern portion of the Guyana Shield (Almeida *et al.* 1981), in the Tapajos-Parima Tectonic Province (Santos *et al.* 2000).

The volcanic rocks of the Iricoume Group (Veiga *et al.* 1979) predominate in the Pitinga Province and have $^{207}Pb/^{206}Pb$ zircon ages between 1881 ± 2 and 1890 ± 2 Ma (Ferron *et al.* 2006). They comprise mostly effusive and hypabyssal rhyolites, highly welded ignimbrites, ignimbritic tuffs, and surge deposits formed in a subaerial environment with cyclic effusive and explosive activities (Pierosan *et al.* 2011a, b; Simoes *et al.* 2014). The Iricoume Group host the Madeira Granite (Fig. 1).

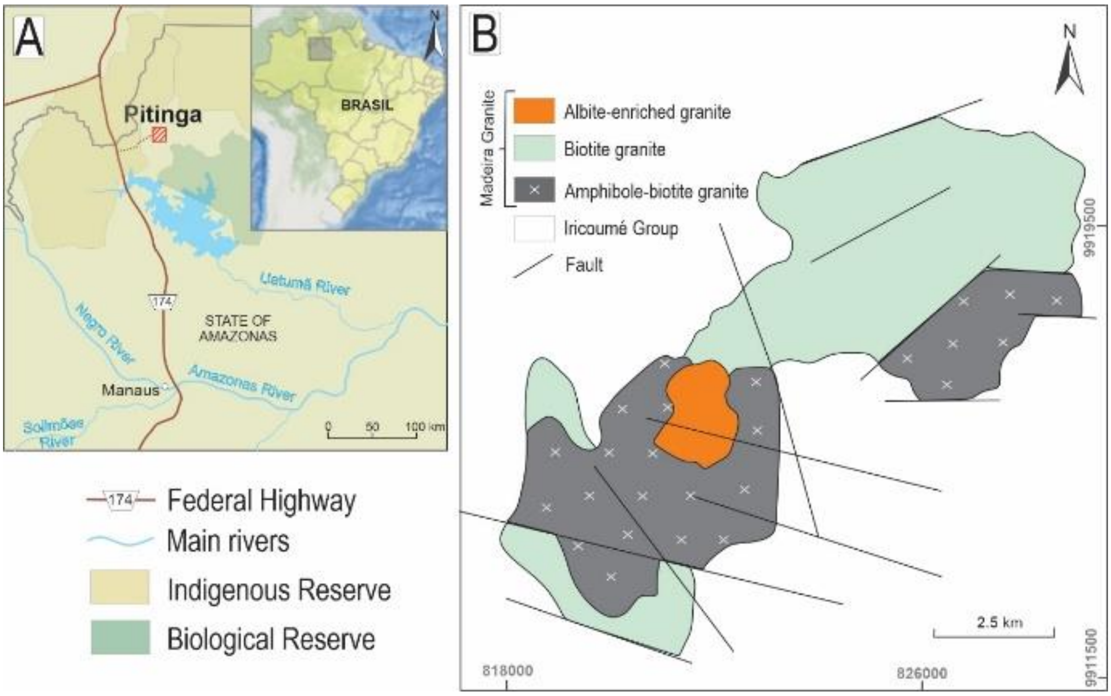

Fig. 1. (A) Location map. (B) Geological map of the Madeira Granite. (Modified from Costi, 2000).

The Madeira granite (Figs. 1 and 2) contains four facies (Horbe *et al.* 1991; Lenharo *et al.* 2003; Costi *et al.* 2005, 2009; Bastos Neto *et al.* 2009). The oldest mostly metaluminous porphyritic amphibole-biotite granite (1824 ± 2 Ma, Costi *et al.* 2000) contains plagioclase-mantled K-feldspar mega crystals, sometimes also reverse-zoned K-feldspar-mantled plagioclase ovoid and is usually referred to as the “rapakivi” subfacies. The amphibole-biotite granite was followed by the metaluminous biotite granite (1822 ± 2 Ma, Costi *et al.* 2000). The younger facies are the hypersolvus porphyritic alkali feldspar granite (1818 ± 2 Ma, Costi *et al.* 2000) and the albite-enriched granite (Fig. 2). The latter is the host of the studied pegmatites. The age of the albite-enriched granite is only very roughly constrained at 1822 ± 22 Ma (Bastos Neto *et al.* 2014) due to the metasomatic alteration of zircons. According to Costi (2000), these younger facies were emplaced simultaneously. The hypersolvus granite has K-feldspar phenocrysts in a fine- to medium-grained matrix dominantly composed of K-feldspar and quartz.

The albite-enriched granite host rock

The albite-enriched granite (Fig. 2) is an oval-shaped body with an aerial extension of approximately 2×1.3 km. It is divided into the subfacies core albite-enriched granite (CAG) and border albite-enriched granite (BAG). The CAG is a peralkaline subsolvus granite, porphyritic to seriate in texture, fine- to medium-grained, and composed of quartz, albite and K-feldspar in approximately equal proportions (25–30% p.vol.). The accessory minerals are cryolite (4% p.vol.), polylithionite (4% p. vol.), annite (3% p. vol.), zircon (2% p.vol.), and riebeckite (2% p.vol.). Pyrochlore, cassiterite, xenotime, columbite, thorite, magnetite and galena occur in minor proportions. The BAG is peraluminous and presents types of texture and essential mineralogy similar to the CAG, except for being richer in zircon, for the presence of fluorite instead of cryolite, and absence of iron-rich silicate minerals, which have almost completely disappeared due to an autometasomatic process (Costi *et al.* 2000, 2009). In the central part of the CAG, there is a massive cryolite deposit formed by several bodies of massive cryolite, intercalated with the CAG and the hypersolvus granite (Fig. 2), with a total of 300 m long and 30 m thick. They are composed of cryolite crystals (~87 vol%), quartz, zircon, and feldspar.

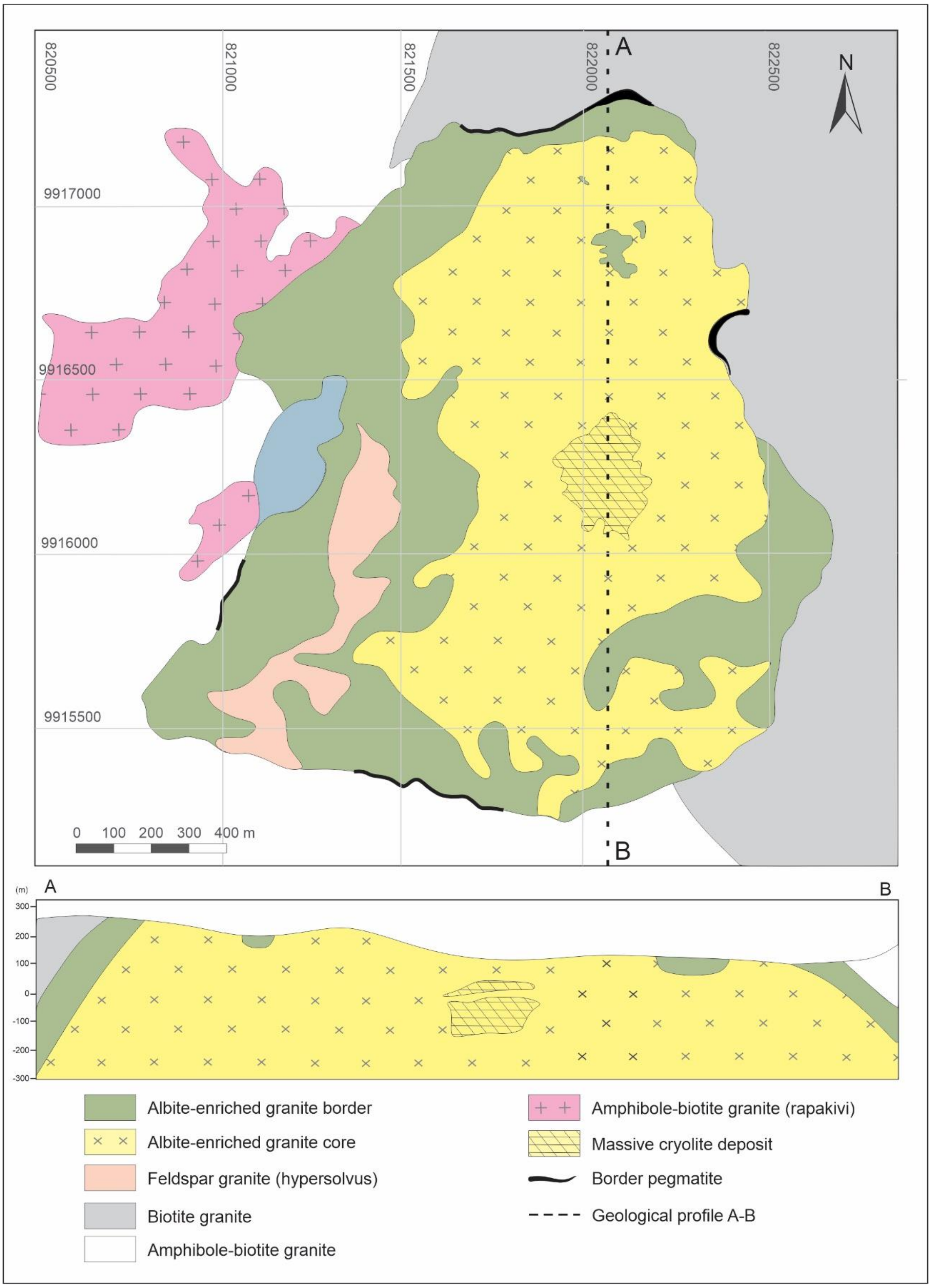

Fig. 2. Geological map of the albite-enriched granite. (Modified from Minuzzi, 2005).

The Madeira rare-metal deposit

The Pitinga Province is the largest Sn producer in Brazil. The alluvial ore deposits were discovered in 1979 (Veiga *et al.* 1979) and are almost exhausted. The primary ores are mainly associated with the Madeira Granite (Fig. 1). The Madeira deposit, which has been exploited since 1989, corresponds to the albite-enriched granite (Fig. 2). The grade of the disseminated ore (CAG + BAG) stands at 0.17 wt.% Sn (cassiterite), 0.20 wt.% Nb_2O_5) and 0.024 wt.% Ta_2O_5 (both in pyrochlore and columbite). The potential by-products of the disseminated ore are F (4.2 wt.% cryolite), Y and HREE (xenotime), Zr and Hf (zircon), Th (0.07 wt.% ThO_2, thorite), and U (pyrochlore). The studied pegmatites have been mined indistinctly together with the disseminated ore at the Pitinga Mine. The massive cryolite deposit contains 10 million tons at a grade of 31.9% of Na_3AlF_6 (Bastos Neto *et al.* 2009).

Materials and methods

For this study, a collection of more than 500 rock samples from the research group at Universidade Federal do Rio Grande do Sul (UFRGS) was reviewed. The pegmatite samples were initially examined using a binocular loupe. Subsequently, 50 thin sections were chosen for detailed petrographic analysis under optical microscopy, to identify the minerals and paragenesis of the pegmatites associated with the albite-enriched granite. To obtain detailed textural data, thin sections were examined by scanning electron microscopy (SEM) with qualitative analysis using an energy-dispersive X-ray detector (Zeiss, model EVO MA10) at the Center for Microscopy and Microanalysis at UFRGS.

Most of the mineral chemistry data of the albite-enriched granite and associated pegmatites were obtained by the research group at UFRGS, and are available in Pires *et al.* (2006), Bastos Neto *et al.* (2012), Schuck (2015), Stolnik (2015), Lengler (2016), Paludo *et al.* (2018), and Hadlich *et al.* (2019). Mineral compositions of pyrochlore and the associated secondary minerals were obtained using electron probe micro-analysis (EPMA) technique (JEOL JXA-8230) at the EPMA Laboratory of the Universidade de Brasília (UnB). The operating conditions are as the following: 15 kV accelerating voltage and 10 nA beam current (F, Mg, Zn, Al, Si, Hf, Nb, P, Cl, S, Bi, Ti, Mn, Y, Ta, Sn, Ca, Zr, Fe, V, Rb), and 20 kV and 20 nA (Na, K, Pb, REE, Sr, Th, Ba, U), 1 μm beam diameter, and interference corrections were applied in all cases of peak overlap. The crystals of Wavelenght Dispersive X-rays Spectrometers (WDS) are as the following: TAP (Si, Zn, Na, Al), PETJ (Nb, P, Hf, Cl, S, K, Bi, Sr, Y, Ta, Sn, Th, Pb), PETH (Rb, Zr, U), LIF (Ti, Mn, Sm, Eu, Gd, Dy, Er, Ho, Tb, Tm, Yb, Lu), LIFH (Ca, Fe, Ba, V, La, Ce, Pr, Nd), and LDE1 (F). The counting times on the peaks were 10s for all elements, and half that time for background counts on both sides of the peaks. The following natural and synthetic standards were used: microcline (Si, K, Al), albite (Na), apatite (P, Ca), andradite (Fe), topaz (F), forsterite (Mg), vanadinite (V, Pb, Cl), pyrite (S), $MnTiO_3$ (Mn), YFe_2O_{12} (Y), $LiNbO_3$ (Nb), $LiTaO_3$ (Ta), $MnTiO_3$ (Ti, Mn), ZnS (Zn), Bi_2O_3 (Bi), RbSi (Rb), $BaSO_4$ (Ba), baddeleyite (Zr), PbS (Pb), HfO_2, $SrSO_4$ (Sr), SnO_2, ThO_2, UO_2, and synthetic REE-bearing glasses. The data base was completed with polylithionite data available in Costi (2000).

The whole-rock geochemical data (268 analyses) of the albite-enriched granite and associated pegmatites were obtained by the UFRGS research group, and are available in Bastos Neto *et al.* (2005, 2009), Minuzzi *et al.* (2005, 2006a, b, 2008), Pires (2005, 2010), Paludo *et al.* (2018), Stolnik (2015), and Lengler (2016). The samples were collected from drill cores and fresh outcrops, and the analyses were performed at Actlabs (Canada). Major elements were determined by ICP-AES, the minor and trace elements by ICP-MS, and the F by ISE.

Results

Miarolitic pegmatites

Structure

Pegmatites in miarolitic cavities are common (Bastos *et al.* 2014; Paludo *et al.* 2018; Ronchi *et al.* 2019). They have centimetric to decimetric sizes, with irregular to rounded shapes (Fig. 3). They are more common closer to the boundary between CAG and BAG. In most cases these cavities do not have structural control (Ronchi *et al.* 2019), less commonly they are aligned filling fractures (Bastos Neto *et al.* 2014). Additionally, there are geodes from 10 to 50 cm in diameter.

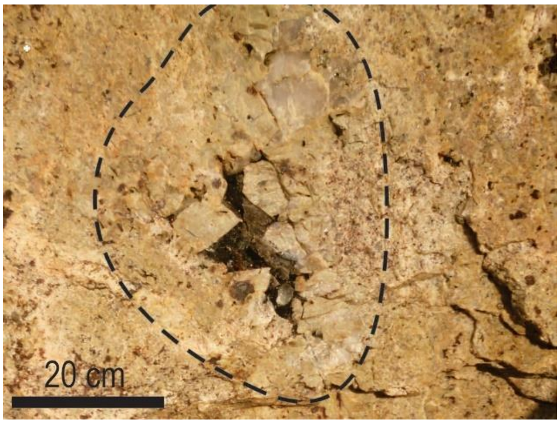

Fig. 3. Occurrence of miarolitic pegmatite. (Modified from Ronchi et al., 2019).

Texture and mineral assemblage

The miarolitic cavities are filled with fine to medium texture aggregates composed of cryolite, polylithionite, zircon and xenotime, in addition to riebeckite, albite, cassiterite and opaque minerals (Bastos *et al.* 2009). In some miarolitic cavities, well-marked zonation is observed (Ronchi *et al.* 2019): the thickness of the edge zone is centimetric, formed by quartz and albite; the wall zone is formed by quartz and albite crystals with hypidiomorphic texture; the intermediate zone is marked by the preferential orientation of minerals perpendicular to the walls, and an abrupt increase in crystal size; the core is normally formed only by cryolite. The geodes are filled with quartz, cryolite, fluorite and chlorite (Bastos Neto *et al.* 2009).

Pegmatite veins

Structure

The pegmatite veins (PEG) occur more commonly in the central, northern, and northwest parts of the CAG. The structural investigation (Ronchi *et al.* 2019) took place from level 210 m to 140 m (altimetric quota). In this quota range, there are two types of pegmatite veins visible in the whole mine front. The prevalent type is that of metric tabular bodies, with no more than 1 meter thick, emplaced in horizontal extension fractures (Fig. 4A). The other group is formed by tabular bodies emplaced in the subvertical reverse fault planes (Fig. 4B). Locally dykes of aplite cut the pegmatite veins (Fig. 4C). The pegmatite veins have centimeter to decimeter thickness and can be discontinuous in a same fault plane.

The geometric arrangement of the pegmatites is settled by contractional brittle structures in the CAG (reverse faults ~N320/60SW, imbrication fans and horses). These fractures and faults served as a conduit for the fluids, with transport from SW to NE, in a compressive system, with horizontal tension and at low solidus temperature. The horizontal pegmatite bodies are perpendicular to the minimum stress axis (σ3) and the subvertical pegmatite veins occur in the reverse fault planes positioned at approximately 60° from σ3. Pegmatite veins are preferably emplaced in fault planes that dip to SW. Horizontal and subvertical planes are physically connected (Fig. 4D) and the textural characteristics of the pegmatites in these places suggest that the fault planes worked as fluid conducts to form the horizontal veins (Ronchi *et al.*, 2019).

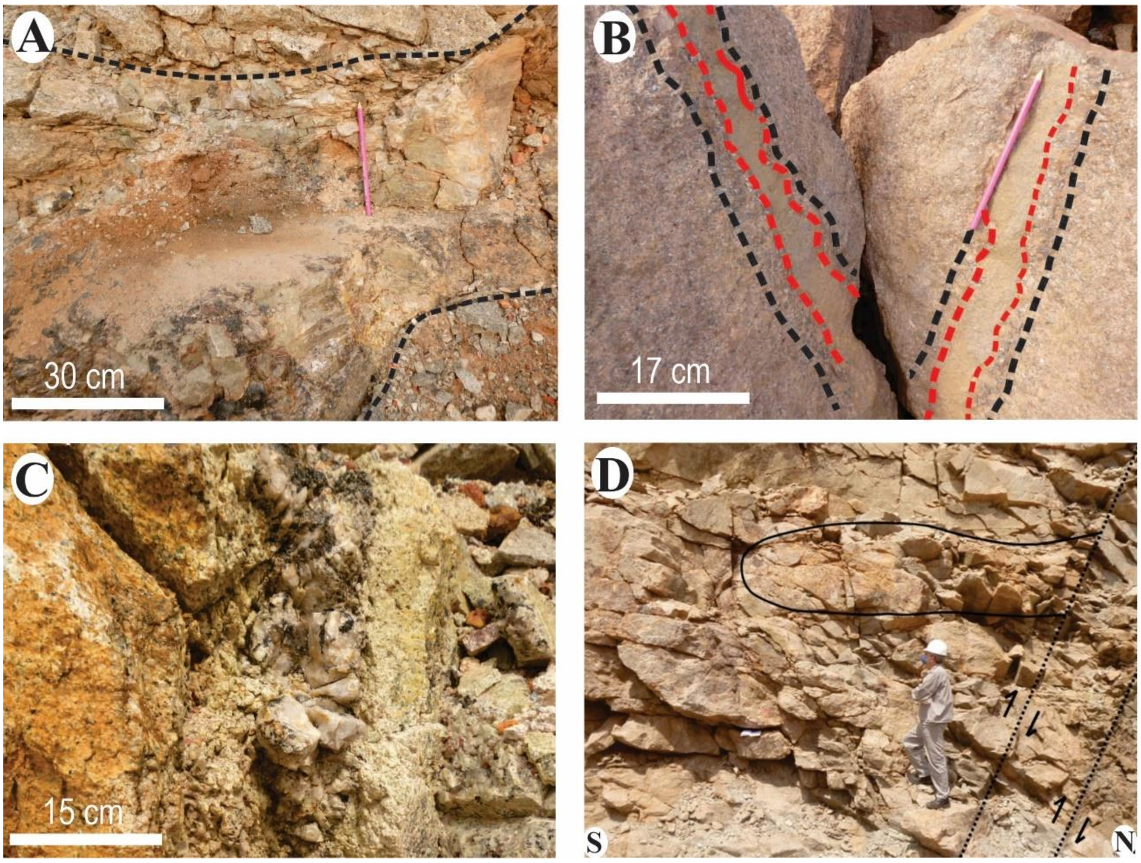

Fig. 4. Occurrence of pegmatite veins. (A) Pegmatite vein emplaced in horizontal extension fracture. (B) Pegmatite vein emplaced in reverse fault plane. (C) Aplite dike (dotted red line) cutting a pegmatite vein (dotted black line). (D) Pegmatite vein emplaced in horizontal extension fracture (black line) associated with reverse fault plane (dotted black lines). (Modified from Ronchi et al., 2019).

Texture

Both the subvertical and horizontal pegmatite veins have a thin, well-marked, border (centimeter) (Fig. 5). From the border to the center of the bodies there is a systematic increase in the size of the minerals, without, however, defining a zoning. The interior of the bodies is homogeneous, with anhedral to subhedral minerals, with minerals sizes ranging from 0.1 to 10 cm.

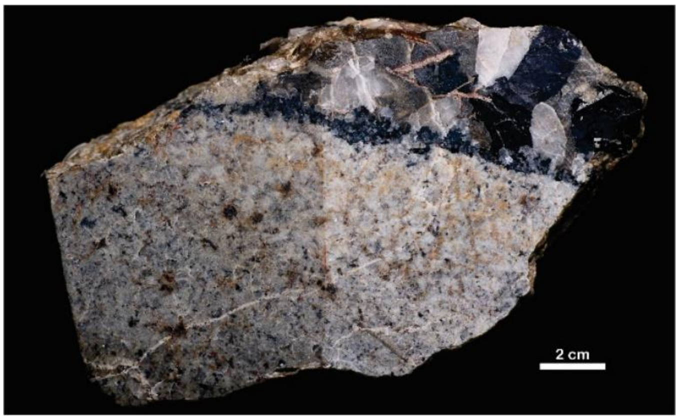

Fig. 5. Typical contact texture between the pegmatite veins with the CAG.

In most veins, the pegmatitic texture (Fig. 6) is well marked by crystals (up to 10 cm) of polylithionite, quartz, cryolite, microcline, and albite, by crystals (up to 7 cm) of riebeckite, xenotime and genthelvite, and crystals (up to 3 cm) of thorite, galena and, more rarely, zircon, cassiterite, and gagarinite. Both the horizontal and the subvertical pegmatite veins have the same mineralogy (see below). However, differences in the modal values of these pegmatites made it possible for Paludo *et al.* (2018) separate them into three groups: (i) amphibole-rich, typically with xenotime and genthelvite well-developed, with intermediate values of K and Na (Fig. 6A); (ii) polylithionite-rich, typically with abundant xenotime and genthelvite, with high values of K (Fig. 6B, C), and (iii) cryolite-rich, with quartz, galena, and xenotime often well developed, with high values of Na (Fig. 6D).

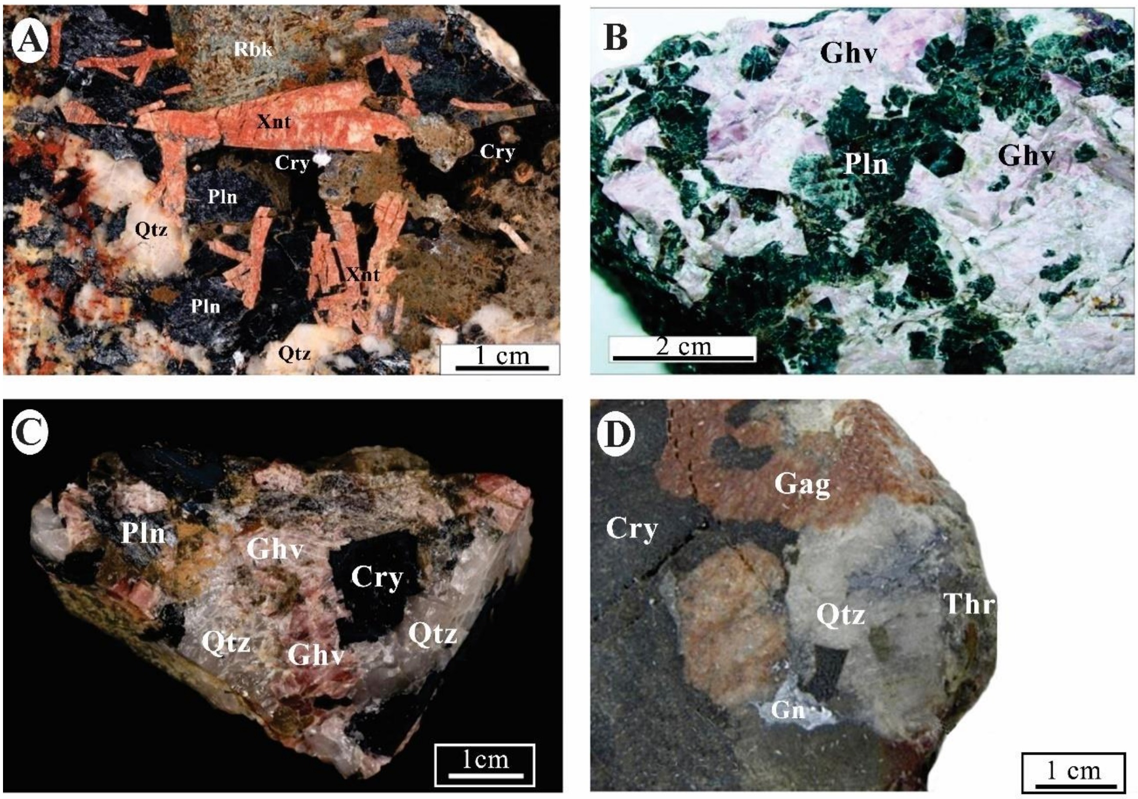

Fig. 6. Macroscopic features of the pegmatite veins. (A) Amphibole-rich pegmatite composed by riebeckite (altered), quartz, xenotime, polylithionite, and cryolite. (B) Polylithionite-rich pegmatite composed by genthelvite and polylithionite. (C) Polylithionite-rich pegmatite formed by quartz, genthelvite, cryolite, and polylithionite. (D) Cryolite-rich pegmatite composed by cryolite, gagarinite, quartz, thorite, and galena. Abbreviations: Xnt = xenotime, Qtz = quartz, Cry = cryolite, Pln = polylithionite, Rbk = riebeckite, Ghv = genthelvite, Gag = gagarinite, Thr = thorite, Gn = galena.

Mineral assemblage

Albite, orthoclase and quartz are the main constituents of the pegmatite matrix (Fig. 7A). In the matrix, these minerals can be anhedral, subhedral or euhedral and more commonly have sizes ranging from 0.3 mm to 1 cm. Albite also occurs included in microcline, quartz, polylithionite, cryolite, xenotime or gagarinite, probably due to inheritance of albite crystals from the host rock. The amphibole (Fig. 7D) is mainly riebeckite; F-arfvedsonite and F-eckermanite are very subordinate (Paludo *et al.* 2018). Riebeckite occurs as disseminated anhedral grains or as aggregated acicular crystals (0.6 mm to 7 cm) and is frequently altered to chlorite (Fig. 6A). In the amphibole-rich PEG, riebeckite crystals are often associated with polylithionite (Fig. 7D). In the polylithionite-rich PEG, polylithionite occurs most frequently as aggregates (up to 15 cm) consisting of anhedral crystals (0.2 mm - 3 cm), rarely subhedral. Polylithionite crystals show corrosion features in contact with cryolite II (Fig. 7E). Total or partial pseudomorphosis of polylithionite by hydrothermal cryolite is common; hematite that was in the polylithionite cleavage remains in alignments within the cryolite (Fig. 7F).

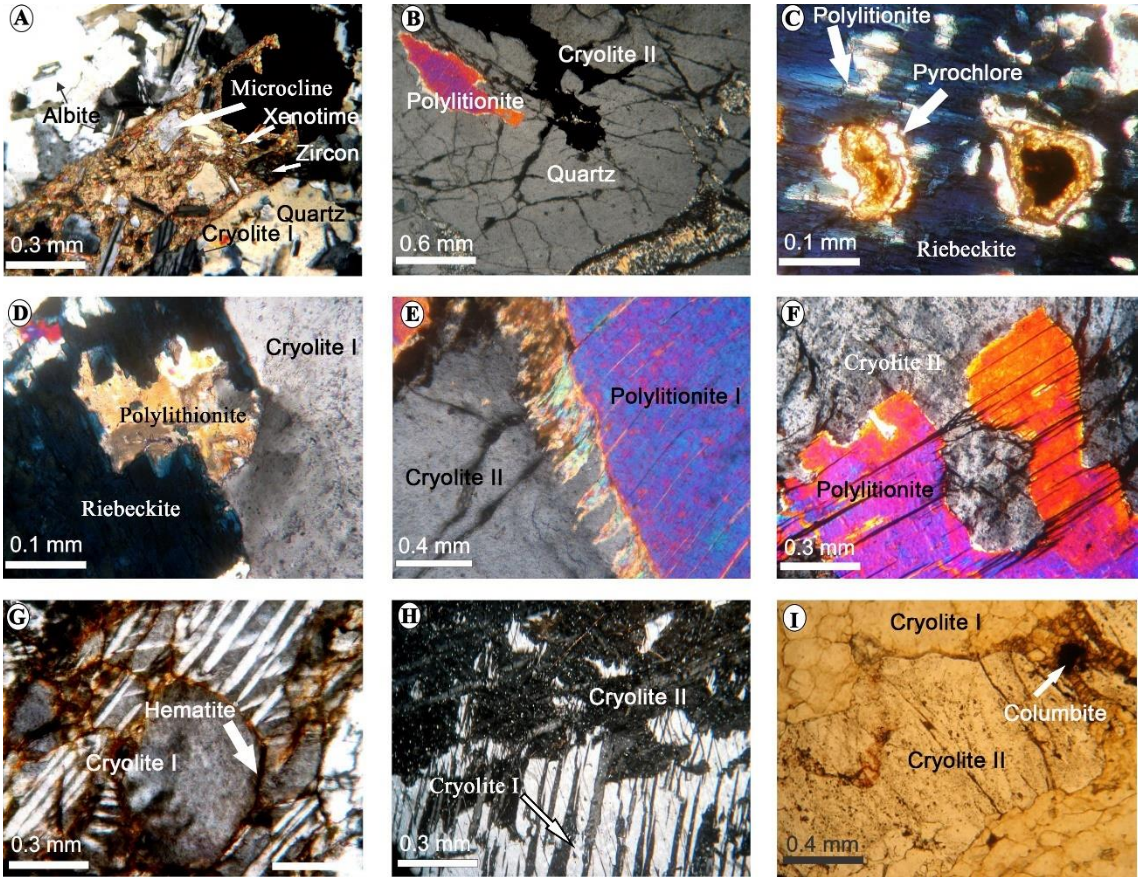

Fig. 7. Photomicrographs of the pegmatite veins. (A) Pegmatite matrix formed of quartz, microcline (upper left and lower right) and xenotime (with inclusions of albite, microcline, quartz and cryolite I) associated with zircon, cross polarized. (B) Quartz with polylithionite inclusion, with fractures filled by cryolite II and clay minerals, cross polarized. (C) Columbitized pyrochlore included in amphibole, natural light. (D) Amphibole and polylithionite associated with cryolite I, cross polarized. (E) Corrosive features in the contact of polylithionite with cryolite II, cross polarized. (F) Polylithionite (with hematite in cleavage) partially replaced by cryolite II (with hematite relicts), cross polarized. (G) Twinned cryolite I with hematite in the bordure, cross polarized. (H) Cryolite I and cryolite II with microinclusions, cross polarized. (I) Textural difference between cryolite I (without inclusions) and cryolite II, natural light. (Modified from Paludo et al., 2018).

Cryolite I (Fig. 7D) is magmatic and, together with polylithionite, is one of the most abundant minerals in the pegmatites. It can form zones of massive cryolite or aggregates of crystals, especially in the cryolite-rich PEG, or it can be disseminated in the rock, interstitial with the other minerals with sharp contact with all magmatic minerals. Macroscopically, the crystals are anhedral, black, or caramel. Under the optical microscope, it is colorless and has first-order birefringence; in crossed polarizers, it has different appearances (Fig. 7A, D, G, H. I), and is predominantly twinned, with complex twinning being common (Fig. 7G and H). Cryolite I also can occur as oriented inclusions (Fig. 8H) in several minerals and is the main constituent of the matrix in the rare cases where it is strongly oriented (Fig. 8I), not showing corrosion features with any other mineral. Cryolite II is hydrothermal, occurs interstitial to the minerals above described or in fractures, shows corrosion features with virtually all minerals and very often has abundant micro inclusions (Fig. 7I).

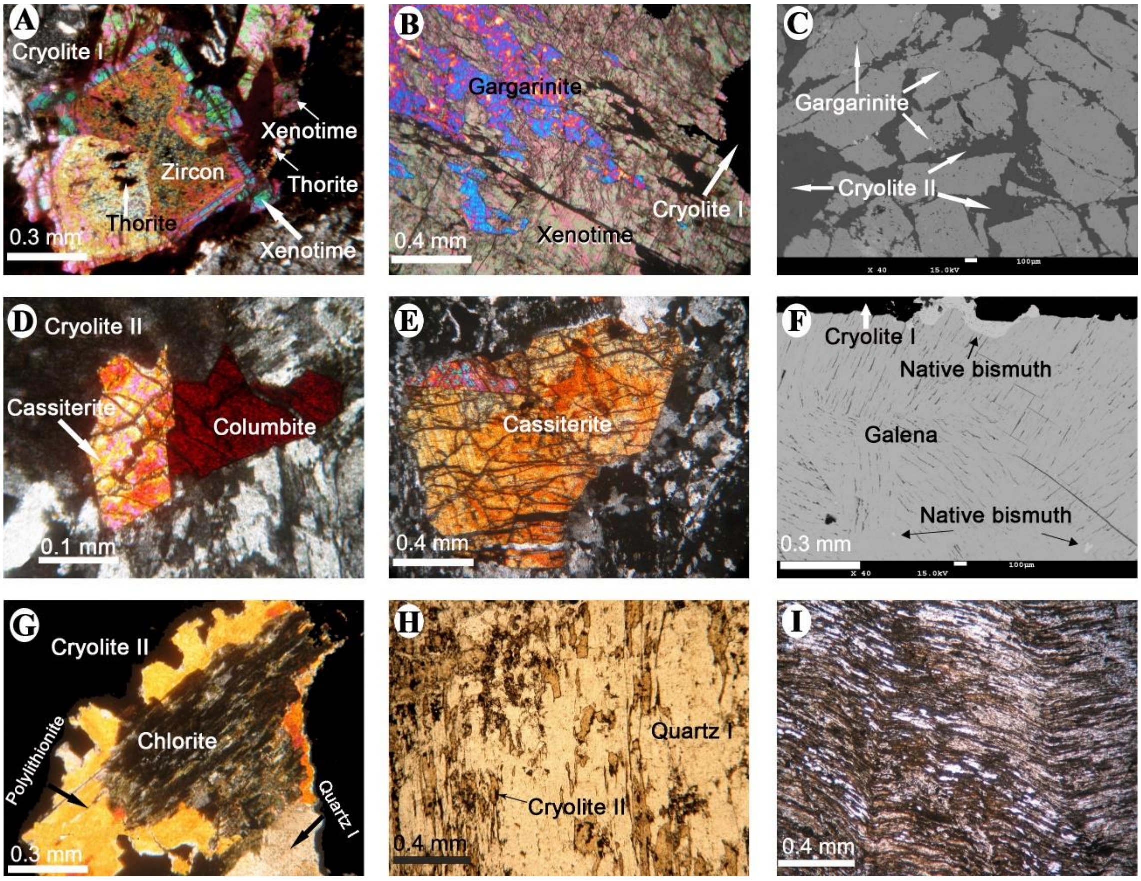

Fig. 8. Photomicrographs and BSE images of the pegmatite veins. (A) Intergrowth of zircon, xenotime and thorite, with associated cryolite I, cross polarized. (B) Gagarinite-(Y) inclusions in xenotime, cross polarized. (C) Brecciated gagarinite-(Y) with cryolite II in the matrix, BSE image. (D) Cassiterite with corrosive features in the contact with cryolite II and with rectilinear edge in the contact with primary columbite and with the matrix (microcrystalline aggregates of quartz and cryolite I), cross polarized. (E) Zoned cassiterite associated with microcrystalline aggregates of quartz and cryolite I, cross polarized. (F) Native bismuth as inclusions in galena and in the border of galena, BSE image. (G) Secondary polylithionite formed from amphibole affected by the fluid that formed cryolite II, the relict amphibole was subsequently chloritized, cross polarized. (H) Cryolite I inclusions oriented within quartz, natural light. (I) Matrix formed by oriented microcrystalline aggregates of cryolite, quartz, amphibole, and hematite. (Modified from Paludo et al., 2018).

Gagarinite-(Y) occurs as crystals 0.2 mm to 4.0 cm, anhedral, pink in natural light, more frequent in cryolite-rich pegmatites. It is intensely affected by corrosion on contact with cryolite II (Fig. 8C). Xenotime is abundant as brown prismatic crystals (0.4 mm - 7 cm, Fig. 5A), scattered in the rock singly or as intergrown aggregates. May contain inclusions of zircon, pyrochlore, cassiterite, albite, microcline or quartz (Fig. 7A). Intergrowths with thorite and zircon are also common (Fig. 8A) and, more rarely, with gagarinite (Fig. 8B). Thorite occurs as dark fully opaque elongated crystals (up to 4 cm in length, more commonly ranging from 2 to 5 mm). Thorite usually occurs in the matrix and is also widely observed included in large polylithionite (Fig. 8A) and xenotime (Fig. 8B) crystals. The association of thorite with xenotime and zircon is evidenced by the intergrowths, more commonly in the case of zircon. The contacts of thorite with all pegmatite primary minerals (polylithionite, riebeckite, pyrochlore, etc.) are mostly abrupt, however, the contact with cryolite II is characterized by corrosive features. Zircon occurs in small quantities, as euhedral or subhedral crystals (0.2 to 2.0 mm), sometimes zoned (Fig. 8A), always with corrosion features in contact with cryolite II. Cassiterite (Fig. 8D, E) usually occurs disseminated as subhedral grains, with dimensions of up to 0.8 mm; more rarely, larger crystals of up to 3 cm occur. Galena associated with minor sphalerite and with inclusions of native Bi (Fig. 8F) is common, in most cases as ~0.3 mm crystals, but larger crystals (up to 10 cm) also occur. Galena also occurs as small crystals associated to pyrochlore alteration.

Genthelvite occurs predominantly as massive crystals (up to 7 cm) surrounding polylithionite and quartz I phenocrysts and includes pyrochlore, thorite and zircon (Fig. 9A). Subordinately, genthelvite occurs arranged interstitially in the matrix with quartz I and orthoclase (Fig. 9B). The contacts with polylithionite, quartz I, pyrochlore, zircon and thorite are reactive. Genthelvite is characterized by corrosion features as cavities and microfractures commonly filled by cryolite II (Fig. 9C).

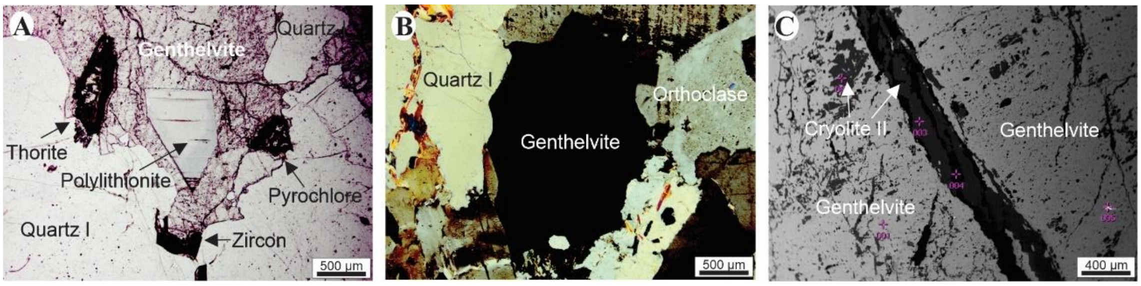

Fig. 9. Photomicrographs and BSE image of genthelvite of the pegmatite veins. (A) Typical genthelvite, filling the space between polylithionite and quartz I crystals, associated with inclusions of pyrochlore, thorite and zircon, natural light. (B) Genthelvite in the matrix with quartz I and orthoclase, cross polarized. (C) Genthelvite with microfractures filled by cryolite II, BSE image. [Modified from Hadlich et al., 2023a (submitted)].

Pyrochlore occurs as single crystals with dimensions ranging from 0.1 to 0.7 mm. It predominates as incipiently to moderate opaque grains, due to its alteration to columbite, and the remaining pyrochlore translucent portions are brownish orange (Fig. 10A, B). Pyrochlore commonly occurs in the matrix (Fig. 10A, B) and is also observed included in large quartz, polylithionite (Fig. 10C, D), xenotime (Fig. 10D) and orthoclase crystals (Fig. 10E). Polylithionite and matrix quartz fills cavities within the pyrochlore (Fig. 10C, F). Crystals surrounded by cryolite II, (Fig. 10B, C, E) display highly reactive contact and are often associated with secondary pyrochlore, columbite, galena, LREE-rich fluorides, and HREE-Y-U-Th-rich silicates. Pyrochlore from these pegmatites is similar to that of the CAG and BAG [Bastos Neto *et al.* 2009; Hadlich *et al.* 2023b (submitted)] in terms of composition, size, shape, color, occurrence and alteration. Because of that is suggested that pyrochlore of the pegmatite veins is inherited from the magmatic phase of the albite-enriched granite.

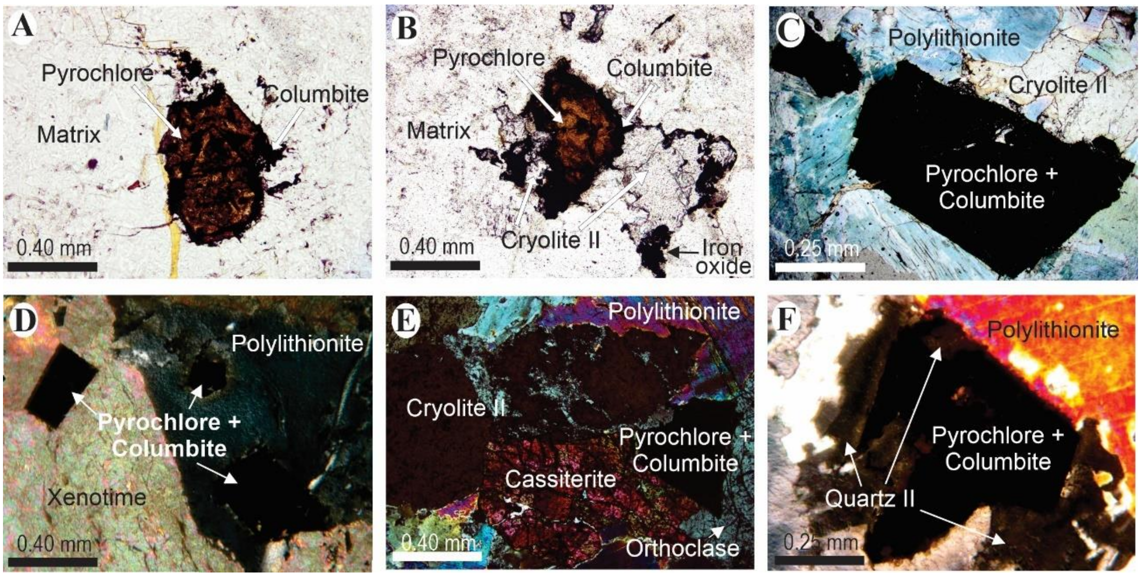

Fig. 10. Photomicrographs displaying various features of pyrochlore from the pegmatite veins. (A) Typical pyrochlore from the pegmatite veins, into the matrix with incipient alteration to columbite, natural light. (B) Pyrochlore and columbite, into the matrix and surrounded by cryolite II, with associated iron oxide, cross polarized. (C) Columbitized pyrochlore grain included in polylithionite and in contact with hydrothermal cryolite, cross polarized. (D) Euhedral pyrochlore grains included in xenotime and polylithionite, cross polarized. (E) Subhedral columbitized pyrochlore included in orthoclase, in association with cassiterite, polylithionite and cryolite II, cross polarized. (F) Anhedral pyrochlore grain with cavities filled by quartz II, cross polarized.

Magnetite is primary and occurs locally and in small amounts as euhedral crystals associated with heterogeneous cryptocrystalline masses resulting from the alteration of other pegmatite minerals. The alteration of amphiboles and of polylithionite (Fig. 8G) generated chlorite. The alteration of amphiboles, Fe-Li-rich annite, polylithionite and feldspars by late hydrothermal fluids (Ronchi *et al.*, 2011) generated clay minerals and quartz II (microcrystalline) which also occurs as very thin veinlets that cut the various minerals of the pegmatite veins.

Pegmatitic core albite-enriched granite

Structure and texture

The dykes and lenses of pegmatitic CAG (Fig. 11A) occur mainly in the central and northern parts of the CAG. They are up to 10 meters in length and up to 50 cm in width. Drillings suggest they are thicker (up to 15 m) at greater depths. These granitic dykes are usually orientated along the N70°E/40°N plane, which is nearly parallel to the strike of magmatic foliations; locally, the relationship between dyke margins suggests right-lateral displacement (Siachoque *et al.* 2020). The contact with the host CAG is commonly abrupt, but gradational contacts also may occur. A feature of these pegmatites is the association of the pegmatitic xenotime with mega crystals and polylithionite clusters (Figs. 11B, C). More rarely the pegmatitic xenotime occur in a quartz feldspatic portion (Fig. 11D). The most common pegmatitic CAG type has a matrix coarser than that of CAG, but quite similar to this rock in terms of mineralogical composition.

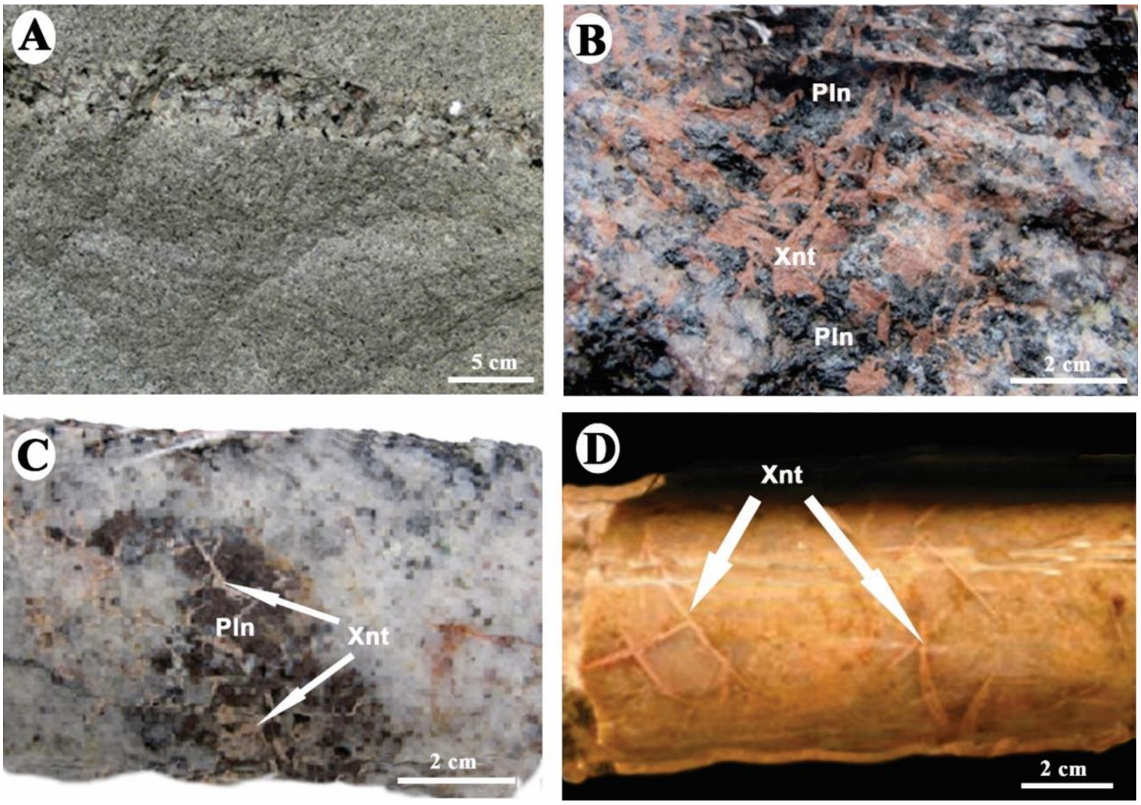

Fig. 11. Macroscopic features of the pegmatitic CAG. (A) Vein of pegmatitic CAG. (B) Detail of a vein with pegmatitic xenotime associated with polylithionite. (C) Drilling core with pegmatitic xenotime associated with polylithionite. (D) Drilling core with pegmatitic xenotime crystals in a quartz-felspathic zone.

Mineral assemblage

The pegmatitic minerals are quartz, riebeckite, Fe-Li-rich annite, polylithionite (all these are more commonly ~2 cm, but may reach 10 cm), xenotime (up to 5 cm) and thorite (up to 3 cm). Pegmatitic crystals of cryolite and albite mega crystals are uncommon. The matrix consists mainly of albite, quartz, orthoclase, and microcline, with dispersed riebeckite, Fe-Li-rich annite, polylithionite, zircon and subordinate xenotime, thorite, cassiterite, pyrochlore and cryolite.

Quartz in the matrix (Fig. 12A) also occurs as primitive poikilitic phenocrysts of up to 5 mm, anhedral to rounded, with corrosion features in contact with albite and cryolite II. K-feldspar pegmatitic crystals are cloudy, with frequent inclusions of polylithionite. Albite occurs mainly in the matrix, forming euhedral to subhedral limpid crystals, with diffuse to clear twinning, with sizes varying between 0.04 mm and 0.4 mm. Albite also occurs as inclusions or on the edge of K-feldspar. Fe-Li-rich annite in the matrix is very commonly altered to polylithionite (Fig. 12B).

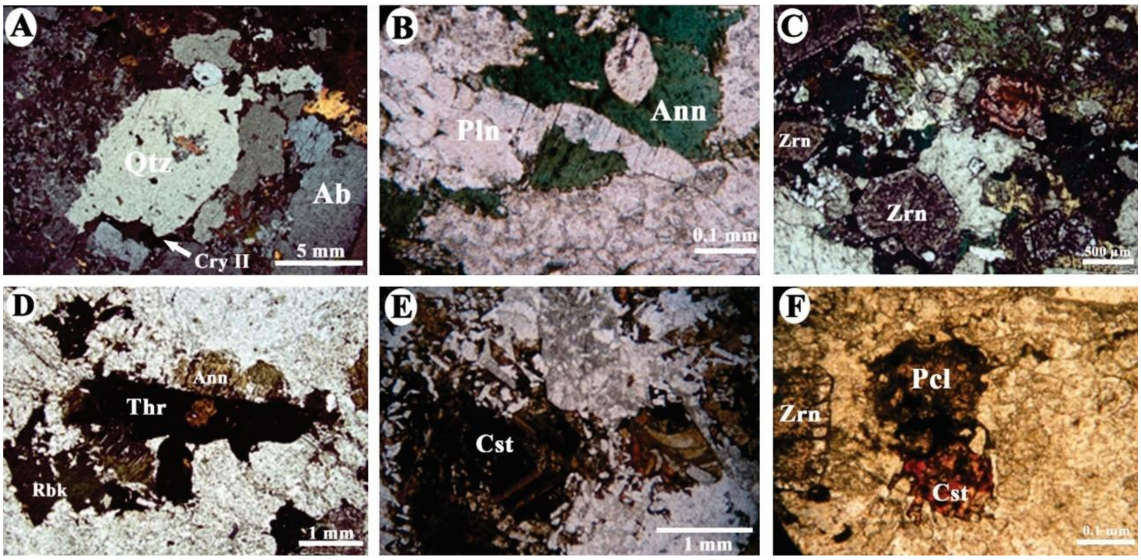

Fig. 12. Microscopic features of the pegmatitic CAG. (A) Anhedral to rounded poikilitic quartz with corrosion features in contact with the matrix composed by albite and cryolite II, cross polarized. (B) Fe-Li-rich annite partially replaced by polylithionite, cross polarized. (C) Late euhedral zircon crystals, cross polarized. (D) Thorite, Fe-Li-rich annite and riebeckite from the matrix. (E) Broken crystals of zoned cassiterite and poikilitic xenotime. (F) Late zircon, pyrochlore, and cassiterite crystals. Abbreviations: Ab = albite, Ann = Fe-Li-rich annite, Cry II = cryolite II, Cst = cassiterite, Qtz = quartz, Pln = polylithionite, Pcl = pyrochlore, Rbk = riebeckite, Thr = thorite, Zrn = zircon.

Disseminated cryolite belongs to two generations, both with low refractive index, almost isotropic and rarely twinned. Cryolite I occurs as crystals (0.02 mm to 1.0 mm) with subhedral to anhedral habits (frequently rounded) disseminated in the matrix, without corrosion features with the other minerals. Cryolite II forms irregular to rounded aggregates that fill spaces at the edges of other minerals, with corrosion features.

Zircon crystals occur in two forms. The early zircon is predominantly skeletal and occurs mostly enclosed in other minerals suggesting being inherited from the host rock. Second-generation zircon (Fig. 12C) occurs as euhedral to subhedral individual crystals (between 0.1 mm and 1.5 mm) or forming aggregates (up to 1 cm). Thorite in the matrix (Fig. 12D), occurs as dispersed individual crystals (up to 0.40 mm). In the pegmatitic portions, the crystals (up to 4 cm) form irregularly distributed concentrations. Cassiterite occurs both in aggregates (Fig. 12E) and in individual crystals (Fig. 12F), in varying sizes up to 0.5 cm. They are usually subhedral to euhedral, and may be, more rarely, anhedral. They are reddish-brown in color and are sometimes intensely fractured. Almost all crystals show zoning, identified by color variation (white edges, transitioning to red and, in the center, brown). The contacts with cryolite and albite of the matrix are characterized by corrosion features by these minerals; despite this corrosion, it is still possible to identify the original shape of the larger crystals.

The xenotime is found in the matrix (Fig. 12E) and as pegmatitic crystals (Fig. 11B, C, D). In both cases, it has a brown/pink color, elongated prismatic habit, varies from euhedral to subhedral, with sizes between 0.05 mm and 5 cm. Pegmatitic crystals occur both as isolated crystals and in clusters, whereas smaller matrix crystals occur dispersed. Xenotime crystals present many inclusions, mainly pyrochlore, thorite, and matrix crystals, which also appear eroding the edges of xenotime crystals. In the matrix, commonly there is a higher concentration of zircon, cassiterite, thorite and polylithionite where there is a higher concentration of xenotime. The xenotime crystallization occurred after the pyrochlore and early zircon, at the same time as the thorite crystallization and partially synchronous to late zircon.

More rarely, the pegmatitic CAG has a matrix with medium granulation, predominantly albitic with a smaller proportion of quartz, also containing zircon, cryolite, pyrochlore, cassiterite, thorite and xenotime. The main pegmatitic crystals are cryolite, quartz, Fe-Li-rich annite, and xenotime. Compared to the other type of pegmatitic CAG, the following features are notable: lower amounts of amphibole and K-feldspar; the abundance of cryolite; xenotime has no association with polylithionite; and polylithionite appears to have been entirely formed by alteration of Fe-Li-rich annite. The pegmatitic xenotime (up to 7 cm) is prismatic and euhedral, include matrix minerals in large amounts, such as albite, quartz, and zircon. On the other hand, small xenotime crystals (<1 mm) do not show these inclusions and appear to be part of the matrix itself or may represent inherited xenotime from the host rock.

Border pegmatites

Structure and texture

The border pegmatites are positioned between the BAG and the host rock, amphibole-biotite granite, or biotite granite, depending on the location in relation with the pluton (Fig. 2). In the case of the eastern border pegmatite, the BAG has no mappable thickness and its existence in depth was confirmed by drilling. The border pegmatites have a length of up to 400 m and thicknesses more commonly from 0.5 to 4 m, locally reaching 20 m. The boundary with the external host rock exhibits an abrupt contact, and the interface with the BAG may be either abrupt or gradational.

Mineral assemblage

The border pegmatite is typically red (Fig. 13), locally yellow or gray due to hydrothermal alteration. The main pegmatitic minerals are K-feldspar (microcline and orthoclase), predominant, in crystals of up to 7 cm, and quartz (up to 5 cm). Crystals of Fe-Li-rich annite (up to 2 cm) occur sparsely. Zircon clusters with dimensions of up to 1 cm are common. The matrix has medium to coarse granulation, is mainly composed of microcline and quartz, with minor albite, zircon, and thorite. Disseminated in the matrix, occur Fe-Li-rich annite, polylithionite, riebeckite, fluorite, pyrite, cassiterite (subhedral) and pyrochlore. Fe-Li-rich annite and riebeckite are intensively chloritized. Zircon, subhedral, always very altered, is much more common than in the pegmatite veins.

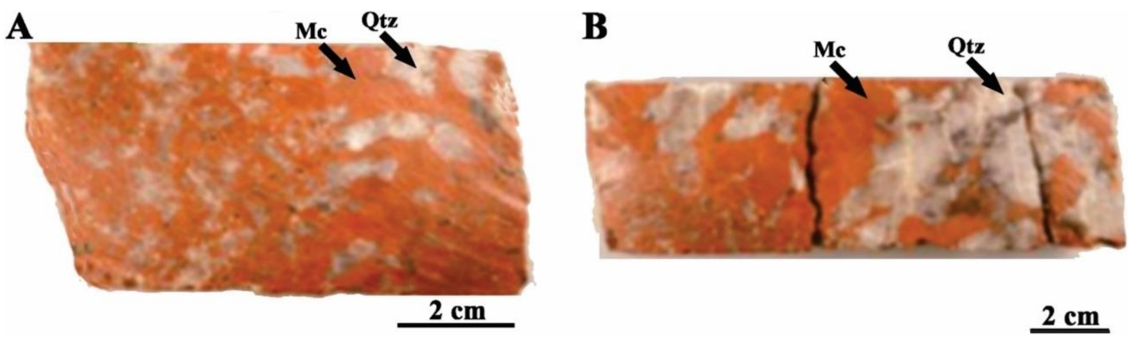

Fig. 13. Typical macroscopic features of the border pegmatites. (A) Microcline predominant and disseminated quartz crystals. (B) Microcline predominant and pegmatitic poikilitic quartz. Abbreviations: Mc = microcline, Qtz = quartz.

Pyrochlore from the border pegmatites occurs as single crystals spread into the quartz-feldspatic matrix, sizing from 0.2 mm to 0.5 mm. In the eastern border pegmatites predominate euhedral light-yellow crystals (Fig. 14A) with incipient substitution to columbite, and subhedral moderate orange crystals, with moderate alteration (Figs. 14B, C). In the northern border pegmatites are much more common anhedral dark opaque grains, with advanced alteration to columbite (Figs. 14D-F), with occurrence of secondary minerals as U-Th-HREE-Y-rich silicates and LREE-rich fluorides. Pyrochlore occurs disseminated in the matrix, often associated with zircon and, more rarely, with polylithionite (Fig. 14B). Growth of zircon in the pyrochlore surface is a common feature in the border pegmatites: late zircon grows from the border of pyrochlore grains, with abrupt and rectilinear contact (Fig. 14D). The contact between pyrochlore and matrix minerals is reactive and invariably the pyrochlore grain is surrounded by a columbite or iron oxide halo. Hydrothermal fluorite is consistently present around pyrochlore and columbite grains (Figs. 14A-E), and their contact is characterized by corrosive features. The observed petrographic relationships show the magmatic character of pyrochlore of the border pegmatites and its subsequent alteration by a F-rich hydrothermal fluid. It presents characteristics like those in the pegmatite veins, suggesting that pyrochlore of both the eastern and northern border pegmatites are inherited from the BAG.

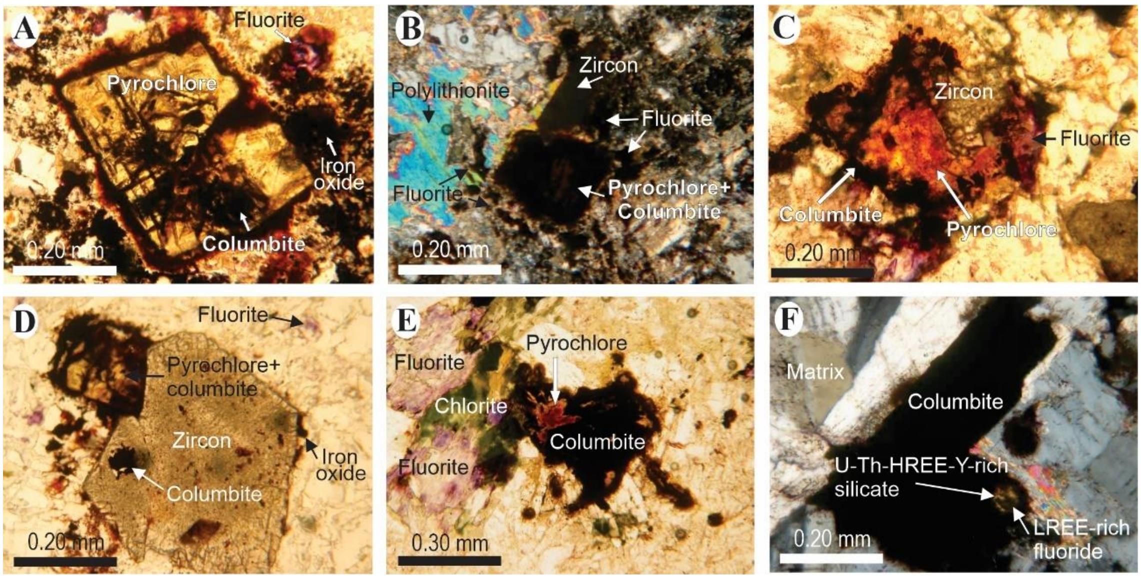

Fig. 14. Photomicrographs displaying various features of pyrochlore from the eastern (A-C), and northern (D-F) border pegmatites. (A) Incipiently altered euhedral pyrochlore grain surrounded by hydrothermal fluorite and iron oxide, natural light. (B) Pyrochlore grain with moderate alteration to columbite, associated with polylithionite and zircon; the set is surrounded by matrix and fluorite, cross polarized. (C) Pyrochlore grain incipiently altered in the edges associated with zircon and fluorite, natural light. (D) Intergrowth between pyrochlore and zircon, a columbitized pyrochlore inclusions occurs into the zircon grain, natural light. (E) Anhedral columbitized pyrochlore surrounded by fluorite and chlorite, natural light. (F) Fully columbitized grains with secondary U-Th-HREE-Y-rich silicate and LREE-rich fluoride, cross polarized.

Thorite crystals ranges from 1 to 2 mm, and frequently presents a halo formed by galena (Fig. 15). Thorite in the eastern border pegmatite is commonly translucent, whereas in the northern and southern border pegmatites thorite is much more frequently opaque. Geminated thorite crystals (Fig. 15A) and the association with zircon (Fig.

15B) are commonly observed, whereas association with xenotime is absent. The common contact with fluorite does not corrode or alter the thorite crystals.

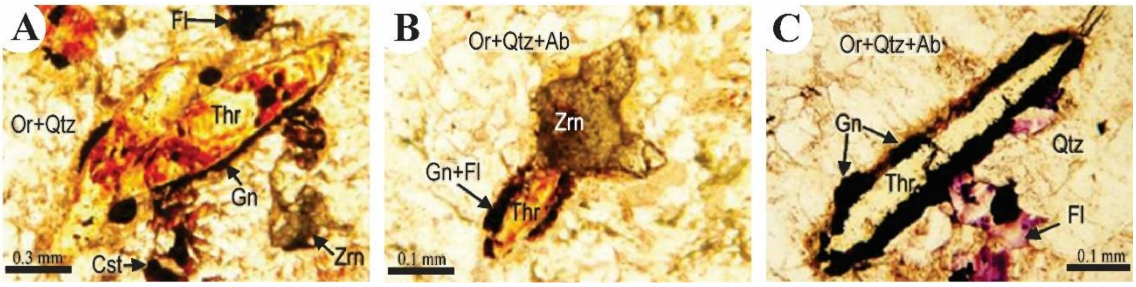

Fig. 15. Photomicrographs of thorite from the border pegmatites. (A) Typical translucid thorite in the eastern border pegmatite, natural light. (B) Thorite and zircon growing in one of the facies of a zircon crystal in the eastern border pegmatite; thorite presents a rim of galena and fluorite, natural light. (C) Translucid thorite with a thick rim of galena and fluorite in the northern border pegmatite, natural light. Abbreviations: Ab = albite, Cst = cassiterite, Fl = fluorite, Gn = galena, Or = orthoclase, Qtz = quartz, Thr = thorite, Zrn = zircon. (Modified from Hadlich et al., 2019).

Fluorite, pyrite (with galena and molybdenite on the edges) and a second generation of quartz (anhedral, up to 15 mm, with inclusions of matrix grains and reddish-brown needles of Fe-oxides), are late minerals which occur disseminated in the matrix and in veins that cut the host rock. Hematite occurs associated with fluorite as well as finely disseminated in the whole rock. Is evident the greater hydrothermal alteration of the northern border pegmatite compared to the eastern border pegmatite and to the pegmatite veins.

Chemical studies of selected minerals

Thorite

In both the CAG, BAG, pegmatite veins and border pegmatites, thorite ($ThSiO_4$) is highly hydrated, with low average Th concentration (48 wt.% ThO_2), and high contents of Fe (0.11 to 29.56 wt.% Fe_2O_3) and F (up to 6.02 wt.% F) (Hadlich *et al.* 2019). The most common variety in the CAG and BAG is a Zr-Fe-rich thorite. Primary thorite from the pegmatite veins are systematically richer in Y and REE than those in the CAG and BAG. Additionally, a primary Y-U-(Fe)-rich thorite was observed only in the northern border pegmatite, and a hydrothermal Y-Al-Fe-rich thorite was observed only in the pegmatite veins.

Xenotime

The xenotime (YPO_4) was analyzed in the CAG and in the pegmatitic CAG by Bastos Neto *et al.* (2014), and in the polylithionite-rich PEG by Paludo *et al.* (2018). While the xenotime in the CAG has the highest REE average content (38.65 wt.% $HREE_2O_3$ and 4.14 wt.% $LREE_2O_5$), xenotime of the polylithionite-rich PEG has the highest Y (30.93 wt.% Y_2O_3). The highest average of F is in xenotime of the CAG (2.83 wt.% F) and the lowest in that of the pegmatitic CAG (1.35 wt.%). The LREE/HREE and Th/U ratios in xenotime decrease in the direction CAG > pegmatitic CAG > polylithionite-rich PEG. In xenotime, components of zircon, coffinite or thorite are very subordinated.

Genthelvite

Compositions of genthelvite of the pegmatite veins are homogeneous and correspond to relatively limited substitutions in the helvine-genthelvite-danalite solid solution system, with relatively high contents of Zn (36.96 to 49.45 wt.% ZnO), low contents of Mn (0.61 to 3.03 wt.% MnO) and variable contents of Fe (2.10 to 10.94 wt.% FeO). Remarkable features are the high contents of U (0.13 to 0.25 wt.% UO2) and REE (up to 0.40 wt.% REE_2O_3) and the higher LREE average content over the HREE [(Hadlich *et al.* 2023b (submitted)].

Gagarinite

Gagarinite-(Y) [($NaCaY(F,Cl)_6$] was firstly described in the CAG by Minuzzi (2005), and specific studies were performed by Pires *et al.* (2006). The crystals are localized in the central portion of the CAG, associated with fluocerite-(Ce) exsolutions. Secondly, gagarinite-(Y) was reported in the cryolite-rich PEG by Paludo *et al.* (2018) with no exsolution observed. Average compositions and structural formula of these minerals are presented in Table 1. In the CAG, gagarinite-(Y) presents higher average Y (31.12 wt.%), LREE (9.03 wt.%) and Ca (8.10 wt.%). In the cryolite-rich PEG, gagarinite-(Y) is richer in average HREE (15.66 wt.%), Na (3.19 wt.%) and F (42.29 wt.%). Fluorine and Na, and Na and HREE have good positive correlations (Fig. 16A, B), while Ca have strong negative correlation with F and with Y+REE (Fig. 16C, D). In the gagarinite-(Y) from the CAG there is only a moderate negative correlation between Y and LREE (Fig. 16E) and between HREE and LREE (Fig. 16F).

Tab. 1. EPMA data (in wt.%) of average exsolved fluocerite-(Ce) and host gagarinite-(Y) from the core albite-enriched granite (CAG) and gagarinite-(Y) from the cryolite-rich pegmatite vein (PEG).

	CAG Fluocerite[a]		CAG Gagarinite[a]		Cryolite-rich PEG Gagarinite[b]	
	Range	2σ	Range	2σ	Range	2σ
	n = 24		n = 16		n = 25	
U	d.l.		d.l.		0.20	0.05
Th	d.l.		d.l.		0.17	0.10
Y	0.36	0.53	31.12	1.32	25.31	1.78
HREE	0.48	2.31	12.15	1.37	15.66	0.82
LREE	66.15	3.21	9.03	3.05	7.12	1.66
Ca	0.14	0.71	8.10	0.48	7.61	1.70
Pb	d.l.		d.l.		0.25	0.08
Sr	d.l.		d.l.		0.14	0.10
Na	d.l.		1.90	1.01	3.19	1.38
F	35.67	3.59	38.22	3.27	42.29	1.42
Total	102.80	4.22	100.52	3.03	101.95	2.59
Structural formula in a.p.f.u.						
U					0.003	0.001
Th					0.002	0.001
Y	0.010	0.010	1.009	0.051	0.917	0.087
HREE	0.003	0.029	0.210	0.030	0.302	0.023
LREE	0.977	0.070	0.139	0.057	0.158	0.034
Ca	0.007	0.037	0.584	0.028	0.609	0.094
Pb					0.004	0.002
Sr					0.005	0.004
Na	0.001	0.012	0.238	0.127	0.450	0.226
F	3.883	0.448	5.808	0.574	5.840	0.288
LREE/HREE	289.08	243.86	0.75	0.40	0.45	0.10

[a]Pires et al. (2006), [b]Paludo et al. (2018). Fluocerite structural formula calculated based on 1 cation. Gagarinite structural formula calculated based on Y+REE+Ca = 2.

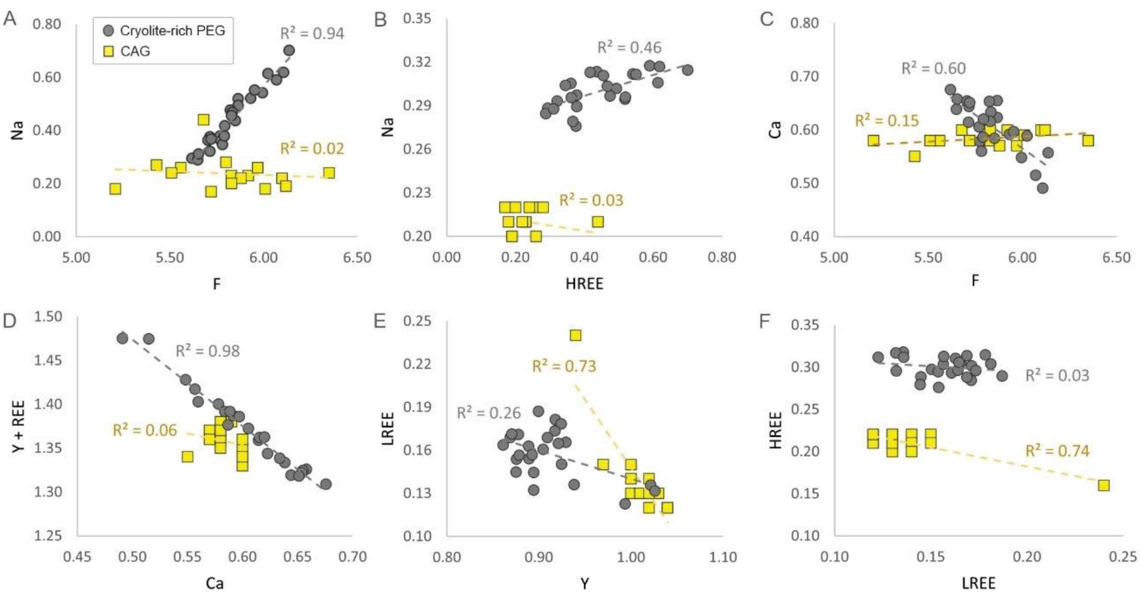

Fig. 16. Binary diagrams for gagarinite-(Y) from the cryolite-rich pegmatite vein (PEG) and from the core albite-enriched granite (CAG). (A) Na versus HREE. (B) Ca versus F. (C) Y+REE versus Ca. (D) Na versus F. (E) LREE versus Y. (F) HREE versus LREE. Concentrations are expressed in atoms per formula unit.

The REE normalized pattern (chondrite of Anders and Grevesse 1989) (Fig. 17) of gagarinite-(Y) from the CAG shows a strong depletion in the LREE, especially in the La and Ce contents, compared with the gagarinite of the cryolite-rich PEG. The exsolved fluocerite-(Ce) presents depletion in the HREE related with the LREE content. The earliest gagarinite-(Y) in the CAG (that prior to fluocerite exsolution), calculated by adding proportionally densities and modal compositions of the gagarinite-(Y) and the exsolved phase, has a flat REE normalized pattern (Fig. 17). The gagarinite-(Y) of the cryolite-rich PEG present enrichment of the HREE relative to the LREE, with LREE contents significantly lower than those of the earliest gagarinite-(Y) in the CAG.

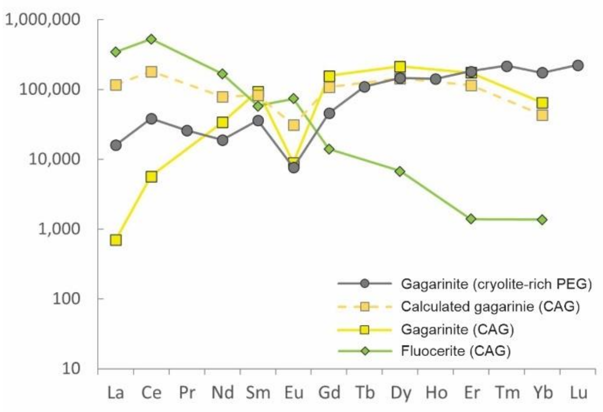

Fig. 17. REE patterns normalized to chondrite (Anders and Grevesse, 1989) of gagarinite in the cryolite-rich pegmatite vein (PEG) (Paludo et al., 2018), and in gagarinite-(Y), fluocerite-(Ce) (exsolved phase), and calculated earliest gagarinite of the core albite-enriched granite (CAG) (Pires et al., 2006).

Riebeckite

Average compositions and structural formula for riebeckite of the amphibole-rich PEG and for the CAG are presented in Table 2. Riebeckite from the amphibole-rich PEG have significatively higher averages of F (2.12 wt.%) compared to riebeckite from the CAG (0.67 wt.% F). Silicon, Al, K, Na and Zn average contents are also slightly higher in riebeckite crystals from the amphibole-rich PEG, what is compensated by higher concentrations of total Fe in riebeckite from the CAG. In riebeckite from the amphibole-rich PEG, fluorine has strong positive correlation with Si (Fig. 18A), Na (Fig. 18B), while in the CAG there is no significative correlation. Fluorine and K (Fig. 18C) have good positive correlation in both the amphibole-rich PEG and CAG riebeckite crystals. The Fe^{3+} negative correlation with F (Fig. 18D) is strong, and the negative correlation with Al (Fig. 18E) is moderate. Manganese and Zn present good positive correlation, probably substituting Fe^{2+}.

Tab. 2. EPMA data (in wt.%) of average riebeckite from the core albite-enriched granite (CAG) and amphibole-rich pegmatite vein (PEG).

	CAG[a]		Amphibole-rich PEG[b]	
	Mean	2σ	Mean	2σ
	n = 43		n = 19	
SiO_2	49.38	1.27	51.14	1.20
TiO_2	0.16	0.39	0.11	0.25
Al_2O_3	0.75	0.42	1.03	0.54
Fe_2O_3	-	-	4.01	8.60
FeO	-	-	25.95	3.89
FeO_T	34.17	3.20	-	-
MnO	0.47	0.54	0.78	0.34
ZnO	2.09	2.64	2.31	0.95
Na_2O	7.43	0.48	7.63	1.51
K_2O	0.27	0.25	1.02	0.79
F	0.67	0.27	2.12	2.27
Cl	d.l.	-	0.01	0.02
H_2O*	1.58	0.14	0.83	1.12
O=F,Cl	-0.28	0.12	-0.90	0.96
Total	96.68	1.93	96.42	3.20
Structural formula based on 23 oxygens (a.p.f.u.)				
Si^{4+}	7.930	0.110	8.343	0.226
$^{IV}Ti^{4+}$	0.001	0.014	0.000	0.000
$^{IV}Al^{3+}$	0.070	0.097	0.000	0.000
$^{IV}Fe^{3+}$	0.001	0.010	0.000	0.000
Sum_T	8.002	0.015	8.343	0.226
Ti^{4+}	0.018	0.044	0.013	0.030
$^{VI}Al^{3+}$	0.073	0.100	0.199	0.105
Fe^{3+}	1.585	0.285	0.486	1.034
Fe^{2+}	2.996	0.334	3.543	0.609
Mn^{2+}	0.064	0.073	0.108	0.048
Zn^{2+}	0.255	0.308	0.278	0.119
Sum_C	4.991	0.092	4.614	0.278
Na^+_B	2.000	0.000	1.998	0.017
Na^+	0.313	0.162	0.417	0.530
K^+	0.054	0.047	0.213	0.168
Sum_A	0.376	0.223	0.631	0.647
F^-	0.339	0.142	1.102	1.195
Cl^-	0.000	0.000	0.002	0.005
OH^-*	1.661	0.142	0.895	1.196

[a]Schuck (2015), [b]Paludo et al. (2018). *OH calculated after Hawthorne et al. (2012).

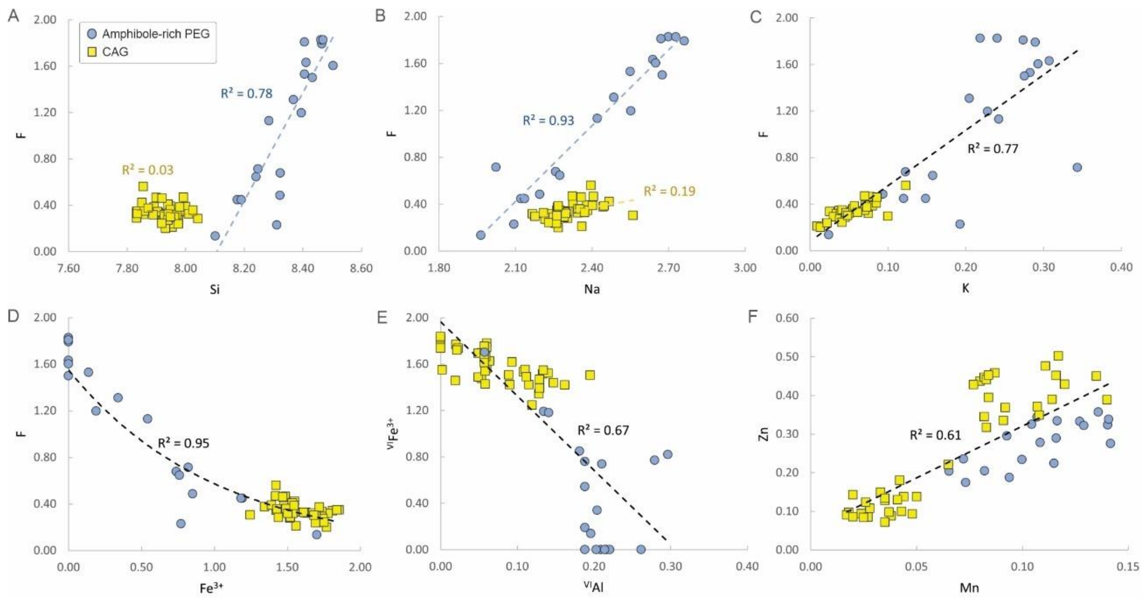

Fig. 18. Binary diagrams for riebeckite from the core albite-enriched granite (CAG) and amphibole-rich pegmatite vein (PEG). (A) F versus Si. (B) F versus Na. (C) F versus K. (D) F versus Fe^{3+}. (E) $^{VI}Fe^{3+}$ versus ^{VI}Al. (F) Zn versus Mn. Concentrations are expressed in atoms per formula unit.

Polylithionite

EPMA data and structural formula of polylithionite from the pegmatite veins and from different elevations (altitude quota) of the CAG are presented in Table 3. Lithium average content ranges from 5.47 to 5.75 wt.% in polylithionite of the CAG and from 6.25 to 6.57 wt.% in the pegmatite veins. There is a strong negative correlation between Li and Fe (Fig. 19A) indicating that Li is substituted by Fe (~0.2 apfu) in the octahedral site. There is also a moderate negative correlation between Li and Al (Fig. 19B). In the polylithionite of the CAG, F average increases with increasing quota (6.40 in 120 m to 7.53 wt.% F in 160 m), and F content gets significatively higher in the pegmatite veins (8.92 to 9.26 wt.% F). In the polylithionite from the pegmatite veins, the F fulfills the entire (OH, F)-site (~2 apfu), while in the CAG, the F-OH proportion is near 1.5 - 0.5 apfu. The F-Fe avoidance effect is not observed in the analyzed polylithionite grains (Fig. 19C). The polylithionite grains of the CAG are the ones with the highest averages of Zn (up to 2.51 wt.%). Zinc and manganese present good positive correlation (Fig. 19D), increasing together towards the shallower levels of the CAG, but decreasing sharply in the polylithionite from the pegmatite veins. Stands out the presence of ^{IV}Al in all samples, and the Al decrease and Si increase in the structure of polylithionite grains of the pegmatite veins compared to those in the CAG (Fig. 19E). The highest average of K is observed in the polylithionite from the polylithionite-rich PEG (9.27 wt.% K_2O). The lowest average of K is observed in the polylithionite from the amphibole-rich PEG

(7.48 wt.% K_2O), due to the occurrence of a set of crystals with low K (Fig. 19F). Rubidium was measured only in the low-K group samples from the amphibole-rich PEG, presenting an average of 3.92 wt.% Rb_2O. Polylithionite from the CAG have significant higher Rb_2O, ranging from 4.62 to 5.57 wt.%.

Tab. 3. EPMA data (in wt.%) of average polylithionite from the core albite-enriched granite (CAG) in different altimetric quotas (120, 140 and 160 m) and from the surface samples (~200-220 m) of the pegmatite veins (PEG): amphibole-rich, polylithionite-rich, and cryolite-rich.

	CAG 120 m[a]		CAG 140 m		CAG 160 m		Amphibole-rich PEG[b]		Polylithionite-rich PEG		Cryolite-rich PEG	
	Mean	2σ	Mean	2σ	Mean	2σ	Mean	2σ	Mean	2σ	Mean	2σ
	n = 11		n = 14		n = 20		n_1 = 32; n_2 = 15[c]		n = 13		n = 10	
SiO_2	53.32	1.71	52.79	1.70	52.34	1.71	55.82	3.77	56.16	2.63	55.05	1.24
TiO_2	0.10	0.06	0.12	0.06	0.13	0.05	0.10	0.23	0.09	0.16	0.13	0.22
UO_2	n.a.	-	n.a.	-	n.a.	-	1.76*	4.14	1.04	0.06	1.01	0.09
Al_2O_3	12.49	0.58	12.63	0.71	12.40	0.65	12.22	1.35	12.61	0.42	12.42	0.38
$HREE_2O_3$	n.a.	-	n.a.	-	n.a.	-	0.07	0.13	0.12	0.15	0.08	0.07
$LREE_2O_3$	n.a.	-	n.a.	-	n.a.	-	0.09	0.17	0.14	0.13	0.10	0.12
FeO	7.55	2.02	6.37	1.88	6.08	1.48	5.86	3.83	7.31	2.97	8.50	1.24
MnO	0.22	0.09	0.34	0.13	0.24	0.38	0.15	0.19	0.12	0.18	0.16	0.11
ZnO	1.14	0.33	1.21	0.43	2.51	0.72	0.54	0.61	0.25	0.18	0.72	0.20
Li_2O[d]	5.75	0.49	5.60	0.49	5.47	0.49	6.47	1.08	6.57	0.75	6.25	0.36
Na_2O	0.02	0.04	0.04	0.13	0.01	0.04	0.06	0.09	0.09	0.07	0.10	0.05
K_2O	8.57	0.41	8.06	0.38	8.24	0.24	7.48	2.74	9.27	0.48	9.01	0.20
Rb_2O	4.62	0.65	5.57	0.00	5.46	0.04	3.92	3.63	n.a.	-	n.a.	-
F	6.40	0.68	6.70	0.00	7.53	0.65	9.18	1.10	9.26	0.48	8.92	0.37
$F=O_2$	2.70	0.29	2.82	0.00	3.17	0.28	-3.86	0.46	3.90	0.20	3.76	0.16
Total	97.51	1.71	96.60	1.19	97.23	1.82	97.73	4.32	103.03	1.22	98.69	1.39
Structural formula based on 11 Oxygens (a.p.f.u.)												
Si^{4+}	3.877	0.035	3.874	0.034	3.860	0.023	3.951	0.071	3.919	0.049	3.904	0.029
Ti^{4+}	0.006	0.004	0.006	0.004	0.007	0.003	0.006	0.012	0.005	0.009	0.007	0.012
$^{IV}Al^{3+}$	0.123	0.035	0.126	0.034	0.140	0.023	0.052	0.060	0.081	0.049	0.096	0.029
$\sum^{IV}$	4.006	0.004	4.006	0.004	4.007	0.003	4.008	0.022	4.005	0.009	4.007	0.012
U^{4+}							0.028	0.066	0.016	0.001	0.016	0.001
$^{VI}Al^{3+}$	0.947	0.027	0.966	0.035	0.938	0.028	0.968	0.066	0.957	0.018	0.942	0.020
$HREE^{3+}$							0.002	0.004	0.003	0.005	0.002	0.003
$LREE^{3+}$							0.002	0.004	0.003	0.003	0.003	0.003
Fe^{2+}	0.207	0.060	0.176	0.056	0.169	0.045	0.157	0.108	0.193	0.083	0.227	0.035
Mn^{2+}	0.014	0.006	0.021	0.008	0.015	0.024	0.009	0.012	0.007	0.011	0.009	0.006
Zn^{2+}	0.062	0.019	0.066	0.025	0.136	0.040	0.026	0.035	0.013	0.010	0.038	0.011
Li^{+}	1.681	0.099	1.652	0.100	1.621	0.094	1.838	0.193	1.842	0.145	1.782	0.071
$\sum^{VI}$	2.911	0.046	2.881	0.046	2.880	0.053	3.031	0.098	3.034	0.057	3.019	0.046
Na^{+}	0.003	0.006	0.005	0.018	0.001	0.005	0.008	0.012	0.012	0.009	0.014	0.007
K^{+}	0.795	0.030	0.755	0.030	0.775	0.024	0.675	0.231	0.825	0.036	0.815	0.023
Rb^{+}	0.216	0.031	0.263	0.007	0.259	0.008	0.085	0.213				
$\sum^{XII}$	1.014	0.039	1.023	0.026	1.035	0.032	0.767	0.079	0.837	0.038	0.829	0.025
OH^{-}[e]	0.527	0.159	0.446	0.043	0.244	0.160	0.009	0.041	0.001	0.010	0.012	0.040
F^{-}	1.473	0.159	1.554	0.043	1.756	0.160	2.053	0.167	2.044	0.072	2.001	0.069
Mn/Mn+Fe	0.063	0.015	0.107	0.026	0.076	0.116	0.050	0.057	0.034	0.045	0.039	0.026
K/Rb	1.69	0.24	1.31	0.06	1.37	0.04	1.62	0.97				
LREE/HREE							2.73	7.34	2.96	9.51	1.82	3.32

[a]Costi (2000). [b]Paludo et al. (2018). [c]Analyses with Rb_2O determination. [d]LiO_2 calculated after Tindle and Webb (1990), [e]Calculated. Abbreviations: n = number of samples, n.a = not analyzed. *The mean value of 1.76 wt.% UO_2 includes two main groups, one averaging 0.61 wt.% UO_2 (n = 24) and the other with an average of 5.52 wt.% UO_2 (n = 8).

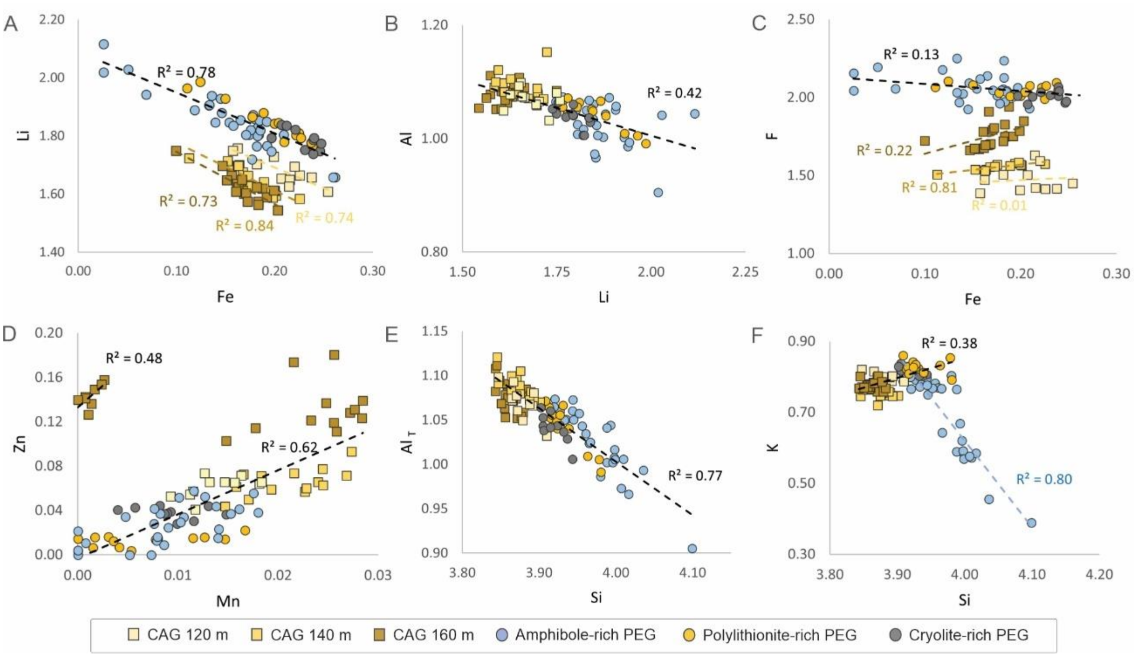

Fig. 19. Binary diagrams for polylithionite from the core albite-enriched granite (CAG) in different altimetric quotas (120 m, 140 m, 160 m), and pegmatite veins (PEG): amphibole-rich, polylithionite-rich, and cryolite-rich. (A) P versus F. (B) Si versus F. (C) P versus Si. (D) Th versus Si. (E) HREE versus Y. (F) HREE versus LREE. Concentrations are expressed in atoms per formula unit.

Uranium and REE contents were determined only in the polylithionite of the pegmatite veins. The lowest and highest contents of U occur in polylithionite from the amphibole-rich PEG: the predominant sample group (n = 24) have an average of 0.61 wt.% UO_2 and a smaller group (n = 8) presented an anomalous high U content, averaging 5.52 wt.% UO_2. The highest REE averages are in polylithionite of the polylithionite-rich PEG, with 0.12 wt.% $HREE_2O_3$ and 0.14 wt.% $LREE_2O_3$. The REE normalized pattern (Fig. 20A) in polylithionite of all the pegmatite vein types shows a strong M-type tetrad effect (Masuda *et al.*, 1987), and a positive Eu anomaly. In general, the LREE are more abundant, with LREE/HREE elemental ratios (Fig. 20B) of 1.82 in the cryolite-rich PEG, 2.73 in the amphibole-rich PEG and 2.96 in the polylithionite-rich PEG.

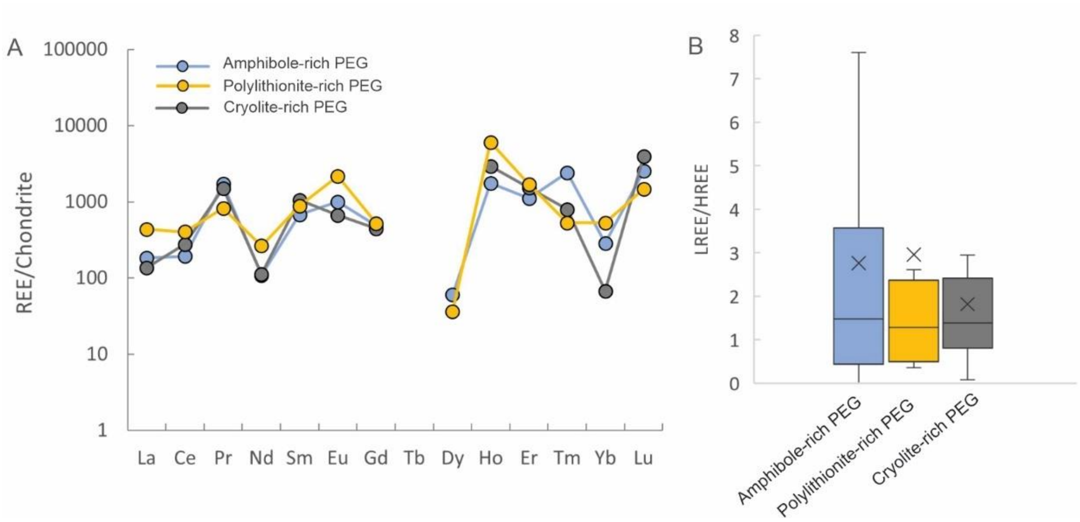

Fig. 20. REE distribution and LREE/HREE ratio in polylithionite of the pegmatite veins (PEG): amphibole-rich, polylithionite-rich, and cryolite-rich. (A) Patterns of REE distribution normalized to chondrite from Anders and Grevesse (1989). (B) Boxplots of the distribution of LREE/HREE ratio. Horizontal lines inside the boxes indicate median and the cross the mean values. The box marks the upper and lower quartile of the data, and the outer brackets mark 1.5 times the upper and lower quartile.

Pyrochlore

Representative compositions and structural formula of pyrochlore are presented in Table 4. In the CAG and BAG, the less altered pyrochlore varieties are U-Pb-LREE-rich pyrochlore (Tab. 4, crystal 1), the predominant variety in the CAG is the U-Pb-rich pyrochlore (Tab. 4, crystal 2), and the Fe-U-rich pyrochlore (Tab. 4, crystal 3), is predominant in the BAG and in the central portion of the CAG, where alteration was stronger close to the massive cryolite deposit [Hadlich *et al.* 2023b (submitted)].

Tab. 4. EPMA data (in wt.%) for pyrochlore: (1) U-Pb-LREE-rich pyrochlore; (2) LREE-U-Pb-rich pyrochlore; (3) Fe-U-rich pyrochlore; (4) LREE-Pb-rich pyrochlore, (5) U-Pb-rich pyrochlore, (6) Na-LREE-Pb-rich pyrochlore, (7) Na-Pb-LREE-rich pyrochlore; (8) Fe-U-Pb-rich pyrochlore, (9) HREE-Y-U-Pb-rich pyrochlore; (10) Ca-Fe-U-Pb-rich pyrochlore, (11) Ca-Fe-Pb-U-rich pyrochlore.

	CAG[1]		BAG[1]	Amphibole-rich PEG				Northern border pegmatite		Eastern border pegmatite	
Crystal	(1)	(2)	(3)	(4)	(5)	(6)	(7)	(8)	(9)	(10)	(11)
Nb_2O_5	46.20	40.10	31.93	47.45	33.20	43.53	43.66	34.36	24.32	34.29	33.83
Ta_2O_5	06.13	02.47	01.69	03.44	04.04	16.99	15.17	12.86	09.23	05.43	05.04
SiO_2	00.21	00.42	13.82	01.09	04.89	00.68	00.58	09.37	16.92	14.61	15.27
SnO_2	01.16	00.72	d.l.	01.53	00.78	01.12	00.62	00.23	00.24	00.57	00.61
TiO_2	01.05	00.92	01.45	00.84	d.l.	00.36	00.28	02.24	02.03	00.00	00.62
UO_2	02.81	06.97	12.64	00.04	08.86	01.13	01.13	06.40	09.76	04.79	05.72
ThO_2	01.77	00.49	00.84	00.73	00.35	00.90	00.98	00.00	00.66	01.44	00.91
Y_2O_3	01.00	00.13	00.25	00.73	00.24	00.68	00.65	01.72	03.53	00.18	00.29
$HREE_2O_3$	00.91	00.20	01.63	00.38	00.07	01.21	01.91	00.24	02.72	00.27	00.26

$LREE_2O_3$	07.02	04.08	01.88	03.87	00.26	07.14	08.05	00.66	00.89	02.32	03.28
$FeO^{(2)}$	00.69	01.70	03.24	00.38	00.00	00.23	00.04	02.70	01.90	03.27	03.76
CaO	01.42	01.04	00.34	00.96	00.00	00.77	01.48	00.61	00.19	02.48	01.78
MnO	00.11	00.23	00.49	02.60	01.33	00.08	00.00	00.12	00.29	00.45	00.41
PbO	07.23	13.98	00.02	23.72	28.87	09.01	05.27	22.00	14.91	05.53	04.93
Na_2O	00.76	00.18	00.31	00.24	00.21	02.80	04.42	d.l.	00.07	00.75	00.27
F	02.73	00.85	00.21	01.51	00.31	04.35	04.47	00.00	00.00	00.14	00.08
$F=O_2$	-01.15	-00.36	-00.09	-00.64	-00.13	-01.83	-01.88	-00.00	-00.00	-00.06	-00.03
Total	**80.08**	**74.18**	**69.34**	**91.00**	**83.29**	**89.18**	**86.86**	**93.29**	**85.49**	**76.22**	**76.70**
Structural formula based on a sum of 2 a.p.f.u. in the $^{[6]}$B site											
U^{4+}	0.052	0.154	0.189	0.033	0.185	0.020	0.020	0.094	0.135	0.067	0.078
Th^{4+}	0.034	0.011	0.013	0.036	0.008	0.016	0.018		0.009	0.021	0.013
Y^{3+}	0.044	0.007	0.009	0.033	0.012	0.028	0.028	0.061	0.117	0.006	0.009
$HREE^{3+}$	0.024	0.006	0.034	0.01	0.002	0.03	0.049	0.005	0.053	0.005	0.005
$LREE^{3+}$	0.213	0.149	0.046	0.117	0.009	0.203	0.235	0.016	0.021	0.054	0.073
Pb^{2+}	0.162	0.373		0.531	0.730	0.189	0.114	0.393	0.251	0.094	0.081
Fe^{2+}	0.048	0.141	0.182	0.027		0.015	0.003	0.150	0.099	0.172	0.193
Mn^{2+}	0.008	0.020	0.028	0.183	0.106	0.005		0.007	0.015	0.024	0.021
Ca^{2+}	0.127	0.111	0.024	0.086		0.064	0.127	0.044	0.013	0.167	0.117
Na^{+}	0.123	0.035	0.041	0.039	0.039	0.422	0.689		0.009	0.092	0.033
$\Sigma_{[8]A}$	**0.835**	**1.006**	**0.565**	**1.094**	**1.090**	**0.992**	**1.284**	**0.769**	**0.722**	**0.701**	**0.624**
Nb^{5+}	1.739	1.795	0.968	1.781	1.408	1.531	1.585	1.029	0.685	0.973	0.936
Ta^{5+}	0.139	0.067	0.031	0.078	0.103	0.360	0.332	0.232	0.157	0.093	0.084
Si^{4+}	0.017	0.042	0.929	0.091	0.460	0.053	0.047	0.622	1.057	0.919	0.937
Sn^{4+}	0.039	0.028		0.051	0.029	0.035	0.020	0.006	0.006	0.014	0.015
Ti^{4+}	0.066	0.069	0.073			0.021	0.017	0.111	0.095		0.029
$\Sigma_{[6]B}$	**2.000**	**2.000**	**2.000**	**2.000**	**2.000**	**2.000**	**2.000**	**2.000**	**2.000**	**2.000**	**2.000**
O^{2-}	4.878	5.328	3.580	5.305	5.061	4.855	5.320	4.068	3.759	3.617	3.504
F^{-}						0.071	0.137				
OH^{-}	1.122	0.672	2.420	0.695	0.939	1.074	0.543	1.932	2.241	2.383	3.498
Σ_X	**6.000**	**6.000**	**6.000**	**6.000**	**6.000**	**6.000**	**6.000**	**6.000**	**6.000**	**6.000**	**6.000**
F-	0.721	0.268	0.046	0.398	0.091	1.000	1.000			0.027	0.016
OH^{-}	0.279	0.732	0.954	0.602	0.909			1.000	1.000	0.973	0.984
Σ_Y	**1.000**	**1.000**	**1.000**	**1.000**	**1.000**	**1.000**	**1.000**	**1.000**	**1.000**	**1.000**	**1.000**
Nb/Ta	12.519	26.957	31.336	22.914	13.633	4.257	4.780	4.440	4.378	10.482	11.152
Fe/Mn	6.064	7.169	6.567	0.145	0	2.949		22.838	6.524	7.219	9.019
LREE/ HREE	8.875	24.833	1.352	11.700	4.500	6.766	4.795	3.200	0.396	10.800	14.600

[1]Hadlich et al. 2023b (submitted). [2]Total Fe as FeO. Abbreviations: d.l. = below detection limit.

In the amphibole-rich PEG, remnants of LREE-Pb-rich pyrochlore (Tab. 4, crystal 4) are surrounded by U-Pb-rich pyrochlore (Tab. 4, crystal 5), with reactive contact. The loss of LREE is accompanied by decreasing F (Fig. 21A) and relative increase of Pb (Fig. 21B). With the advancement of alteration occurs the progressive loss of Pb and relative U enrichment (Fig. 21C). This relatively Pb-U-Si enriched hydrothermal phase is the predominant pyrochlore variety in the amphibole-rich PEG. However, in grains with advanced alteration also occur remaining portions of heterogeneous pyrochlore graduating from Na-Pb-LREE-rich pyrochlore (Tab. 4, crystal 6) in the center to Na-LREE-Pb-rich pyrochlore (Tab. 4, crystal 7) in the border. Despite its occurrence in a highly hydrothermally altered context, these pyrochlore varieties present high amounts of LREE (up to 8.05 wt.% $LREE_2O_3$) and F (up to 4.47 wt.% F) and a trend of Na enrichment up to 4.42 wt.% Na_2O (Fig. 21D).

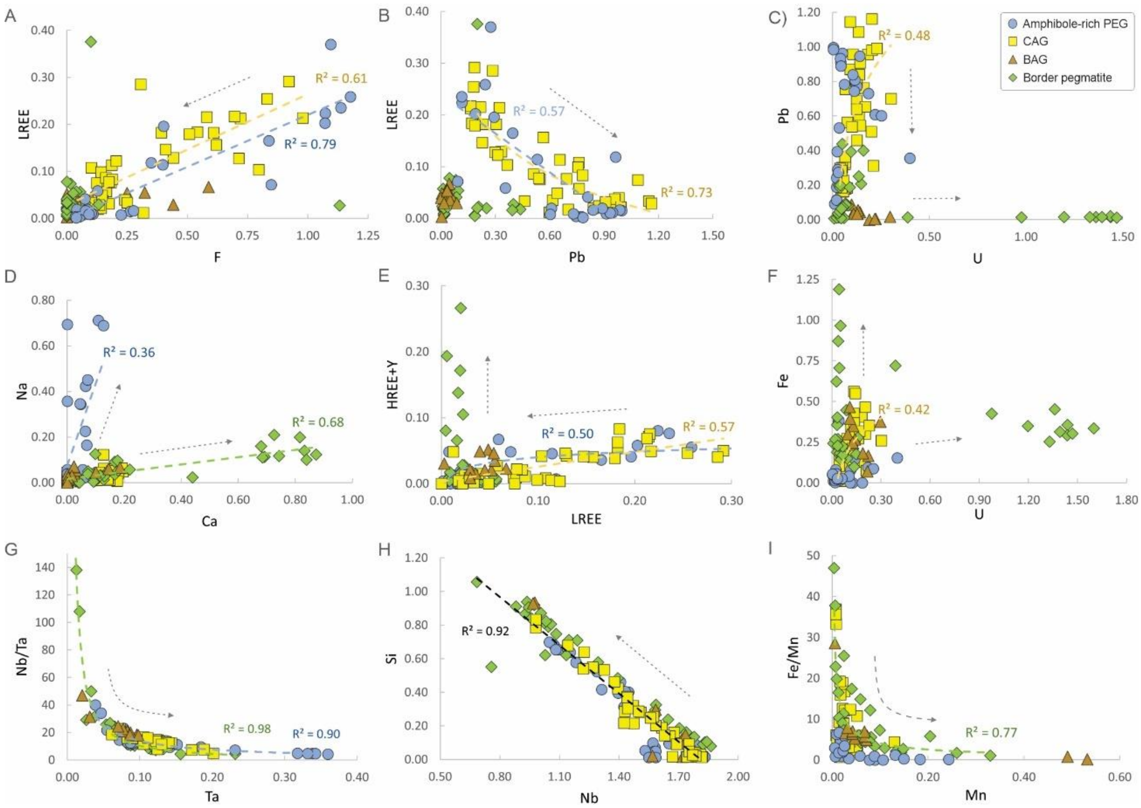

Fig. 21. Binary diagrams for pyrochlore from the CAG and BAG [Hadlich et al., 2023b (submitted)], amphibole-rich pegmatite vein (PEG), and border pegmatites. (A) LREE versus F. (B) LREE versus Pb. (C) Pb versus U. (D) Na versus Ca. (E) HREE+Y versus LREE. (F) Fe versus U. (G) Nb/Ta versus Ta. (H) Si versus Nb. (I) Fe/Mn versus Mn. Concentrations are expressed in atoms per formula unit. Arrows indicate the direction of hydrothermal alteration.

In the highly altered pyrochlore grains from the northern border pegmatite occur relicts of hydrothermal Fe-U-Pb-rich pyrochlore (Tab. 4, crystal 8), and HREE-Y-U-Pb-rich pyrochlore (Tab. 4, crystal 9), which stands out for the incorporation of HREE (up to 2.72 $HREE_2O_3$) and Y (up to 3.53 wt.% Y_2O_3) (Fig. 21E). In the eastern border pegmatite, incipiently to moderate altered pyrochlore grains are Ca-Fe-U-Pb-rich pyrochlore (with high Si, ~14 wt.% SiO_2, Tab. 4, crystal 10) and Ca-Fe-Pb-U-rich pyrochlore (~15 wt.% SiO_2, Tab. 4, crystal 11). These varieties present a Ca concentration ranging from 1.78 to 2.48 wt.% CaO, which is higher than the Ca content in the pyrochlore of the amphibole-rich PEG (up to 1.48 wt.% CaO) and is correspondent to the Ca content of the less altered grains in the CAG. In the borders and microfractures of all these grains with irregular and reactive contact, as well as spread in the surrounding matrix, occurs a hydrothermal non-stoichiometric Ca-U-rich pyrochlore

(Tab. 5, crystal 1), with incorporation of up to 34.56 wt.% UO_2 and 4.71 wt.% CaO (Fig. 21C, D, F).

Tab. 5. EPMA data (in wt.%) for hydrothermal phases associated with pyrochlore alteration: (1) Ca-U-rich pyrochlore; (2) U-HREE-Y-Th-rich silicate; (3) LREE-rich fluoride; (4) HREE-Y-U-rich silicate; (5) HREE-U-Y-rich silicate; and (6) LREE-rich fluoride.

Facies	Eastern border pegmatite	Amphibole-rich PEG		Northern border pegmatite		
Crystal	(1)	(2)	(3)	(4)	(5)	(6)
Nb_2O_5	22.26	01.48	02.62	03.19	02.79	00.26
Ta_2O_5	00.27	00.38	01.05	00.00	01.17	00.00
P_2O_5	00.00	01.82	00.00	01.07	06.80	00.00
SiO_2	00.93	09.51	00.10	14.76	16.24	00.03
UO_2	34.56	01.57	00.30	29.23	12.48	00.31
ThO_2	00.16	35.69	00.49	00.25	07.69	00.05
ZrO_2	00.00	00.40	d.l.	00.00	00.00	00.00
Y_2O_3	00.17	03.02	00.22	15.09	13.34	00.28
$HREE_2O$	00.00	02.59	00.29	10.88	07.92	00.18
$LREE_2O$	00.30	00.59	55.40	00.33	00.40	56.26
FeO[1]	01.75	01.28	00.17	00.50	00.27	00.00
CaO	04.71	00.88	d.l.	00.32	00.48	00.27
MnO	00.41	d.l.	d.l.	d.l.	00.26	00.16
PbO	00.31	01.16	d.l.	02.71	01.09	00.00
Na_2O	00.37	d.l.	d.l.	00.00	d.l.	00.00
F	00.00	04.33	08.65	02.61	02.80	07.13
$F=O_2$	-00.00	-01.82		-01.10	-01.18	
Total	**67.10**	**63.03**	**69.67**	**79.87**	**72.62**	**64.93**

[1]Total Fe as FeO. Abbreviations: d.l. = below detection limit.

The average Nb/Ta ratio in pyrochlore (Fig. 22A) is lower in the northern border pegmatite (10.2), in the CAG (12.9) and in the amphibole-rich PEG (13.7), while the highest Nb/Ta averages occur in the BAG (23.5) and in the eastern border pegmatite (42.5). The Nb/Ta ratio variation have strong negative correlation with Ta content (Fig. 21G) in all subfacies, and no significant correlation with Nb. Extreme low values of Nb/Ta ratio (<5) occur only in the Na-enriched hydrothermal pyrochlore of the amphibole-rich PEG. Niobium presents strong negative correlation with Si (Fig. 21H) in all samples analyzed. The average Fe/Mn ratio (Fig. 22B) is higher in the pyrochlore grains of the northern border pegmatite (14.9) and lower in those of the amphibole-rich PEG (2.0). The Fe/Mn distribution is directly proportional to the Mn content in pyrochlore (Fig. 21I). The average LREE/HREE ratio (Fig. 22C) in pyrochlore grains are lowest in the northern border pegmatite (1.0). and highest in the CAG (10.2). Accordingly, the average normalized REE pattern (chondrite of Anders and Grevesse, 1985) (Fig. 23) shows that the pyrochlore of the CAG have the highest absolute content of LREE and the lowest HREE content. The exception is the pyrochlore of the eastern border pegmatite, which presents the lowest LREE and HREE contents.

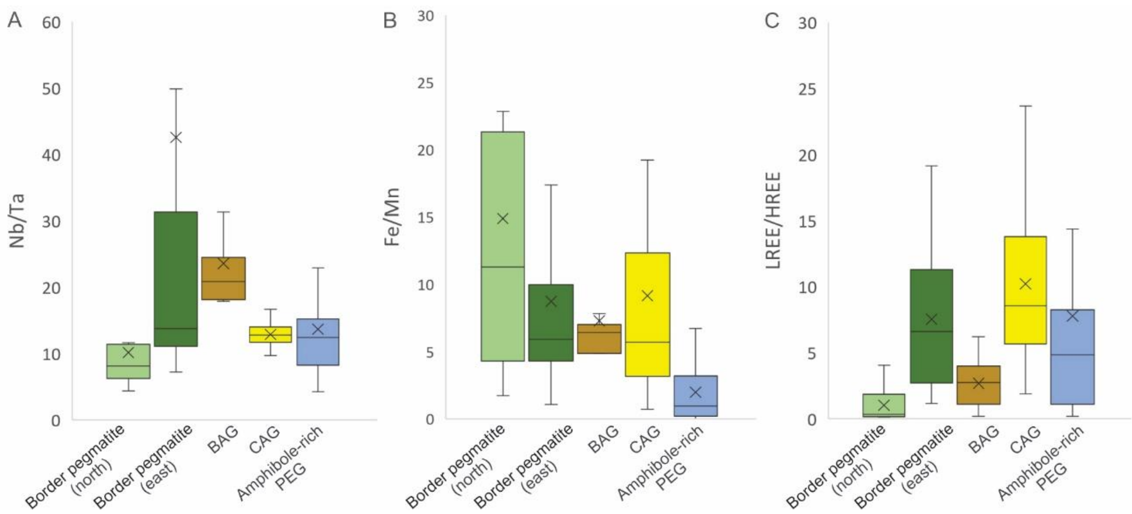

Fig. 22. Boxplots of the distribution of (A) Nb/Ta, (B) Fe/Mn, and (C) LREE/HREE ratios in pyrochlore of the CAG and BAG [(Hadlich et al., 2023b (submitted)], amphibole-rich pegmatite vein (PEG), and border pegmatites. Horizontal lines inside the boxes indicate median and the cross the mean values. The box marks the upper and lower quartile of the data, and the outer brackets mark 1.5 times the upper and lower quartile.

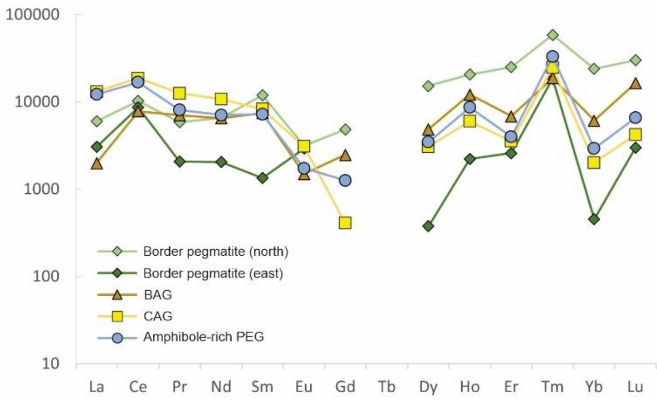

Fig. 23. Patterns of REE distribution (normalized to chondrite from Anders and Grevesse, 1989) in pyrochlore of the CAG and BAG [Hadlich et al., 2023b (submitted)], amphibole-rich pegmatite vein (PEG), and border pegmatites.

Columbite

In the CAG and BAG, the collapse of the pyrochlore phase led to the formation of columbite. Representative compositions and structural formula of columbite are presented in Table 6. In the CAG the predominant species is a Mn-Fe-rich columbite (Tab. 6, crystal 1). In the BAG it is relatively common a U-Mn-Fe-rich columbite (Tab. 6, crystal 2) with up to 3.64 wt.% UO_2. In the amphibole-rich PEG the only variety of columbite is Mn-Fe-rich columbite (Tab. 6, crystals 3, 4), which occur filling cavities and microfractures in hydrothermal pyrochlore or surrounding its remnants. In the eastern border pegmatite, it was not observed columbite, differently of the northern border pegmatite, in which occurs Fe-Mn-rich columbite (Tab. 6, crystal 5), and U-Fe-Mn-rich columbite (Tab. 6, crystal 6), with up to 1.28 wt.% UO_2, surrounding hydrothermal pyrochlore remnants.

Tab. 6. EPMA data (in wt.%) for columbite: (1) Mn-Fe-rich columbite; (2) U-Mn-Fe-rich columbite; (3, 4) Mn-Fe-rich columbite; (5) Fe-Mn-rich columbite; and (6) U-Fe-Mn-rich columbite.

Facies	CAG[1]	BAG[1]	Amphibole-rich PEG		Northern border pegmatite	
Crystal	(1)	(2)	(3)	(4)	(5)	(6)
Nb_2O_5	66.74	65.61	73.87	73.32	66.51	65.04
Ta_2O_5	03.32	05.72	01.46	04.67	06.65	08.08
SiO_2	00.51	00.57	00.05	00.13	00.20	00.25
SnO_2	d.l.	d.l.	00.30	00.00	00.00	00.00
TiO_2	02.57	02.36	00.84	00.43	00.15	01.61
UO_2	01.15	03.64	00.73	00.28	00.32	01.28
ThO_2	d.l.	00.18	00.04	00.00	d.l.	00.03
Y_2O_3	00.12	00.07	d.l.	00.09	00.00	d.l.
$HREE_2O_3$	00.00	00.62	00.15	00.23	00.26	00.45
$LREE_2O_3$	00.30	00.41	00.47	00.13	00.27	00.23
FeO[2]	15.33	16.13	13.38	14.27	03.62	08.53
CaO	00.40	d.l.	00.00	00.00	d.l.	00.51
MnO	06.70	04.92	07.84	07.07	17.54	11.74
PbO	00.81	00.06	00.81	00.00	00.00	01.23
Na_2O	d.l.	00.04	00.03	00.00	00.02	00.03
F	d.l.	d.l.	00.00	00.00	00.00	00.00
$F{=}O_2$	-00.00	-00.00	-00.00	-00.00	-00.00	-00.00
Total	**97.89**	**99.74**	**99.99**	**100.63**	**95.44**	**99.04**
Fe^{2+}	0.725	0.771	0.632	0.676	0.181	0.415
Mn^{2+}	0.321	0.238	0.375	0.339	0.886	0.578
$\mathbf{\Sigma_{[8]A}}$	**1.046**	**1.009**	**1.036**	**1.015**	**1.067**	**0.993**
Nb^{5+}	1.704	1.693	1.886	1.875	1.792	1.709
Ta^{5+}	0.051	0.089	0.023	0.072	0.108	0.128
Si^{4+}	0.029	0.032	0.003	0.007	0.012	0.015
Sn^{4+}			0.007			
Ti^{4+}	0.109	0.101	0.036	0.018	0.007	0.070
U^{4+}	0.014	0.046	0.009	0.004	0.004	0.017
Th^{4+}		0.002	0.001			
Y^{3+}	0.004	0.002		0.003		
$HREE^{3+}$		0.011	0.003	0.004	0.005	0.008
$LREE^{3+}$	0.006	0.008	0.010	0.003	0.004	0.005
Pb^{2+}	0.012	0.001	0.012			0.019
Ca^{2+}	0.025					0.032
Na^{+}		0.004	0.004		0.002	0.004
$\mathbf{\Sigma_{[8]B}}$	**1.954**	**1.991**	**1.964**	**1.985**	**1.933**	**2.007**
O^{2-}	5.576	5.694	5.837	5.895	5.738	5.693
OH^{-}*	0.424	0.306	0.163	0.105	0.262	0.307
$\mathbf{\Sigma_{X}}$	**6.000**	**6.000**	**6.000**	**6.000**	**6.000**	**6.000**
Nb/Ta	33.413	19.041	83.732	26.087	16.617	13.366
Fe/Mn	2.260	3.236	1.685	1.993	0.204	0.717
LREE/ HREE		0.756	3.746	0.672	0.772	0.602

[1]Hadlich et al. 2023b (submitted). [2]Total Fe as FeO. *Calculated. Abbreviations: d.l. = below detection limit.

The average Fe/Mn ratio (Fig. 24A) of columbite decreases in the direction BAG (2.8) > CAG (2.7) > amphibole-rich PEG (2.0) > northern border pegmatite (0.5). The Fe/Mn ratio distribution presents better correlation with Mn (Fig. 25A) than with Fe (Fig. 25B). In general, manganese shows good negative correlation with Fe (Fig. 25C). The average Nb/Ta ratio of columbite (Fig. 24B) is lower in the northern border pegmatite (14.8) and higher in the amphibole-rich PEG (41.7). The Nb/Ta ratio distribution in columbite is directly associated with variations in Ta content (Fig. 25D). Silicon substitutes for Nb (Fig. 25E) up to 0.015 apfu in the B-site of columbite, and columbite of the pegmatites presents considerably lower Si content than in the CAG and BAG. The average LREE/HREE ratios in columbite are lower in the northern border pegmatite (0.8) and in the BAG (1.9). This ratio is higher in the columbite of the CAG (3.10) and the amphibole-rich PEG (3.14), in which presents good positive correlation with LREE content (Fig. 25F). The average REE normalized patterns (Fig. 26) shows that the REE absolute contents in columbite are lower in the CAG, followed by the amphibole-rich PEG, the BAG, and the northern border pegmatite.

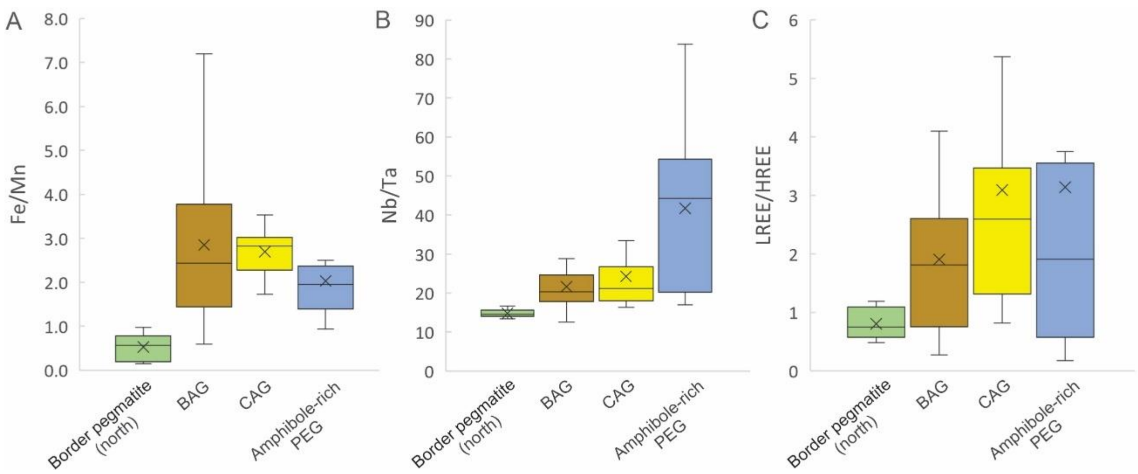

Fig. 24. Boxplots of the distribution of (A) Fe/Mn, (B) Nb/Ta, and (C) LREE/HREE ratios in columbite of the CAG and BAG [Hadlich et al., 2023b (submitted)], amphibole-rich pegmatite vein (PEG), and northern border pegmatite. Horizontal lines inside the boxes indicate median and the cross the mean values. The box marks the upper and lower quartile of the data, and the outer brackets mark 1.5 times the upper and lower quartile.

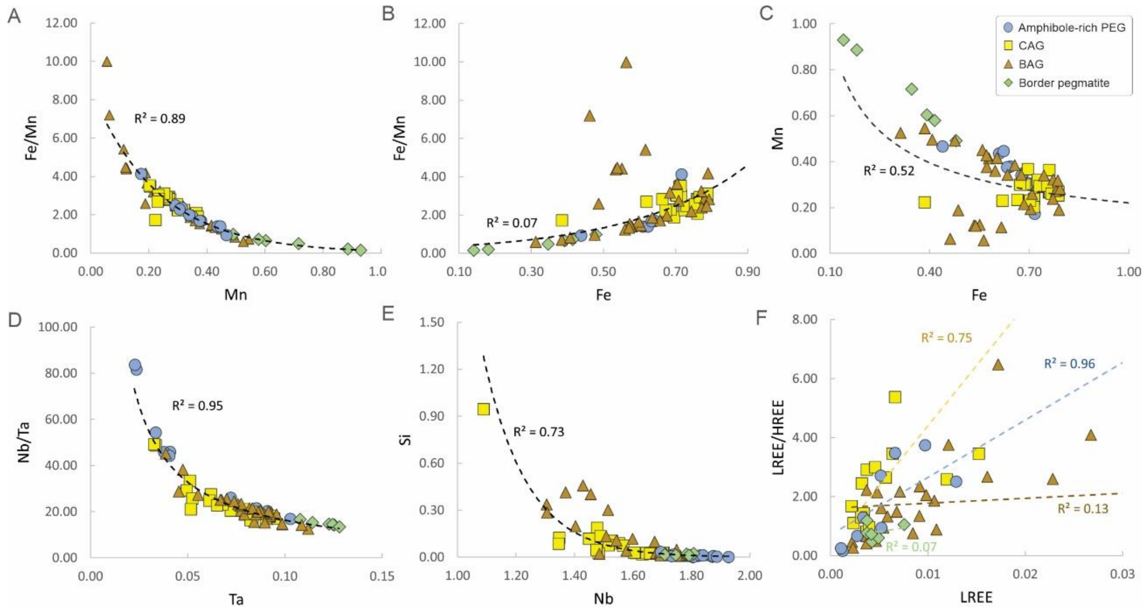

Fig. 25. Binary diagrams for columbite from the CAG and BAG [Hadlich et al., 2023b (submitted)], amphibole-rich pegmatite vein (PEG), and border pegmatites. (A) Fe/Mn versus Mn. (B) Fe/Mn versus Fe. (C) Mn versus Fe. (D) Nb/Ta versus Ta. (E) Si versus Nb. (F) LREE/HREE versus LREE. Concentrations are expressed in atoms per formula unit.

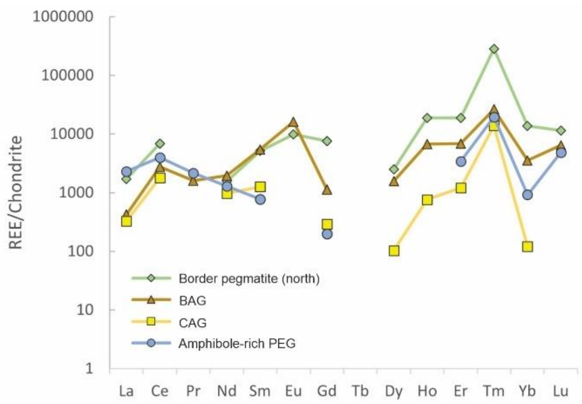

Fig. 26. Patterns of REE distribution (normalized to chondrite from Anders and Grevesse, 1989) in columbite of the CAG and BAG [Hadlich et al., 2023b (submitted)], amphibole-rich pegmatite vein (PEG), and northern border pegmatite.

Other products of pyrochlore alteration

In the amphibole-rich PEG, in addition to columbite and galena, the most frequent secondary mineral associated with pyrochlore alteration are: (i) U-HREE-Th-rich silicate (Tab. 4, crystal 2), with up to 35.68 wt.% ThO_2, 9.51 wt.% SiO_2, and 4.33 wt.% F, occurring disseminated into columbite grains; and, (ii) LREE-rich fluorides (Tab. 4, crystal 3), which occur partially replacing pyrochlore grains, surrounding remnants of hydrothermal pyrochlore, and included in columbite. In the northern border pegmatite, associated with columbite occur silicates enriched in HREE, Y, U and Th with different proportions of these cations (Tab. 4, crystals 4, 5), with up to 29.23 wt.% UO_2, 30.71

wt.% ThO_2, 15.09 wt.% Y_2O_3, and 10.88 wt.% $HREE_2O_3$. Silica content ranges from 14.76 to 19.60 wt.% SiO_2, Nb from 2.79 to 9.10 wt.% Nb_2O_5 and F from 1.45 to 2.80 wt.% F. It also occurs LREE-rich fluorides (Tab. 4, crystal 6) and galena.

The REE normalized pattern (Fig. 27A) for (HREE-Y-U-Th)-rich silicates from the northern border pegmatites and the amphibole-rich PEG are similar to those of the CAG and BAG, with a flat HREE pattern. The silicates with the highest HREE are in the northern border pegmatite and the silicates with the lowest HREE are in the amphibole-rich PEG. The REE normalized pattern for LREE-rich fluoride (Fig. 27B) is remarkably similar in all the rocks.

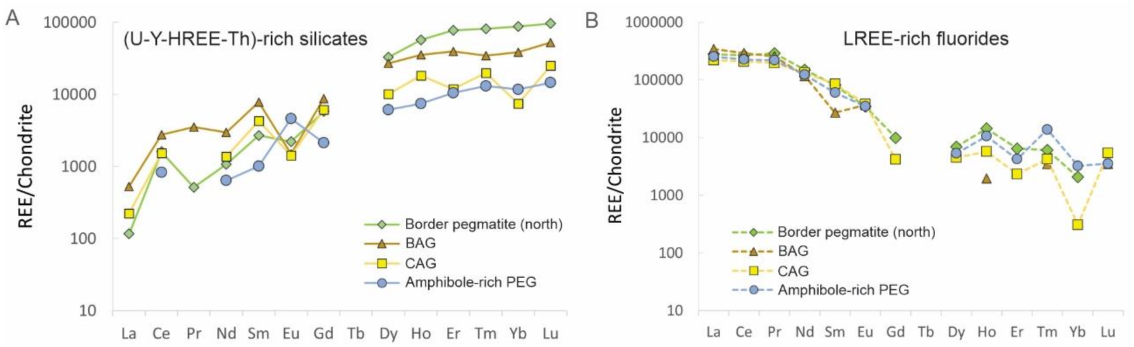

Fig. 27. Average patterns of REE distribution (normalized to chondrite from Anders and Grevesse, 1989) in secondary (A) (U-Y-HREE-Th)-rich silicate and (B) LREE-rich fluoride associated with pyrochlore alteration in the CAG and BAG [Hadlich et al., 2023b (submitted)], in the amphibole-rich pegmatite vein (PEG), and in the northern border pegmatite.

Secondary pyrochlore, columbite, LREE-rich fluorides, silicate phases and galena were formed in the early hydrothermal stage. In the amphibole-rich PEG, the columbitized borders of the grains are intensely dissolved, and columbite has irregular and reactive contact with hydrothermal cryolite, quartz and iron oxide, which also fills columbite cavities through the grain. These features and minerals were generated during the late hydrothermal stage. The late hydrothermal stage in the border pegmatites also affected all previously formed minerals, corroded the mineral borders and was responsible for the crystallization of fluorite and quartz in the borders and cavities of pyrochlore and columbite grains.

Whole rock geochemical data

Trends of compositional variation

Whole-rock data is presented for the CAG and BAG, for the pegmatitic CAG and for the border pegmatites with focus in strategical major (Tab. 7) and trace elements (Tab. 8). Pegmatite veins (amphibole-rich, polylithionite-rich, and cryolite-rich) analyses were also added to the compilation, but cautiously interpretated due to the inherent difficulties in getting representative chemical analyses from pegmatite samples.

Tab. 7. Major element analyses (wt.%) for the CAG, BAG, border pegmatite, and the pegmatite veins (PEG): amphibole-rich, polylithionite-rich, and cryolite-rich.

	CAG		BAG		Border pegmatite[1]		Amphibole-rich PEG[2]		Polylithionite-rich PEG[2]		Cryolite-rich PEG[2]	
	Mean	2σ	Mean	2σ	Mean	2σ	Mean	2σ	Mean	2σ	Mean	2σ
	n = 64		n = 57		n = 5		n = 23		n = 11		n = 10	
SiO_2	69.95	5.81	72.31	11.60	73.39	3.98	66.92	6.82	58.35	18.22	12.41	24.55
TiO_2	0.03	0.11	0.03	0.05	0.06	0.06	0.03	0.03	0.06	0.06	0.02	0.03
Al_2O_3	12.80	1.98	12.19	3.93	11.92	1.37	11.29	4.39	10.90	4.26	18.34	11.62
CaO	0.28	1.39	0.73	1.86	0.79	0.86	0.06	0.10	0.14	0.27	0.60	3.17
FeO[3]	2.21	1.12	2.67	4.49	1.95	1.14	3.63	2.74	4.79	2.87	0.24	0.61
MgO	0.02	0.10	0.03	0.12	0.03	0.01	0.01	0.01	0.04	0.02	0.05	0.11
MnO	0.06	0.08	0.06	0.12	0.02	0.01	0.09	0.08	0.16	0.16	0.02	0.02
K_2O	4.26	1.14	4.33	2.86	5.92	1.35	2.87	2.98	5.95	3.15	0.11	0.25
Na_2O	5.55	3.23	3.87	3.20	2.95	1.05	6.62	3.15	3.13	4.26	33.01	21.06
P_2O_5	0.03	0.07	0.05	0.26	0.03	0.01	0.27	0.65	1.03	3.48	0.09	0.33
LOI	1.70	1.27	1.39	2.30	1.15	0.37	2.30	1.73	3.64	2.86	14.40	10.02
F	2.31	4.49	0.59	1.49	0.32	0.36	3.09	4.63	5.69	6.04	35.00	19.31
F=O	-0.97	1.89	-0.25	0.63	-0.13	0.15	-1.30	1.95	-2.39	2.54	-14.74	8.13
Total	97.91	2.84	97.88	4.56	98.39	0.67	95.88	4.93	91.48	9.38	99.54	29.91
Fe/Mn	46.64	37.61	53.59	49.62	79.58	31.55	42.66	20.94	34.44	31.90	10.91	28.61
A/CNK	1.28	0.24	1.39	0.36	1.24	0.13	1.19	0.37	1.22	0.41	0.54	0.11
A/NK	1.33	0.41	1.53	0.57	1.34	0.06	1.20	0.37	1.24	0.42	0.55	0.06

[1]Lengler (2016), [2]Paludo et al. (2018). [3]Total Fe as FeO.

Tab. 8. Trace element analyses for the CAG, BAG, border pegmatite, the pegmatite veins (PEG): amphibole-rich, polylithionite-rich, and cryolite-rich, and the pegmatitic CAG.

	CAG		BAG		Border pegmatite[1]		Amphibole-rich PEG[2]		Polylithionite-rich PEG[2]		Cryolite-rich PEG[2]		Pegmatitic CAG	
	Mean	2σ	Mean	2σ	Mean	2σ	Mean	2σ	Mean	2σ	Mean	2σ	Mean	2σ
	n1 = 64; n2 = 133		n1 = 57; n2 = 72		n = 5		n = 23		n = 11		n = 10		n = 75	
Nb^{5+}	1578.88	2101.09	1354.75	1092.53	693.20	111.04	998.48	14.60	913.00	385.23	159.60	365.31	1979.65	1443.57
Ta^{5+}	444.69	2656.00	231.34	311.97	90.88	22.68	237.57	129.92	194.95	224.58	3.37	8.60	441.72	390.08
Sn^{4+}	1722.63	3336.91	1445.47	2203.54	92.20	20.25	988.35	111.76	751.27	708.93	262.50	658.59	2459.14	2353.19
U^{4+}	293.04	382.26	311.34	321.27	261.32	127.98	290.67	232.01	71.41	104.82	1.80	4.39	511.91	518.60
Th^{4+}	831.09	2670.89	714.90	1734.86	386.80	220.56	1779.22	936.88	1223.45	1867.51	193.48	560.56	5026.85	7318.83
Zr^{4+}	5218.30	4153.28	4676.56	6759.94	5624.00	1505.69	5886.09	4853.42	939.45	1991.83	25.90	42.98	6753.56	7356.04
Hf^{4+}	317.01	305.31	306.42	324.07	242.20	88.42	635.74	484.63	158.27	314.14	18.27	65.11	n.a.	-
Y^{3+}	1546.98	6076.98	1129.73	5962.74	1617.00	2573.24	2121.13	4978.48	3773.36	7840.26	1690.30	6238.30	1870.29	2779.06
$HREE^{3+}$	352.52	1082.90	746.28	5149.99	1098.22	1506.67	2110.42	3601.88	2915.28	4824.19	1449.73	4761.78	n.a.	-
$LREE^{3+}$	498.29	2909.07	377.03	1837.77	679.28	443.23	320.21	392.97	688.30	1535.92	1062.06	6339.04	n.a.	-
Bi^{3+}	39.08	192.07	14.49	39.74	n.a.	-	10.83	12.21	53.76	165.80	49.48	166.43	n.a.	-
Zn^{2+}	942.00	1068.84	1036.32	4424.25	838.00	1385.34	1860.43	3924.70	3675.45	4609.66	1060.00	1528.86	n.a.	-
Pb^{2+}	1133.67	2715.57	994.68	3204.83	345.60	377.67	1100.87	2496.62	1928.27	4976.10	5360.90	9795.87	n.a.	-
Sr^{2+}	34.96	59.09	25.75	81.31	27.00	11.27	42.57	31.35	271.64	239.91	185.40	213.31	n.a.	-
Be^{2+}	30.74	64.93	18.71	47.31	21.80	12.15	118.74	794.42	591.27	2234.32	11.60	33.23	n.a.	-

Li^+	668.46	518.77	226.49	1096.46	6.00	3.39	880.65	711.35	7938.18	4234.05	192.50	415.71	n.a.	-
Rb^+	6184.52	3821.08	4456.58	5374.03	1000.00	0.00	1000.00	0.00	1000.00	0.00	316.80	693.24	6192.30	5680.93
Cs^+	92.61	147.28	25.66	78.12	13.70	10.27	112.82	134.08	275.00	234.08	6.79	15.59	n.a.	-
S^-	120.89	376.29	256.07	393.27	n.a.	-	417.39	1361.35	827.27	2895.64	7730.00	26155.27	n.a.	-
Nb/Ta	9.69	33.06	7.93	3.16	7.75	0.72	4.45	1.97	7.18	10.42	40.41	18.60	4.88	3.22
Th/U	3.90	8.71	1.79	3.94	1.51	0.35	6.61	4.55	17.96	32.57	152.96	507.82	17.87	98.71
LREE/ HREE	1.20	1.79	1.17	1.62	1.09	0.68	0.32	0.61	0.25	0.22	0.39	0.83	n.a.	-

[1]Lengler (2016). [2]Paludo et al. (2018). For the pegmatite veins and border pegmatite, maximum detection limit is 1,000 ppm for Nb, Sn, Rb and REE, 2,000 ppm for Th, and 10,000 ppm for Pb, Y and Zr.

There are three general trends of compositional variation between the analyzed subfacies and associated pegmatites. In the type-A trend (Fig. 28) occurs the decreasing of Ca and K average contents concomitantly to the increasing of Na, F, S, and Pb in the direction border pegmatite > BAG > CAG > amphibole-rich PEG > polylithionite-rich PEG > cryolite-rich PEG. The border pegmatite stands out by its higher averages of Ca (0.78 wt.%) and K (5.91 wt.%). In its turn, the cryolite-rich PEG presents extremally high average F (~35 wt.%), Na (~34 wt.%), S (~7,730 ppm) and Pb (4,845 ppm). The exception to the type-A trend is the polylithionite-rich PEG, presenting relatively higher average K (5.94 wt.%) and lower Na (3.1 wt%). Other exception is the higher S average content in BAG (207 ppm) relative to CAG (120 ppm).

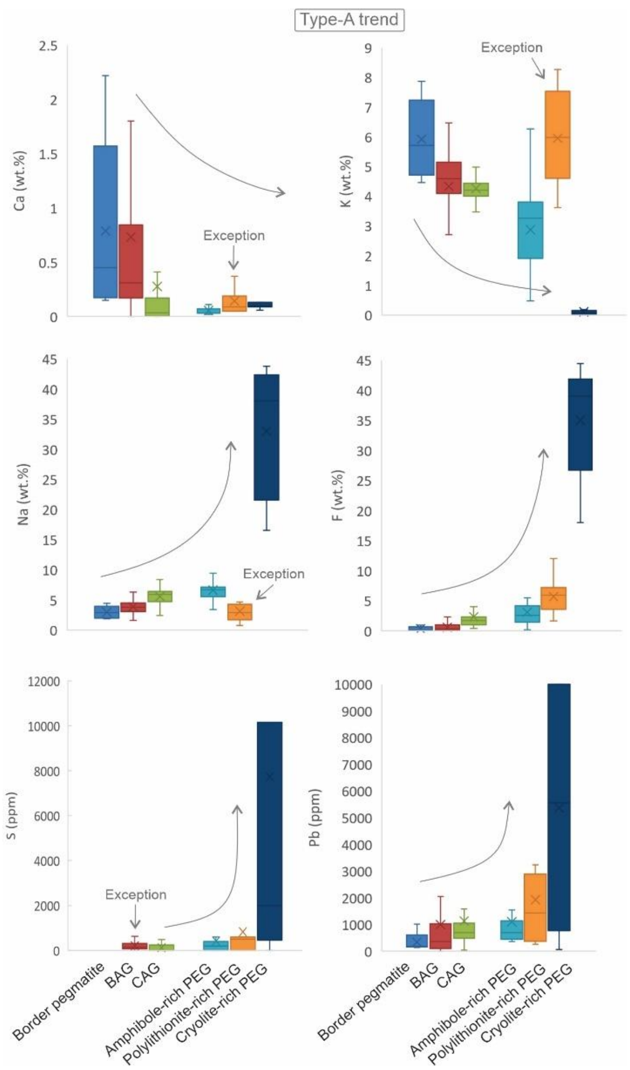

Fig. 28. Boxplots of the distribution of Type-A geochemical trend (Ca, K, Na, F, S, Pb) for the CAG, BAG, pegmatitic CAG, and pegmatite veins (PEG): amphibole-rich, polylithionite-rich, and cryolite-rich. Horizontal lines inside the boxes indicate median and the cross the mean values. The box marks the upper and lower quartile of the data, and the outer brackets mark 1.5 times the upper and lower quartile. Gray arrows indicate the main trend direction.

In the type-B trend (Fig. 29) is observed the increasing of Y, Li, Be and Zn in the direction CAG > amphibole-rich PEG > polylithionite-rich PEG followed by a decrease of these elements in the cryolite-rich PEG. This pattern highlights the considerably enrichment of polylithionite-rich PEG in Y (3,773 ppm), Li (7,938 ppm), Be (591 ppm), and Zn (3,675 ppm). The border pegmatite contains higher concentrations of Y and Be relative to the BAG.

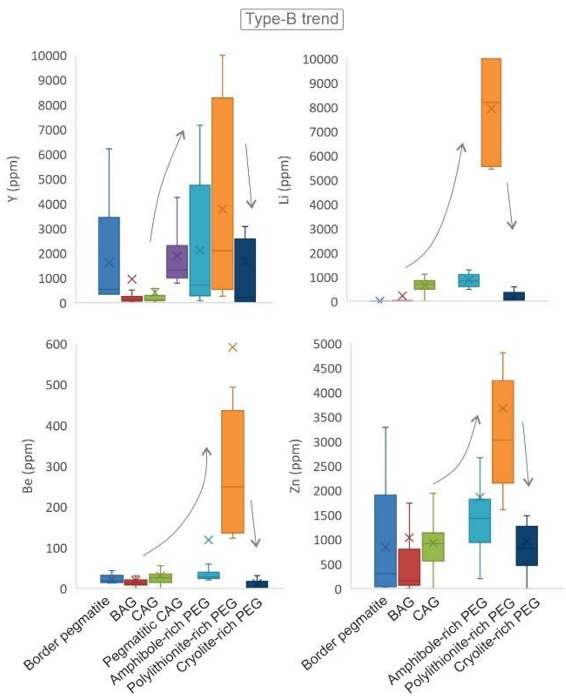

Fig. 29. Boxplots of the distribution of Type-B geochemical trend (Y, Li, Be, Zn) for the BAG, CAG, border pegmatite, pegmatitic CAG, and the pegmatite veins (PEG): amphibole-rich, polylithionite-rich, and cryolite-rich. Horizontal lines inside the boxes indicate median and the cross the mean values. The box marks the upper and lower quartile of the data, and the outer brackets mark 1.5 times the upper and lower quartile. Gray arrows indicate the main trend direction.

The type-C trend (Fig. 30) shows the increase of Nb, Ta, U, Th, Zr and Sn in the direction border pegmatite > BAG > CAG > pegmatitic CAG, followed by a decrease of these elements in the direction amphibole-rich PEG > polylithionite-rich PEG > cryolite-ich PEG. Thus, the pegmatitic CAG presents the highest average values of Nb (1978 ppm), Ta (451 ppm), Rb (6192 ppm), U (511 ppm), Th (5026 ppm), Zr (6753 ppm) and Sn (2459 ppm). The cryolite-rich PEG has the lowest concentration for these elements. The exception to this trend is the Zr average content of the border pegmatite (5624 ppm Zr), which is higher than the albite-enriched granite averages (4708 ppm Zr in the BAG and 4606 ppm Zr in the CAG). The border pegmatite also presents the lower Sn contents (92 ppm Sn). Considering the analytical constraints, it can be cautiously affirmed that the Rb contents also align with the type-C trend, exhibiting the highest average value in the pegmatitic CAG (6,026 ppm) and undergoing a significant decline in the cryolite-rich PEG (240 ppm).

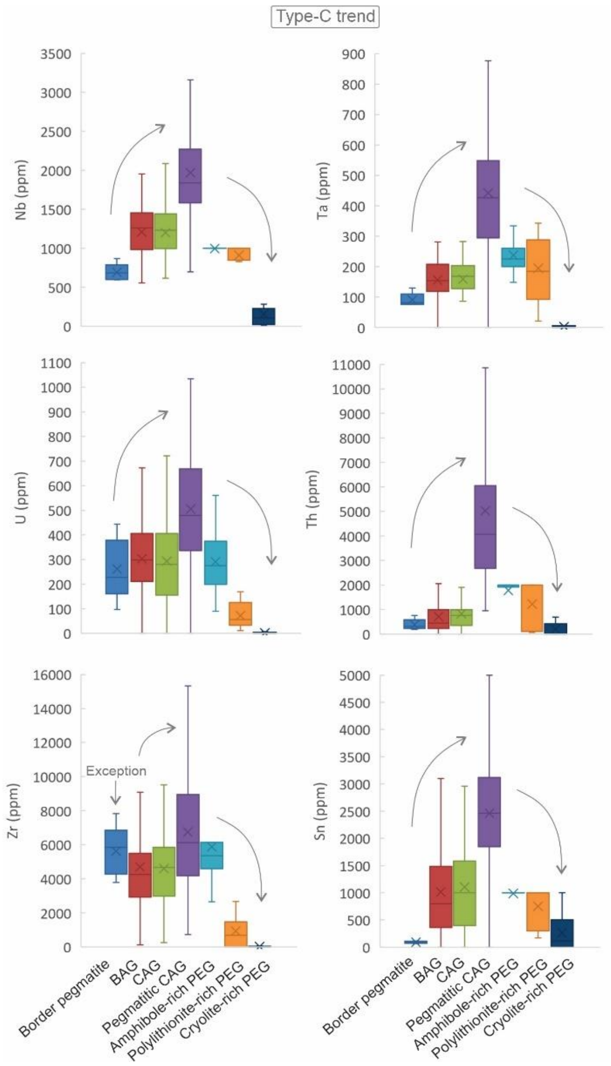

Fig. 30. Boxplots of the distribution of Type-C geochemical trend (Nb, Ta, U, Th, Zr, Sn) for the BAG and CAG, the border pegmatite, the pegmatitic CAG, and the pegmatite veins (PEG): amphibole-rich, polylithionite-rich, and cryolite-rich. Horizontal lines inside the boxes indicate median and the cross the mean values. The box marks the upper and lower quartile of the data, and the outer brackets mark 1.5 times the upper and lower quartile. Gray arrows indicate the main trend direction.

REE contents and patterns

All the investigated rocks present different degrees of fractionation, regarding the chondrite normalized REE distribution pattern (Fig. 31A). The CAG presents the lowest fractionation, with high LREE (average 598 ppm) and the lowest HREE content (average 397 ppm). The BAG and border pegmatite have similar REE signatures, but the border pegmatite have slightly higher concentrations (679 ppm LREE, 1,098 ppm HREE) than the BAG (473 ppm LREE, 1,015 ppm HREE). The pegmatite veins have lower LREE and higher HREE relative to the host rock. Among the pegmatite vein, there is a decrease of LREE and HREE in the direction polylithionite-rich PEG (688 ppm LREE, 2,915 ppm HREE) > amphibole-rich PEG (320 ppm LREE, 2,110 ppm

HREE) > cryolite-rich PEG (59 ppm LREE, 833 ppm HREE). The general REE pattern for amphibole-rich PEG and polylithionite-rich PEG presents a well-defined M-type tetrad effect (Masuda *et al.*, 1987). Despite the LREE and HREE concentration variations, the LREE/HREE average ratio (Fig. 31B) is remarkably similar in both the BAG (1.09), the border pegmatite (1.10) and in the CAG (1.13). The pegmatite veins present a LREE/HREE ratio significatively lower, with 0.32 in the amphibole-rich PEG, 0.25 in the polylithionite-rich PEG and 0.27 in the cryolite-rich PEG.

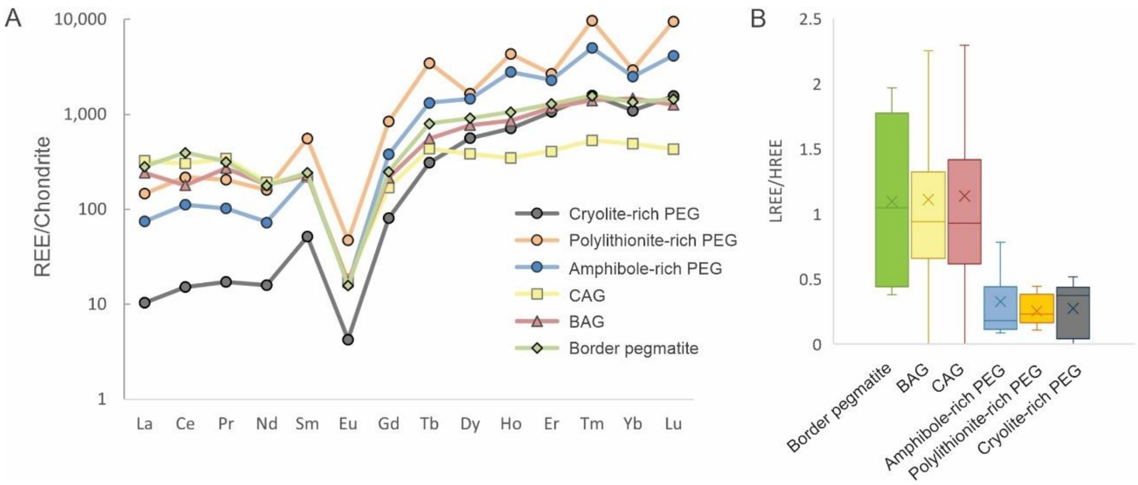

Fig. 31. REE data for the CAG, BAG, border pegmatite and pegmatite veins: amphibole-rich, polylithionite-rich, and cryolite-rich. (A) Chondrite-normalized (Anders and Grevesse, 1989) REE average patterns. (B) LREE/HREE ratio.

Chemical correlations

In the amphibole-rich PEG and polylithionite-rich PEG, there is a good positive correlation of LREE and U (Fig. 32A). In the cryolite-rich PEG, LREE content is not correlated with U, but presents good correlation with Ca (Fig. 32B), as it is also observed in the amphibole-rich PEG and polylithionite-rich PEG. The HREE elements are strongly correlated with P (Fig. 32C) in the amphibole-rich PEG and polylithionite-rich PEG, but not in the cryolite-rich PEG. In both the amphibole-rich PEG and in the border pegmatite there is a good negative correlation between FeO and SiO_2 + Al_2O_3 (Fig. 32D), and a good positive correlation between FeO and MnO (Fig. 32E). The polylithionite-rich PEG does not have correlations regarding Fe content. In the cryolite-rich PEG is observed good positive correlation of FeO versus K_2O (Fig. 32F) and of K_2O versus Rb (Fig. 32G). In the polylithionite-rich PEG, stands out the good correlation between Be and Zn (Fig. 32H). Better correlations are obtained for polylithionite-rich PEG, amphibole-rich PEG and cryolite-rich PEG considering Zn +

Pb + Zn versus S (Fig. 32I). Fluorine content presents good negative correlation with sulfur (Fig. 32J) and with Si (Fig. 32K), especially in the cryolite-rich PEG. No correlations were observed between Na and Ca (Fig. 32L).

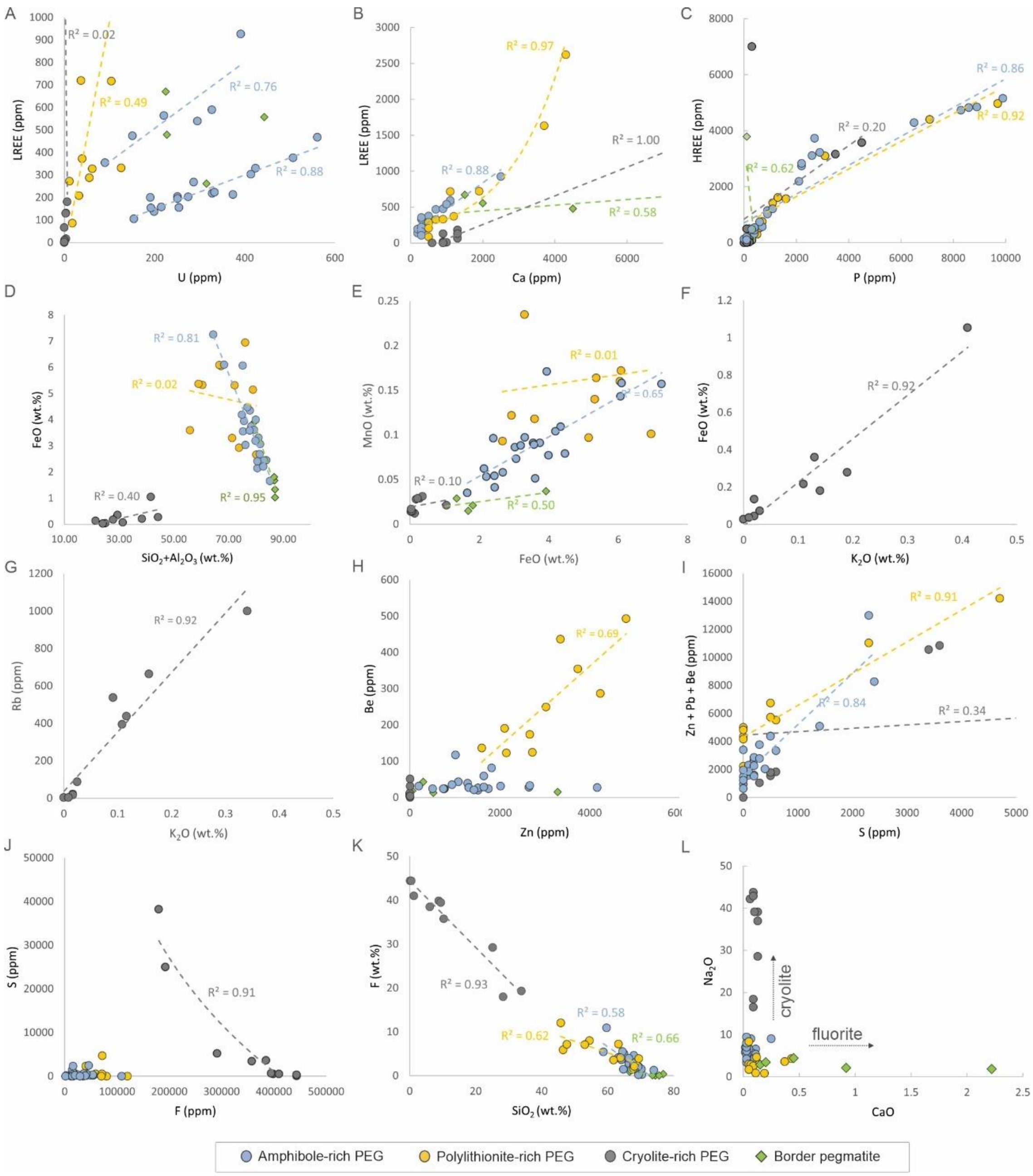

Fig. 32. Binary diagrams for bulk rock of the pegmatite veins (PEG): amphibole-rich, polylithionite-rich, cryolite-rich; and of the border pegmatite. (A) LREE versus U. (B) LREE versus Ca. (C) HREE versus P. (D) FeO versus SiO_2 + Al_2O_3. (E) MnO versus FeO. (F) Fe versus K_2O. (G) Rb versus K_2O. (H) Be versus Zn. (I) Zn + Pb + Be versus S. (J) S versus F. (K) F versus SiO_2. (L) Na_2O versus CaO.

Discussion

Paragenetic evolution in the magmatic and hydrothermal stages in the studied pegmatites

Several important minerals record the behavior of trace elements in the melt. For example, with fractionation, the grades of Li, Rb and Cs of K-feldspar and of muscovite increase, and the Nb/Ta ratio in the columbite group minerals decrease (Černý 1989). Depending on the general composition of the melt, there is a competition for the Al and alkalis of the melt between the HFSE and the fluxing elements (Van Lichtervelde *et al.* 2010). In the set of pegmatites studied, 28 minerals were identified, and a crystallization order (Fig. 33) was established for the magmatic and hydrothermal phases identified.

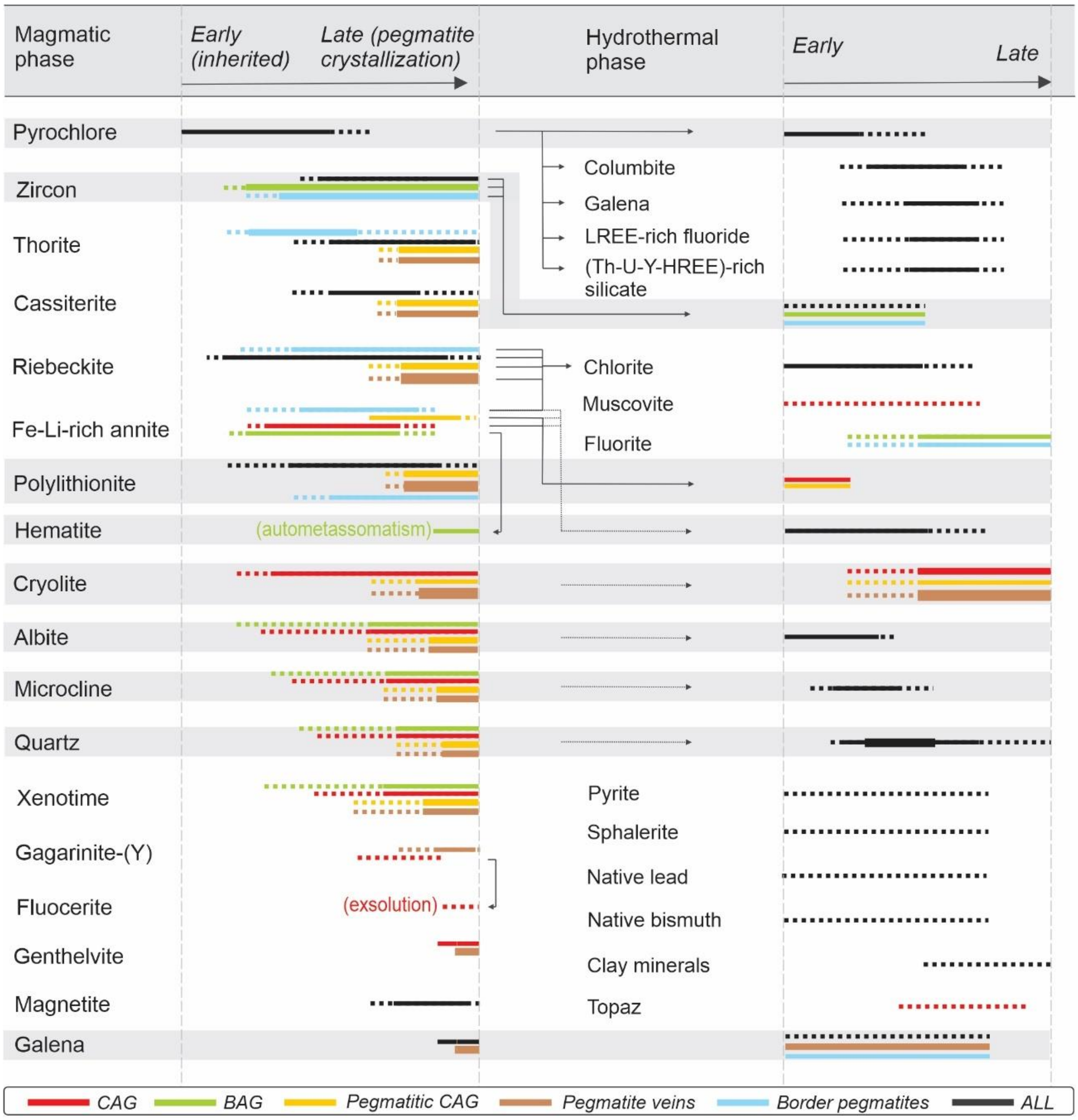

Fig. 33. Paragenetic evolution in the CAG and BAG and associated pegmatites. Thickness of the lines are indicative of abundance of the mineral. The precursor minerals for the most important

replacement reactions are indicated by arrows. Black lines represent all the subfacies and pegmatite types not specified by colored lines.

Magmatic phases

***Early magmatic stage**:* During the initial magmatic stage of the albite-enriched granite, LREE and U contents were incorporated in the primary U-Pb-LREE-rich pyrochlore [Hadlich *et al.* 2023b (submitted)]. This early magmatic phase is considered to have been inherited by the pegmatite veins and the border pegmatites, where it concentrated most of the Ca, LREE, and U bulk contents. The relative Ca enrichment in the pyrochlore from the eastern border pegmatite probably reflects the Ca fractionation process in the early magmatic stages of the albite-enriched granite crystallization rather than with influences of the external host rocks. The onset of crystallization for zircon, thorite, and cassiterite was postponed due to the high F content in the system. Thus, in the albite-enriched granite, the formation of these minerals occurred at a later stage, in a melt previously depleted in LREE and U (Hadlich *et al.* 2019). In the pegmatite veins, the presence of anomalous large crystals of primary thorite and their relative enrichment in HREE and Y provide evidence of their formation from a melt that was further enriched in these elements during the pegmatitic stage. On the other hand, the occurrence of U-rich primary thorite in the border pegmatite indicates an earlier formation for this mineral.

***Early to late magmatic stage**:* The crystallization of riebeckite, Fe-Li-rich annite and polylithionite buffered the Fe content within the albite-enriched granite melt from its early magmatic stage. In the BAG, these iron-rich silicate minerals have almost completely disappeared due to an autometasomatic process (Costi *et al.* 2000, 2009), resulting in abundant hematite formation. Riebeckite also contributed to buffer the Na and F content, especially in the BAG and border pegmatites. Due to the continuous enrichment of F in the residual melt, riebeckite of the amphibole-rich PEG has significatively higher averages of F (2.12 wt.%) compared to riebeckite from the CAG (0.67 wt.% F). The richness in F and consequent rejection of Fe due to the Fe-F avoidance effect (Rosenberg and Foit 1977; Munoz 1984), favored the entrance of Na, K and Si in the riebeckite of the amphibole-rich PEG. In the literature, few sodic amphiboles can be found as F-rich as those in the studied pegmatite veins, such as in the Katugin cryolitic deposit (Transbaikalia, Russia), where the sodic amphibole has up to 2.5 wt.% F (Sharygin *et al.* 2016).

Polylithionite partially buffered the K, Li and F contents in the albite-enriched granite melt, from the early to the late magmatic stage. Due to the progressive enrichment of HREE, Li, Si, and F in the melt, the composition of polylithionite became increasingly enriched in these elements from the CAG to the amphibole-rich PEG, culminating in the highest concentrations within the polylithionite-rich PEG. According to Breiter (2023), the elemental content in micas (not just rare metals) is more influenced by the minerals that crystallized prior to them than by the mineral's inherent structure. Consequently, when polylithionite formed within the cryolite-rich PEG, the continuous and gradual buffering of Li and F through earlier polylithionite and cryolite formation might have reduced their availability in the fluid of the cryolite-rich PEG. The average K/Rb elemental ratio in polylithionite from the CAG (ranging from 1.31 to 1.69) and the amphibole-rich PEG (1.62) are among the lowest in the literature. According to Costi (2000), these ratios indicate that the melt from which the polylithionite of the CAG crystallized exhibited an extreme fractionation, comparable only to those observed in pegmatitic bodies mineralized in Rb and Cs, such as the pegmatites from Tanco (Černý *et al.* 1985) (Fig. 33). The continuous and abundant crystallization of Rb-bearing K-feldspar and polylithionite (Costi, 2000) in the CAG (and likely also in the pegmatitic CAG) could elucidate the decline in Rb availability when polylithionite crystallized in the amphibole-rich PEG.

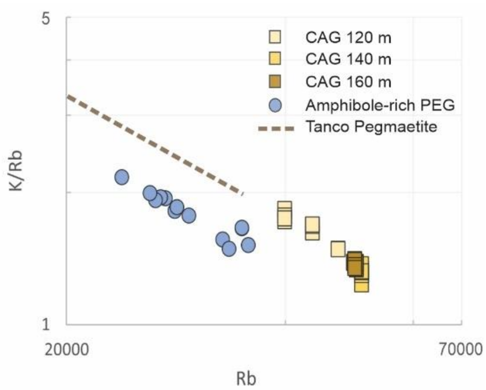

Fig. 34. Rb (ppm) *versus* K/Rb diagram for polylithionite from the amphibole-rich pegmatite vein (PEG) (this study) and from different elevations of the CAG (Costi, 2000). The dotted line represents the trend of the micas from the Tanco pegmatite (Cerny et al., 1985).

Additionally, during the intermediate to late magmatic stage, abundant albite, microcline, and quartz formed in all studied rocks. In the CAG, pegmatitic CAG, and pegmatite veins, cryolite I continuously buffered the Na and F content of the melt, achieving maximum modal values in the cryolite-rich PEG.

***Late magmatic stage**:* The elements Y, HREE, and P were concentrated within the residual melt, and they were subsequently incorporated into late disseminated xenotime within the CAG. Furthermore, these elements abundantly formed large xenotime crystals in both the amphibole-rich and polylithionite-rich PEG. Regarding the xenotime found in the CAG, F substitutes O, generating PO_3F tetrahedra (Bastos Neto *et al.* 2012). This caused the shortening of xenotime structure and favored the incorporation of larger cations such as Er and Yb at the expense of Y, also making the incorporation of LREE much more difficult. This deduction is corroborated by the lower F content and higher Y content observed in xenotime of the polylithionite-rich PEG. In the cryolite-rich PEG, HREE were predominantly incorporated into gagarinite-(Y). In contrast, no primary phases bearing HREE and Y were identified in the border pegmatites.

During the late magmatic stage in the CAG, residual LREE was buffered by gagarinite-(Y). In the gagarinite-(Y) of the CAG, the presence of fluocerite-(Ce) inclusions were attributed to the exsolution of LREE with ionic radii larger than that of Sm. This exsolution was triggered by the contraction of the initial gagarinite structure due to cooling (Pires *et al.* 2006). Consequently, this process resulted in the formation of the host gagarinite-(Y) (rich in HREE and poor in LREE), and the exsolved phase fluocerite-(Ce) (rich in LREE). However, such LREE exsolution was not observed in the gagarinite-(Y) of the cryolite-rich PEG. This absence can be attributed to insufficient LREE content to destabilize its structure during cooling, given that it formed from a previously LREE-depleted melt. Conversely, gagarinite derived from the cryolite-rich PEG showed higher average concentrations of HREE, Na and F. Therefore, the compositions of the gagarinite crystals indicate that they crystallized at various stages within the granite-pegmatite system, reflecting the evolving composition (including the REE pattern) of the surrounding environment, which progressively became enriched in HREE, Na, and F. Genthelvite was preceded by the crystallization of polylithionite and early quartz I and formed before the hydrothermal cryolite II. Thus, genthelvite and galena were likely the last magmatic minerals to crystallize, incorporating the Zn, Be, Pb and S contents within the residual melt of the pegmatite veins.

Hydrothermal phases

Early hydrothermal stage: In the early hydrothermal stage riebeckite alteration extensively forms chlorite, and the remaining Na is probably incorporated in secondary albite. In the CAG and pegmatitic CAG, the Fe-Li-rich annite break down forms polylithionite and hematite. Stands out that the hydrothermal fluids were responsible for major Fe redistribution in albite-enriched granite system, resulting in the precipitation of significant hematite in all analyzed rocks. The abundance of Fe, Pb, Zn, Bi, and S in the hydrothermal fluid allowed precipitation of pyrite, sphalerite, galena, native lead, and native bismuth. Hydrothermal albite, microcline and quartz attests the richness in Na, K and Si in the hydrothermal fluid since the early hydrothermal stage.

Pyrochlore alteration*:* In the amphibole-rich PEG, the incorporation of notably contents of Na, LREE and F in the hydrothermal Na-LREE-Pb-rich pyrochlore, implies that the hydrothermal fluids that affected the amphibole-rich PEG possessed a composition with greater Na and F activity. This is attested by the abundant formation of both pegmatitic and hydrothermal cryolite in the amphibole-rich PEG. In addition, the absence of association with predominantly U-enriched silicates (observed in the CAG and BAG) may be explained by the preferential incorporation of U in other pegmatitic minerals, as the commonly surrounding polylithionite (average of 1.72 wt.% UO_2).

In its turn, in the border pegmatites, the high availability of Ca in the hydrothermal fluids, attested by the formation of abundant hydrothermal fluorite, led to the formation of Ca-enriched hydrothermal pyrochlore. In the eastern border pegmatite, the weaker alteration of pyrochlore inhibited columbite formation. In the northern border pegmatite, the higher availability of HREE, Y and Mn in the hydrothermal fluid was responsible for the formation of secondary HREE-Y-enriched pyrochlore, (U)-Fe-Mn-rich columbite, and (Th, U, Y, HREE)-rich silicates.

Late hydrothermal stage: Both the magmatic and early hydrothermal phases were affected by residual late fluids further enriched in Na, F, and Si in the CAG and pegmatite veins, precipitating cryolite II and quartz II. In the BAG and border pegmatites, the residual fluid was enriched in Ca instead of Na, precipitating abundant hydrothermal fluorite. As the hydrothermal fluid gradually cooled, a series of successive processes took place, including oxidation, silicification, and clay mineral transformation, affecting the magmatic and early hydrothermal paragenesis (Ronchi *et al.* 2011).

The parental rock

In the fractional crystallization process, if the trace elements that are inherited in the melt at their source behave as perfectly incompatible in all resulting crystalline phases, then the pegmatites would carry an amplified signature of that trace element pattern. Through this signature, the origin of pegmatites can commonly be attributed to granites in which the source characteristics themselves are known and distinguishable (Černý *et al.* 2012). In the pegmatitic CAG and pegmatite veins, the anomalous concentration of key rare metals (Na, F, S, Pb, Y, Li, Be, Zn, Sr, Nb, Ta, HREE, Th, U) represent the amplified signature of the CAG, as observed in the geochemical trends of type-A, -B, and -C. Conversely, the border pegmatite presents the lowest average F and the highest average Ca. This is a key factor, along with pyrochlore chemistry, for concluding that these pegmatites represent one of the less evolved albite-enriched granite melts. The geochemical similarity and evolution pattern associated with BAG indicates that the border pegmatite is derived of the BAG magma.

Pegmatites migrate to different environments from those of their places of origin and, in the vast majority of cases, they lodge in structures external to its parent rock (Dill 2015). However, in Pitinga, the coherent geochemical evolution pattern and the outstanding similarity of the paragenesis of the host rock with that of the pegmatites, evidence that the host albite-enriched granite is also the parent rock of all pegmatite types studied: the miarolitic pegmatites, the pegmatite veins, the pegmatitic albite-enriched granite and the border pegmatites.

Fluorine role in magmatic-hydrothermal systems

The parental magma of highly evolved granites and pegmatites is commonly enriched in fluxing components such as F, Cl, Li, P and B, having the effect to reduce the viscosity and solidus of the melt, and increase H_2O solubility up to 30 wt.% (e.g., Thomas *et al.* 2005, 2012; Thomas and Davidson 2012). Flux elements also increase the solubility of elements that would otherwise precipitate as accessory minerals. These same flux elements facilitate the rapid growth of large and perfect silicate crystals (London and Morgan 2012). Despite that, flux elements abundance appears to be low in most pegmatites. Even the most chemically fractionated bodies contain <1 wt.% total B, P and F (Stilling *et al.* 2006), and simple pegmatites have much lower concentrations.

World-wide known fluorine-rich granitic pegmatites are the Quartz Creek, Colorado, with 100 to 6,000 ppm F (Staatz and Trites 1955); Pohjanma, Finland, with 2,000 ppm F (Haapala 1966); Bernic Lake, Manitoba, with 5,000 ppm F (Mulligan 1965); Mongolia, with 7,700 ppm F (Gundsambuu 1974); Mora, New Mexico, with 9,000 ppm F (Jahns 1953); and Ivigtut, Greenland, with 5,000 to 30,000 ppm F (Boggild 1953). In the albite-enriched granite, the average fluorine content reaches 2.31 wt.% F in the CAG, 3.09 wt.% F in the amphibole-rich PEG, 5.69 wt.% in the polylithionite-rich PEG, with the highest average content recorded in the cryolite-rich PEG at 35.00 wt.% F. Given these distinctive characteristics, the albite-enriched granite of Pitinga, along with its associated pegmatites, presents an unprecedented case. In both the CAG and its associated pegmatites, F played a significant role in enriching elements within Group I of the periodic table (Li, Na, K, Rb), and to a lesser extent, Cs. Furthermore, these formations exhibited abnormally elevated concentrations of REE, U, Th, Be, Zr, Nb, and Ta when compared to pegmatites found in the aforementioned locations.

The REE typically form complexes with alkalis and with F, and these migrate to the apical portions of granitic intrusions (Mineyev 1963). The HREE are more strongly complexed with F than the LREE (Wood 1990). This could explain the LREE-richness in the CAG, incorporated in the first minerals to crystallize (e.g. LREE-rich pyrochlore), and the HREE progressive enrichment towards the latest paragenesis of the albite-enriched granite and pegmatites (e.g. xenotime, gagarinite), as well as its occurrence in the residual F-rich hydrothermal fluid, responsible for the precipitation of secondary HREE-rich phases.

Furthermore, the study of Williams-Jones and Vasyukova (2023) evidenced the different effects of neutral and acidic water on pyrochlore alteration. While the neutralization of the weathering fluid facilitates the replacement of Na and Ca in the primary pyrochlore by various combinations of Ba, Sr, Ce, and K, the continued leaching of pyrochlore by acidic fluids leaves behind nothing more than a skeleton of Nb_2O_5. In the albite-enriched granite, the acidity of the hydrothermal fluids, and, therefore, the degree of alteration of pyrochlore, is mainly controlled by the concentration of F. This deduction can be extended to the other altered minerals of the albite-enriched granite and associated pegmatites.

Nb/Ta ratio behavior in magmatic-hydrothermal systems

Magmatic-hydrothermal processes involving fluids and hydrosaline melts play a critical role in Nb-Ta geochemical fractionation and HFSE enrichment in general (Ballouard *et al.* 2020). In the Nb/Ta versus Nb and Ta diagrams (Fig. 35A, B), the analyses presented in this work partially overlaps the bottom field of rare-metal A1-type granitoids of the compilation of Ballouard *et al.* (2020), including metasomatic rocks (e.g. greisens, albitites, skarns) related to these igneous rocks, and also present similar Nb/Ta proportions and Nb and Ta contents to the Ririwai arfvedsonite albite granite (Nigeria, Ogunleye *et al.* 2006) and the albitized portions of the Ivigtut alkali granite (Greenland, Goodenough *et al.* 2000). However, both CAG, BAG and pegmatitic CAG have several samples that go beyond this field, entering the magmatic-hydrothermal domain (Nb/Ta < 5) delimited by Ballouard *et al.* (2016) for peraluminous granites. Therefore, the albite-enriched granite from Pitinga presents Nb and Ta contents similar (or even higher) with the most fractionated peralkaline rare-metal A1-type granitoids worldwide but achieving an average Nb/Ta ratio significatively lower, especially in the pegmatitic CAG. This underscores the notable level of fractionation exhibited by the albite-enriched granite, which possesses a distinct pegmatitic composition of its own. The pegmatitic CAG and amphibole-rich PEG intensify this fractionation phenomenon. In contrast, the formation of polylithionite-rich PEG, cryolite-rich PEG, and the border pegmatites appear to implicate additional mechanisms beyond fractionation, which played a role in determining their Nb/Ta ratio.

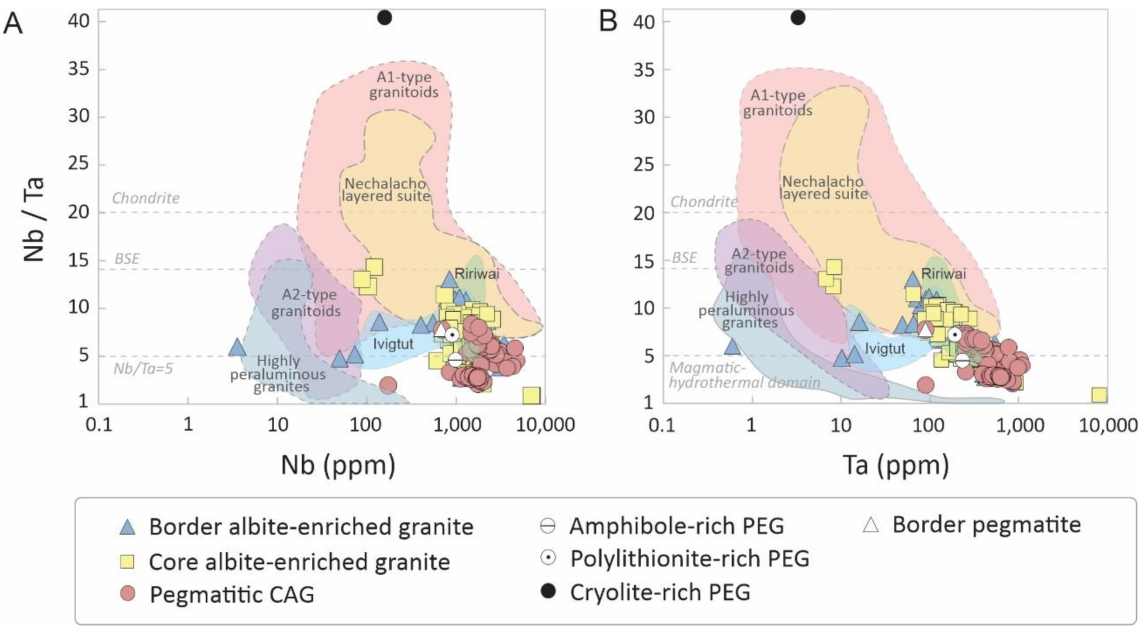

Fig. 35. Nb/Ta versus (A) Nb and (B) Ta content diagrams showing the whole-rock composition of the CAG and BAG, pegmatitic CAG and the average composition for the border pegmatite and pegmatite veins (PEG) varieties: amphibole-rich, polylithionite-rich and cryolite-rich. It is also indicated the general fields of highly peraluminous granites (Ballouard et al., 2016), A-type granitoids (Ballouard et al., 2020), and of the alkali to peralkaline Nechalacho layered suite (Canada, Möller and Williams-Jones, 2016), the Ririwai albite arfvedsonite granite (Nigeria, Ogunleye et al., 2006) and the Ivigtut alkali granite (Greenland, Goodenough et al., 2000). The dashed grey dashed line at Nb/Ta = 5 delimits the magmatic-hydrothermal domain defined by Ballouard et al. (2016) for highly peraluminous granites. Chondrite and bulk silicate Earth (BSE) values after Münker et al. (2003).

Emplacement of the host rock and the studied pegmatites

Pegmatites are placed relative to the available space created by geological processes. Consequently, they are closely interconnected both temporally and spatially with structural disturbances, often as a part of an orogenic event or even within the broader geodynamic evolution of a particular section of the crust and its underlying subcrustal region (Dill 2015).

Host rock

Bastos Neto *et al.* (2009, 2014) consider that the A-type magmatism in Pitinga evolved from a post-collisional extensional setting, likely in a within-plate scenario in which extensional and transtensional tectonic regimes dominated. In this context, the albite-enriched granite magma would have been related to the third step of the isotherm rise, which occurred when the mantle fluid ascended further into the crust promoting fenitization-type reactions (Martin 2006) in rocks previously enriched in Sn, and introduced elements such as F, Nb, Y, REE, and Th in anomalous concentrations.

Pegmatite veins

Due to its limited surface dimensions (2 x 1.5 km), the albite-enriched granite underwent relatively rapid cooling. The brittle structures in the CAG likely formed as a result of the final stages of the amalgamation of juvenile terrains. The vergence to NE of the contractional structures of the CAG is consistent with the expected orientation of the foreland structures in the Ventuari-Tapajós orogeny (Ronchi *et al.* 2019). The placement of the albite-enriched granite within the cold upper crust, combined with a low *solidus* temperature, allowed the formation of pegmatites. The structural characteristics exhibited by both the pegmatite veins and the host rock indicate that the albite-enriched granite crystallized at the same structural level where these pegmatites were stablished.

The presence of reverse fault planes and extension fractures, both with and without pegmatite, indicates that the fractures hosting the pegmatite veins did not form solely due to fluid pressure. Given that the CAG was positioned above the critical crustal depth, the reverse fault planes were not the primary sites for the pegmatite veins emplacement; instead, the horizontal extension fractures associated with these planes played a more significant role. These reverse fault planes primarily served as conduits for fluid movement.

Miarolitic pegmatites and pegmatitic CAG

The crystallization process of the miarolitic pegmatites resembles that of other types of granitic pegmatites, such as pegmatite veins (Thomas *et al.* 2009). According to these authors, the differences among the various pegmatite types can be partly explained by the efficiency of the drainage networks for residual magmatic fractions rich in volatiles. Miarolitic pegmatites reflect inefficient drainage, whereas larger pegmatites indicate a preference for filling the most favorable nodes within the drainage network. For example, in Königshain, the size and placement of miarolitic pegmatites appears to be controlled by the percolation of residual magma along grain-boundary scale pathways through late-magmatic fractures (Thomas *et al.* 2009).

In the albite-enriched granite, when the separation of supercritical aqueous fluid from the pegmatitic melt took place, the volatile-rich fluids migrate through grain-scale pathways toward the transition zone between the CAG and the BAG. The advanced cooling of the BAG in this area prevents the fluids from ascending further, resulting in the emplacement of miarolitic pegmatites within this region. Siachoque *et al.* (2020) described miarolitic cavities with pegmatite texture filling fractures that are frequently subparallel, and occasionally perpendicular to the trend of granitic dykes. In this study, the granitic dykes are represented by the pegmatitic CAG.

Border pegmatites

The border pegmatites or "stockscheiders" were interpreted as rocks placed in cracks formed due to the contraction of the main stock during its cooling, forming fractures parallel to the intrusion walls, allowing the injection of late residual pegmatitic magma at the contact boundaries between magmatic intrusions and their oldest host rocks (Baumann 1970; Lukkari 2002). Examples of border pegmatites are those located in Alaska (Soloviev *et al.* 2019), Algeria (Bouabsa *et al.* 2010), Germany and Czech Republic (Baumann 1970; Breiter *et al.* 2005; Müller *et al.* 2018), Brazil (Pereira *et al.* 2011), China (Zhu *et al.* 2001), Finland (Haapala and Ojanperä 1972; Lukkari 2002), and Greenland (Zirner *et al.* 2015).

In the case of the border pegmatite of the Black Pearl albitite (Schmitz and Burn 1990), the orientation of the crystals perpendicular to the contact (towards the center of the stock) added to the presence of pegmatitic autoliths in the albitite are interpreted by the authors as evidence that the pegmatite is not a late dyke placed along the contact, but rather a rock formed at or near the time of emplacement. Similarly, in the early magmatic stage of the albite-enriched granite, a fluid derived from the BAG melt most likely migrated to the contraction fractures generated when the border of the pluton experienced a more rapid cooling rate than the central core. That is most important, because it settles a chronological timing, in which the border pegmatites formed at the beginning of the albite-enriched granite evolution rather than later. In its turn, the pegmatite veins formed later, derived from the CAG melt, when the CAG was with advanced crystallization in progress, and the residual magmatic fluid migrated to spaces opened by reverse faults and horizontal extension fractures.

Classification of the studied pegmatites

The pegmatite classification by Černý *et al.* (2012) distinguish pegmatitic classes based on the environment of their host rock (abyssal class), mineralogy (muscovite class), elemental composition (rare element class), and texture (miarolitic class). According to this classification, the border pegmatites, and the pegmatite veins exhibit characteristics of the moderate-depth rare-element class, specifically falling under the REE subclass and NYF family. This classification is based on their pronounced enrichment in REE, Y, U, Th, Be, Nb>Ta, Zr, and F. However, the pegmatite veins also display significant enrichment in Li, Rb and Sn, and the typical minerals are riebeckite, polylithionite, xenotime, thorite, pyrochlore-columbite, genthelvite, and cryolite (fluorite in the border pegmatite) instead of the type-minerals allanite-monazite, euxenite, and gadolinite of the NYF family. The miarolitic pegmatites are classified within the miarolitic class, encompassing a variety of instances such as shallow-level miarolitic pegmatites, geode-bearing pegmatite facies, and intrusive pegmatites found within granites and schists. These formations solidify at relatively low pressures, reaching as low as 1 kbar (Černý *et al.* 2012). Remarkably, in the albite-enriched granite, both the pegmatite veins and miarolitic cavities are considered to have formed at the same shallow crustal level, within the cold upper crust, situated above the critical crustal depth, under low solidus temperatures.

The novel pegmatite classification introduced by Dill (2015) is referred to by the acronym CMS, which stands for the assessed parameters: chemical composition, mineral assemblage, and structural geology. Within this framework, the pegmatites are categorized based on specific groups of elements and mineral assemblages, which are further grouped by their respective commodities. These commodities are then examined in terms of their geological and geodynamic significance within both temporal and spatial contexts. Following the CMS scheme, the pegmatites associated with the albite-enriched granite can be classified as follow: (i) amphibole-rich PEG: cm-sized unzoned vein-type REE-Y-Sn-U-Zr-Hf-Zn-Pb-Be-Li-F granite pegmatite (riebeckite); (ii) polylithionite-rich PEG: cm-sized unzoned vein-type REE-Y-Sn-Th-Zr-K-Zn-Pb-Be-Li-F granite pegmatite (polylithionite-genthelvite); (iii) Cryolite-rich PEG: cm-sized unzoned vein-type REE-Y-Zn-Pb-Na-F granite pegmatite (cryolite); (iv) Miarolitic pegmatite: cm-sized zoned miarolitic cryolite-albite granite pegmatite; and (v) Border pegmatite: m-sized unzoned border REE-Y-Ca-U-Zr-F granite pegmatite (fluorite).

These pegmatite types fall within the [24dE]-type classification, primarily due to their significant REE-Y ore content and their location within an alkaline igneous rock setting, in a setting of intra-platonic rift.

Pegmatite genesis

Granite pegmatites were firstly considered as products of the continuous fractional crystallization of a low-viscosity granitic melt (Cameron *et al.* 1949), in which rare elements (Li, Be, Ta, etc.), fluxing (B, P, F, etc.) and volatile components (H2O, Cl, etc.) would increase steadily as crystallization advances towards the center of magma chamber in a decreasing fraction of residual melt. Afterwards, it was proposed that pegmatites formed through separation by density of an aqueous fluid from a silicate melt, based on the incongruous partitioning of the alkalis (Jahns and Burnham 1969). In this process, the aqueous fluid becomes enriched in K and the melt becomes enriched in Na. In this model, textures and mineralogical zoning of pegmatites are assigned to crystallization from the aqueous fluid, that incorporated certain elements from the silicate melt and redistributed them to growing crystals in all parts of the pegmatite body. Jahns (1982) explained the mass transfer of solutes by the rise of the aqueous fluid by density difference, and inferred the incongruous splitting of K, rare alkalis, and other trace elements in the aqueous fluid to explain the chemical fractionation found in pegmatites.

More recently, London (2008) suggested that pegmatites originated by the formation of a layer of a silicate fluid that concentrated flux elements at the limit of the crystallization front (constitutional zone refining). This fluid would have undercooling conditions of ~200°C below the *liquidus*, and together with the viscosity and the delay in crystal nucleation, would propitiate formation of typical pegmatitic textures. This would occur over short periods of time, on the scale of hours to days, rather than through slow cooling as previously thought (London and Kontak 2012). The model proposed by Thomas *et al.* (2000, 2005, 2006, 2008, 2009, 2012) differs from London's (2008) model by suggesting that pegmatites crystallize not through a boundary layer of low-viscosity aqueous fluid, but rather from an entire evolutionary-magmatic-hydrothermal system of low viscosity, very dynamic, boiling and with violent convections. They argue that pegmatites are a product of the magmatic crystallization of H_2O-rich residual magmatic fractions, produced by melt-melt immiscibility during the late stages of the granitic magma fractionation, combined with metasomatic reactions. Based on melt and fluid inclusion studies, these authors demonstrated the coexistence of at least three phases in complex natural systems, including a high viscosity H_2O-poor aluminosilicate magma, a low viscosity H_2O-rich hydrosaline magma (silicate poor), and a low salinity aqueous fluid. London (2014) suggested that the H_2O-rich hydrosaline magma may represent flux-enriched boundary layers.

There is no conclusive understanding of when and how pegmatites are derived from their parent granites. Regardless of the origins of predominantly aqueous low-density phases (i.e., melt-melt immiscibility versus constitutional zone refining), their formation likely marks the transition from a magmatic toward a magmatic-hydrothermal system (London and Morgan 2012).

Polylithionite-rich PEG and cryolite-rich PEG

In the albite-enriched granite, the type-A geochemical trend shows the progressive fractional crystallization and F increasing towards the center of the pluton, as expected in the model for pegmatite genesis of Cameron *et al.* (1949). Nevertheless, fractional crystallization cannot explain alone the features observed in the studied pegmatites. In the type-A trend, there exists a major exception regarding the polylithionite-rich PEG, which contains higher average K and lower Na relative to all other rocks. This could represent the separation by density of a K-rich aqueous fluid and a Na-rich silicate melt, based on the incongruous partitioning of the alkalis of the Jahns and Burnham (1969) model. However, in this model the silicate melt is only the source of elements for the fluid, and the aqueous fluid “sweeps” incompatible elements from the melt at the bottom of the magmatic body and transports these components upward to crystallize the pegmatites. In the albite-enriched granite both the K- and Na-rich phases originated pegmatites, the polylithionite-rich PEG and the cryolite-rich PEG, respectively. In this sense, the model proposed by Thomas *et al.* (2006) with melt-melt immiscibility appears to explain better the genesis of the studied pegmatite veins but maintaining the alkali partitioning. In the latest residual melt of the magmatic stage, occurred the immiscibility of a K-F-rich aluminosilicate melt (low H_2O, average 58.35 wt.% SiO_2; 5.69 wt.% F), and of a Na-F-rich aqueous melt with low Si (average 12.4 wt.% SiO_2; 35 wt.% F), originating the polylithionite-rich PEG and the cryolite-rich PEG, respectively.

Furthermore, the solubility of Nb and Ta increases in F-rich aqueous solutions at elevated temperature (> 100°C), and experimental studies suggest that Nb is more mobile than Ta under most conditions (Zaraisky *et al.* 2010; Timofeev *et al.* 2017). Experiments reproducing fluoride-silicate melt immiscibility suggest that Nb partitions preferentially into the fluoride melt compared to Ta (Veksler *et al.* 2012). Experiments with aqueous F-rich fluids and aluminosilicate melts indicate that Nb and Ta preferentially partition into the melt (Chevychelov *et al.* 2005). Analyses of fluid inclusions hosted in quartz and topaz from the Beauvoir rare-metal granite and its country-rock indicate that trapped magmatic-hydrothermal fluids are enriched in Nb relative to Ta (Harlaux *et al.* 2017). Thus, in the cryolite-rich PEG, the drastic decrease of Nb and Ta contents and increase in the Nb/Ta ratio relative to the polylithionite-rich PEG also corroborates with an immiscibility pattern. If indeed occurred an immiscibility between the polylithionite-rich PEG and cryolite-rich PEG melts, then Y, Li, Be, Zn, Sr, and HFSE in general were partitioned preferentially in the K-rich aluminosilicate melt.

Pegmatitic CAG and amphibole-rich PEG

In the final stages of the magmatic evolution, it is likely that the formation of both the pegmatitic CAG and the amphibole-rich PEG occurred prior to the occurrence of immiscibility between the polylithionite-rich PEG and cryolite-rich PEG fluids. Interestingly, the pegmatitic CAG, in contrast to the other pegmatite veins, does not exhibit the same richness in cryolite. In the other hand, it presents the incorporation of notably higher levels of Nb, Ta, Rb, U, Th, Zr, and Sn in comparison to the host rock, highlighting the role of fractional crystallization and saturation in these elements in the genesis of the melt of the pegmatitic CAG.

Within the melt of the amphibole-rich PEG, notable increases in elements such as Y, Li, Be, Zn, and F were evident in comparison to the pegmatitic CAG. Besides, the formation of remarkably coarse-grained crystals, including minerals like riebeckite, genthelvite, xenotime, polylithionite, and cryolite, marks the starting point of an additional mechanism for crystal growth beyond fractional crystallization. The high concentration of H_2O and anomalous abundance of F within the pegmatite melt played a crucial role in reducing melt viscosity and fostering conditions of undercooling that proved conducive to the development of the observed texture in the amphibole-rich

PEG. Moreover, in this context, the contribution of the constitutional zone refining process proposed by London (2008) cannot be ruled out.

Miarolitic pegmatites

The formation of miarolitic cavities emerges from the oversaturation of the residual pegmatite melt with volatile components, primarily water. Černý (2000) discusses three key mechanisms contributing to the separation of supercritical aqueous fluid from the pegmatitic melt: (1) decompression of the melt due to magma ascent or uplift induced by tectonic forces (pressure quench); (2) fractional crystallization and volatile saturation during very late isobaric solidification; and (3) depletion in solubility-enhancing fluxing components due to mineral crystallization containing these elements, liberating supercritical fluids (chemical quench). In the albite-enriched granite, miarolitic pegmatites share mineralogical characteristics with amphibole-rich pegmatite veins (Ronchi *et al.* 2019), implying their origin from the same melt. The significant crystallization of cryolite within this melt acted to some extent as a buffer for fluorine. Additionally, the pegmatite veins emerged within a tectonically dynamic environment, tied to reverse fault displacement, while the formation of miarolitic pegmatites occurred in less favorable parts of the drainage network. Consequently, the genesis of miarolitic cavities is primarily attributed to pressure quenching, resulting in the separation of supercritical aqueous fluids and system undercooling; however, chemical quenching of the melt remains a viable mechanism.

Border pegmatites

In most cases, the border pegmatites or stockscheiders have been interpreted as late-stage fluids (e.g., Baumann 1970; Berni *et al.* 2020), however, other occurrences have brought to light alternative mechanisms to the genesis for these pegmatites. The relatively barren border pegmatites positioned in contact with Sn-mineralized granites in Tasmania and South Africa formed from aqueous fluids that were concentrated at the apexes of the intrusions (Groves and McCarthy 1978). The border pegmatite of the Black Pearl albitite is considered a rock formed in the presence of low-viscosity aqueous fluids, with the magma becoming saturated in fluids at or near the time of emplacement. Additionally, the abrupt change from pegmatite to magmatic albitite (fine grains) was explained by a sudden reduction in confinement pressure and the loss of magma volatiles (Schmitz and Burn 1990).

In the studied border pegmatites, the large size of the minerals and the prevalence of K over Sn-Na-F, relative to the host BAG, lend support to their crystallization in the presence of a low-viscosity, F-poor aqueous fluid. In this scenario, the magma that gave rise to the BAG likely reached a state of fluid-saturation shortly after emplacement. The low-viscosity aqueous melt would have possessed the capacity to flow and infiltrate more readily through the surrounding rock matrix, accumulating at the intrusion's apexes. This process could have led to the preferential transport and concentration of specific elements, such as K, Ca, Y, Zr, Sr, and Be, while excluding others. This phenomenon might explain the relatively limited Sn-Li content in the border pegmatites compared to the BAG, along with significatively lower levels of Na, F, Nb, Ta, U, Th, and Pb. The abrupt contact of the border pegmatite with the host rocks might indicate the occurrence of a pressure quench, resulting from a sudden decrease in confining pressure brought about by the ascent of albite-enriched granite magma during the pluton's emplacement into shallower crustal depths. This early fluid saturation within the BAG melt could also be tied to the virtually absence of iron-rich silicate minerals in the BAG, which disappeared due to an autometasomatic process (Costi *et al.* 2000, 2009).

Composition and source of the hydrothermal fluids

Hydrothermal fluids in the amphibole-rich PEG and the border pegmatite

Insights into the composition and source of the hydrothermal fluids that affected both the border pegmatites and the amphibole-rich pegmatite veins can be deduced from the secondary minerals formed during pyrochlore alteration. In columbite, the average LREE/HREE ratio is lower in the northern border pegmatite (0.8) and higher in the amphibole-rich PEG (3.14). Notably, the secondary silicatic phases associated with pyrochlore alteration in the northern border pegmatite exhibit greater richness in HREE and Y, whereas those from the amphibole-rich PEG displays lower levels. Additionally, hydrothermal pyrochlore in the northern border pegmatite incorporates HREE and Y, while this is not the case for the hydrothermal pyrochlore in the amphibole-rich PEG. These distinct characteristics suggest a correlation between the availability of HREE and Y in the hydrothermal fluid and the magmatic paragenesis of the host rock: in the amphibole-rich PEG, which contains abundant xenotime and gagarinite-(Y), there was a reduced availability of HREE and Y in the hydrothermal fluid. Conversely, in the northern border pegmatite, where magmatic HREE- and Y-rich phases are scarce, the hydrothermal fluid exhibited a higher availability of HREE and Y.

Important implications of that are that the composition of the hydrothermal fluid was different in the border pegmatites and in the pegmatite veins, and that the HREE and Y content in the hydrothermal fluid was not incorporated through the leaching of magmatic HREE-Y-rich phases. Instead, the hydrothermal fluid represents a residual aqueous phase exsolved from the crystallized rock, reflecting in a local scale the degree of melt fractionation at the point of H_2O saturation. In the early stages of magmatic evolution, in the border pegmatite, the pegmatitic F-poor aqueous melt did not reach sufficient saturation in HREE-Y to form their own minerals (e.g., xenotime, gagarinite). Because of this, the HREE-Y was concentrated in the exsolved deuteric fluids and incorporated into secondary hydrothermal phases. As the magmatic evolution progressed from the BAG to the CAG, the HREE-Y was mostly concentrated in the residual melt, in the form of complexes with F, and when the amphibole-rich PEG was formed the abundant crystallization of xenotime and minor gagarinite caused a depletion of HREE and Y in the exsolved deuteric fluid.

Additionally, the occurrence of Ca-enriched hydrothermal pyrochlore and fluorite in the border pegmatites, in contrast to the Na-enriched hydrothermal pyrochlore and cryolite in the amphibole-rich PEG, further supports a connection between the composition of the hydrothermal fluid and the fractionated composition of the host rock. These features provide strong evidence that the hydrothermal fluids that affected the studied pegmatites originated as a residual aqueous phase rather than having an external source. Considering that the border pegmatites and vein pegmatites formed during distinct stages of the albite-enriched granite system’s evolution, their hydrothermal alteration processes also occurred at different stages.

Hydrothermal fluid in the BAG and CAG

In the pluton scale, alteration of pyrochlore was more intense in the BAG and in the central portion of the CAG [Hadlich *et al.* 2023b (submitted)]. In the relatively thinner BAG, the significant alteration of pyrochlore could be associated with the autometasomatism process described by Costi *et al.* (2000, 2009). In the much thicker CAG, alteration was stronger in the surroundings of the large massive cryolite deposit in the center of the CAG and, therefore, is strongly linked to the concentration of H_2O-F-rich fluids towards the center of the pluton.

To explain the formation of the massive cryolite deposit at the albite-enriched granite pluton's center, Lenharo (1998) and Costi (2000) proposed that the albite-enriched granite magma evolved into an extremely Na- and F-enriched residual melt. Costi (2000) suggested that, at the point of H_2O saturation, this highly F-enriched residual fluid separated into an aqueous, relatively F-poor portion and a low-H_2O, Na-Al-F-rich portion. In this scenario, the H_2O-depleted, Na–Al–F-rich fraction led to the formation of massive cryolite bodies, and the H_2O-rich fraction are believed to have formed the polylithionite-feldspar-quartz-bearing aureole surrounding the massive cryolite deposit (Minuzzi *et al.* 2006; Bastos Neto *et al.* 2009). In accordance with Bastos Neto *et al.* (2009), the extreme fluorine enrichment in the residual melt is unlikely to have been attained, since the F content was buffered by crystallization of magmatic cryolite (Dolejs and Baker 2007). Paludo *et al.* (2018) suggested that the extreme F-enrichment could have been occurred in very restricted portions of the magma, and that the cryolite-rich PEG could represent this most evolved residual magmatic fluid in the albite-enriched granite system.

Nevertheless, fluid inclusions data (Bastos Neto *et al.* 2009; Ronchi *et al.* 2011) supported the conclusion that the massive cryolite deposit is hydrothermal in origin, formed through the exsolution of hydrothermal saline deuteric fluids (salinity between 0 and 25% eq. NaCl and homogenization temperatures from 100 to 400ºC) from a magma originally rich in volatiles. These authors concluded that the exsolved fluids lowered the solidus curve of the system, allowing the formation of several and varied portions with pegmatitic texture inside the albite-enriched granite. In this study, it is suggested that additional processes, as the pressure quenching caused by tectonic activity and the melt-melt immiscibility played an important role to the formation of the pegmatite veins and miarolitic pegmatites. In addition, it is proposed that hydrothermal alteration in the pegmatite bodies is a response to local processes involving exsolution of deuteric fluids, rather than a product of the main hydrothermal fluid concentrated in the central region of the CAG.

By extending this notion, it becomes conceivable that the magmatic-hydrothermal transition within the albite-enriched granite's system took place independently for each body – the border pegmatites, BAG, CAG, and pegmatite veins – as a result of their distinct crystallization process (compositionally and chronologically). In this context, the starting point of the magmatic-hydrothermal transition in the CAG could be identified by the exsolution of the hydrothermal fluids that gave rise to the hydrothermal massive cryolite deposit and exerted significant alteration on the central portion of the pluton. Within the pegmatite veins and border pegmatites, the exsolution of hydrothermal fluids resulted in the formation of cryolite II (fluorite in the border pegmatites), quartz II, and the alteration (autometasomatism) of primary minerals.

Conclusion

The albite-enriched granite hosts four types of pegmatites: border pegmatites, pegmatitic CAG, miarolitic pegmatites, and pegmatite veins. The host rock and the pegmatites were emplaced in the same crustal level. The border pegmatites were emplaced within contraction fractures situated between the BAG and the surrounding country rocks. The pegmatitic CAG developed in centimetric fractures, while the miarolitic pegmatites were emplaced within fractures with ineffective drainage. The pegmatite veins were emplaced within reverse faults and extension fractures.

All pegmatite types exhibit the same mineralogy as the CAG, primarily composed of pyrochlore, riebeckite, polylithionite, zircon, thorite, xenotime, gagarinite-(Y), genthelvite, galena, microcline, albite, quartz and cryolite. However, the border pegmatites differ, sharing the mineralogy of the BAG with fluorite instead of cryolite and lacking genthelvite. The host albite-enriched granite serves as the source of all the fluids that contributed to the formation of the studied pegmatites. The border pegmatite originated from the BAG melt, while the pegmatitic CAG, miarolitic pegmatites, and pegmatite veins are derived from the CAG melt.

The albite-enriched granite showcases extreme fractionation patterns, exceeding those of most fractionated peralkaline rare-metal A1-type granitoids worldwide. The pegmatitic CAG and the amphibole-rich PEG amplify this fractionation phenomenon. Additionally, the richness of F in both the albite-enriched granite and the pegmatites (reaching up to 35 wt.% F in the cryolite-rich PEG) stands as an unprecedented occurrence. Fluorine-complexes enriched the residual melt with Li, Na, K, Rb, and rare metals (REE, U, Th, Be, Zr, Nb, Ta), contributing to the progressive enrichment of HREE toward the later paragenesis of the pegmatites.

All pegmatites underwent significant alteration due to highly acidic, F-rich hydrothermal fluids, resulting in the corrosion of magmatic minerals and the formation of secondary mineral phases. The hydrothermal fluid in the border pegmatites was enriched in Ca and HREE, leading to the formation of minerals such as fluorite and HREE-enriched hydrothermal pyrochlore, columbite and silicates. Conversely, in the pegmatite veins, the hydrothermal fluid was richer in Na and less abundant in HREE, causing the precipitation of cryolite and secondary phases with reduced HREE content.

This study yielded the following conclusions regarding the magmatic-hydrothermal evolution of the albite-enriched granite system and its associated pegmatites:

(1) The ascent of the albite-enriched granite magma towards shallower crustal depths resulted in a rapid reduction in confining pressure. This abrupt pressure change caused the separation of a F-poor aqueous phase, which exhibited enrichment in K, Ca, Sr, Zr, Y, and HREE, from the BAG melt. This aqueous fluid ascended towards the intrusion's apexes, giving rise to the border pegmatites during the early stages of magmatic evolution.

(2) Continuing fractional crystallization within the CAG, the final residual melt of the magmatic stage resulted in the formation of pegmatitic CAG, characterized by an extreme enrichment in Rb, Nb, Ta, Th, and other HFSE.

(3) At this juncture, reverse fault displacement might have caused a secondary pressure quench, leading to the separation of supercritical aqueous fluids, and resulting in the undercooling of the system. This circumstance allowed for the injection of a residual Y-Li-Be-Zn-F-enriched aqueous melt into veins, leading to the formation of the amphibole-rich PEG, as well as into miarolitic cavities.

(4) It was during this period that melt-melt immiscibility occurred, leading to the partitioning of distinct phases. This segregation resulted in a K-F-rich aluminosilicate melt (low H_2O) with additional enrichment in Y-Li-Be-Zn, as well as an extremely Na-F-rich aqueous melt (low SiO_2). These melts formed the polylithionite-rich PEG and the cryolite-rich PEG, respectively.

(5) The magmatic-hydrothermal transition occurred independently for each body – the border pegmatites, BAG, CAG, and pegmatites veins – when the residual aqueous phase exsolved from the crystallized rock. This aqueous phase exhibited a composition that, on a local scale, mirrored the degree of melt fractionation at the point of H_2O saturation.

(6) Within the pegmatite veins and the border pegmatites, the exsolution of F-rich hydrothermal fluids led to the formation of cryolite II and fluorite,

respectively, along with the significant alteration (autometasomatism) of primary minerals. On a much larger scale, the exsolution of F-rich hydrothermal fluids in the CAG gave rise to the hydrothermal massive cryolite deposit, while also causing substantial alteration in the central portion of the pluton.

Acknowledgements: This work was supported by Conselho Nacional de Desenvolvimento Científico e Tecnológico (CNPq) through the Project 405839/2013-2018 and for granting scholarship. The authors thank the reviewers and editors for contributing to improve the manuscript.

Competing interests: The authors declare that they have no known competing financial interests or personal relationships that could have appeared to influence the work reported in this paper.

References

Almeida, F.F.M., Hasui, Y., Brito Neves, B.B., and Fuck, R.A., 1981, Brazilian structural Provinces: an introduction: Earth Sciences Review, v. 17, p. 1-29.

Anders, E., and Grevesse, N., 1989, Abundances of the elements: Meteoritic and solar: Geochimica et Cosmochimica Acta, v. 53(1), p. 197–214 .

Ballouard, C., Poujol, M., Boulvais, P., Branquet, Y., Tartèse, R., and Vigneresse, J.L., 2016, Nb-Ta fractionation in peraluminous granites: a marker of the magmatic-hydrothermal transition: Geology, v. 44, p. 231–234.

____, Massuyeau, M., Elburg, M.A., Tappe, S., Viljoen, F., and Brandenburg, J.T., 2020, The magmatic and magmatic-hydrothermal evolution of felsic igneous rocks as seen through Nb-Ta geochemical fractionation, with implications for the origins of rare-metal mineralizations: Earth Science Reviews, v. 203, 103115.

Bastos Neto, A.C., Pereira, V.P., Lima, E.F., Ferron, J.M., Minuzzi, O., Prado, M., Ronchi, L.H., Flores, J.A., Frantz, J.C., Pires, A., Pierosan, R., Hoff, R., Botelho, N.F., Rolim, S.B., Rocha, F., and Ulmann, L., 2005, A jazida de criolita da Mina Pititnga (Amazonas), *in* Marini, O.J., Queiroz, E.T., and Ramos, B.W., eds., Caracterização de Depósitos Minerais em Distritos Mineiros da Amazônia: Brasília, DNPM-CT/MINERAL-ADIMB, p. 481–547.

____, Pereira, V.P., Ronchi, L.H., Lima, E.F., and Frantz, J.C., 2009, The world-class Sn, Nb, Ta, F (T, REE, Li) deposit and the massive cryolite associated with the albite-enriched facies of the Madeira A-type granite, Pitinga Mining District, Amazonas State, Brazil: The Canadian Mineralogist, v. 47, p. 1329–1357.

____, Pereira, V.P., Pires, A.C., Barbanson, L., and Chauvet, A., 2012, Fluorine-rich xenotime from the Nb-Ta-Sn Madeira world-class deposit associated with the albite-enriched granite at Pitinga, Amazonia, Brazil: The Canadian Mineralogist, v. 50, p. 1019–1032.

____, Ferron, T.M.M., Chauvet, A., Chemale, F., Lima, E.F., Barbanson, L., and Costa, C.F.M., 2014, U-Pb dating of the Madeira Suite and structural control of the albite-enriched granite at Pitinga (Amazônia, Brazil): evolution of the A-type magmatism and implications for the genesis of the Madeira Sn-Ta-Nb (REE, cryolite) world-class deposit: Precambrian Research, v. 243, p. 181–196.

Bettencourt, J.S., *et al*., 2016, Metallogenetic systems associated with granitoid magmatism in the Amazonian Craton: An overview of the present level of understanding and exploration significance: Journal of South American Earth Sciences, v. 68, p. 22–49.

Cameron, E.N., *et al.*, 1949, Internal structure of granitic pegmatites: Economic Geology, Monograph 2, 115 p.

Černý, P., Meintzer, R.E., and Anderson, A.J., 1985, Extreme fractionation in rare-element granitic pegmatites: selected examples of data and mechanisms: The Canadian Mineralogist, v. 23, p. 381–421.

____, 1989, Exploration strategy and methods for pegmatite deposits of tantalum, *in* Möller, P., Černý, P., and Saupé, F., eds., Lanthanides, Tantalum and Niobium: Springer-Verlag, Heidelberg, p. 274–310.

____, 2000, Constitution, petrology, affiliations and categories of miarolitic pegmatites, *in* Pezzotta, F., ed., Mineralogy and Petrology of Shallow Depth Pegmatites: Memorie de la Società Italiana di Scienze Naturali e del Museo Civico di Storia Naturale di Milano, v. 30, p. 5–12.

____, London, D., and Novak, M., 2012, Granitic pegmatites as reflections of their sources: Elements, v. 8, p. 289–294.

Chevychelov, V.Y., Zaraisky, G.P., Borisovskii, S.E., Borkov, D.A., 2005, Effect of melt composition and temperature on the partitioning of Ta, Nb, Mn, and F between granitic (alkaline) melt and fluorine-bearing aqueous fluid: fractionation of Ta and Nb and conditions of ore formation in rare-metal granites: Petrology, v. 13(4), 305–321.

Costi, H.T., 2000, Petrologia de granitos alcalinos com alto flúor mineralizados em metais raros: o exemplo do Albita-granito da Mina Pitinga, Amazonas, Brasil [Ph.D. thesis]: Belém, Brasil, Universidade Federal do Pará, 345 p.

____, Dall’agnoll, R., and Moura, C.A.V., 2000, Geology and Pb-Pb Geochronology of Paleoproterozoic volcanic and granitic rocks of Pitinga province, Amazonian craton, northern Brazil: International Geology Reviews, v. 42, p. 832–849.

____, Borges, R.M., and Dall'Agnol, R., 2005, Depósitos de estanho da mina Pitinga, estado do Amazonas, *in* Marini, O.J., Queiroz, E.T., and Ramos, B.W., eds., Caracterização de Depósitos Minerais em Distritos Mineiros da Amazônia: Brasília, DNPM-CT/MINERAL-ADIMB, p. 391–475.

____, Dall'agnol, R., Pichavant, M., and Ramo, O.T., 2009, The peralkaline tin-mineralized Madeira cryolite albite-rich granite of Pitinga, Amazonian Craton, Brazil: petrography, mineralogy and crystallization processes: The Canadian Mineralogist, v. 47, p. 1177–1203.

Dill, H.G., 2015, Pegmatites and aplites: Their genetic and applied ore geology: Ore Geology Reviews, v. 69, p. 417-561.

____, 2018, Geology and chemistry of Variscan-type pegmatite systems (SE Germany) - With special reference to structural and chemical pattern recognition of felsic mobile components in the crust: Ore Geology Reviews, v. 92, p. 205–239.

____, 2019, Coupling restites and mobilizates – Geological and litho-chemical investigations of paired belts of calcsilicate fels and quartzite (SE German Basement) - Quo vadis David London´s pegmatology?: Ore Geology Reviews, v. 105, p. 636–666.

Dolejs, D., and Baker, D.R., 2007, Liquidus equilibria in the system K_2O-Na_2O-Al_2O_3-SiO_2-F_2O to 100 MPa 2: differentiation paths of fluorosilicic magmas in hydrous systems: Journal of Petrology, v. 48, p. 807–828.

Ferron, J.M.T.M., Bastos Neto, A.C., Lima, E.F., Costi, H.T., Moura, C.A.V., Prado, M., and Galarza, M.A., 2006, Geologia e cronologia Pb-Pb de rochas graníticas e vulcânicas ácidas a intermediárias paleoproterozóicas da Província de Pitinga, Cráton Amazônico: Revista Brasileira de Geociências, v. 36(3), p. 499–512.

____, Bastos Neto, A.C., Lima, E.F., Nardi, L.V.S., Costi, H.T., Pierosan, R., and Prado, M., 2010. Petrology, geochemistry, and geochronology of Paleoproterozoic volcanic and granitic rocks (1.89 to 1.88 Ga) of the Pitinga province, Amazonian Craton, Brazil: Journal of South American Earth Sciences, v. 29, p. 483–497.

Goodenough, K.M., Upton, B.G.J., and Ellam, R.M., 2000, Geochemical evolution of the Ivigtut granite, South Greenland: a fluorine-rich “A-type” intrusion: Lithos, v. 51(3), p. 205–221.

Groves, D.I., and McCarthy, T.S., 1978, Fractional crystallization and the origin of tin deposits in granitoids: Mineralium Deposita, v. 13, p. 11–26.

Gundsambuu, T., 1974, Genetic relationship between the tin-tungsten deposits and granitic magmatism of Mongolia: Geological Survey, p. 99–103.

Haapala, I., 1966, On the granitic pegmatites in the Peraseinajoki-Alavus area, south Pohjanmaa, Finland: Bulletin de la Commission Géologique de Finlande, v. 224, p. 1–98.

____, and Ojanperä, P., 1972, Genthelvite-bearing greisens in southern Finland, Geological Survey of Finland, bulletin 259, 27 p.

Hadlich, I.W., Bastos Neto, A.C., Botelho, N.F., and Pereira, V.P., 2019, The thorite mineralizations in the Madeira Sn-Nb-Ta world-class deposit (Pitinga, Brazil): Ore Geology Reviews, v. 105, p. 445–466.

____, Bastos Neto, A.C., Pereira, V.P., Botelho, N.F., Ronchi, L.H., and Dill, H.G., 2023a (submitted), Mn-Fe-rich genthelvite from pegmatites associated with the Madeira Sn-Nb-Ta world-class deposit (Pitinga, Brazil): new constraints on the magmatic-hydrothermal transition in the albite-enriched granite system, Mineralogical Magazine.

____, Bastos Neto, A.C., Pereira, V.P., Dill, H.G., and Botelho, N.F., 2023b (submitted), Uranium mineralization in the Madeira Sn-Nb-Ta (U, Th, REE, F) world-class deposit (Pitinga, Amazonas State, Brazil): pyrochlore and its alteration products under hypogene conditions, Economic Geology.

Harlaux, M., Mercadier, J., Bonzi, W.M.-E., Kremer, V., Marignac, C., and Cuney, M., 2017, Geochemical signature of magmatic-hydrothermal fluids exsolved from the Beauvoir Rare-Metal Granite (Massif Central, France): insights from LA-ICPMS analysis of primary fluid inclusions: Geofluids, v. 2017, 25 p.

Horbe, M.A., Horbe, A.C., Costi, H.T., and Teixeira, J.T., 1991, Geochemical characteristics of cryolite-tin-bearing granites from the Pitinga mine, northwestern Brazil – a review: Journal of Geochemical Exploration, v. 40, p. 227–249.

Jahns, R.H., 1953, The genesis of pegmatites: American Mineralogist, v. 38, p. 1078–1112.

____, and Burnham, C.W., 1969, Experimental studies of pegmatite genesis; l, A model for the derivation and crystallization of granitic pegmatites: Economic Geology, v. 64(8), p. 843–864.

____, 1982, Internal evolution of pegmatite bodies: MAC Short Course Handbook, v. 8, p. 293–327.

Lengler, H.F., 2016, Pegmatitos do albita granito Madeira: avaliação do minério para fins de beneficiamento [Monography]: Porto Alegre, Brasil, Universidade Federal do Rio Grande do Sul, 118 p.

Lenharo, S.L.R., 1998, Evolução magmática e modelo metalogenético dos granitos mineralizados da região de Pitinga, Amazonas, Brasil [Ph.D. thesis]: São Paulo, Brasil, Universidade de São Paulo, 290 p.

____, Pollard, P.J., and Born, H., 2003, Petrology and textural evolution of granites associated with tin and rare-metals mineralization at the Pitinga mine, Amazonas, Brazil: Lithos, v. 66, p. 37–61.

London, D., 2008, Pegmatites: The Canadian Mineralogist Special Publication, v. 10, 347 p.

____, and Kontak, D.J., 2012, Granitic pegmatites: Scientific wonders and economic bonanzas: Elements, v. 8, p. 257–261.

____, and Morgan, G.B.V.I., 2012, The pegmatite puzzle: Elements, v. 8, p. 263–268.

____, 2014, A petrologic assessment of internal zonation in granitic pegmatites: Lithos, v. 184-187, p. 74–104.

Lukkari, S., 2002, Petrography and geochemistry of the topaz-bearing granite stocks in Artjärvi and Sääskjärvi, western margin of the Wiborg rapakivi granite batholith: Bulletin of the Geological Society of Finland, v. 74(1–2), p. 115–132.

Martin, R.F., 2006, A-type granites of crustal origin ultimately result from open-system fenitization-type reactions in an extensional environmental: Lithos, v. 91, p. 125–136.

Mineyev, D.A., 1963, Geochemical differentiation of the rare earths: Geochemistry (USSR), v. 12, p. 1129–1149.

Minuzzi, O.R.R., 2005, Gênese e evolução da mineralização de criolita, pirocloro e columbita da subfacies albita granito de núcleo, Mina Pitinga, Amazonas, Brasil [Ph.D. thesis]: Porto Alegre, Brasil, Universidade Federal do Rio Grande do Sul, 249 p.

____, Bastos Neto, A.C., Pereira, V.P., and Flores, J.A.A., 2006a, The massive cryolite deposit and the disseminated ore of cryolite from the Pitinga mine (Amazon, Brazil): Revista Brasileira de Geociências, v. 36, p. 104–123.

____, Bastos Neto, A.C., Pereira, V.P., and Nunes, L., 2006b, A columbitização do pirocloro do albita granito na mina de Pitinga (AM): relações com a mineralização de criolita: Revista Brasileira de Geociências, v. 35(1), p. 123–137.

____, Bastos Neto, A.C., Formoso, M.L.L., Andrade, S., Janasi, V.A., and Flores, J.A., 2008, Rare Earth elements and yttrium geochemistry applied to the genetic study of cryolite ore at the Pitinga Mine (Amazon, Brazil): Anais da Academia Brasileira de Ciências, v. 80(4), p. 719–733.

Müller, A., Herklotz, G., and Giegling, H., 2018, Chemistry of quartz to the Zinnwald/Cínovec Sn-W-Li greisen-type deposit, Eastern Erzgebirge, Germany: Journal of Geochemical Exploration, v. 190, p. 357–373.

Mulligan, R., 1965, Geology of Canadian lithium deposits: Economic Geology, v. 21, p. 1–131.

Münker, C., Pfänder, J.A., Weyer, S., Büchl, A., Kleine, T., and Mezger, K., 2003, Evolution of planetary cores and the earth-moon system from Nb/Ta systematics: Science, v. 301, p. 84–87.

Munoz, J.L., 1984, F-OH and Cl-OH exchange in micas with applications to hydrothermal ore deposits: Reviews in Mineralogy and Geochemistry, v. 13(1), p. 469–493.

Ogunleye, P.O., Garba, I., and Ike, E.C., 2006, Factors contributing to enrichment and crystallization of niobium in pyrochlore in the Kaffo albite arfvedsonite granite, Ririwai Complex, Younger Granites province of Nigeria: Journal of African Earth Sciences, v. 44(3), p. 372–382.

Paludo, C.M., Bastos Neto, A.C., Pereira, V.P., and Botelho, N.F., 2018, Mineralogia e geoquímica de pegmatitos ricos em ETR, F e metais alcalinos associados à facies albita granito no depósito de Sn-Nb-Ta-(F, ETR, U, Th) Madeira (mina Pitinga, AM, Brasil): Pesquisas em Geociências, v. 45, p. 1–28.

Pereira, R.M., Rodrigues, D., Avila, C.A., and Neumann, R., 2011, Stockscheider quartzo-muscovítico e pegmatíticos na zona de cúpula do granitoide Ritápolis, região de São João del Rei, Minas Gerais: Anuário do Instituto de Geociências UFRJ, v. 34(2), p. 59–69.

Pierosan, R., Lima, E.F., Nardi, L.V.S., Campos, C.P., Bastos Neto, A.C., Ferron, J.M.T.M., and Prado, M., 2011a, Paleoproterozoic (~ 1.88 Ga) felsic volcanism of the Iricoumé Group in the Pitinga Mining District area, Amazonian Craton, Brazil: insights in ancient volcanic processes from field and petrological data: Anais da Academia Brasileira de Ciências, v. 83, p. 921–937.

____, Lima, E.F., Nardi, L.V.S., Bastos Neto, A.C., Campos, C.P., Ferron, J.M.T.M., and Prado, M., 2011b, Geochemistry of Paleoproterozoic volcanic rocks of the Iricoumé Group, Pitinga Mining District, Amazonian craton, Brazil: International Geology Reviews, v. 53, p. 946–976.

Pires, A.C., 2005, A gagarinita e fases associadas no Granito Madeira (Pitinga, Amazonas) [M.Sc. thesis]: Porto Alegre, Brasil, Universidade Federal do Rio Grande do Sul, 122 p.

____, Bastos Neto A.C., Pereira V.P., Botelho N.F., and Minuzzi O.R.R., 2006, Gagarinita-(Y) com polimorfo de fluocerita: provável caso de formação de um novo mineral por exsolução de ETRL a partir de fluoreto de ETRLP (Mina Pitinga – AM): Revista Brasileira de Geociências, v. 36(1), p. 155–164.

____, 2010, Xenotima, gagarinita, fluocerita e waimirita da Mina Pitinga (AM): mineralogia e avaliação preliminar do potencial do albita granito para exploração de elementos terras raras e ítrio [Ph.D. thesis]: Porto Alegre, Brasil, Universidade Federal do Rio Grande do Sul, 201 p.

Ronchi, L.H., Bastos Neto, A.C., Gedoz, S.C., Weber, M.L., Pereira, V.P., and Andrek, M., 2011, A transição magmático-hidrotermal registrada por inclusões fluidas no albita-granito de núcleo, Mina Pitinga, Amazonas, *in* Frantz, J.C., Charão, J.M., and Jost, H., eds., Contribuições à metalogenia do Brasil: Porto Alegre, CPRM-UFRGS, cap. 10.

Ronchi, F.C., Althoff, F.J., Bastos Neto, A.C., and Dill, H.G., 2019, Structural control of REE-pegmatites associated with the world-class Sn-Nb-Ta-cryolite deposit at the Pitinga mine, Amazonas, Brazil: Pesquisa em Geociências, v. 46 (1), e0734.

Rosenberg, P.E., and Foit, F.F., 1977, Fe^{2+}-F avoidance in silicates: Geochimica et Cosmochimica Acta, v. 41, p. 345–346.

Santos, J.O.S., Hartmann, L.A., Gaudete, H.E., Groves, D.I., McNaughton, N.J., and Fletcher, L.R.A., 2000, New understanding of the Provinces of Amazon Craton based on Integration of Field Mapping and U-Pb and Sm-Nd geochronology: Gondwana Research, v. 3(4), p. 453–488.

Schmitz, C., and Burt, D.M., 1990, The Black Pearl Mine, Arizona: Wolframite veins and stockscheider pegmatite related to an albitic stock, *in* Stein, H.J., and Hannah, J.L., eds., Ore-bearing granite systems: petrogenesis and mineralizing processes, Geological Society of America Special Paper, v. 246, p. 221–232.

Schuck, C., 2015, Contribuição à mineralogia do albita granito Madeira (Mina Pitinga, Amazonas): estudo do anfibólio, biotita e polilitionita [Monography]: Porto Alegre, Brasil, Universidade Federal do Rio Grande do Sul, 100 p.

Sharygin, V.V., Zubkova, N.V., Pekov, I.V., Rusakov, V.S., Ksenofontov, D.A., Nigmatulina, E.N., and Pushcharovsky, D.Y., 2016, Lithium-containing Na-Fe amphibole from cryolite rocks of the Katugin rare-metal deposit (Transbaikalia, Russia): chemical features and crystal structure: Russian Geology and Geophysics, v. 57, p. 1191–1203.

Siachoque, A., Garcia, R., and Vlach, S.R.F., 2020, Occurrence and composition of columbite-(Fe) in the reduced A-type Desemborque Pluton, Graciosa Province (S-SE Brazil): Minerals, v. 10, p. 411–428.

Simões, M.S.S., Almeida, M.E., Souza, A.G.H., Silva, B.D.P.B., and Rocha, P.G., 2014, Characterization of the volcanic and hypabyssal rocks of the Paleoproterozoic Iricoumé Group in the Pitinga region and Balbina Lake area, Amazonian craton, Brazil: petrographic distinguishing features and emplacement conditions: Journal of Volcanology and Geothermal Research, v. 286, p. 138–147.

Soloviev, S.G., Kryazhev, S., and Dvurechenskaya, S., 2019, Geology, igneous geochemistry, mineralization, and fluid inclusion characteristics of the Kougarok tin-tantalum-lithium prospect, Seward Peninsula, Alaska, USA: Mineralium Deposita, p. 1–28.

Staatz, M.H., and Trites, A.F., 1955, Geology of the Quartz Creek pegmatite district, Gunnison country, Colorado: U.S. Geological Survey, v. 26, p. 1-111.

Stilling, A., Černý, P., and Vanstone, P.J., 2006, The Tanco pegmatite at Bernic Lake, Manitoba. XVI. Zonal and bulk compositions and their petrogenetic significance: The Canadian Mineralogist, v. 44, p. 599–623.

Stolnik, D., 2015, Caracterização da xenotima na fácies pegmatítica do albita granito de núcleo, Pitinga (AM) [Monography]: Porto Alegre, Brasil, Universidade Federal do Rio Grande do Sul, 67 p.

Thomas, R., Webster, J.D., and Heinrich, W., 2000, Melt inclusions in pegmatite quartz: Complete miscibility between silicate melts and hydrous fluids at low pressure: Contributions to Mineralogy and Petrology, v. 139, p. 394–401.

____, Forster, H., Rickers, K., and Webster, J.D., 2005, Formation of extremely F-rich hydrous melt fractions and hydrothermal fluids during differentiation of highly evolved tin-granite magmas: a melt/fluid-inclusion study: Contributions to Mineralogy and Petrology, v. 148, p. 582–601.

____, Webster, J.D., Rhede, D., Seifert, W., Rickers, K., Förster, H.J., Heinrich, W., and Davidson, P., 2006, The transition from peraluminous to peralkaline granitic melts: evidence from melt inclusions and accessory minerals: Lithos, v. 91, p. 137–149.

____, and Davidson, P., 2008, Water and melt/melt immiscibility, the essential components in the formation of pegmatites; evidence from melt inclusions: Z geol Wiss, v. 36, p. 347–364.

____, Davidson, P., Rhede, D., and Leh, M., 2009, The miarolitic pegmatites from the Königshain: a contribution to understanding the genesis of pegmatites: Contributions to Mineralogy and Petrology, v. 157, p. 505–523.

____, Davison, P., and Beurlen, H., 2012, The competing models for the origin and internal evolution of granitic pegmatites in the light of melt and fluid inclusion research: Mineralogy Petrology, v. 106, p. 55–73.

____, and Davidson, P., 2012, Water in granite and pegmatite forming melts: Ore Geology Reviews, v. 46, p. 32–46.

Timofeev, A., Migdisov, A.A., and Williams-Jones, A.E., 2017, An experimental study of the solubility and speciation of tantalum in fluoride-bearing aqueous solutions at elevated temperature, Geochimica and Cosmochimica Acta, v. 197, p. 294–304.

Van Lichtervelde, M., Holtz, F., and Hanchar, J.M., 2010, Solubility of manganotantalite, zircon and hafnon in highly fluxed peralkaline to peraluminous pegmatitic melts. Contributions to Mineralogy and Petrology, v. 160, p. 17–32.

Veiga Jr., J.P., Nunes, A.C.B., Fernandes, A.S., Amaral, J.E., Pessoa, M.R., and Cruz, S.A.S., 1979, Projeto Sulfetos de Uatumã. Relatório Final: Manaus, DNPM/CPRM.

Veksler, I.V., Dorfman, A.M., Dulski, P., Kamenetsky, V.S., Danyushevsky, L.V., Jeffries, T., and Dingwell, D.B., 2012, Partitioning of elements between silicate melt and immiscible fluoride, chloride, carbonate, phosphate and sulfate melts, with implications to the origin of natrocarbonatite, v. 79, p. 20–40.

Williams-Jones, A.E., Vasyukova, O. V., 2023, Niobium, Critical Metal, and Progeny of the Mantle: Economic Geology, v. 118(4), p. 837–855.

Wise, M.A., Černý, P., and Falster, A.U., 1998, Scandium substitution in Columbite-group minerals and ixiolite: The Canadian Mineralogist, v. 36, p. 673–680.

Wood, S.A., 1990, The aqueous geochemistry of the rare earth elements and yttrium–2: Theoretical predictions of speciation in hydrothermal solutions to 350ºC at saturated water pressure: Chemical Geology, v. 88, p. 99–125.

Zaraisky G. P., Korzhinskaya V. S. and Kotova N. P., 2010, Experimental studies of Ta2O5 and columbite-tantalite solubility in fluoride solutions from 300 to 550°C and 50 to 100 MPa: Mineralogy and Petrology, v. 99, p. 287–300.

Zhu, J.C., Li, R.K., Li, F.C., Xiong, X.L., Zhou, F.Y., and Huang, X.L., 2001, Topaz-albite granites and rare-metal mineralization in the Limu District, Guagxi Province, southeast China: Mineralium Deposita, v. 36, p. 393–405.

Zirner, A.L.K., Marks, M.A.W., Wenzel, T., Jacob, D.E., Markl, G., 2015, Rare earth elements in apatite as a monitor of magmatic and metasomatic processes: the Ilimaussaq complex, South Greenland: Lithos, v. 228–229, p. 15–22.

6.3 *Mn-Fe-rich genthelvite from pegmatites associated with the Madeira Sn-Nb-Ta world-class deposit (Pitinga, Brazil): new constraints on the magmatic-hydrothermal transition in the albite-enriched granite system*

Artigo submetido à revista Mineralogical Magazine (A4) dia 16/04/2023.

Submission Confirmation for Mn-Fe-rich genthelvite from pegmatites associated with the Madeira Sn-Nb-Ta world-class deposit (Pitinga, Brazil): new constraints on the magmatic-hydrothermal transition in the albite-enriched granite system - [EMID:a38fea096f0d7bdb]

De Mineralogical Magazine <em@editorialmanager.com>
Remetente <em.minmag.0.82ba47.0f19b099@editorialmanager.com>
Para Ingrid Weber Hadlich <ingrid.hadlich@ufrgs.br>
Responder p... Mineralogical Magazine <helen@minersoc.org>
Data 2023-04-16 23:57

CC: "Artur Cezar Bastos Neto" artur.bastos@ufrgs.br, "Vitor Paulo Pereira" vitor.pereira@ufrgs.br, "Nilson Francisquini Botelho" nilsonfb@unb.br, "Luiz Henrique Ronchi" luiz.ronchi@ufpel.edu.br, "Harold G. Dill" dillhara@uni-mainz.de

Dear Mrs. Hadlich,

Your submission entitled "Mn-Fe-rich genthelvite from pegmatites associated with the Madeira Sn-Nb-Ta world-class deposit (Pitinga, Brazil): new constraints on the magmatic-hydrothermal transition in the albite-enriched granite system" has been received by journal Mineralogical Magazine

You will be able to check on the progress of your paper by logging on to Editorial Manager as an author. The URL is https://www.editorialmanager.com/minmag/.

Your manuscript will be given a reference number once an Editor has been assigned.

Thank you for submitting your work to this journal.

As Mineralogical Magazine offers Open Access (OA) publication, you might also like to find out more about publishing OA such as the benefits of doing so and things you need to know by visiting our Publishing Open Access information page:

https://www.cambridge.org/core/services/authors/journals/publishing-open-access

Kind regards,

Helen

Production Editor
Mineralogical Magazine

A manuscript number has been assigned to Mn-Fe-rich genthelvite from pegmatites associated with the Madeira Sn-Nb-Ta world-class deposit (Pitinga, Brazil): new constraints on the magmatic-hydrothermal transition in the albite-enriched granite system - [EMID:fe49ef4ae077deb3]

De Mineralogical Magazine <em@editorialmanager.com>
Remetente <em.minmag.0.82ba47.0f19b099@editorialmanager.com>
Para Ingrid Weber Hadlich <ingrid.hadlich@ufrgs.br>
Responder p... Mineralogical Magazine <helen@minersoc.org>
Data 2023-04-16 23:57

CC: "Artur Cezar Bastos Neto" artur.bastos@ufrgs.br, "Vitor Paulo Pereira" vitor.pereira@ufrgs.br, "Nilson Francisquini Botelho" nilsonfb@unb.br, "Luiz Henrique Ronchi" luiz.ronchi@ufpel.edu.br, "Harold G. Dill" dillhara@uni-mainz.de

Due to the COVID-19 outbreak and the uncertainty it is creating, some reviews are currently taking longer than usual. We want to reassure authors that the journal remains open to submissions and we're doing our best to minimize any delays.

Dear Mrs. Hadlich,

Your submission entitled "Mn-Fe-rich genthelvite from pegmatites associated with the Madeira Sn-Nb-Ta world-class deposit (Pitinga, Brazil): new constraints on the magmatic-hydrothermal transition in the albite-enriched granite system" has been been assigned the following manuscript number: MINMAG-D-23-00039.

You will be able to check on the progress of your paper by logging on to Editorial Manager as an author.
The URL is https://www.editorialmanager.com/minmag/.

As Mineralogical Magazine offers Open Access (OA) publication, you might also like to find out more about publishing OA such as the benefits of doing so and things you need to know by visiting our Publishing Open Access information page:

https://www.cambridge.org/core/services/authors/journals/publishing-open-access

Thank you for submitting your work to this journal.

Kind regards,

Mineralogical Magazine

Mn-Fe-rich genthelvite from pegmatites associated with the Madeira Sn-Nb-Ta world-class deposit (Pitinga, Brazil): new constraints on the magmatic-hydrothermal transition in the albite-enriched granite system

I. W. Hadlich[1]*, A. C. Bastos Neto[1], V. P. Pereira[1], N. F. Botelho[2], L. H. Ronchi[4] and H. G. Dill[5]

[1]Instituto de Geociências, Universidade Federal do Rio Grande do Sul, Av. Bento Gonçalves 9500, 91501-970 Porto Alegre, RS, Brazil; [2]Instituto de Geociências, Universidade de Brasília, Campus Universitário Darcy Ribeiro, Asa Norte, 70910-900 Brasília, DF, Brazil; [3]Centro de Desenvolvimento Tecnológico, Universidade Federal de Pelotas, Praça Domingos Rodrigues 2, 96010-440 Pelotas, RS, Brazil; [4]Gottfried Wilhelm Leibniz University, Welfengarten 1, D-30167 Hannover, Germany
*Corresponding author e-mail: ingrid.hadlich@ufrgs.br

Abstract

We studied the genthelvite from pegmatites associated with the albite-enriched granite (ca.1.820 Ma) which corresponds to the world-class Sn-Nb-Ta (F, REE, Li, Zr, U, Th) Madeira deposit (Amazonas, Brazil). Genthelvite, the only Be-bearing mineral, occurs as massive crystals of up to 4.7 cm surrounding polylithionite and quartz phenocrysts. Compositions are homogeneous and correspond to relatively limited substitutions in the helvine-genthelvite-danalite solid solution system, with relatively high contents of Zn (36.96 to 49.45 wt.% ZnO), low contents of Mn (0.61 to 3.03 wt.% MnO) and variable contents of Fe (2.10 to 10.94 wt.% FeO), filling an up-to-date compositional gap in this system. Remarkable features are the high contents of U (0.13 to 0.25 wt.% UO_2) and REE (up to 0.40 wt.% REE_2O_3) and the higher LREE average content over the HREE. Genthelvite formed in an alkaline and subaluminous environment, at a stable condition in the late evolved fluids under a relatively high temperature (>375°C) and reducing conditions. The extremely high concentration of fluorine in the magma and the crystallisation of large amounts of galena led to an effective decrease in the H_2S fugacity, allowing the stability of genthelvite between late magmatic and early hydrothermal stages of the albite-enriched granite evolution. The variable content of Fe in genthelvite and the wide formation of Mn and Fe oxides (columbite, hematite) attests an O activity too high to favour danalite formation. Genthelvite was affected by F-rich low-temperature aqueous fluids. The rebalance allowed the incorporation of Fe, Mn, Mg, Pb, Ba, Na, K, U and REE in the Zn^{2+} structural site, and the allocation of excess Si, Al, Ti and P in the ^{IV}Si and ^{IV}Be structural sites. The high content of U and REE replacing Zn and of Si replacing Be are charge balanced by vacancies at the A-site ($Zn^{2+} + Be^{2+} \leftrightarrow \square + Si^{4+}$).

Key words: genthelvite, beryllium, solid solution, albite-enriched granite, Pitinga, Brazil.

Introduction

Helvine-group minerals are anhydrous sulfossilicates, isometrics and isostructural with the space group P43n and have the general formula $A_8Be_6(SiO_4)_6S_2$, in which the species are defined by the cation in the A crystallographic site. The species helvine ($Mn_4Be_3Si_3O_{12}S$), danalite ($Fe_4Be_3Si_3O_{12}S$) and genthelvite ($Zn_4Be_3Si_3O_{12}S$) form a solid solution, whose proportions are defined by the states of reduction, sulfidation and alkalinity of the system (Burt, 1980). Complete miscibility should exist between the three final terms (Hassan and Grundy, 1985), however, there are apparent gaps between the end-members Zn-Fe, Zn-Mn and Mn-Fe and no pure danalite was observed in nature (Oftaedal and Saebo, 1936; Clark and Fejer, 1976; Dunn, 1976; Larsen, 1988; Perez et al., 1990; Langhof et al., 2000; Bilal, 2013).

The helvine-group have occurrence restricted to peralkaline and alkaline granites, syenites, rare metal pegmatites, albitites, greisens, skarns and contact zones (Deer et al., 2004). In this work, we study the genthelvite that occurs in pegmatites associated with the albite-enriched granite (AEG) facies of Madeira granite. This facies corresponds to the Madeira world-class deposit, which is characterized by an association of Sn with cryolite, Nb, Ta (Y, REE, Li, Zr, U and Th) in the same AEG that hosts a massive cryolite deposit. The genthelvite crystals occur in pegmatites found in the most differentiated portion in the centre of the pluton. These pegmatites fit in the CMS (Dill, 2016) classification as the 24dE type because they are hosted in alkaline igneous rocks and are carriers of REE-Y ores. According to the classification by Černý and Ercit (2005), they belong to the Rare Elements class and the NYF family, as they are rich in REE, Nb, Y and F, and are associated with A-type granites in environments with low pressures and temperatures.

We demonstrate the existence of natural genthelvite along the upper part of the joint Zn-Fe in the Zn-Fe-Mn ternary diagram, filling an up-to-date compositional gap in the helvine-group. This feature, together with the high REE and U concentrations, make this genthelvite unique in the world. The study of genthelvite brought new constraints on the conditions of the magmatic-hydrothermal transition in the AEG system. Genthelvite formed in an alkaline and subaluminous environment, at a stable condition in the late evolved fluids, under relatively high temperature (>375°C), low H_2S fugacity and high O activity.

Previous work

Geological setting

The Pitinga Province is located (Fig. 1) in the southern portion of the Guyana Shield (Almeida et al., 1981), in the Tapajos-Parima Tectonic Province (Santos et al., 2000). The Pitinga Province is the largest Sn producer in Brazil. The alluvial ore deposits were discovered in 1979 (Veiga et al., 1979) and are almost exhausted. The primary ores are associated with two main tin-bearing granites: the Madeira and Agua Boa A-type granites (Fig. 1). Both are part of the ca. 1.830 Ma Madeira Suite (Costi, 2000). The Madeira deposit, which has been exploited since 1989, is associated with the Madeira granite (Fig. 2). Moreover, several small greisens associated with the Agua Boa granite have been intermittently exploited.

The volcanic rocks of the Iricoume Group (Veiga et al., 1979) predominate in the Pitinga Province and host the Madeira Granite (Fig. 1). They have $^{207}Pb/^{206}Pb$ zircon ages between 1881 ± 2 and 1890 ± 2 Ma (Ferron et al., 2006). They comprise mostly effusive and hypabyssal rhyolites, highly welded ignimbrites, ignimbritic tuffs, and surge deposits formed in a subaerial environment with cyclic effusive and explosive activities (Pierosan et al., 2011; Simões et al., 2014).

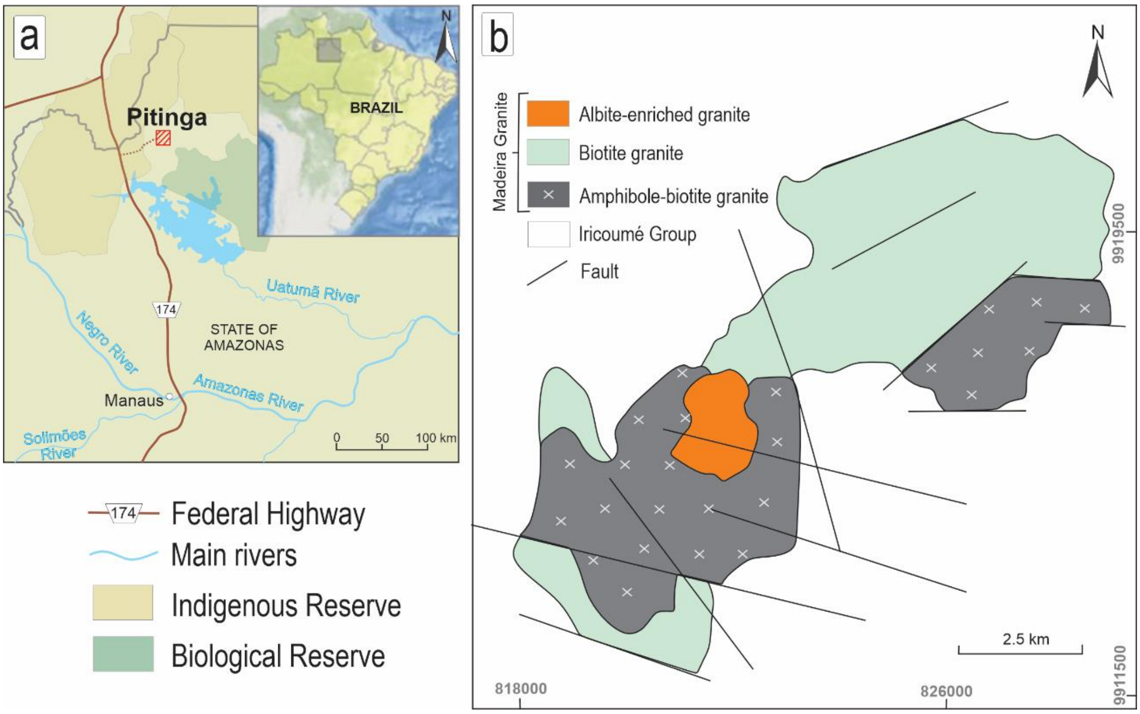

Fig. 1. (a) Location map; (b) geological map of the Madeira Granite (modified from Costi, 2000).

The Madeira granite contains four facies (Figs. 1, 2). The older biotite-K-feldspar granite facies is peraluminous, equigranular, and locally porphyritic. The alkali feldspar hypersolvus porphyritic granite facies have K-feldspar phenocrysts in a fine- to medium-grained matrix dominantly composed of K-feldspar and quartz. According to Costi (2000), the hypersolvus granite and the albite-enriched granite were emplaced simultaneously, and then interacted and intruded into the older facies.

The albite-enriched granite (AEG) is an oval-shaped body with an outcropping surface of approximately 2×1.3 km. It is divided into subfacies albite-enriched granite core (AGC) and albite-enriched granite border (AGB). The AGC is a peralkaline subsolvus granite, porphyritic to seriate in texture, fine- to medium-grained, and composed of quartz, albite and K-feldspar in approximately equal proportions (25–30%). The accessory minerals are cryolite (5%), polylithionite (4%), green–brown mica (3%), zircon (2%) and riebeckite (2%). Pyrochlore, cassiterite, xenotime, columbite, thorite, magnetite and galena occur in minor proportions. The AGB is peraluminous and presents types of texture and essential mineralogy similar to that in the AGC, except for being richer in zircon, for the presence of fluorite instead of cryolite and for the absence of iron-rich silicate minerals, which have almost completely disappeared due to an autometasomatic process (Costi et al., 2000, 2010).

Despite the disseminated character of the AEG mineralization, there are small zones of enrichment associated with the granite in which specific minerals may be considerably abundant, and these are:

(1) ~50 cm thick pods and bands of the pegmatitic albite-enriched granite (rarely up to 10 m thick; Stolnik, 2015) that show gradational contacts with the albite-enriched granite itself; it has the same minerals as the AGC, but polylithionite, riebeckite, xenotime and thorite are more abundant and larger than in the AGC.

(2) Border pegmatites (BPEG) that are at the contact between the AGB and the older facies (Fig. 2). They are characterized by the increased sizes and amounts of quartz and zircon, advanced alterations of K-feldspar and biotite and by local enrichments in fluorite, polylithionite, thorite and secondary hematite (Lengler, 2016).

(3) Pegmatite veins which are not mappable, occur more commonly in the central, northern and northwest parts of the AGC and have thicknesses ranging from a few centimetres up to 2 m. They are heterogeneous and more commonly porphyritic. The phenocrystals may be of quartz, K-feldspar, xenotime, thorite, cryolite, polylithionite and riebeckite. The matrix is composed of albite, quartz, K-feldspar, polylithionite, cryolite and riebeckite; the accessory minerals are zircon, cassiterite, pyrochlore, columbite, galena, sphalerite, hematite, gagarinite and genthelvite (Paludo, 2015). Genthelvite occurs only in these pegmatite veins and it was identified by Ronchi et al. (2011). These pegmatites occur either in veins or in tabular bodies associated with fractures and faults. The main bodies have thicknesses up to 1 m and the veins located in the fault planes are centimetric. These fractures and faults served as a conduit for the fluids, with transport from SW to NE, in a compressive system, with horizontal tension and at low solidus temperature (Ronchi et al., 2019). Differences in the composition and modal values of these pegmatites made it possible for Paludo et al. (2018) separate them into three groups: (i) rich in amphiboles (riebeckite, fluorarfvedsonite, fluoreckermanite), with intermediate values of K and Na; (ii) rich in polylithionite, with high values of K; (iii) rich in cryolite, with high values of Na.

(4) Several bodies of massive cryolite intercalated with AGC and hypersolvus granite; these are sub-horizontal, up to 300 m long and 30 m thick and composed of cryolite crystals (~87 vol.%), quartz, zircon and feldspar (Minuzzi et al., 2006).

Costi et al. (2010) consider the albite-enriched granite core (AGC) to be the result of a phase-separation process, or immiscibility, similar to that registered by Thomas et al. (2006) in the Variscan Erzgebirge granites, Germany. Bastos Neto et al. (2009, 2014) consider that the A-type magmatism in Pitinga evolved from a post-collisional extensional setting, probably in a within-plate scenario in which extensional and transtensional tectonic regimes dominated. In this context, the AEG magma would have been related to the isotherm rise, which occurred when the mantle fluid ascended further into the crust promoting fenitization-type reactions (Martin, 2006) in rocks previously enriched in Sn, and introduced elements such as F, Nb, Y, REE and Th in anomalous concentrations. The input of a F-rich fluid took place and generated metasomatism causing the rock to become fusible.

Horbe et al. (1985) and Teixeira et al. (1992) attributed a metasomatic genesis to the AEG. Lenharo (1998) and Costi (2000) considered that the magma evolved towards an extremely Na-, F-enriched residual melt. Costi (2000) interpreted that, at the point of H_2O saturation, the extremely F-enriched residual fluid was separated into an aqueous, relatively F-poor portion and a low-H_2O, Na-Al-F-rich portion. The H_2O-depleted, Na–Al–F-rich fraction resulted in the formation of massive cryolite bodies, whereas the H_2O-rich fraction formed the associated quartz-, feldspar- and mica-bearing pegmatitic rocks. In accordance with Bastos Neto et al. (2009), the extreme fluorine enrichment in the residual melt is improbably to have been attained, because the F content was buffered by crystallisation of magmatic cryolite (Dolejs and Baker, 2007). Furthermore, fluid inclusions data (Bastos Neto et al., 2009; Ronchi et al., 2011) show that the massive cryolite deposit was formed from an aqueous, saline hydrothermal fluid. The higher homogenization temperature of 400°C, measured in massive cryolite, determines the minimum starting temperature for the hydrothermal process.

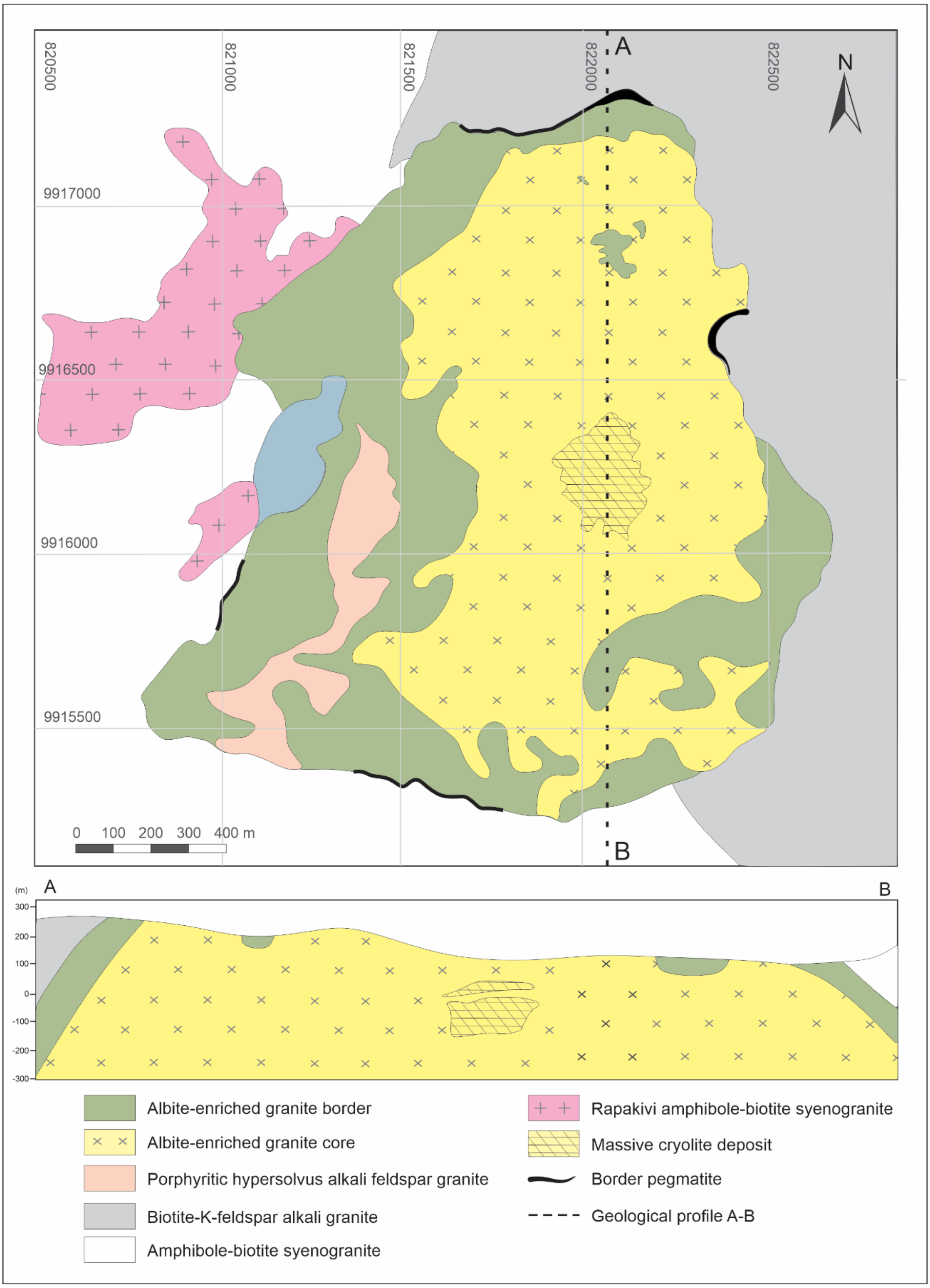

Fig. 2. Geological map of the albite-enriched granite (modified from Minuzzi, 2005).

Methods

Genthelvite crystals belonging to several pegmatitic veins were described and identified by combining optical properties, chemical analyses and powder-diffraction data. The pegmatite veins are spread throughout the AGC and are non-mappable due to its small size (up to 2 m thick). Sampling was carried out mainly in the central area of the AGC, on the surface of the open pit. Over 50 thin sections of the pegmatites were analysed and, among those which contained genthelvite, 10 were examined by back-scattered electron microscopy (BSE image), with qualitative analysis using an energy-dispersive X-ray detector (Zeiss, model EVO MA10) at the Centre for Microscopy and Microanalysis in Universidade Federal do Rio Grande do Sul (UFRGS).

In all, five samples were selected for electron-probe microanalysis (EPMA) carried out at the EPMA Laboratory of the Universidade de Brasília (UnB), with a JEOL JXA-8230 equipped with five WDS spectrometers for quantitative analyses and one EDS for qualitative analyses. The concentrations of F, Mg, Zn, Al, Si, Hf, Nb, P, Cl, S, Bi, Ti, Mn, Y, Ta, Sn, Ca, Zr, Fe, V and Rb were determined with an accelerating voltage of 15 kV and 10 nA of sample current, whereas the concentrations of Na, Er, Tm, Yb, Ho, Lu, K, Pb, Dy, Tb, Sm, Gd, Eu, Sr, Th, Pr, Nd, Ce, La, Ba and U were determined with an accelerating voltage of 20 kV and 50 nA. Each element was analysed with a beam diameter of 1 μm. The counting times on the peaks were 10 s for all elements, and half that time for background counts on both sides of the peaks.

The *K*α lines were used for the determination of: Fe, Mn, Mg, S, F, Na, K, Si, Al, Cl, Ti, V and P; *K*β lines for Ca; *L*α lines for Zn, Sn, Ba, Rb, Sr, La, Ce, Nd, Eu, Gd, Tb, Er, Tm, Yb, Lu and Y; *L*β lines for: Pr, Sm, Dy, Ho, Zr and Nb; *M*α lines for: Ta, Th and Hf; and *M*β lines for Bi, U and Pb. The following crystals were used: TAP for Si, Zn, Na and Al; PETJ for Nb, P, Hf, Cl, S, K, Bi, Sr, Y, Ta, Sn, Th and Pb; PETH for Rb, Zr and U; LIF for Ti, Mn, Sm, Eu, Gd, Dy, Er, Ho, Tb, Tm, Yb and Lu; LIFH for Ca, Fe, Ba, V, La, Ce, Pr and Nd; and LDE1 for F. Interference corrections were applied in all cases of peak overlap. The following standards were used: microcline (Si, K and Al), albite (Na), apatite (P and Ca), andradite (Fe), topaz (F), forsterite (Mg), vanadinite (V, Pb and Cl), pyrite (S), $MnTiO_3$ (Mn), YFe_2O_{12} (Y), $LiNbO_3$ (Nb), $LiTaO_3$ (Ta), $MnTiO_3$ (Ti and Mn), ZnS (Zn), Bi_2O_3 (Bi), RbSi (Rb), $BaSO_4$ (Ba), baddeleyite (Zr), HfO_2, $SrSO_4$ (Sr), SnO_2, ThO_2, UO_2 and synthetic REE-bearing glasses.

Crystallographic studies were performed in the X-Ray Diffraction Laboratory at UFRGS using a Siemens D5000 X-ray Diffractometer (XRD) with a scanning step of 0.05°2θ, a time of 1 s, between 5 and 100°2θ, Cu*K*α radiation (1.5418 Å) and a Ni filter. Crystallographic parameters were determined using the UnitCell program (Holland and

Redfern, 1997), being processed the diffractions of 19 (reflections) faces. The error in the processed values was 0.00017, with 95% reliability.

Results

Mineralogy, petrography and BSE

For this work, we completed the study by Paludo et al. (2018) and defined the paragenetic succession shown in Fig. 3. The phenocrystals may be of quartz I, K-feldspar, xenotime, thorite, cryolite I, polylithionite and riebeckite. The matrix is composed of albite, quartz I and II, K-feldspar, polylithionite, cryolite I and II, riebeckite, fluoroarfvedsonite and fluoroeckermanite; the accessory minerals are zircon, cassiterite, pyrochlore, columbite, galena, sphalerite, native-bismuth, hematite, gagarinite-(Y) and genthelvite.

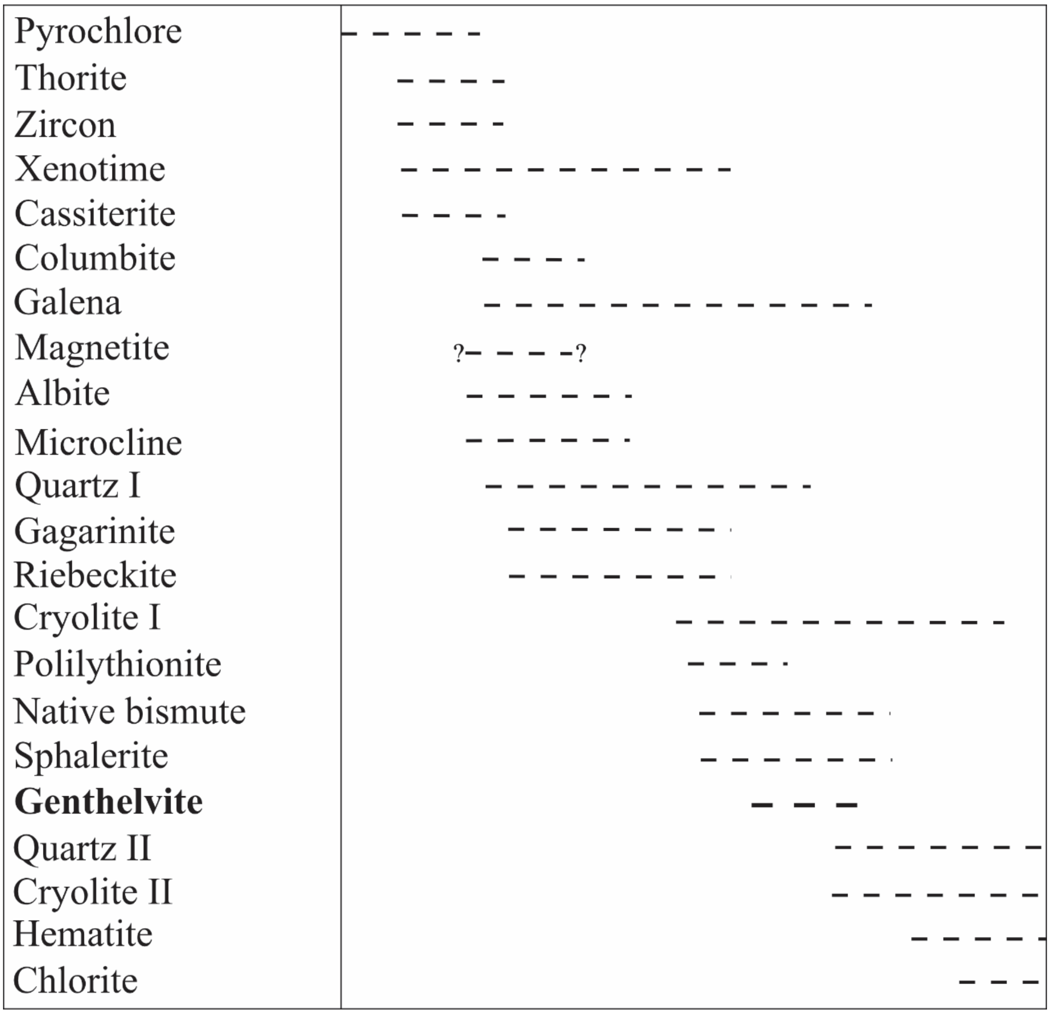

Fig. 3. Paragenesis evolution in pegmatites from the albite-enriched granite (modified from Paludo et al., 2018).

Genthelvite crystals from the pegmatites associated with the AEG have sizes from 1.0 mm to 4.7 cm and present a light pink colour in macroscopic samples (Fig. 4). Under optical microscope its grains are commonly anhedral, colourless in natural light and isotropic in polarized light (Fig. 5a, b).

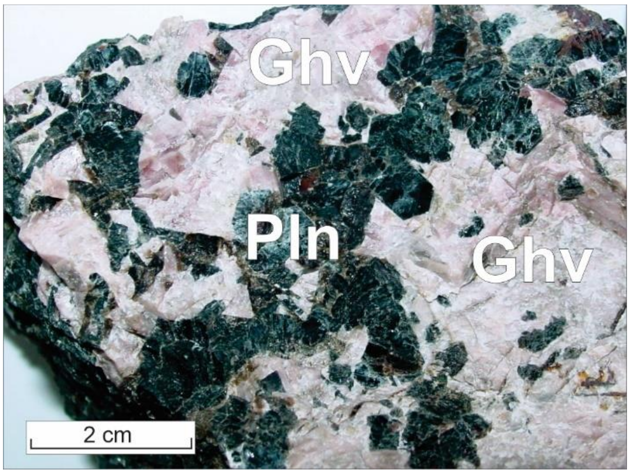

Fig. 4. Macroscopic sample of genthelvite from the pegmatite associated with the albite-enriched granite. Genthelvite (Ghv) occurs surrounding polylithionite (Pln) crystals.

In the pegmatites genthelvite occurs predominantly as massive crystals surrounding polylithionite and quartz I phenocrysts and includes crystals of accessory minerals as pyrochlore, thorite and zircon (Fig. 5a-d). Subordinately genthelvite occurs filling voids and microfractures in quartz I (Fig. 5e) and polylithionite phenocrysts or arranged interstitially in the matrix with quartz I and orthoclase (Fig. 5f).

The contact with polylithionite is rectilinear and slightly reactive. The contact with quartz I is undulated and reactive. The contact with pyrochlore, zircon and thorite is undulated and reactive, and these minerals have a partially dissolved aspect. The samples present hydrothermal alteration. Genthelvite is characterized by corrosion features as cavities and microfractures which are commonly filled by cryolite II (Fig. 5g). Hydrothermal quartz II also occurs associated with genthelvite, specially filling the channels opened along genthelvite growth lines (Fig. 5h).

For all these characteristics, genthelvite is considered a mineral of late crystallisation, preceded by the crystallisation of polylithionite and early quartz I and formed before the hydrothermal cryolite II.

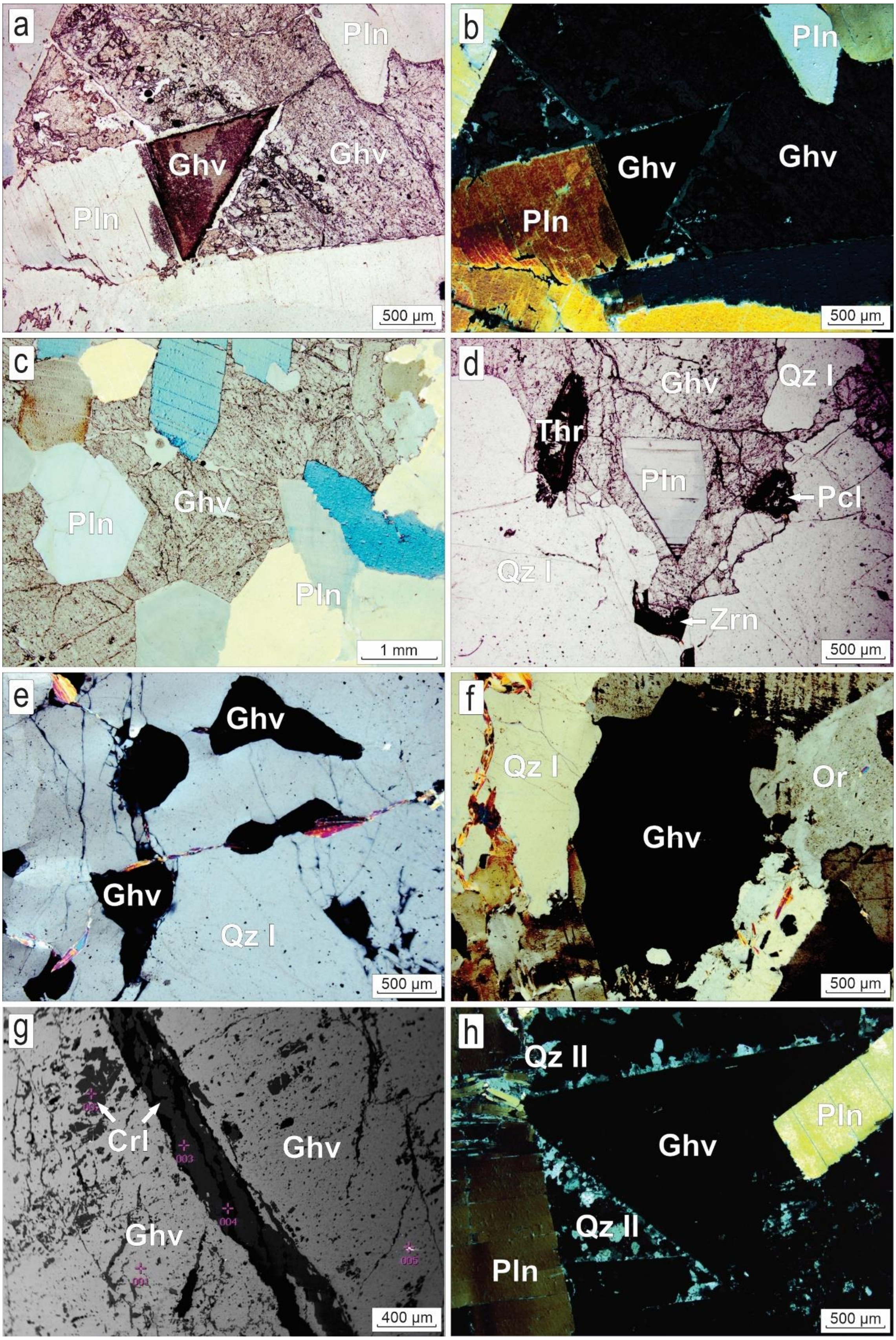

Fig. 5. Photomicrographs and BSE image of genthelvite from the pegmatites associated with the albite-enriched granite: (a) typical genthelvite from the pegmatites, with triangular cleavage, associated with polylithionite, NL; (b) same as in a, PL; (c)

genthelvite filling the space between polylithionite crystals, NL; (d) genthelvite associated with quartz I, pyrochlore, thorite and zircon, NL; (e) genthelvite filling voids in quartz I, PL; (f) genthelvite in the matrix with quartz I and orthoclase, PL; (g) BSE image of genthelvite with microfractures filled by cryolite II; (h) Quartz II along genthelvite growth lines, PL. Abbreviations: Ghv = genthelvite, Crl II = hydrothermal cryolite II, Qz II = hydrothermal quartz II, Or = orthoclase, Pln = polylithionite, Pcl = pyrochlore, Qz I = quartz I, Thr = thorite, Zrn = zircon, NL = natural light transmitted, PL = polarized light.

Genthelvite composition

The helvine-group minerals can be represented by the general formula $A^{2+}{}_8Be_6Si_6O_{24}S_2$. Calculations on the basis of 26 O and S atoms and Be = 6 apfu (Zito and Hanson, 2017) shows cations systematically in deficit on the A-site and in excess on the Si-site. Therefore, in this study calculations were performed through the following assumptions: the crystal structure is charge balanced; the anion site is fully occupied (*i.e.* O + S = 26); the Si site is fully occupied by P^{5+}, Si^{4+}, Ti^{4+}, Al^{3+} (preferential order of occupation is P > Si > Ti > Al according to ionic potential); the excess in the Si site (*i.e.* $^{IV}Si > 6$ apfu) is allocated in the ^{IV}Be site with the preferential order of occupation Al > Ti > Si > P. Be^{2+} is calculated to yield a total of Be + Si = 12 apfu (*i.e.* site $^{IV}Be = 6$) (Dunn, 1976; Finch, 1990); the A site has a vacancy (□) and is occupied by U^{4+}, A^{3+} (Ce, Pr, Nd, Sm, Eu, Gd, Ho and Er), A^{2+} (Zn, Fe, Mn, Mg, Pb and Ba) and A^{+} (Na and K) (*i.e.* site $^{IV}A = 8 - □$).

Representative compositions for genthelvite are given in Table 1. Low concentrations (hundreds to thousands of ppm) of V, Th, Cr, La, Dy, Tm, Yb, Lu, Bi, Ca, Ni, Sr and Cl were detected. These elements were not considered in the totals of the analyses and in structural calculations.

Table 1. EPMA data (wt.%) for Mn-Fe-rich genthelvite (Pitinga pegmatites).

Sample	P09.B.2	P09.C.1	P09.C.2	P09.D.15	P09.D.20	P09.D.24	P14.2.4	P14.3.1	P14.3.2	P26.1.3	P26.1.4	P26.1.8	P26.1.9
P_2O_5	0.14	0.38	0.11	n.d.	n.d.	n.d.	0.09	0.26	0.37	n.d.	n.d.	n.d.	n.d.
SiO_2	29.30	29.52	29.79	30.39	32.19	31.27	30.17	30.30	30.27	31.55	31.37	31.55	31.07
UO_2	0.13	0.21	0.23	0.13	0.13	0.14	0.25	0.17	0.22	0.18	0.16	0.14	0.17
TiO_2	n.d.	0.30	0.15	0.13	n.d.	n.d.	0.18	n.d.	n.d.	0.07	n.d.	n.d.	n.d.
Al_2O_3	n.d.	n.d.	0.03	0.04	n.d.	n.d.	0.16	n.d.	n.d.	0.03	n.d.	n.d.	0.25
Ce_2O_3	n.d.	n.d.	n.d.	n.d.	0.11	n.d.	n.d.	n.d.	n.d.	0.08	0.05	n.d.	0.05
Nd_2O_3	n.d.	n.d.	n.d.	0.06	n.d.	n.d.	n.d.	n.d.	0.05	0.03	0.03	n.d.	n.d.
Sm_2O_3	n.d.	n.d.	n.d.	n.d.	n.d.	n.d.	n.d.	0.11	n.d.	n.d.	0.11	n.d.	n.d.
Eu_2O_3	n.d.	n.d.	0.05	0.04	0.07	n.d.	n.d.	0.08	n.d.	n.d.	n.d.	n.d.	0.08
Gd_2O_3	n.d.	n.d.	0.05	n.d.	n.d.	n.d.	n.d.	n.d.	n.d.	n.d.	n.d.	n.d.	n.d.
Ho_2O_3	n.d.	n.d.	0.08	n.d.	n.d.	0.17	n.d.	n.d.	n.d.	n.d.	n.d.	n.d.	n.d.

Er_2O_3	n.d.	n.d.	n.d.	n.d.	0.05	0.04	0.08	n.d.	n.d.	n.d.	0.10	0.04	n.d.
ZnO	44.00	41.41	43.18	41.70	36.96	44.90	49.45	40.56	40.22	46.95	45.76	45.44	45.02
FeO	6.37	08.18	7.66	7.60	10.94	6.03	2.10	9.02	8.95	4.41	4.50	4.84	3.71
MnO	1.13	02.08	1.80	2.64	3.03	1.63	0.61	1.63	2.11	1.52	1.43	1.72	1.75
MgO	0.05	0.02	n.d.	0.02	n.d.	0.02	n.d.	n.d.	n.d.	n.d.	n.d.	n.d.	0.06
PbO	0.03	0.04	n.d.	n.d.	n.d.	n.d.	n.d.	n.d.	n.d.	n.d.	0.04	0.03	0.03
BaO	0.02	0.03	n.d.	0.08	0.06	0.13	0.05	n.d.	n.d.	n.d.	n.d.	0.14	n.d.
BeO*	12.17	12.31	12.49	12.40	12.08	12.41	12.06	12.16	12.19	12.31	12.05	12.11	11.73
Na_2O	n.d.	n.d.	n.d.	0.32	0.03	0.20	n.d.	n.d.	n.d.	0.03	n.d.	n.d.	0.26
K_2O	0.03	n.d.	n.d.	0.02	n.d.	n.d.	0.05	n.d.	n.d.	n.d.	n.d.	0.02	n.d.
S	5.30	5.36	5.52	5.07	5.26	5.33	5.33	5.49	5.51	5.43	5.34	5.43	5.28
$S = O_2$	-2.64	-2.67	-2.75	-2.53	-2.63	-2.66	-2.66	-2.74	-2.75	-2.71	-2.67	-2.71	-2.63
Total	96.01	97.16	98.37	98.12	98.28	99.60	97.92	97.04	97.13	99.87	98.29	98.74	96.83
Structural formula based on 26 O + S and a sum of 12 apfu in the $^{[IV]}$Be and $^{[IV]}$Si sites													
U^{4+}	0.006	0.010	0.010	0.006	0.006	0.006	0.011	0.008	0.010	0.008	0.007	0.006	0.008
Ce^{3+}	n.d.	n.d.	n.d.	n.d.	0.008	n.d.	n.d.	n.d.	n.d.	0.005	0.004	n.d.	0.003
Nd^{3+}	n.d.	n.d.	n.d.	0.004	n.d.	n.d.	n.d.	n.d.	0.004	0.002	0.002	n.d.	n.d.
Sm^{3+}	n.d.	n.d.	n.d.	n.d.	n.d.	n.d.	n.d.	0.008	n.d.	n.d.	0.008	n.d.	n.d.
Eu^{3+}	n.d.	n.d.	0.003	0.003	0.005	n.d.	n.d.	0.005	n.d.	n.d.	n.d.	n.d.	0.005
Gd^{3+}	n.d.	n.d.	0.003	n.d.	n.d.	n.d.	n.d.	n.d.	n.d.	n.d.	n.d.	n.d.	n.d.
Ho^{3+}	n.d.	n.d.	0.005	n.d.	n.d.	0.010	n.d.	n.d.	n.d.	n.d.	n.d.	n.d.	n.d.
Er^{3+}	n.d.	n.d.	n.d.	n.d.	0.003	0.002	0.005	n.d.	n.d.	n.d.	0.006	0.002	n.d.
Zn^{2+}	6.642	6.143	6.367	6.122	5.348	6.511	7.347	6.010	5.942	6.793	6.722	6.638	6.686
Fe^{2+}	1.089	1.374	1.280	1.265	1.793	0.991	0.354	1.514	1.497	0.723	0.749	0.801	0.624
Mn^{2+}	0.196	0.353	0.304	0.445	0.503	0.271	0.105	0.278	0.358	0.252	0.241	0.288	0.299
Mg^{2+}	0.015	0.006	n.d.	0.007	n.d.	0.005	n.d.	n.d.	n.d.	n.d.	n.d.	n.d.	0.019
Pb^{2+}	0.002	0.002	n.d.	n.d.	n.d.	n.d.	n.d.	n.d.	n.d.	n.d.	0.002	0.001	0.001
Ba^{2+}	0.002	0.002	n.d.	0.006	0.005	0.010	0.004	n.d.	n.d.	n.d.	n.d.	0.011	n.d.
Na^{+}	n.d.	n.d.	n.d.	0.123	0.011	0.075	n.d.	n.d.	n.d.	0.013	n.d.	n.d.	0.103
K^{+}	0.008	n.d.	n.d.	0.006	n.d.	n.d.	0.012	n.d.	n.d.	n.d.	n.d.	0.004	n.d.
$\Sigma_{[IV]A}$	7.959	7.891	7.972	7.986	7.682	7.882	7.838	7.822	7.810	7.797	7.742	7.752	7.748
Be^{2+}	5.977	5.942	5.995	5.925	5.689	5.857	5.831	5.864	5.862	5.797	5.759	5.758	5.668
Al^{3+}	n.d.	n.d.	0.005	0.012	n.d.	n.d.	0.051	n.d.	n.d.	0.008	n.d.	n.d.	0.081
Ti^{4+}	n.d.	0.045	n.d.	0.020	n.d.	n.d.	0.027	n.d.	n.d.	0.010	n.d.	n.d.	n.d.
Si^{4+}	0.023	0.013	n.d.	0.043	0.311	0.143	0.091	0.136	0.138	0.185	0.241	0.242	0.251
$\Sigma_{[IV]Be}$	6.000	6.000	6.000	6.000	6.000	6.000	6.000	6.000	6.000	6.000	6.000	6.000	6.000
P^{5+}	0.032	0.082	0.023	n.d.	n.d.	n.d.	0.020	0.056	0.081	n.d.	n.d.	n.d.	n.d.
Si^{4+}	5.968	5.918	5.950	6.000	6.000	6.000	5.980	5.944	5.919	6.000	6.000	6.000	6.000
Ti^{4+}	n.d.	n.d.	0.022	n.d.	n.d.	n.d.	n.d.	n.d.	n.d.	n.d.	n.d.	n.d.	n.d.
Al^{3+}	n.d.	n.d.	0.005	n.d.	n.d.	n.d.	n.d.	n.d.	n.d.	n.d.	n.d.	n.d.	n.d.
$\Sigma_{[IV]Si}$	6.000	6.000	6.000	6.000	6.000	6.000	6.000	6.000	6.000	6.000	6.000	6.000	6.000
O^{2-}	23.969	23.982	23.934	24.112	24.067	24.040	23.990	23.935	23.934	24.004	24.008	23.987	24.011
S^{2-}	2.031	2.018	2.066	1.888	1.933	1.960	2.010	2.065	2.066	1.996	1.992	2.013	1.989
Σ_X	26.000	26.000	26.000	26.000	26.000	26.000	26.000	26.000	26.000	26.000	26.000	26.000	26.000

*BeO calculated considering a total of Be + Si = 12 apfu; n.d. = not detected.

Genthelvite has homogeneous composition within grains and is a Mn-Fe-rich genthelvite, expressing a solid solution in the genthelvite-danalite-helvine system, with relatively limited substitutions between Zn^{2+}, Fe^{2+} and Mn^{2+}. These elements vary in a range of 36.96 to 49.45 wt.% ZnO, 2.10 to 10.94 wt.% FeO and 0.61 to 3.03 wt.% MnO. The composition of genthelvite plotted in terms of the relative proportions of Zn, Fe and Mn (expressed as percentages of [Zn + Fe + Mn] atoms) (Fig. 6) reflect the predominance of compositions along the upper part of the joint Zn-Fe, although invariably the presence of a small component of helvine occurs.

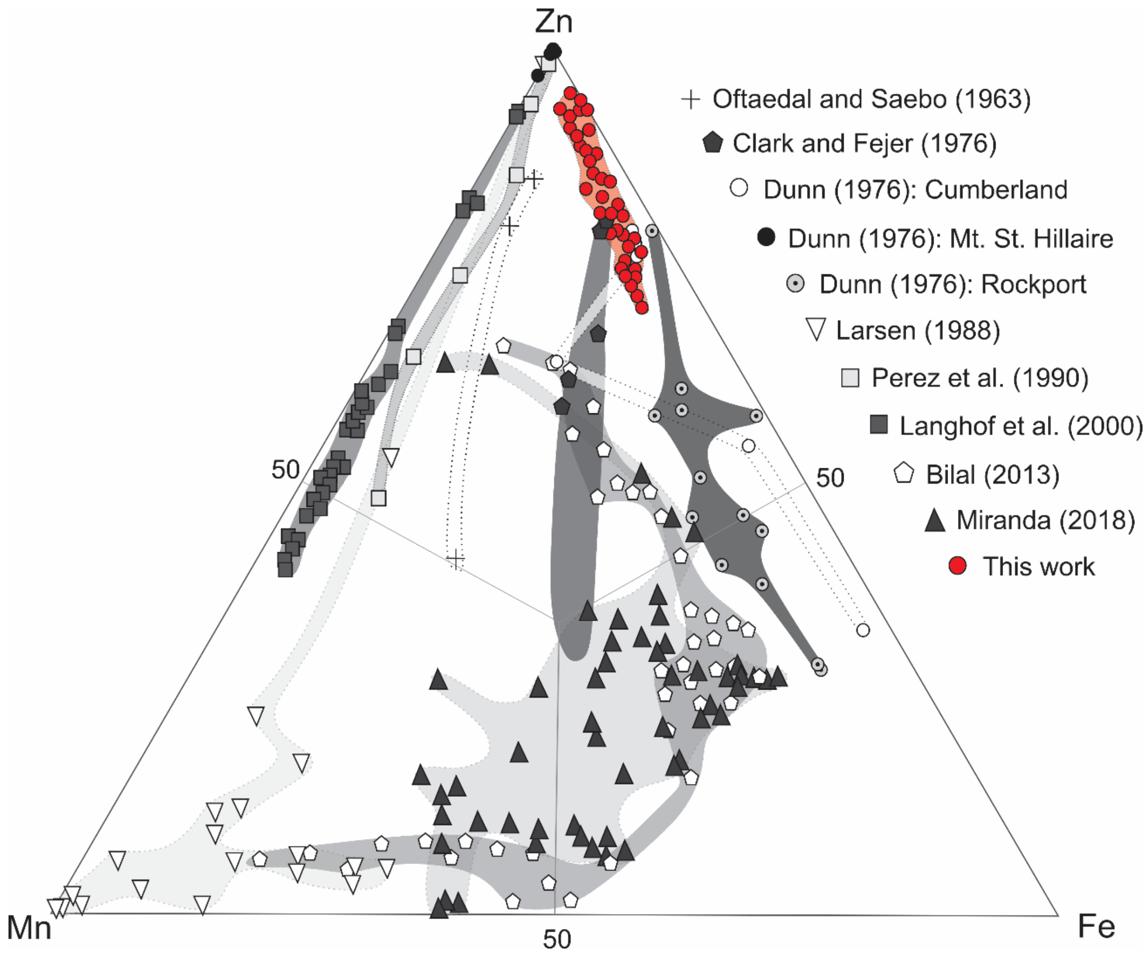

Fig. 6. Compositions of genthelvite, danalite and helvine expressed as percentages of Zn + Fe + Mn atoms.

In genthelvite, other cations that occupy the structural site of Zn, besides the Mn and Fe, are uncommon, and trace concentrations of K, Ca and Mg are the most reported. In genthelvite from Pitinga were observed maximum values of 0.062 wt.% MgO, 0.061 wt.% PbO, 0.14 wt.% BaO, 0.33 wt.% Na_2O and 0.05 wt.% K_2O, and they appear to be related to fluid composition. U concentrations have not been reported in genthelvite from other localities, but in Pitinga it occurs in all genthelvite samples in a range from 0.13 to 0.25 wt.% UO_2. Additionally, the studied genthelvite samples presents high contents of REE (maximum 0.40 wt.% REE_2O_3) relative to REE observed in genthelvite from Cheyenne Canyon (USA, 4.1 ppm REE_2O_3; Zito and Hanson, 2017) and in other helvine-group minerals such as the Mn-Zn-rich danalite from Sucuri (Brazil, maximum 363 ppm REE_2O_3; Raimbault and Bilal, 1993) and the Zn-Fe-rich helvine from Dajishan (China, maximum 13 ppm REE_2O_3; Raimbault and Bilal, 1993). The average concentration of LREE (723 ppm) is slightly higher than that of HREE (565 ppm) in genthelvite from Pitinga.

Genthelvite from this work has a REE normalised pattern (Fig. 7) similar to the host pegmatite, except for a positive anomaly in Pr and Eu, and the absence of La, Tb, Dy, Tm, Yb and Lu. It incorporated preferentially LREE, although helvine-group minerals present high affinity with HREE (Raimbault and Bilal, 1993; Deer et al., 2004).

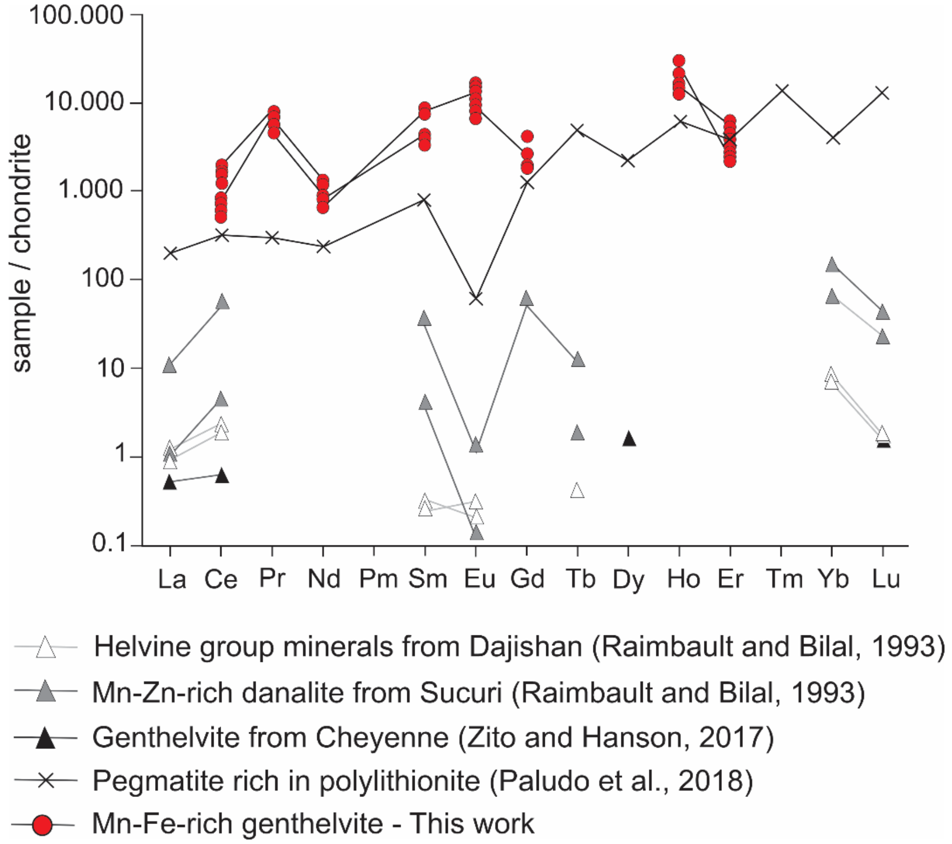

Fig. 7. REE normalised patterns (chondrite of Anders and Grevesse, 1989).

The strong negative correlation (-0.98) between Zn and the sum of the cations Fe, Mn, Mg, Pb, Ba, Na, K, U and REE attest their location at the A site (Fig. 8a). The positive correlation of Mn and Fe (0.82, Fig. 8b) is evidence of their concomitant entrance substituting Zn. There is also a weak positive correlation (0.61) between U and S (Fig. 8c), which probably mean that the mineral structure incorporated the U that was complexed with S in the fluid ($2ZnS \leftrightarrow US_2$).

Concerning the elements in the ^{IV}Be and ^{IV}Si structural sites, the analyses are similar in all the samples, with little variations in the concentrations of Si (29.30 to 32.19 wt.% SiO_2), S (5.07 to 5.52 wt.% S) and calculated Be (11.73 to 12.49 wt.% BeO). The BeO concentration is similar to those found by ICP-AES analyses in danalite, which presented an average content of 13.1% BeO (Raimbault and Bilal, 1993). In addition, maximum values of 0.38 wt.% P_2O_5, 0.30 wt.% TiO_2 and 0.25 wt.% Al_2O_3 were observed. Differently from all other minerals in the pegmatites, genthelvite does not present fluorine content, probably due to competition between S and F.

The Al presented a better negative correlation (-0.87, Fig. 8d) with Si + Be then with only Si (-0.76), therefore, Al is probably entering both the ^{IV}Be and ^{IV}Si structural sites, unlike the genthelvite from Finch (1990) in which Al entered the A-site. P and Ti are considered to preferentially substitute the ^{IV}Si site, due to their ionic potential, however, in most samples there is an excess of Si in the ^{IV}Si structural site, which is allocated in the ^{IV}Be structural site along with Ti and Al. The ΣA-site presented a positive correlation with Be (0.95) and a negative correlation with Si + Al + P + Ti (-0.95, Fig. 8e), meaning that the Si substituting Be is with charge balanced by vacancies at the A site, through the substitution mechanism: $A^{2+} + Be^{2+} \leftrightarrow \square + Si^{4+}$.

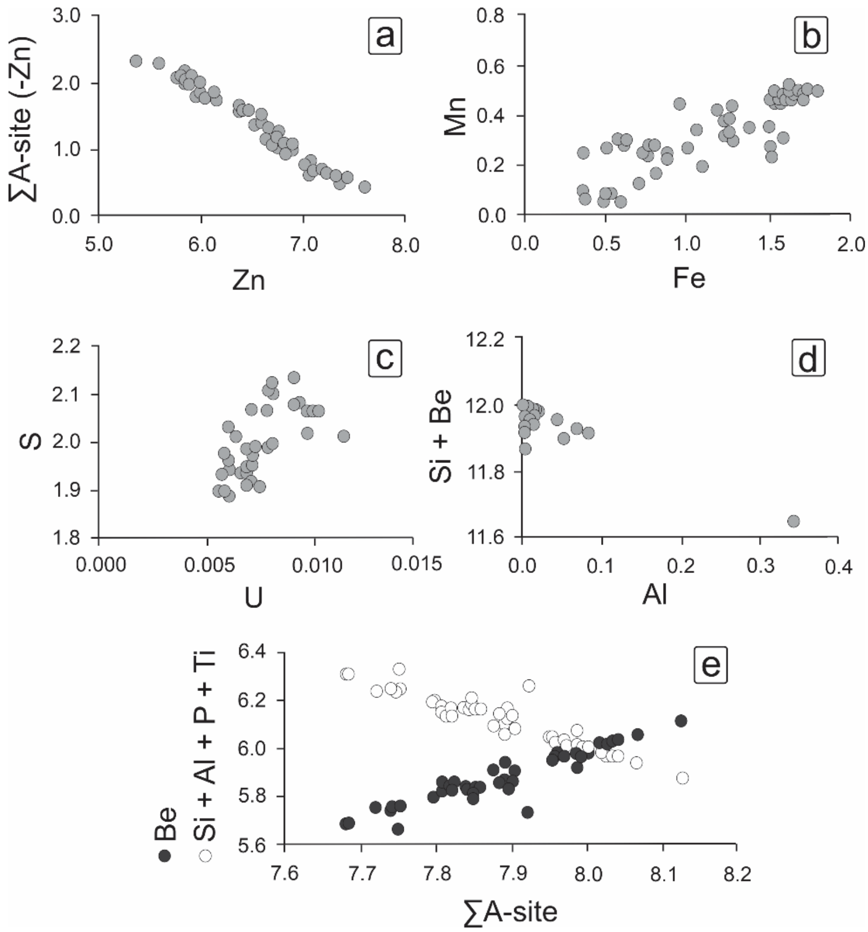

Fig. 8. Binary diagrams for genthelvite from the pegmatites associated with the albite-enriched granite: (a) ΣA-site (- Zn) versus Zn; (b) Mn versus Fe; (c) S versus U; (d) Si + Be versus Al; (e) ΣA-site versus Be and ΣA-site versus Si + Al + P + Ti.

Concentrations are expressed in apfu.

Lattice parameters of genthelvite

Genthelvite from the pegmatites associated with the AEG have an average *a* parameter of 8.127 Å, varying between 8.117 Å and 8.134 Å, which is in accordance with the expected values for this mineral (Table 2). In the helvine-group minerals the constancy of the structural dimensions of the BeO_4 and SiO_4 tetrahedrons meant that they were not affected by the size difference of the interstitial A-site cations (Hassan and Grundy, 1985). Therefore, there is a certain correlation between the unit cell parameter and the Mn-Zn-Fe proportions (Oftedal and Saebo, 1963), as well as the proportions of other elements in the A-site. For genthelvite from Pitinga and other localities (Table 2) the correlation between the average *a* parameter and the average Mn content is strongly positive (0.92, Fig. 9a), but with the average Zn + Fe content this parameter presents a strong negative trend (-0.94, Fig. 9b).

Table 2. Crystallographic parameters of genthelvite from Pitinga and other localities, in descending order of the average of parameter *a*.

Locality	↓ *a* (Å)	Average wt. %			Reference
		Zn	Fe	Mn	
Air Mountains, Nigeria	8.165	39.61	1.31	10.52	Perez et al. (1990)
Kymi, Finland	8.140	44.79	2.47	6.55	Haapala and Ojanperã (1972)
Cairngorm, Scotland	8.139	42.60	7.30	2.80	Clark and Fejer (1976)
Cairngorm, Scotland	8.133	37.00	9.90	5.80	Morgan (1967)
Pitinga, Brazil	8.127	43.5	6.49	1.78	This work
Jos, Nigeria	8.120	40.56	11.73	1.72	Von Knorring and Dyson (1959)
Mt. St. Hilaire, Canada	8.119	52.20	0.01	0.12	Antao and Hassan (2010)

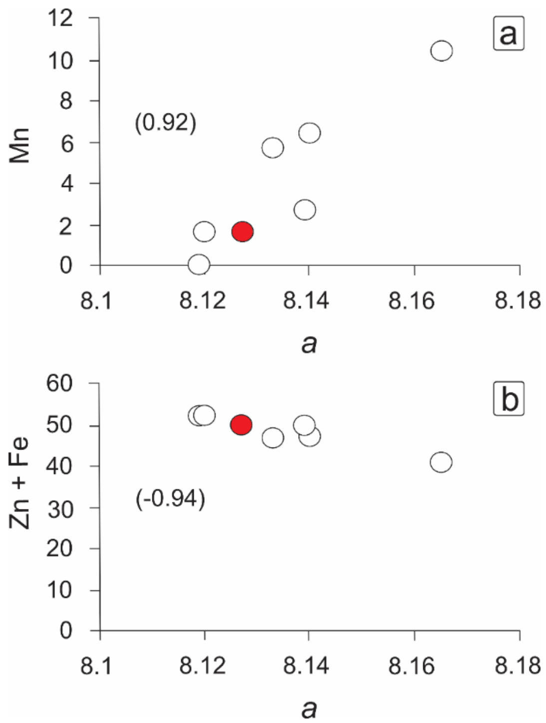

Fig. 9. Correlation of the unit-cell parameter *a* (Å) versus the Mn (a) and Zn + Fe (b) concentrations of genthelvite from Pitinga (this study, filled circle) and other localities (open circles, Table 2). Mn, Zn and Fe are expressed as wt.%.

Discussion

Genthelvite composition

The vast majority of occurrences of genthelvite are in pegmatites and in late formation rocks as hydrothermal veins, greisens and skarns, associated with alkaline to peralkaline granites and sienites (Table 3). These occurrences have in common a highly evolved magma enriched in HFSE and associated events of hydrothermalism and/or metasomatism. Genthelvite from Pitinga occurs in pegmatites that represent the most evolved fluid of a peralkaline magmatic system, but contrast with other genthelvite occurrences of the world showing an unusual mineralogical association and geochemical trend.

Considering the stability fields of minerals, genthelvite can be formed from willemite and phenakite; willemite can be altered to sphalerite; genthelvite can be altered to sphalerite and phenakite or bertrandite; and all of them along with quartz (Burt, 1988). Therefore, commonly associated minerals with genthelvite are quartz, feldspar, micas and other Zn-bearer phases as sphalerite, willemite and gahnite, as well as other Be-bearer phases as phenakite and bertrandite (Burt, 1988). There is also willemite in these associations, especially in peralkaline rocks. In metasomatic peralkaline rocks from Russia were reported genthelvite with willemite, phenakite, with Na-fluorides as gagarinite, weberite and pachnolite (Kudrin, 1978). In the Ilimaussaq Complex it was reported willemite with chkalovite as the only Be-bearer mineral, with genthelvite occurring in another place from the complex (Metcalf-Johnson, 1977). In Mont St. Hilaire (Canada) was reported willemite and genthelvite, along with sphalerite and galena (Bank, 1975; Dunn, 1976).

In this study, genthelvite is the only Be-bearing phase, and it is associated with polylithionite, quartz, feldspar, albite and the accessory phases pyrochlore, columbite, xenotime, zircon, gagarinite, sphalerite, galena and hematite. Beryl, willemite and phenakite or bertrandite were not observed. This occurrence also stands out because along with genthelvite does not occur danalite or helvine, as it has been seen in other deposits, and that is probably related to the physic-chemical conditions contemplated in the discussion on the genthelvite formation conditions. In peralkaline associations, genthelvite with aluminous minerals as beryl and topaz are restricted, but Na-fluorides are typical (Burt, 1988), as observed in the genthelvite-cryolite association in the Pitinga pegmatites.

In the pegmatites from the AEG, the formation of genthelvite after polylithionite shows that genthelvite is between one of the last minerals to form, but not later than hydrothermal cryolite (cryolite II), which is corroding genthelvite grains. That brings up the question if genthelvite is a mineral from the late magmatic stage or the early hydrothermal stage.

Table 3. The genthelvite from Pitinga and comparison with other occurrences in the world.

Location	Host rock	Mineral paragenesis (secondary)		Reference
		Major	Accessory	
Madeira Granite, Pitinga, Brazil	Pegmatite vein in albite-enriched granite	Quartz I, albite, orthoclase, polylithionite, cryolite I (cryolite II, quart II)	xenotime, zircon, thorite, pyrochlore, columbite, cassiterite, gagarinite	This work
El Paso County, Colorado, USA	Pegmatite cavity in Pikes Peak granite	Quartz, microcline, albite, mica, (sericite), fluorite	Danalite, Fe-columbite, ilmenite, Ce-bastnaesite, (goethite)	Glass et al. 1944; Zito and Hanson, 2017
Utö, Sweden	Granitic LCT-type Pegmatite	Albite, K-feldspar	Sphalerite, helvine, milarite, chiavennite	Langhof et al., 2000
Keivy Alkaline Province, Russia	Pegmatite in peralkaline granite	Quartz, amazonite, albite, biotite, muscovite	Beryl, garnet, covellite, gadolinite	Vasil'ev ,1961
Younger Granite, Jos-Bukuru, Nigeria	Albite vein in biotite-enriched granite	Albite, Li-mica	Thorite, columbite inclusions, zircon, cassiterite	Von Knorring and Dyson, 1959
	Pegmatite in biotite-enriched granite	Microcline, amazonite, Li-mica		
Rovgora, Kola Peninsula, Russia	Pegmatite associated with alkaline granite	Amazonite, quartz, biotite	Ilmenite, fluorite, pyrochlore	Lunts and Saldau, 1963
Cairngorm Mountains, Scotland	Pegmatite cavity in quartz monzonite	Quartz, microcline, oligoclase	Chlorite, bertrandite, (kaolin)	Morgan, 1967; Clark and Fejer, 1976

	(adamellite)			
Lovozero, Russia	Nepheline syenite pegmatite	Feldspar, sodalite	Mn-ilmenite, zircon, apatite	Es'kova, 1957
Oslo region, Norway	Nepheline syenite pegmatite	Analcime, mica	Zircon, bastnaesite, natrolite, pyrophanite, eudidymite	Oftaedal e Saebø, 1963
	Nepheline syenite pegmatite	Analcime, albite, muscovite	Sphalerite, galena, aegirine, catapleiite, astrophyllite, pyrophanite, monazite, fluorite	
Stokkøy, Langesundsfjord, Norway	Nepheline syenite pegmatite associated with monzonite	Nepheline, microcline, acmite, biotite, albite	Helvine, magnetite, zircon, melanite, titanite, pyrochlore, apatite, fluorite, analcime, meliphanite, sulfides	Larsen, 1988
Bratthagen, Lågendalen, Norway	Syenite pegmatite associated with monzonite	Microcline	Catapleiite, pyrochlore, analcime	Larsen, 1988
Ilimaussaq, Greenland	Albite vein in alkaline intrusion	Albite, aegirine	Neptunite, catapleite	Bollinberg and Petersen, 1967
Sucuri Granite, Goiás, Brazil	Hydrothermal albitite associated with biotite granite	Albite	Biotite, fluorite, danalite, allanite, chalcopyrite, sphalerite, pyrite, pyrrohtite, galena, cubanite	Raimbault and Bilal, 1993; Bilal, 2013; Miranda, 2018
Rhode Island, USA	Granite	Quartz	Fluorite, aegirine, zircon	Dunn, 1976
Treburland, Cornwall, England	Calc-silicate rock associated with granite	Calcite, garnet, chlorite, diopside	Wollastonite, idocrase, axinite, galena, molybdenite, pyrite, pyrrhotite, arsenopyrite	Kingsbury, 1961
Pitkäranta, Karella, Russia	Calc-silicate rock near rapakivi granite	Fluorite, biotite, chlorite	Vesuvianite	Bulakh A.G. and Frank-Kamenetsky V.A., 1961
Eurajoki Massive, Finland	Greisen in rapakivi granite	Quartz, (sericite), (chlorite)	Topaz, sphalerite, cassiterite, galena, chalcopyrite, fluorite, (Fe-Ti oxides)	Haapala and Ojanperã, 1972
Granitic Complex, Kymi, Finland	Greisen in biotite-enriched rapakivi granite	Muscovite phengite, (chlorite), ± quartz, ± relict feldspar	Fluorite, ± apatite, ± cassiterite, monazite, zircon, (Fe-Ti oxides, chalcocite, malachite)	Haapala and Ojanperã, 1972; Haapala and Lukkari, 2005
Mangabeira Granite, Goiás, Brazil	Greisen associated with topaz-albite-enriched granite	Quartz, Li-mica	Topaz, helvine	Botelho, 1992; Freitas, 2000
Bolshaya Turupya, Mankhambovsky, Urals, Russia	Alkaline metassomatite associated with granitoid	Quartz	Columbite, pyrochlore, bastnaesite, allanite, zircon, euclase, phenacite, fluorite	Dushin et al., 2018
Sterling Hill, Ogdensburg, New Jersey, USA	Rhodonite skarn and augite skarn	Rhodonite, augite, actinolite, quartz, calcite, albite	Willemite, galena, scheelite, barite, titanite, zircon, sphalerite	Cianciulli and Verbeek, 2003; Leavens et al., 2009

Crystallographic and structural results, the ionic radius of the A-site cations and the structural geometric model, indicated that complete miscibility should exist between the three end-members of the helvine-genthelvite-danalite solid solution (Hassan and Grundy, 1985), however, there are apparent compositional gaps in the Zn-Fe, Zn-Mn and Mn-Fe trends, and no pure danalite was observed in nature (Oftaedal and Saebo, 1936; Clark and Fejer, 1976; Dunn, 1976; Larsen, 1988; Perez et al., 1990; Langhof et al., 2000; Bilal, 2013). According to Antao and Hassan (2010) the absence of pure danalite in nature may simply indicate that another phase must be more stable compared to danalite.

Genthelvite from Pitinga presents high concentrations of Zn and small concentrations of Fe in comparison with the genthelvite from the Rockport Deposit (Dunn, 1976) and the one from the Cairngorm Mountains (Clark and Fejer, 1976). It also has a higher Zn content and smaller Fe and Mn content than the more Mn-Fe-enriched genthelvite reported from Cumberland (Dunn, 1976) and from the Sucuri Granite in Brazil (Miranda, 2018). It is also different from the typical Fe-Mn-rich genthelvite from Oftaedal and Saebo (1963), from Larsen (1988), from Perez et al. (1990) and from Uto in Sweden (Langhof et al., 2000). Finally, with this work we demonstrate the existence of natural genthelvite in the upper Zn-Fe trend of the Zn-Fe-Mn ternary diagram (Fig. 6), filling an up-to-date compositional gap. This specific composition is due to equally specific crystallochemical and environmental conditions.

Genthelvite is virtually the only silicate in which Zn and Be occur together. Despite Zn (ionic radius 0.60 Å; Shannon, 1976) and the much smaller Be (ionic radius 0.27 Å; Shannon, 1976) present different chemical affinity, they both have the tendency to concentrate by fractionated crystallisation and to seek IV coordination (Burt, 1988). In its turn, Fe and Mn (^{IV}Mn = 0.66 Å, ^{IV}Fe = 0.63 Å; Shannon, 1976) are forced into IV coordination. In the magmatic stage of the AGC and in the associated pegmatites, Fe was extensively buffered by amphibole and tetraferric green-brown mica (Costi, 2000); in the early hydrothermal stage, Fe was incorporated in altered thorite and altered pyrochlore and both Fe and Mn were widely incorporated in secondary Mn-Fe-rich columbite; in late hydrothermal stage, Fe formed hematite surrounding all the previous minerals.

Nevertheless, compositional variations in helvine-group minerals have been shown to have a direct association with temperature and S and O fugacity, rather than with the availability of Zn, Fe and Mn in the fluid. The study of several genthelvite crystals in a granitic massif (Antao and Hassan, 2010) have shown that the temperature to form Mn-rich genthelvite was lower than to form Mn-poor genthelvite. In the Taghouaji Alkaline Complex the Mn-poor genthelvite occurs with sphalerite and galena in low $f(O_2)$ and high $f(S_2)$ and crystallisation temperature higher than 375°C, while the Mn-rich genthelvite occurs with hematite in temperatures around 288°C (Perez et al., 1990).

Additionally, compositional zoning or intergrowth between helvine-group minerals is relatively common (Haapala and Ojanperä, 1972; Clark and Fejer, 1976; Perez et al., 1990; Antao and Hassan, 2010), and it is also attributed to changes in the physic-chemical conditions during crystallisation, such as temperature and S fugacity. The preservation of this zoning or intergrowth would require low temperature crystallisation and a quick crystallisation process, with the absence of diffusion between Zn, Mn and Fe (Antao and Hassan, 2010). Through these patterns, it is possible to assume that the Mn-poor homogeneous composition in genthelvite grains from Pitinga may be evidence of a stable condition in the late evolved fluids under higher temperatures (>375°C).

Beryllium is a rare element both in meteorites and on Earth, and it is a crustal element par excellence, with an average of 2.1 ppm BeO in rocks of the upper continental crust, in contrast to 1.4 ppm BeO in the lower crust and 0.07 ppm BeO in the mantle (Rudnick and Gao, 2005). The first paragenesis of magmas are formed by minerals whose structure inhibits the capture of Be in melting. Therefore, Be enrichment occurs in the final stages of magmatic crystallisation, mainly in granitic pegmatites and alkaline rocks (Grew, 2002). In the later stages of differentiation, there is a supersaturation of SiO_2 and accumulation of alkalis and volatiles, allowing the formation of Be minerals and quartz (Pulz et al., 1998).

Few Be bearing minerals form in the magmatic stage of pegmatite consolidation, with beryl being dominant among them (Černý, 2002). However, in complex lithium-bearing pegmatites, the activities of beryl-forming components are reduced, requiring higher BeO concentrations (900 ppm BeO, or ~325 ppm Be) to reach beryl saturation (London and Evensen, 2002). In the other hand, Be minerals paragenetically late (supercritical to hydrothermal) are divided in two great categories: alteration products of the early phases of Be, on the one hand, and minerals covering the miarolitic cavities and fissures, on the other (Černý, 2002). In this way, genthelvite filling cavities in a pegmatite can be interpreted as a crystallisation of the late evolved fluid, in which Be was conserved by complexation (with F, for example), because no other Be mineral can be found.

The mineralogical and petrographic variations of the AEG were mapped and described in detail by Bastos Neto et al. (2009), and the fluid inclusion assemblies or associations (FIA) by Ronchi et al. (2011). In these papers, it was concluded that the large hydrothermal massive cryolite deposit in the centre of AEG is part of an evolutionary process of a magma originally rich in volatiles, which during its polyphase crystallisation process allowed the exsolution of hydrothermal saline deuteric fluids (salinity between 0 and 25% eq. NaCl and homogenization temperatures from 100 to 400ºC). Furthermore, the authors concluded that these fluids lowered the *solidus* curve of the system, forming inside the AEG several and varied portions with pegmatitic texture. In this process, phases rich in minerals such as microcline, genthelvite, polylithionite and cryolite were formed and hydrothermal alterations were promoted, such as albitization, silicifications, claying, fluoritization and oxidation of iron-rich minerals. Therefore, the occurrence of genthelvite in the pegmatites of the AEG is strongly associated with the transition between the late magmatic and early hydrothermal stages.

In this context, the presence of U in genthelvite could be related to the alteration of the U-Pb-rich pyrochlore into columbite in the early hydrothermal alteration of the AEG, releasing U and Pb in the alteration fluids (Bastos Neto et al., 2009). The Pb released was largely incorporated by galena and in smaller amounts in sphalerite, and the U was partially incorporated by U-rich columbite, solid solutions of thorite-coffinite-xenotime and late zircon (unpublished data, Hadlich, 2018).

Differently from all other minerals in the pegmatites, genthelvite does not present fluorine content, although the late magmatic processes of pegmatite genesis occurred with a significant increase in the contents of this anion. The fluorine contents in the AEG are very variable, the pegmatites rich in amphibole have ~3.35 wt.% F, the ones rich in polylithionite have ~4.80 wt.% F and those rich in cryolite have an average of 37.32 wt.% F. Although fluorine was abundantly consumed by minerals that crystallised before genthelvite in the same paragenesis (among these, cryolite I, xenotime and polylithionite stand out), the absence of F in genthelvite is probably due to competition between S and F.

These variations in composition are also verified in the REE contents. Genthelvite from Pitinga has a REE pattern enriched in LREE relative to its host pegmatite. The average LREE content is slightly higher than that of HREE content, which differs from those of other localities, which have higher HREE contents. The HREE enrichment in relation to the LREE in the helvine-group minerals from Sucuri-Brazil and Dajishan-China (Raimbault and Bilal, 1993) was attributed by these authors only to crystallographic controls. The higher concentration of HREE in danalite from Cheyenne, USA (Zito and Hanson, 2017), was attributed to the presence of late F-enriched fluids. In Pitinga, the REE contents are largely concentrated in xenotime (mainly HREE as Dy, Yb and Lu, Bastos Neto et al., 2012) and polylithionite, and due to the crystallisation of these minerals prior to that of genthelvite, the REE contents in genthelvite are smaller and richer in LREE. The Eu positive anomaly probably reflects a reducing magma in which the Eu^{2+} could preferentially substitute Zn^{2+} and because of the crystallisation of albite instead of anorthite in the pegmatites.

Genthelvite formation conditions

Genthelvite is a rare mineral compared with other Be-bearing minerals or even to the other members of the helvine-group, resulting from its small stability field. The elements that constitute genthelvite (Zn, Mn, Fe, Be, S) are commonly found as trace elements in highly fractionated granitic systems, therefore, this mineral is typical of systems at a late stage of differentiation, whose stability is due to local and transient conditions, generally atypical in the consolidation of granitic pegmatites, including low alumina activity and relatively reductive conditions that accommodate the coexistence of sulphides and silicates (Burt, 1980, 1988; Bilal and Fonteilles, 1988).

Genthelvite stability in a paragenesis is restricted to systems with low S activity (Burt, 1988). Because of the chalcophile behaviour of Zn>>Fe>Mn, in systems with high SO_{-1} (under highly enough H_2S fugacity) the Zn_2SiO_4 component would have been destabilized to form an assemblage with sphalerite and quartz (Burt, 1988). On the contrary, under low SO_{-1} conditions danalite and helvine are not stable, and the instability of FeS and MnS components would lead to the formation of silicates or oxides (Burt, 1988). The low content of Fe in genthelvite also indicates high O_2 fugacity level during crystallisation, with the crystallisation of hematite (Burt, 1980).

The wide compositional variation in helvine-group minerals (genthelvite in the core and danalite in the border) in the albitites associated to the Sucuri Granite (Brazil) suggest that the increased alkalinity (albitization) in the system favoured genthelvite growth and the subsequent increase in S fugacity favoured danalite crystallisation by $Zn_8Be_6Si_6O_{24}S_2 + 8FeS_2 \leftrightarrow Fe_8Be_6Si_6O_{24}S_2 + 8ZnS + 4S_2$ (Miranda, 2018).

While genthelvite is favoured in alkaline conditions, danalite is formed in more acidic fluids, in a narrow field of oxygen fugacity, above which occur assemblages with hematite or magnetite (Burt, 1980; Nimis et al., 1996). Helvine crystallises in more Mn-rich fluids in a wider S fugacity than genthelvite (Burt, 1988). High activity of Na and K in an alkaline melt leads to the formation of phenakite and feldspar instead of beryl, and the available Al forms feldspathoids instead of beryl (Burt, 1980; Finch, 1990; Perez et al., 1990).

In the AEG, the pegmatites formed from a continuous fractionation of the magma, which led to a peralkaline composition highly enriched in HFSE. The abundant crystallisation of microcline, albite and polylithionite buffered the Al content in the late fluid, lowering the alumina activity in the system. At the same time, the extremely high concentration of fluorine and the crystallisation of large amounts of galena (and minor sphalerite and pyrite), led to an effective decrease in the H_2S fugacity, allowing the stability of genthelvite in the late magmatic and early hydrothermal stages of the AEG evolution. The low content of Fe in genthelvite and the wide formation of Mn and Fe oxides (columbite, hematite) attests an O activity too high to favour danalite formation.

Conclusion

The study of genthelvite in the pegmatites associated with the Madeira albite-enriched granite led to the following conclusions.

Among the different pegmatites existing in the AEG, the genthelvite-bearing bodies are rich in polylithionite and xenotime, confirming the observations by Paludo et al. (2018).

Genthelvite was formed in the transition of the late magmatic stage and the early hydrothermal stage of the AEG evolution and is the only Be-bearing mineral. It is a crystallisation product from Be conserved in the late evolved fluid by complexation with F, filling the cavities in the pegmatite, surrounding polylithionite, quartz I, xenotime, pyrochlore, thorite, zircon, and it is corroded by hydrothermal cryolite (cryolite II).

Genthelvite has homogeneous composition within grains and is a Mn-Fe-rich genthelvite, expressing a solid solution in the genthelvite-danalite-helvine system, with relatively high contents of Zn (36.96 to 49.45 wt.% ZnO), low contents of Mn (0.61 to 3.03 wt.% MnO) and variable contents of Fe (2.10 to 10.94 wt.% FeO) in comparison to those of other localities, filling an up-to-date compositional gap along the upper part of the joint Zn-Fe in the Zn-Fe-Mn ternary diagram. Genthelvite presents high U (up to 0.25 wt.% UO_2) and REE (up to 0.40 wt.% REE_2O_3); the average LREE content is higher than the average HREE content, which differs from those of other localities, which have higher HREE contents; and there is no F content. Despite the compositional differences, the crystallographic parameters (a = 8.127 Å) of genthelvite from the AEG are similar to those described for crystals from other localities.

This unique genthelvite composition is due to the buffering of F and HREE in minerals crystallised prior to genthelvite as xenotime, polylithionite and cryolite I. The presence of U is due to the alteration of U-Pb-pyrochlore in the early hydrothermal stage, which was responsible for the releasing of U and Pb in the fluid. The released Pb widely formed galena (Bastos Neto et al., 2009).

Genthelvite was affected by the late hydrothermal stage related to F-rich aqueous fluids that formed the massive cryolite deposit, as well as hydrothermal cryolite (cryolite II) disseminated in the AEG. The highest homogenization temperature of 400°C, measured in hydrothermal cryolite (Bastos Neto et al., 2009), determines the minimum starting temperature of the hydrothermal process. The rebalance of genthelvite allowed the incorporation of Fe, Mn, Mg, Pb, Ba, Na, K, U and REE in the

Zn^{2+} structural site, and the allocation of excess Si, Al, Ti and P in the ^{IV}Si and ^{IV}Be structural sites. The high content of U and REE replacing Zn and of Si replacing Be are charge balanced by vacancies at the A site, as in the substitution mechanism $Zn^{2+} + Be^{2+} \leftrightarrow \square + Si^{4+}$.

The crystallochemical study of genthelvite made it possible to verify that it was formed in an alkaline and subaluminous environment, at a stable condition in the late evolved fluids under relatively high temperatures (>375°C) and under reducing conditions. The extremely high concentration of fluorine and the crystallisation of large amounts of galena (and minor sphalerite and pyrite), led to an effective decrease in the H_2S fugacity, allowing the stability of genthelvite between the late magmatic and early hydrothermal stages of the albite-enriched granite evolution. The variable content of Fe in genthelvite and the wide formation of Mn and Fe oxides (columbite, hematite) attests an O activity too high to favour danalite formation.

Acknowledgements

This work was supported by Conselho Nacional de Desenvolvimento Científico e Tecnológico (CNPq) through the Project 405839/2013-2018 and for granting scholarship. The authors thank the reviewers and editors for contributing to improve the manuscript.

Competing interests: The authors declare none.

References

Almeida F.F.M., Hasui Y., Brito Neves B.B. and Fuck R.A. (1981) Brazilian structural Provinces: an introduction. *Earth Sciences Reviews*, **17**, 1-29.

Anders E. and Grevesse N. (1989) Abundances of the elements: Meteoritic and solar. *Geochimica et Cosmochimica Acta*, **53**, 197-214.

Antao S.M., Hassan I. (2010) A two-phase intergrowth in genthelvite from Moint Saint-Hilaire, Quebec. *Canadian Mineralogist*, **48**, 1217-1223.

Bank H. (1975) Durchsichtiger schleifwuerdiger blauer Willemit vom Mt. St. Hilaire in Kanada. *Zeitschrift der Deutsche Gemnologische Gesellschaft*, **24**, 250-256.

Bastos Neto A.C. et al. (2005) A jazida de criolita da Mina Pitinga (Amazonas). Pp. 481-547 in: *Caracterização de Depósitos Minerais em Distritos Mineiros da Amazônia* (O.J. Marini, E.T. Queiroz and B.W. Ramos, editors). DNPM-CT/MINERAL-ADIMB, Brasília.

Bastos Neto A.C., Pereira V.P., Ronchi L.H., Lima E.F. and Frantz J.C. (2009) The worldclass Sn, Nb, Ta, F (T, REE, Li) deposit and the massive cryolite associated with the albite-enriched facies of the Madeira A-type granite, Pitinga Mining District, Amazonas State, Brazil. *Canadian Mineralogist*, **47**, 1329-1357.

Bastos Neto A.C., Pereira V.P., Pires A.C., Barbanson L. and Chauvet A. (2012) Fluorine-rich xenotime from the Nb-Ta-Sn Madeira world-class deposit associated with the albite-enriched granite at Pitinga, Amazonia, Brazil. *Canadian Mineralogist*, **50**, 1019-1032.

Bastos Neto A.C., Ferron T.M.M., Chauvet A., Chemale F., Lima E.F., Barbanson L. and Costa C.F.M. (2014) U-Pb dating of the Madeira Suite and structural control of the albite-enriched granite at Pitinga (Amazônia, Brazil): evolution of the A-type magmatism and implications for the genesis of the Madeira Sn-Ta-Nb (REE, cryolite) world-class deposit. *Precambrian Research*, **243**, 181-196.

Bilal E. and Fonteilles M. (1988) Conditions d'apparition respectives de l'helvite, de la phénacite et du béryl dans l'environnement granitique: exemple du massif de Sucuri (Brésil). *Comptes Rendus de l'Académie des Sciences*, **307**, 273-276.

Bilal, E. (2013) Geochimie et conditions de cristallisation des mineraux du groupe de l'helvite, *Geonomos*, **2**, 1-13.

Bollinberg H. and Petersen O.V. (1967) Genthelvite from the Ilimaussaq alkaline intrusion, south Greenland. *Medelelser om Gronland*, **181(4)**, 1-9.

Botelho N.F. (1992) *Les ensembles granitiques subalcalins a peralumineux mineralisés em Sn et In de la sous-province Paraná, état de Goiás, Brésil*. PhD dissertation, Université de Paris VI, France.

Bulakh A.G. and Frank-Kamenetsky V.A. (1961) *Geological excursion in the vicinity of Pitkyaranta (in Russian)*. Publishing house of the KASSR, Petrozavodsk, 108 pp.

Burt D.M. (1980) The stability of danalite $Fe_4Be_3(SiO_4)S$. *American Mineralogist*, **65**, 355-360.

Burt D.M. (1988) Stability of genthelvite, Zn4(BeSiO4)3S: an exercise in chalcophilicity using exchange operators. *American Mineralogist*, **73**, 1384-1394.

Černý P. (2002) Mineralogy of beryllium in granitic pegmatites. Pp. 405-444 in: *Beryllium: Mineralogy, petrology, and geochemistry*, Vol. 50 (E.S. Grew, editor). Reviews in Mineralogy and Geochemistry, Mineralogical Society of America, Virginia.

Černý P. and Ercit T.S. (2005) The classification of granitic pegmatites revisited.

Canadian Mineralogist, **43**, 2005-2026.

Cianciulli J.C. and Verbeek E.R. (2003) Genthelvite from Ogdensburg, New Jersey. *The Picking Table*, **44(2)**, 23-26.

Clark A.M. and Fejer E.E. (1976) Zoned genthelvite from the Cairngorm Mountains, Scotland. *Mineralogical Magazine*, **40**, 637-639.

Costi H.T. (2000) *Petrologia de granitos alcalinos com alto flúor mineralizados em metais raros: o exemplo do Albita-granito da Mina Pitinga, Amazonas, Brasil*. PhD dissertation, Universidade Federal do Pará, Brazil.

Costi H.T., Dall'agnoll R. and Moura C.A.V. (2000) Geology and Pb-Pb Geochronology of Paleoproterozoic volcanic and granitic rocks of Pitinga province, Amazonian craton, northern Brazil. *International Geology Review*, **42**, 832-849.

Costi H.T., Dall'Agnol R., Pichavant M. and Ramo O.T. (2010) The peralkaline tin-mineralized Madeira cryolite albite-rich granite of Pitinga, Amazonian craton, Brazil: petrography, mineralogy and crystallization processes. *Canadian Mineralogist*, **47**, 1301-1327.

Deer W.A., Howie R.A., Wise W.S. and Zussman J. (2004) *The Rock-forming Minerals Series: framework silicates (silica minerals, feldspathoids and the zeolites)*. The Geological Society, London, 988 pp.

Dill H.G. (2016) The CMS classification scheme (Chemical composition-Mineral assemblage-Structural geology)-linking geology to mineralogy of pegmatitic and aplitic rocks. *Journal of Mineralogy and Geochemistry*, **193(3)**, 231-263.

Dolejs D. and Baker D.R. (2007) Liquidus equilibria in the system K_2O-Na_2O-Al_2O_3-SiO_2-F_2O to 100 MPa 2: differentiation paths of fluorosilicic magmas in hydrous systems. Journal of Petrology, **48**, 807-828.

Dunn P.J. (1976) Genthelvite and the helvine group. *Mineralogical Magazine*, **40**, 627-636.

Dushin V.A., Prokopchuk D.I., Koz'min V.S., Zhuklin E.A. and Trutnev A.K. (2018) Geology and mineral resources of the Mankhambovsky Block (subpolar Urals). *News of the Ural State Mining University,* **3**, 19-33.

Eskova E.M. (1957) Genthelvite from alkaline pegmatites (in Russian). *Doklady Akademii Nauk.* **153(3)**, 681-683.

Glass J.J., Jahns R.H. and Stevens R.H. (1944) Helvite and danalite from New Mexico and the helvite group. *American Mineralogist,* **29**, 163-191.

Grew E.S. (2002) Mineralogy, petrology and geochemistry of beryllium: An introduction and list of beryllium minerals. Pp. 487-549 in: *Beryllium: Mineralogy, petrology, and geochemistry*, Vol. 50 (E.S. Grew, editor). Reviews in Mineralogy and Geochemistry, Mineralogical Society of America, Virginia.

Ferron J.M.T.M., Bastos Neto A.C., Lima E.F., Costi H.T., Moura C.A.V., Prado M. and Galarza M.A. (2006) Geologia e cronologia Pb-Pb de rochas graníticas e vulcânicas ácidas a intermediárias paleoproterozóicas da Província de Pitinga, Cráton Amazônico. *Revista Brasileira de Geociências*, **36(3)**, 499-512.

Finch A.A. (1990) Genthelvite and willemite, zinc minerals associated with alkaline magmatism from the Motzfeldt centre, south Greenland. *Mineralogical Magazine*, **54**, 407-412.

Freitas M.E. (2000) *A evolução dos greisens e mineralização estanífera no Morro do Laranjinha – Maciço Granítico Mangabeira – Goiás*. PhD dissertation, Universidade de Brasília, Brazil.

Haapala I. and Ojanperã P. (1972) Genthelvite-bearing greisens in southern Finland. *Geological Survey of Finland*, Bulletin, 259.

Haapala I. and Lukkari S. (2005) Petrological and geochemical Evolution of the Kymi stock, a topaz granite cupola within the Wiborg rapakivi batholith, Finland. *Lithos*, **80**, 347-362.

Hassan I. and Grundy H.D. (1985) The crystal structure of helvite group minerals, $(Mn, Fe, Zn)_8(Be_6Si_6O_{24})S_2$. *American Mineralogist*, **70**, 186-192.

Holland T.J.B. and Redfern S.A.T. (1997) Unit cell refinement from powder diffraction data: the use of regression diagnostics. *Mineralogical Magazine*, **61**, 65-77.

Horbe M.A., Horbe A.C., Teixeira J.T. and Costi H.T. (1985) Granito Madeira: petrologia, petroquímica e mineralizações. Pp. 53-72 in: *Simpósio de Geologia da Amazônia*. Sociedade Brasileira de Geologia, 2, Belém, Brazil.

Kingsbury A.W.G. (1961) Beryllium minerals in Cornwall and Devon: helvine, genthelvite, and danalite. *Mineralogical Magazine*, **32**, 921-940.

Kudrin V.S. (1978) Rare metal alkaline quartz-albite-microcline metasomatites (qualmites) of zones of regional metamorphism (in Russian). Pp. 183-194 in: *Metasomatism and ore deposition* (D.S. Korzhinskii, editor). Nauka Press, Moscow.

Langhof J., Holtstam D. and Gustafsson L. (2000) Chiavennite and zoned genthelvite-helvite as late-stage minerals of the Proterozoic LCT pegmatites at Utö, Stockholm, Sweden. *GFF*, **122(2)**, 207-212.

Larsen A.O. (1988) Helvite group minerals from syenite pegmatites in the Oslo Region, Norway. *Norsk Geologisk Tidsskrift*, Report, 68.

Leavens P.B., Zullo J. and Verbeek E. (2009) A complex, genthelvite-bearing skarn from the Passaic pit, Sterling Hill mine, Ogdensburg, New Jersey. *Axis***, 5(1)**, 1-26.

Lengler H.F. (2016) *Pegmatitos do albita granito Madeira: avaliação do minério para fins de beneficiamento*. Monography, Universidade Federal do Rio Grande do Sul, Brazil.

Lenharo, S.L.R. (1998) *Evolução magmática e modelo metalogenético dos granitos mineralizados da região de Pitinga, Amazonas, Brasil*. PhD dissertation, Universidade de São Paulo, Brazil.

London D. and Evensen J.M. (2002) Beryllium in silicic magmas and the origin of beryl-bearing pegmatites. Pp. 445-486 in: *Beryllium: Mineralogy, petrology, and geochemistry*, Vol. 50 (E.S. Grew, editor). Reviews in Mineralogy and Geochemistry, Mineralogical Society of America, Virginia.

Lunts A.J. and Saldau E.P. (1963) Genthelvite from pegmatites on the Kola peninsula (in Russian). *Zapiski Vserossiyskogo Mineralogicheskogo Obshchestva*, **92(1)**, 81-84.

Martin R.F. (2006) A-type granites of crustal origin ultimately result from open-system fenitization-type reactions in an extensional environmental. *Lithos*, **91**, 125-136.

Metcalf-Johnson J. (1977) Willemite from the Ilimaussaq alkaline intrusion. *Mineralogical Magazine*, **41**, 71-75.

Minuzzi O.R.R. (2005) *Gênese e evolução da mineralização de criolita, pirocloro e columbita da subfacies albita granito de núcleo, Mina Pitinga, Amazonas, Brasil*. PhD dissertation, Universidade Federal do Rio Grande do Sul, Brazil.

Minuzzi O.R.R., Bastos Neto A.C., Pereira V.P. and Flores J.A.A. (2006) The massive cryolite deposit and the disseminated ore of cryolite from the Pitinga mine (Amazon, Brazil). *Revista Brasileira de Geociências*, **36**, 104-123.

Miranda A.C.R. (2018) *Caracterização da mineralização de estanho e índio do maciço Sucuri, província estanífera de Goiás*. Master dissertation, Universidade de Brasília, Brazil.

Morgan W.C. (1967) Genthelvite and bertrandite from the Cairngorm Mountains, Scotland. *Mineralocal Magazine*, **36(277),** 60-63.

Nimis P., Molin G. and Visonà D. (1996) Crystal chemistry of danalite from Daba Shabeli Complex (N Somalia). *Mineralogical Magazine*, **60(399)**, 375-379.

Oftaedal I. and Saebø P.C. (1963) Classification of some Norwegian members of the helvine group. *Norsk Geologisk Tidsskrift*, **43**, 405-409.

Paludo C.M. (2015) *Caracterização dos minerais de ETR e Y nos pegmatites do Albita Granito Madeira, Pitinga, AM*. Monography, Universidade Federal do Rio Grande do Sul, Brazil.

Paludo C.M., Bastos Neto A.C., Pereira V.P. and Botelho N.F. (2018) Mineralogia e geoquímica de pegmatitos ricos em ETR, F e metais alcalinos associados à fácies albita granito no depósito de Sn-Nb-Ta-(F, ETR, U, Th) Madeira (mina Pitinga, AM, Brasil). *Pesquisas em Geociências*, **45**, 1-28.

Perez J.-P., Dusausov Y., Babkine J. and Pagel M. (1990) Mn zonation and fluid inclusions in genthelvite from the Taghouaji complex (Aïr Mountains, Niger). *American Mineralogist*, **75**, 909-914.

Pierosan R., Lima E.F., Nardi L.V.S., Bastos Neto A.C., Campos C.P., Jarvis K., Ferron J.M.T.M. and Prado, M. (2011) Geochemistry of Paleoproterozoic volcanic rocks of the Iricoume Group, Pitinga Mining District, Amazonian craton, Brazil. *International Geology Review*, **53**, 946-976.

Pulz G.M., Cunha M.C.L. and Formoso, M.L.L. (1998) Revisão sobre a geoquímica do berílio nos materiais naturais. *Pesquisas*, **25(2)**, 29-40.

Raimbault L. and Bilal E. (1993) Trace-element contents of helvite-group minerals from metasomatic albitites and hydrothermal veins at Sucuri, Brazil and Dajishan, China. *Canadian Mineralogist*, **31**, 119-127.

Ronchi F.C., Althoff F.J., Bastos Neto A.C. and Dill, H.G. (2019) Structural control of REE-pegmatites associated with the world-class Sn-Nb-Ta-cryolite deposit at the Pitinga mine, Amazonas, Brazil. *Pesquisas em Geociências*, **46(1)**, 1-14.

Ronchi L.H., Bastos Neto A.C., Gedoz S.C., Weber M.L., Pereira V.P. and Andrek, M. (2011) A transição magmático-hidrotermal registrada por inclusões fluidas no albita-granito de núcleo, Mina Pitinga, Amazonas. Pp. 71-88 in: *Contribuições à metalogenia do Brasil*, (J.C. Frantz, J.M. Charão and H. Jost, editors). Serviço Geológico do Brasil, Porto Alegre.

Rudnick R.L. and Gao S. (2005) Composition of the continental crust. Pp. 1-61 in: *The crust*, Vol. 3 (R.L. Rudnick, editor). Treatise on Geochemistry, Elsevier-Pergamon, Oxford.

Santos J.O.S., Hartmann L.A., Gaudete H.E., Groves D.I., McNaughton N.J. and Fletcher L.R.A. (2000) New understanding of the Provinces of Amazon Craton based on Integration of Field Mapping and U-Pb and Sm-Nd geochronology. *Gondwana*

Research, **3(4)**, 453-488.

Shannon R.D. (1976) Revised effective ionc radii and systematic studies of interatomic distances in halides and chalcogenides. *Acta Crystallographica*, **A32**, 751-767.

Simões M.S.S., Almeida M.E., Souza A.G.H., Silva B.D.P.B. and Rocha P.G. (2014) Characterization of the volcanic and hypabyssal rocks of the Paleoproterozoic Iricoumé Group in the Pitinga region and Balbina Lake area, Amazonian craton, Brazil: petrographic distinguishing features and emplacement conditions. *Journal of Volcanology and Geothermal Research*, **286**, 138-147.

Stolnik D. (2015) *Caracterização da xenotima na fácies pegmatítica do albita granito de núcleo, Pitinga (AM).* Monography, Universidade Federal do Rio Grande do Sul, Brazil.

Teixeira J.T., Costi H.T., Minuzzi O.R.R. and Soares E.A.A. (1992) Depósitos Primários de Criolita, Cassiterita, Xenotima e Columbita em Apogranito - Mina de Pitinga (AM). Pp. 212-213 in: *Congresso Brasileiro de Geologia*. Sociedade Brasileira de Geologia, São Paulo, 1992, 37.

Thomas R., Webster J.D., Rhede D., Seifert W., Rickers K., Förster H.J., Heinrich W. and Davidson P. (2006) The transition from peraluminous to peralkaline granitic melts: evidence from melt inclusions and accessory minerals. *Lithos*, **91**, 137-149.

Vasil’ev V.A. (1961) On genthelvite (in Russian). *Zapiski Vsesoyuznogo Mineralogicheskogo Obshchestva*, **90**, 571-578.

Veiga Jr. J.P., Nunes A.C.B., Fernandes A.S., Amaral J.E., Pessoa M.R. and Cruz S.A.S. (1979) Projeto Sulfetos de Uatumã. *Departamento Nacional de Pesquisa Mineral/Serviço Geológico do Brasil*, Relatório Final, 7.

Von Knorring O. and Dyson P. (1959) An occurrence of genthelvite in the Younger Granite Province of northern Nigeria. *American Mineralogist*, **44**, 1294-1298.

Zito G. and Hanson S.L. (2017) Genthelvite overgrowths on danalite cores from a pegmatite miarolitic cavity in Cheyenne Canyon, El Paso County, Colorado. *Canadian Mineralogist*, **55**, 195-206.

7 CONCLUSÃO

A mineralização de U no depósito Madeira ocorre disseminada na fácies albita granito (núcleo + borda). O minério primário de U é exclusivamente o U-Pb-ETRL-pirocloro. Este depósito é classificado como do tipo intrusivo (IAEA, 2020), apresenta teores (328 ppm UO_2) comparáveis aos principais depósitos deste tipo e reservas significativas (52 kt U). Nos pegmatitos associados ao albita granito, a mineralização de U também é disseminada, e o pirocloro é herdado da rocha hospedeira.

O albita granito hospeda quatro tipos de pegmatitos: albita granito de núcleo pegmatítico (maior concentração de U), pegmatitos de borda, pegmatitos miarolíticos e veios de pegmatito. Os pegmatitos de borda foram posicionados em fraturas de contração situadas entre o albita granito de borda e as rochas circundantes. O albita granito de núcleo pegmatítico desenvolveu-se em fraturas centimétricas, enquanto os pegmatitos miarolíticos foram colocados em fraturas com drenagem pouco eficiente. Os veios de pegmatito estão colocados em falhas reversas e fraturas de extensão. O albita granito hospedeiro serve como fonte de todos os fluidos que contribuíram para a formação dos pegmatitos estudados. O pegmatito de borda originou-se do magma do albita granito de borda, enquanto o albita granito de núcleo pegmatítico, os pegmatitos miarolíticos e os veios de pegmatito são derivados do magma do albita granito de núcleo.

Todos os tipos de pegmatitos exibem a mesma mineralogia do albita granito de núcleo, composto principalmente de pirocloro, riebeckita, polilitionita, zircão, torita, xenótima, gagarinita-(Y), genthelvita, galena, microclinio, albita, quartzo e criolita. A exceção são os pegmatitos de borda, que compartilham a mineralogia do albita granito de borda, com fluorita ao invés de criolita e sem presença de gentelvita. Nos veios de pegmatito, a genthelvita é o único mineral portador de Be e foi o último mineral magmático a se formar, marcando a transição do estágio magmático tardio e do estágio hidrotermal inicial da evolução albita granito. Este mineral possui teores relativamente elevados de Zn (36,96 a 49,45% em peso de ZnO), baixos teores de Mn (0,61 a 3,03% em peso de MnO) e teores variáveis de Fe (2,10 a 10,94% em peso de FeO), preenchendo uma lacuna composicional no diagrama ternário Zn-Fe-Mn, comparado às ocorrências de outras localidades. Esta composição exclusiva se deve a condições de formação igualmente singulares.

O albita granito apresenta padrões extremos de fracionamento, excedendo aqueles da maioria dos granitóides peralcalinos fracionados do tipo-A1 em todo o mundo. O albita granito de núcleo pegmatítico e os veios de pegmatito amplificam esse fenômeno de fracionamento. Além disso, a riqueza de F tanto no albita granito quanto nos pegmatitos (atingindo até 35% em peso de F no veio de pegmatito rico em criolita) se destaca como uma ocorrência sem precedentes. As condições especiais impostas pela natureza rica em flúor do magma peralcalino fizeram com que a mineralização de U no depósito Madeira contrastasse fortemente com os principais depósitos intrusivos do mundo em três aspectos principais: dispersão homogênea da mineralização; pirocloro como minério primário exclusivo; e, mineralizações de U e Th formadas em diferentes estágios magmáticos. Além disso, os complexos de flúor enriqueceram a fusão residual com Li, Na, K, Rb e metais raros (U, Th, ETR, Be, Zr, Nb, Ta), contribuindo para o enriquecimento progressivo de ETRP em direção à posterior paragênese dos pegmatitos. O Be conservado no fluido tardio pela complexação com F foi responsável pela formação de genthelvita nos veios de pegmatitos, preenchendo as cavidades, circundando a polilitionita, quartzo I, xenotima, pirocloro, torita e zircão. A incorporação de ETRP em minerais cristalizados antes da genthelvita (ex. xenotima) acarretaram na composição da genthelvita com conteúdo médio de ETRL superior ao de ETRP.

Todos os cristais de pirocloro no albita granito (borda + núcleo) e nos pegmatitos associados sofreram alteração hidrotermal causada por fluidos aquosos altamente ácidos e ricos em F, resultando na corrosão de minerais magmáticos e na formação de fases minerais secundárias. No albita granito, o processo de alteração do pirocloro liberou diferentes cátions de forma seletiva (tais como ETRL, Nb e F), enquanto outros (como Fe e Si) foram incorporados. Isto resultou na formação sucessiva de diversas variedades secundárias de pirocloro e ao enriquecimento relativo de U, como no Fe-Mn-U-pirocloro (com até 13,82% em peso de UO_2). A alteração do pirocloro culminou na quebra da sua estrutura, resultando na formação de columbita-(Fe) pseudomórfica, e na precipitação de fluoretos ricos em ETRL, silicatos de U (com até 34,35% em peso de UO_2) e galena dentro das cavidades do pirocloro. A alteração mais intensa ocorreu na parte central do albita granito de núcleo, próximo ao depósito de criolita maciça, e no albita granito de borda, onde são mais abundantes os pirocloros secundários mais ricos em U e a columbita-(Fe) portadora de U.

Nos pegmatitos, os produtos de alteração do pirocloro herdado do albita granito refletem a composição do fluido hidrotermal localmente. A disponibilidade de F, Ca, Mn, Y e ETRP no fluido hidrotermal nos pegmatitos de borda, resultou na formação de pirocloro hidrotermal enriquecido em Ca, Y e ETRP, columbita-(Mn) (com ou sem U), silicatos ricos em HREE (Y, U, Th), galena e fluorita. Por outro lado, nos veios de pegmatito, a riqueza de F e Na no fluido hidrotermal, associado à depleção em Y e ETRP, levou à formação de pirocloro hidrotermal rico em Na, ETRL e Pb, columbita-(Fe) e à precipitação de silicatos ricos em Th (Zr, U), com conteúdo reduzido de Y e ETRP, e galena, associados com criolita. Nos veios de pegmatito, o reequilíbrio da genthelvita no estágio hidrotermal inicial permitiu a incorporação de Fe, Mn, Mg, Pb, Ba, Na, K e U no sítio estrutural Zn^{2+}, e a alocação do excesso de Si, Al, Ti e P nos sítios estruturais ^{IV}Si e ^{IV}Be. A presença de U (até 0,25% em peso UO_2) na genthelvita se deve à alteração do pirocloro no estágio hidrotermal inicial, em que parte do U foi incorporado pelo fluido. Em todo o albita granito e nos pegmatitos associados, a paragênese primária (inclusive a genthelvita) e a paragênese secundária, gerada durante o hidrotermalismo precoce, foram afetadas pelo hidrotermalismo tardio, causando corrosão e precipitação continuada de criolita e fluorita.

A partir da integração dos resultados apresentados nesta tese, foram elaboradas as seguintes considerações sobre a evolução metalogenética e a transição magmático-hidrotermal do sistema albita granito e seus pegmatitos associados:

(1) A ascensão do magma do albita granito em direção a profundidades crustais mais rasas resultou em uma rápida redução na pressão confinante. Esta mudança abrupta de pressão causou no magma do albita granito de borda a separação de uma fase aquosa pobre em F, com enriquecimento em K, Ca, Sr, Zr, Y e ETRP. Este fluido aquoso ascendeu em direção ao ápice da intrusão, dando origem aos pegmatitos de borda durante os estágios iniciais da evolução magmática.

(2) O magma peralcalino, a riqueza de F e a baixa temperatura do magma permitiram a dispersão homogênea da mineralização de U por todo o albita granito, e condicionaram a cristalização do pirocloro ao invés da columbita nos estágios magmáicos iniciais. Nos estágios mais tardios da evolução magmática, à medida que a cristalização do zircão se tornou mais intensa e acompanhada por xenotima e torita, o magma já estava previamente empobrecido em U, Nb, Ta e ETRL.

(3) Com a progressiva cristalização fracionada do albita granito de núcleo, a fusão residual final do estágio magmático resultou na formação de albita granito de núcleo pegmatítico, caracterizado por um enriquecimento extremo em elementos de alto potencial iônico.

(4) Neste estágio magmático final, o deslocamento da falha reversa pode ter causado uma segunda redução abrupta na pressão, levando à separação de fluidos aquosos

supercríticos e resultando no sub-resfriamento do sistema. Esta circunstância permitiu a injeção de uma fusão aquosa residual enriquecida em Y-Li-Be-Zn-F em cavidades miarolíticas, bem como nos planos de falha e fraturas de extensão horizontais, levando à formação dos veios de pegmatito ricos em anfibólio.

(5) Foi durante este período que também ocorreu a imiscibilidade magma-magma, levando à segregação de um magma aluminossilicático rico em K e F (baixo H_2O) com enriquecimento adicional em Y-Li-Be-Zn, e de um magma aquoso extremamente rico em Na e F (baixo SiO_2). Estes magmas formaram os veios de pegmatito ricos em polilitionita e ricos em criolita, respectivamente.

(6) Nos veios de pegmatito, a concentração extremamente elevada de flúor e a cristalização de grandes quantidades de galena (além de esfalerita e pirita), levaram a uma diminuição efetiva na fugacidade do H_2S, permitindo a formação da genthelvita em condição estável na fusão tardia, em um ambiente alcalino e subaluminoso, sob temperaturas relativamente altas (>375°C), condições redutoras e alta atividade de O.

(7) A transição magmático-hidrotermal ocorreu independentemente para cada corpo – os pegmatitos de borda, o albita granito de borda, o albita granito de núcleo e os veios de pegmatitos – quando a fase aquosa residual foi exsolvida da rocha cristalizada. Esta fase aquosa exibiu uma composição que, em escala local, refletiu o grau de fracionamento do magma no ponto de saturação de H_2O.

(8) Dentro dos veios de pegmatitos e dos pegmatitos de borda, a exsolução de fluidos hidrotermais ricos em F levou à formação de criolita II e fluorita, respectivamente, juntamente com a alteração significativa (autometassomatismo) de minerais primários. Em uma escala muito maior, a exsolução de fluidos hidrotermais ricos em F no albita granito de núcleo deu origem ao depósito hidrotemal de criolita maciça, ao mesmo tempo que causou alterações significativas na porção central do plúton. A temperatura máxima de homogeneização de 400°C, medida na criolita hidrotermal (Bastos Neto *et al*., 2009), determina a temperatura mínima inicial do processo hidrotermal.

8 BIBLIOGRAFIA

Almeida, F.F.M., Hasui, Y., Brito Neves, B.B. & Fuck, R.A. 1981. Brazilian structural Provinces: an introduction. *Earth Sciences Reviews*, 17: 1-29.

Atencio, D., Andrade, M. B., Christy, A. G., Giere, R. & Kartashov P. M. 2010. The pyrochlore supergroup of minerals: Nomenclature. *The Canadian Mineralogist*, 48: 673-698.

Bastos Neto, A.C., Pereira, V.P., Lima, E.F., Ferron, J.M., Minuzzi, O., Prado, M., Ronchi, L.H., Flores, J.A., Frantz, J.C., Pires, A., Pierosan, R., Hoff, R., Botelho, N.F., Rolim, S.B., Rocha, F. & Ulmann, L. 2005. A jazida de criolita da Mina Pititnga (Amazonas). *In*: Marini, O.J., Queiroz, E.T. & Ramos, B.W. (Eds.). *Caracterização de Depósitos Minerais em Distritos Mineiros da Amazônia*. Brasília, DNPM-CT/MINERAL-ADIMB, p. 481-547.

Bastos Neto, A.C., Pereira, V.P., Ronchi, L.H., Lima, E.F. & Frantz, J.C. 2009. The world-class Sn, Nb, Ta, F (T, REE, Li) deposit and the massive cryolite associated with the albite-enriched facies of the Madeira A-type granite, Pitinga Mining District, Amazonas State, Brazil. *The Canadian Mineralogist*, 47: 1329-1357.

Bastos Neto, A.C., Pereira, V.P., Pires, A.C., Barbanson, L. & Chauvet, A. 2012. Fluorine-rich xenotime from the Nb-Ta-Sn Madeira world-class deposit associated with the albite-enriched granite at Pitinga, Amazonia, Brazil. *The Canadian Mineralogist*, 50: 1019-1032.

Bastos Neto, A.C., Ferron, T.M.M., Chauvet, A., Chemale, F., Lima, E.F., Barbanson, L. & Costa, C.F.M. 2014. U-Pb dating of the Madeira Suite and structural control of the albite-enriched granite at Pitinga (Amazônia, Brazil): evolution of the A-type magmatism and implications for the genesis of the Madeira Sn-Ta-Nb (REE, cryolite) world-class deposit. *Precambrian Research*, 243: 181-196.

Bates, R.L. & Jackson, J.A. (Eds.). 1987. *Glossary of Geology*. Virginia, American Geological Institute, 788 p.

Baumann, L. 1970. Tin deposits of the Erzgebirge. *Institution of Mining and Metallurgy Transactions*, 79(B): 68-75.

Bettencourt, J.S., Juliani, C., Xvier, R.P., Monteiro, L.V.S., Bastos Neto, A.C., Klein, E.L., Assis, R.R., Leite Jr, W.B., Moreto, C.P.N., Fernandes, C.M.D. & Pereira, V.P. 2016. Metallogenetic systems associated with granitoid magmatism in the

Amazonian Craton: An overview of the present level of understanding and exploration significance. *Journal of South American Earth Sciences*, 68: 22-49.

Burt, D.M. 1980. The stability of danalite, $Fe_4Be_3(SiO_4)S$. *American Mineralogist,* 65: 355-360.

Burt, D.M. 1988. Stability of genthelvite, $Zn_4(BeSiO_4)_3S$: an exercise in chalcophilicity using exchange operators. *American Mineralogist*, 73: 1384-1394.

Cameron, E.N., Jahns, R.H., McNair, A.H. & Page, L.R. 1949. Internal Structure of Granitic Pegmatites. *Economic Geology*, Monograph (2), 115 p.

Černý, P. & Ercit, T.S. 2005. The classification of granitic pegmatites revisited. *The Canadian Mineralogist,* 43: 2005-2026.

Černý, P., London, D. & Novak, M. 2012. Granitic pegmatites as reflections of their sources. *Elements*, 8: 289-294.

Costi, H.T. 2000. *Petrologia de granitos alcalinos com alto flúor mineralizados em metais raros: o exemplo do Albita-granito da Mina Pitinga, Amazonas, Brasil*. Belém, 345 p. Tese de Doutorado, Curso de Pós-graduação em Geociências, Centro de Geociências, Universidade Federal do Pará.

Costi, H.T., Dall'agnoll, R. & Moura, C.A.V. 2000. Geology and Pb-Pb Geochronology of Paleoproterozoic volcanic and granitic rocks of Pitinga province, Amazonian craton, northern Brazil. *International Geology Review,* 42: 832-849.

Costi, H.T., Borges, R.M. & Dall'agnol, R. 2005. Depósitos de estanho da mina Pitinga, estado do Amazonas. *In*: Marini, O.J., Queiroz, E.T. & Ramos, B.W. (Eds.). Caracterização de Depósitos Minerais em Distritos Mineiros da Amazônia. Brasília: DNPM-CT/MINERAL-ADIMB, p. 391-475.

Costi, H.T., Dall'agnol, R., Pichavant, M. & Ramo, O.T. 2009. The peralkaline tin-mineralized Madeira cryolite albite-rich granite of Pitinga, Amazonian Craton, Brazil: petrography, mineralogy and crystallization processes. *The Canadian Mineralogist*, 47: 1177-1203.

Costi, H.T., Dall'Agnol, R., Pichavant, M. & Ramo, O.T. 2010. The peralkaline tin-mineralized Madeira cryolite albite-rich granite of Pitinga, Amazonian craton, Brazil: petrography, mineralogy and crystallization processes. *The Canadian Mineralogist,* 47: 1301-1327.

Cuney, M. & Kyser, T.K. 2008. Recent and not-so-recent developments in uranium deposits and implications for exploration. *Mineralogical Association of Canada*, Short Course (39), 257 p.

Deer, W.A., Howie, R.A., Wise, W.S. & Zussman, J. (Eds.). 2004. *The rock-forming minerals series*: *framework silicates (silica minerals, feldspathoids and the zeolites)*. London, The Geological Society, 988 p.

Dill, H.G. 2015. Pegmatites and aplites: their genetic and applied ore geology. *Ore Geology Reviews*, 69: 417-561.

Dill, H.G. 2010. The "chessboard" classification scheme of mineral deposits: mineralogy and geology from aluminium to zirconium. *Earth Science Reviews*, 100: 1-420.

Drysdall, A.R., Jackson, J., Ramsay, C.R., Douch, C.J. & Hackett, D. 1984. Rare element mineralization related to Precambrian alkali granites in the Arabian Shield. *Economic Geology*, 79(6): 1366-1377.

Ferron, J.M.T.M., Bastos Neto, A.C., Lima, E.F., Costi, H.T., Moura, C.A.V., Prado, M. & Galarza, M.A. 2006. Geologia e cronologia Pb-Pb de rochas graníticas e vulcânicas ácidas a intermediárias paleoproterozóicas da Província de Pitinga, Cráton Amazônico. *Revista Brasileira de Geociências*, 36(3): 499-512.

Grew, E.S. (Ed.). 2002. Beryllium: Mineralogy, Petrology, and Geochemistry. *Reviews in Mineralogy and Geochemistry*, 50(1), 76 p.

Hadlich, I.W., Bastos Neto, A.C., Botelho, N.F. & Pereira, V.P. 2019. The thorite mineralization in the Madeira Sn-Nb-Ta world-class deposit. *Ore Geology Reviews*, 105: 445-466.

Hogarth, D.D. 1977. Classification and nomenclature of the pyrochlore group. *American Mineralogist*, 62, 403-410.

Horbe, M.A., Horbe, A.C., Teixeira, J.T. & Costi, H.T. 1985. Granito Madeira: petrologia, petroquímica e mineralizações. *In*: SIMPÓSIO DE GEOLOGIA DA AMAZÔNIA, 2, 1985, Belém. *Anais*... Belém, SBG, v. 2, p. 284-320.

IAEA. 2016. Climate Change and Nuclear Power 2016. *International Atomic Energy Agency*, 98 p. Disponível em: <http://www-pub.iaea.org/MTCD/Publications/PDF/CCANP16web-86692468.pdf>. Acesso em: 05 out. 2018.

IAEA. 2020. Annual Report 2020. *International Atomic Energy Agency*, 191 p. Disponível em: <https://www.iaea.org/sites/default/files/publications/reports/2020/gc65-5.pdf>. Acesso em: 15 ago. 2022.

Jahns, R.H. & Burnham, C.W. 1969. Experimental studies of pegmatite genesis. I. A model for the derivation and crystallization of granitic pegmatites. *Economic Geology*, 64: 843-864.

Lengler, H.F. 2016. *Pegmatitos do albita granito Madeira: avaliação do minério para fins de beneficiamento*. Porto Alegre, 118 p. Monografia de Conclusão de Curso, Curso de Geologia, Instituto de Geociências, Universidade Federal do Rio Grande do Sul.

Lenharo, S.L.R. 1998. *Evolução magmática e modelo metalogenético dos granitos mineralizados da região de Pitinga, Amazonas, Brasil*. São Paulo, 290 p. Tese de Doutorado, Curso de Pós-Graduação em Geociências, Instituto de Geociências, Universidade de São Paulo.

Lenharo, S.L.R., Pollard, P.J. & Born, H. 2003. Petrology and textural evolution of granites associated with tin and rare-metals mineralization at the Pitinga mine, Amazonas, Brasil. *Lithos*, 66: 37-61.

London, D. 2008. Pegmatites. *The Canadian Mineralogist,* Special Publication 10, 347 p.

London, D. & Kontak, D.J., 2012, Granitic pegmatites: Scientific wonders and economic bonanzas, *Elements*, 8: 257-261.

London, D. & Morgan, G.B.V.I. 2012. The pegmatite puzzle. *Elements*, 8: 263-268.

Lumpkin G. R. & Ewing R. C. 1992. Geochemical alteration of pyrochlore group minerals: Microlite subgroup. *American Mineralogist*, 77: 179-188.

Lumpkin G. R. & Ewing R. C. 1995. Geochemical alteration of pyrochlore group minerals: Pyrochlore subgroup. *American Mineralogist*, 80: 732-743.

Lumpkin G. R. & Ewing R. C. 1996. Geochemical alteration of pyrochlore group minerals: betafite subgroup. *American Mineralogist*, 81: 1237-1248.

Martin, R.F. & Vito, C. 2005. The patterns of enrichment in felsic pegmatites ultimately depend on tectonic setting. *The Canadian Mineralogist*, 43: 2027-2048.

McMaster, S.A. 2016. *Investigations into the synthesis, characterization and uranium extraction of the pyrochlore mineral betafite*. Melbourne, 244 p. Thesis, College of Science, Engineering and Health, RMIT University.

Minuzzi, O.R.R. 2005. *A columbitização do pirocloro da subfácies albita-granito de núcleo do Granito Madeira, Pitinga-AM: relações com a gênese da mineralização criolítica*. Porto Alegre, 156 p. Tese de Doutorado, Curso de Pós-graduação em

Geociências, Instituto de Geociências, Universidade Federal do Rio Grande do Sul.

Minuzzi, O.R.R., Bastos Neto, A.C., Pereira, V.P. & Nunes, L. 2006. A columbitização do pirocloro do albita granito na mina de Pitinga (AM): relações com a mineralização de criolita. *Revista Brasileira de Geociências*, 35(1): 123-137.

Minuzzi, O.R.R., Bastos Neto, A.C., Formoso, M.L.L., Andrade, S., Janasi, V.A. & Flores, J.A. 2008. Rare earth elements and yttrium geochemistry applied to the genetic study of cryolite ore at the Pitinga Mine (Amazon, Brazil). *Annals of the Brazilian Academy of Sciences*, 80(4): 719-733.

Nardi, L.V.S., Formoso, M.L.L., Jarvis, K., Oliveira, L., Bastos Neto, A.C. & Fontana, E. 2012. REE, Y, Nb, U and Th contents and tetrad effect in zircon from a magmatic-hydrothermal F-rich system of Sn-rare metal-cryolite mineralized granites from the Pitinga Mine, Amazonia, Brazil. *Journal of South American Earth Sciences*, 33: 34-42.

Paludo, C.M., Bastos Neto, A.C., Pereira, V.P. & Botelho, N.F. 2018. Mineralogia e geoquímica de pegmatitos ricos em ETR, F e metais alcalinos associados à fácies albita granito no depósito de Sn-Nb-Ta-(F, ETR, U, Th) Madeira (mina Pitinga, AM, Brasil). *Pesquisas em Geociências*, 45(3): 1-24.

Pierosan, R., Lima, E.F., Nardi, L.V.S., Bastos Neto, A.C., Campos, C.P., Ferron, J.M.T.M. & Prado, M. 2011. Geochemistry of Paleoproterozoic volcanic rocks of the Iricoumé Group, Pitinga Mining District, Amazonian craton, Brazil. *International Geology Reviews*, 53: 946-976.

Pires, A.C. 2010. *Xenotima, gagarinita, fluocerita e waimirita da Mina Pitinga (AM): mineralogia e avaliação preliminar do potencial do albita granito para exploração de elementos terras raras e ítrio*. Porto Alegre, 201 p. Tese de Doutorado, Curso de Pós-Graduação em Geociências, Instituto de Geociências, Universidade Federal do Rio Grande do Sul.

Pointer, C.M. 1987. *Remobilisation of uranium and thorium by ore-forming fluids: a mineralogical study*. Birmingham, 311 p. Tese de Doutorado, Universidade de Aston.

Pöml P., Geisler T., Cobos-Sabate´ J., Wiss T., Raison P. E., Schmidt-Beurmann P., Deschanels X., Jégou C., Heimink J. & Putnis A. 2011. The mechanism of the hyrothermal alteration of cerium- and plutonium-doped zirconolite. *Journal of Nuclear Materials*, 410: 10-23.

Pownceby, M.I. & Johnson, C. 2014. Geometallurgy of Australian uranium deposits. *Ore Geology Reviews*, 56: 25-44.

Roberts, S.K., Bourcier, W.L. & Shaw, H.F. 2000. Aqueous dissolution kinetics of pyrochlore, zirconolite and brannerite at 25, 50, and 75 C. *Radiochimica Acta*, 88: 539-543.

Ronchi, F.C., Althoff, F.J., Bastos Neto, A.C. & Dill, H.G. 2019. Structural control of REE-pegmatites associated with the world-class Sn-Nb-Ta-cryolite deposit at the Pitinga mine, Amazonas, Brazil. *Pesquisas em Geociências*, 46(1): 1-14.

Ronchi, L.H., Bastos Neto, A.C., Gedoz, S.C., Weber, M.L., Pereira, V.P. & Andrek, M. 2011. A transição magmático-hidrotermal registrada por inclusões fluidas no albita-granito de núcleo, Mina Pitinga, Amazonas. *In*: Frantz, J.C., Charão, J.M. & Jost, H. (Eds.). 2011. Contribuições à metalogenia do Brasil. Porto Alegre, CPRM-UFRGS.

Siachoque, A., Salazar, C.A. & Trindade, R. 2017. Emplacement and deformation of A-type granite (Amazonian Craton, Brazil). *Lithos*, 277: 284-301.

Sørensen, H., Bailey, J.C. & Rose-Hansen, J. 2011. The emplacement and crystallization of the U-Th-REE-rich agpaitic and hyperagpaitic lujavrites at Kvanefjeld, Ilímaussaq alkaline complex, South Greenland. *Bulletin of the Geological Society of Denmark*, 59: 69-92.

Staatz, M.H. 1978. I and L uranium and thorium vein system, Bokan Mountain, southern Alaska. *Economic Geology*, 73(4): 512-523.

Stilling, A., Černý, P. & Vanstone, P.J. 2006. The Tanco pegmatite at Bernic Lake, Manitoba: XVI. Zonal and bulk compositions and their petrogenetic significance. *The Canadian Mineralogist*, 44: 599-623.

Stolnik, D. 2015. *Caracterização da xenotima na fácies pegmatítica do albita granito de núcleo, Pitinga (AM)*. Porto Alegre, 67 p. Monografia de Conclusão de Curso, Curso de Geologia, Instituto de Geociências, Universidade Federal do Rio Grande do Sul.

Thomas, R., Webster, J.D. & Heinrich, W. 2000. Melt inclusions in pegmatite quartz: complete miscibility between silicate melts and hydrous fluids at low pressure. *Contributions to Mineralgy and Petrografy*, 139: 394-401.

Thomas, R., Davidson, P., Rhede, D. & Leh, M. 2008. The miarolitic pegmatites from the Königshain: a contribution to understanding the genesis of pegmatites. *Contributions to Mineralogy and Petrology*, 157: 505-523.

Thomas, R. 2009a. What can melt and fluid inclusion tell us about pegmatite-forming processes? *Estudos Geológicos*, 19: 15-19.

Thomas, R., Davidson, P., Rhede, D. & Leh, M. 2009b. The miarolitic pegmatites from the Königshain: a contribution to understanding the genesis of pegmatites. *Contributions to Mineralogy and Petrology*, 157(4): 505-523.

Valley, J.W. 2012. Migma vs. Magma. *Elements*, 8: 243-244.

Veiga Jr., J.P., Nunes, A.C.B., Fernandes, A.S., Amaral, J.E., Pessoa, M.R. & Cruz, S.A.S. 1979. *Projeto Sulfetos de Uatumã: Relatório Final*. Manaus: DNPM/CPRM.

Weber, M.L., Gedoz, S.C., Benetti, F., Petry, A.C., Ronchi, L.H., Bastos Neto, A.C., Pereira, V.P. & Althoff, F.J. 2007. Variações mineralógicas e petrográficas na porção central do albita-granito Madeira, Pitinga, AM. *Gaea Journal of Geoscience*, 3(1): 9-17.

Xu, H., Wang, Y., Zhao, P., Bourcier, W.L., Konynenburg, R. & Shaw, H. 2004. Investigation of pyrochlore-based Ubearing ceramic nuclear waste: Uranium leaching test and TEM observations. *Environment Science Technology*, 38: 1480-1486.

9 ANEXOS

9.1 *Anexo A – Mapa Geológico Regional*

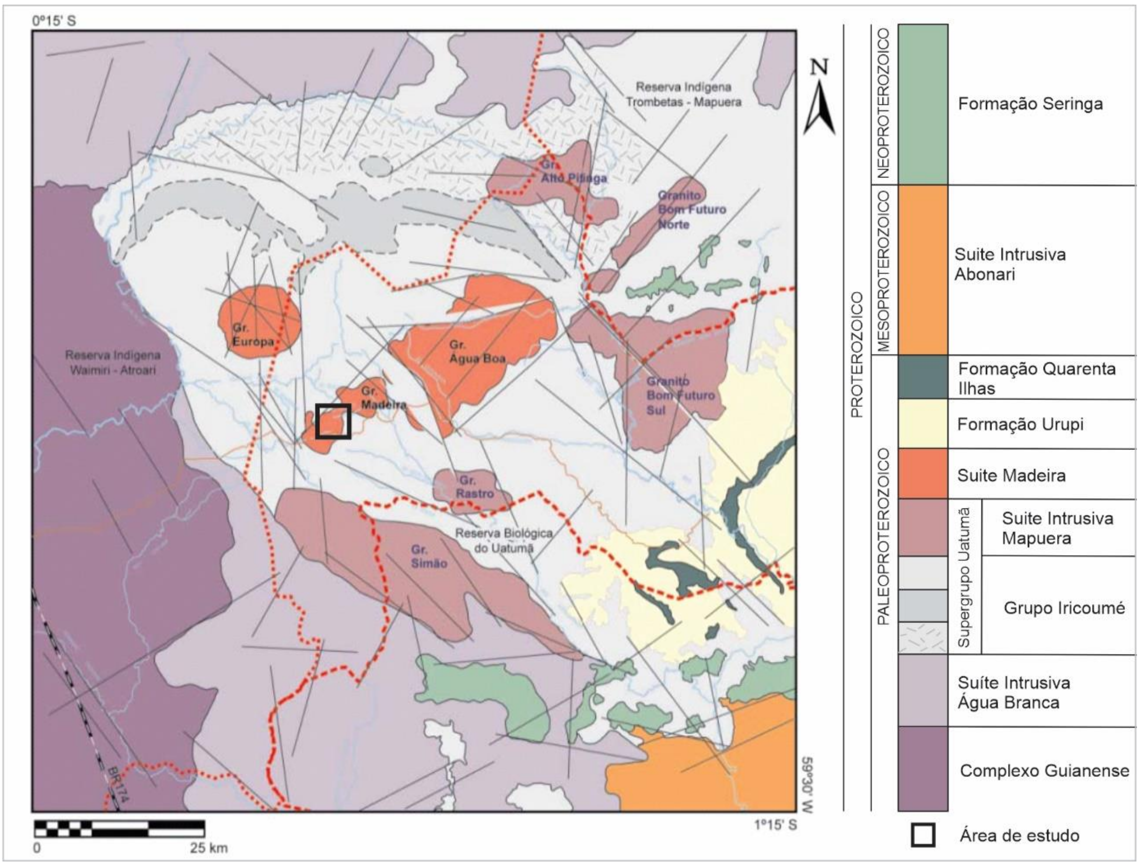

(adaptado de Bastos Neto et al., 2005)

9.2 *Anexo B – Minerais da Mina de Pitinga e suas fórmulas químicas*

Mineral	*Fórmula Química*
Albita	$NaAlSi_3O_8$
Annita	$K(Fe^{2+},Li)_3AlSi_3O_{10}(OH,F)_2$
Cassiterita	SnO_2
Clorita	$(Al, Fe^{2+},Fe^{3+},Li,Mg,Mn,Ni)_{5\text{-}6}(Al, Si, Fe^{3+})_4O_{10}(OH)_8$
Columbita	$(Fe,Mn)(Nb,Ta)_2O_6$
Criolita	Na_3AlF_6
Esfalerita	$(Zn,Fe)S$
Fluocerita	$(La,Ce)F_3$
Fluorita	CaF_2
Gagarinita-(Y)	$NaCaYF_6$
Galena	PbS
Genthelvita	$Zn_4Be_3(SiO_4)_3S$
Hematita	Fe_2O_3
Magnetita	Fe_3O_4
Microclínio	$K(AlSi_3O_8)$
Muscovita	$KAl_2Si_3AlO_{10}(OH,F)_2$
Polilithionita	$KLi_2AlSi_4O_{10}(OH,F)_2$
Pirita	FeS_2
Pirocloro	$(Na,Ca,Pb,U,ETR)_2(Nb,Ta)_2O_6(OH,F)$
Quartzo	SiO_2
Riebeckita	$Na_2(Fe,Mg)_5Si_8O_{22}(OH,F)_2$
Torita	$ThSiO_4$
Topázio	$Al_2SiO_4(F,OH)_2$
Xenotima	$(Y,ETRP)PO_4$
Zircão	$ZrSiO_4$

ANEXO I

Título da Tese:

“ESTUDO INTEGRADO DOS PEGMATITOS, DA MINERALIZAÇÃO DE URÂNIO E DA GENTHELVITA NO DEPÓSITO Sn-Nb-Ta (ETR, U, Th, F) MADEIRA (MINA PITINGA, AM): A TRANSIÇÃO MAGMÁTICO-HIDROTERMAL E SUAS IMPLICAÇÕES METALOGENÉTICAS”

Área de Concentração: Geoquímica

Autora: **Ingrid Weber Hadlich**

Orientador: Prof. Dr. Artur Cezar Bastos Neto (UFRGS/PPGGEO)
Coorientador: Prof. Dr. Vitor Paulo Pereira (UFRGS/IGEO)

Examinador:
Prof. Dr. José Carlos Frantz

Data:
17 de novembro de 2023

Conceito:
A

PARECER:

A Tese de Doutorado submetida, cuja defesa foi realizada em apresentação pública, atendeu a todos os requisitos para a obtenção do Título de Doutor. Trata-se de um trabalho composto por: 1-Objetivos, apresentados de forma clara e bem definidos; Estrutura da Tese, bem organizada; 2-Geologia Local, com foco na Suíte Estanífera Madeira, fácies mineralizada do albita granito, Depósito Madeira e modelo genético do albita granito; 3-Urânio, depósitos, minerais, pirocloro, alteração do pirocloro e geoquímica do urânio; 4-Pegmatitos Graníticos, o que são, composição, colocação, pegmatitos de borda, classificação e gênese de pegmatitos graníticos, comparação de modelos; 5-Genthelvita, cristaloquímica, estabilidade e ocorrências; 6-Resultados, com a apresentação de três artigos como segue: a) *Uranium mineralization in the Madeira Sn-Nb-Ta (U, Th, REE, F) world-class deposit (Pitinga, Amazonas State, Brazil): pyrochlore and its alteration products under hypogene conditions* (Economic Geology); b) *Pegmatites hosted by the albite-enriched granite at the Madeira Sn-Nb-Ta-F world class deposit, Pitinga Province, Amazonas, Brazil* (International Geology Review); c) *Mn-Fe-rich genthelvite from pegmatites associated with the Madeira Sn-Nb-Ta world-class deposit (Pitinga, Brazil): new constraints on the magmatic-hydrothermal transition in the albite-enriched granite system* (Mineralogical Magazine); 7-Conclusões; 8-Bibliografia.
No primeiro artigo, é apresentado um depósito de Urânio no albita granito Madeira equiparado a depósitos do tipo intrusivo, com a alteração hidrotermal e uma discussão sobre processos na formação do depósito.
No segundo artigo, são abordadas as diferentes origens e modelos de formação de pegmatitos presentes no albita granito, com dados estruturais, texturais, mineralógicos e composicionais, em especial a química de minerais de pegmatitos e albita granito para suportar a discussão sobre a origem do fluido hidrotermal e a transição magmático-hidrotermal no sistema granito/pegmatito.
No terceiro artigo, o objeto é a ocorrência de genthelvita nos pegmatitos e sua variação composicional que pode representar as condições de formação.
A defesa presencial foi de excelente qualidade e cumpriu plenamente com os objetivos dessa etapa com a candidata mostrando um grande conhecimento sobre os assuntos abordados na Tese.
Na avaliação realizada, entendemos que a candidata INGRID WEBER HADLICH atendeu a todos os requisitos necessários para a aprovação da Tese de Doutorado e para a obtenção do Título de Doutor.
É o parecer.

Assinatura: Data: 17/11/2023

Ciente do Orientador:

Ciente do Aluno:

ANEXO I
Título da Tese:
“ESTUDO INTEGRADO DOS PEGMATITOS, DA MINERALIZAÇÃO DE URÂNIO E DA GENTHELVITA NO DEPÓSITO Sn-Nb-Ta (ETR, U, Th, F) MADEIRA (MINA PITINGA, AM): A TRANSIÇÃO MAGMÁTICO-HIDROTERMAL E SUAS IMPLICAÇÕES METALOGENÉTICAS”
Área de Concentração: Geoquímica
Autora: **Ingrid Weber Hadlich**
Orientador: Prof. Dr. Artur Cezar Bastos Neto (URFGS/PPGGEO) Coorientador: Prof. Dr. Vitor Paulo Pereira (UFRGS/IGEO)
Examinadora: Dra. Lucy Takehara Chemale
Data: 17/11/2023
Conceito: A (Excelente)
PARECER: A tese de doutorado da discente Ingrid Weber Hadlich está de acordo com os critérios formais e materiais estabelecidos pelo Programa de Pós-graduação Geociências. Está estruturada na forma de entrega de artigos submetidos, possui uma introdução com apresentação dos objetivos e discussão dos temas abordados no artigo, no desenvolvimento são apresentados três artigos submetidos e na conclusão é feito um fechamento inter-relacionando as conclusões dos três artigos. Os artigos submetidos para revistas expressivas na área das geociências. A tese está muito bem escrita e foi apresentada de forma clara, por vezes, com textos descritivos longos. Observa-se que foram utilizados dados analíticos robustos que foram bem discutidos nos artigos que corroboraram com as conclusões obtidas. Assim, não há observações adicionais a serem indicadas para serem incorporadas no trabalho desenvolvido. Esta tese traz grande contribuição para o conhecimento geológico do Depósito polimetálico de Pitinga que poderão contribuir para otimizar o desenvolvimento da rota tecnológica de aproveitamento dos demais commodities deste depósito. A doutoranda fez uma apresentação de sua defesa de tese excelente e respondeu aos questionamentos mostrando pleno domínio do conteúdo.
Assinatura: Lucy Takehara Chemale Data: 17/11/2023.

Ciente do Orientador:

Ciente do Aluno:

ANEXO I

Título da Tese:

“ESTUDO INTEGRADO DOS PEGMATITOS, DA MINERALIZAÇÃO DE URÂNIO E DA GENTHELVITA NO DEPÓSITO Sn-Nb-Ta (ETR, U, Th, F) MADEIRA (MINA PITINGA, AM): A TRANSIÇÃO MAGMÁTICO-HIDROTERMAL E SUAS IMPLICAÇÕES METALOGENÉTICAS”

Área de Concentração: Geoquímica

Autora: **Ingrid Weber Hadlich**

Orientador: Prof. Dr. Artur Cezar Bastos Neto (URFGS/PPGGEO)
Coorientador: Prof. Dr. Vitor Paulo Pereira (UFRGS/IGEO)

Examinadora: Profa. Dra. Lydia Maria Lobato

Data: 17-Nov-2023

Conceito: **A**

PARECER: Candidata cumpriu de forma exemplar as exigências para o grau de Doutor. Seu texto é bem escrito e científicamente muito bom. Fez boa apresentção, explanando cuidadosamente o conteúdo do seu trabalho.

Assinatura:

Data: 17-Nov-2023

Ciente do Orientador:

Ciente do Aluno: